Научном већу Института за физику у Београду

Предмет: Молба за покретање поступа за избор у звање научни сарадник

М О Л Б А

С обзиром да испуњавам критеријуме прописане од стране Министарства просвете, науке и технолошког развоја за избор у звање научни сарадник, молим Научно веће Института за физику у Београду да покрене поступак за мој избор у звање научни сарадник.

У прилогу достављам:

1. мишљење руководиоца лабораторије са предлогом комисије за избор у звање;
2. стручну биографију;
3. преглед научне активности;
4. елементе за квалитативну и квантитативну оцену научног доприноса са доказима;
5. списак и копије објављених радова и других публикација
6. податке цитираности
7. уверење о одбрањеној докторској дисертацији

С поштовањем,

B.Sataric

др Богдан Сатарић

Научном већу Института за физику у Београду

Предмет: Мишљење руководиоца лабораторије о избору др Богдана Сатарића у звање научни сарадник

Др Богдан Сатарић је сарадник Лабораторије за примену рачунара у науци, у оквиру Националног центра изузетних вредности за изучавање комплексних система Института за физику у Београду. У истраживачком раду бави се темама везаним за примену нумеричких метода у вишечестичним комплексним системима. С обзиром да испуњава све предвиђене услове у складу са Правилником о поступку, начину вредновања и квантитативном исказивању научноистраживачких резултата истраживача МПНТР, сагласан сам са покретањем поступка за избор др Богдана Сатарића у звање научни сарадник.

За састав комисије за избор др Богдана Сатарића у звање научни сарадник предлажем:

(1) др Антун Балаж, научни саветник, Институт за физику у Београду
(2) др Ивана Васић, виши научни сарадник, Институт за физику у Београду
(3) др Срђан Шкрбић, редовни професор Природно-математичког факултета Универзитета у Новом Саду

др Антун Балаж
научни саветник
Руководилац Лабораторије за примену рачунара у науци

Стручна биографија
Богдана Сатарића

Богдан Сатарић је рођен 12. децембра 1983. године у Београду. Основну школу “Светозар Марковић - Тоза” завршио је у Новом Саду, као и Гимназију “Исидора Секулић”. Основне студије је похађао на Факултету Техничких Наука Универзитета у Новом Саду на смеру Рачунарство и аутоматика у периоду од 2002. до 2008. године. Током студија добио је стипендију Министарства науке Републике Србије и Владе Републике Србије. Мастерирао је 2008. године са просечном оценом 9.25. Мастер рад под називом “Једно решење веб базираног подсистема за управљање ТВ тестним уређајима” урадио је под руководством проф. др Николе Теслића.

У периоду од 2008. до 2010. године радио је као софтвер инжењер у компанији РТ-РК у Новом Саду на пројектима развоја веб апликација и аудио драјвера.

Докторске студије на Факултету Техничких Наука Универзитета у Новом Саду уписао је 2009. године. Докторску дисертацију под насловом „Паралелно транспоновање података у оквиру нумеричког алгоритма за решавање Грос-Питаевски једначине“ урађену под менторством др Антуна Балажа, одбранио је 28. јуна 2017. године.

Богдан Сатарић је активно запослен на позицији софтвер инжењера у ЦЕРН-у (Женева) као корисник (USER) у оквиру CMS експеримента као и на позицији доцента на Факултету Техничких Наука у Новом Саду (у замрзнутом статусу).

Др Богдан Сатарић је до сада објавио 8 радова у међународним часописима.

Преглед научне активности
Богдана Сатарића

Богдан Сатарић је започео свој истраживачки рад 2012. године под менторством др Антуна Балажа. Научна активност кандидата је у области кондензоване материје, и он се бави проблемима ултрахладних бозонским гасова у присуству дипол-дипол интеракције, као и развојем паралелних нумеричких алгоритама и програма за нумеричке симулације ових физичких система.

Кандидат је успешно развио хибридни алгоритам који омогућава проширење раније развијеног нумеричког алгоритма за решавање Грос-Питаевски једначине уз помоћ Кренк-Николсон методе. Ранији алгоритам развијен је за рачунаре са дељеном меморијом недовољан је за проучавање система код којих је неопходно коришћење високе резолуције за таласну функцију система. Ово ограничење произилази из недовољне количине радне меморије на једном рачунару за системе проучаване у високој резолуцији, као и због недовољне брзине обраде великог скупа података који би такав систем описивао. Хибридни алгоритам развијен од стране кандидата се огледа у дистрибуирању и обради података на кластеру рачунара, чиме се имплицитно омогућава временска еволуција физичког система са великим нивоом детаља. Као подршка остварењу основног циља, развијено је више верзија алгоритама дистрибуције и транспоновања тродимензионалних матрица, при чему је коначан алгоритам искоришћен за формулисање и имплементацију хибридног алгоритма за решавање Грос-Питаевски једначине. У сврху верфикације тачности рада новог алгоритма и његове имплементације, развијено је аутоматско тестирање нумеричке тачности хибридног алгоритма у односу на алгоритам који користи дељену меморију. Развијени су и аутоматски тестови за мерење убрзања и скалирања који су показали одличне перформансе и скалабилност новог хибридног решења. Резултат рада је представљен у следећем међународном часопису:

- **B. Satarić,** V. Slavnić, A. Belić, A. Balaž, P. Murugandam, S. K. Adhikari, “Hybrid OpenMP/MPI programs for solving the time-dependent Gross-Pitaevskii equation in a fully anisotropic trap”, Computer Physics Communications 200, 411 (2016). DOI: 10.1016/j.cpc.2015.12.006, IF(2016)=3.936

Елементи за квалитативну оцену научног доприноса др Богдана Сатарића

1 Квалитет научних резултата

1.1 Значај научних резултата

Најзначајнији рад др Богдана Сатарића је:

- **B. Satarić,** V. Slavnić, A. Belić, A. Balaž, P. Murugandam, S. K. Adhikari, "Hybrid OpenMP/MPI programs for solving the time-dependent Gross-Pitaevskii equation in a fully anisotropic trap", Computer Physics Communications 200, 411 (2016). DOI: 10.1016/j.cpc.2015.12.006, IF(2016)=3.936

У овом раду кандидат је искористио нумерички алгоритам за решавање Грос-Питаевски једначине за ултрахладне бозонске системе са диполном интеракцијом и унапредио га у хибридну верзију. Временски зависна диполна Грос-Питаевски једначина је парцијална диференцијална једначина по просторним координатама и времену и има структуру нелинеарне Шредингерове једначине, тако да садржи први извод таласне функције по времену и друге изводе по просторним координатама. Диполни интеракциони члан је описан помоћу просторног интеграла, пошто је у питању дугодометна интеракција. Развијени метод подељеног корака за решавање Грос-Питаевски једначине укључује дискретизацију по простору и времену, појединачну интеграцију по просторним координатама и временску пропагацију дискретизоване једначине. С обзиром на велику нумеричку захтевност тродимензионалних симулација као и великог скупа података који је неопходан за опис оваквих система у великом броју тачака кандидат је развио алгоритме који су паралелизовани за хибридну архитектуру у комбинацији дељене и дистрибуиране меморије.

1.2 Параметри квалитета часописа

Кандидат др Богдан Сатарић је објавио укупно 8 радова у међународним часописима и то:

- 1 рад у међународним часописима изузетних вредности M21a: *Computer Physics Communications* импакт фактора IF(2016) = 3.936, SNIP(2016) = 2.00

- 1 рад у врхунском међународном часопису M21: *Chaos* следећих импакт фактора IF(2016) = 2.283, SNIP(2016) = 0.95

- 5 радова у истакнутим међународним часописима M22: *BioSystems*, Prog*ress in Biophysics a*nd Molecular B*iology, Journal of Biosciences, European Physical Journal E* следећих импакт фактора IF(2020) = 1.623, IF(2018) = 1.623, IF(2015) = 2.581, IF(2015) = 1.419, IF(2011) = 1.944, SNIP(2020) = 0.88, SNIP(2018) = 0.88, SNIP(2015) = 0.92, SNIP(2015) = 0.95, SNIP(2011) = 0.91

- 1 рад у међународном часопису M23: *International Journal of Modern Physics B* следећих импакт фактора IF(2009) = 0.408, SNIP(2009) = 0.38

Библиометријски показатељи су сумирани у наредној табели.

	IF	M	SNIP
Укупно	15.817	48	7.87
Усредњено по чланку	1.977	4.8	0.98
Усредњено по аутору	3.4681	11.02	1.7445

1.3 Позитивна цитираност научних радова

Према подацима из базе Web of Science на дан 29. октобра 2020. године, радови др Богдана Сатарића цитирани су укупно 132 пута. Хиршов индекс је 5.

1.4 Међународна сарадња

Кандидат је учествовао у међународној сарадњи што обухвата активну сарадњу са групом др Вилијама Жалбија са Универзитета Версај Сан-Квентин у Версају (Француска) у оквиру које је у настанку заједнички рад настао у периоду 2018-2019. године.

2 Нормирање броја коауторских радова, патената и техничких решења

Окосница рада кандидата је развој хибридних нумеричких метода за проучавање особина кондензата у којима дипол-дипол интеракција игра важну улогу због нарушења симетрије услед анизотропије система. Рад кандидата категорије М21а има 6 аутора, па нормирање не мења на битан начин број бодова. На радовима категорија М21 и М22 број аутора доприноси разлици између укупног ненормираног (48) и нормираног (39) броја бодова.

3 Учешће у пројектима, потпројектима и пројектним задацима

Кандидат је учествовао на следећим националним пројектима:

- пројекат Министарства просвете, науке и технолошког развоја Републике Србије ОН171017 *Моделирање и нумеричке симулације сложених вишечестничких система (од новембра 2012. до децембра 2019. године)*
- пројекат Министарства просвете, науке и технолошког развоја Републике Србије ОН171009 *Утицај елементарних ексцитација и конформација на физичка својства нових материјала базираних на јако корелисаним нискодимензионалним системима (од 2011. до 2019. године)*
- пројекат Министарства просвете, науке и технолошког развоја Републике Србије ОН174027 *Рачунарска механика у структурном инжењерингу (од 2011. до 2019. године)*

4 Активност у научним и научно-стручним друштвима

4.1 Педагошки рад

Др Богдан Сатарић је активно учествовао у настави на Факултету Техничких Наука у Новом Саду од 2010. до 2018. године. Прво у својству сарадника у настави, потом асистента и на крају као доцент.

У оквиру наставних актинвости држао је вежбе и предавања на предметима Архитектура рачунара и Оперативни системи. Такође био је ментор неколико дипломских и мастер радова из области паралелног и дистрибуираног програмирања.

5 Утицај научних резултата

Утицај и значај резултата кандидата су описани у тачки 1, укључујући и податке о цитираности. Овде се може навести и чињеница да је један М21а рад, на коме је кандидат први аутор, високо цитиран (тренутни број цитата је 52) и да је омогућио објављивање низа других публикација.

6 Конкретан допринос кандидата у реализацији радова у научним центрима у земљи и иностранству

Кандидат је своје главне истраживачке активности реализовао сарадњи са Институтом за физику у Београду. Кандидат је дао кључни допринос у објављеним раду где је први аутор, а његов допринос се огледа у изради хибридних алгоритама нумеричких симулација, добијању, интерпретацији и презентацији нумеричких резултата.

Елементи за квантитативну оцену научног доприноса
др Богдана Сатарића

1 Остварени М-бодови по категоријама публикација:

Категорија	М бодова по публикацији	Број публикација	Укупно М бодова (нормирано)
M21a	10	1	**10 (8.33)**
M21	8	1	**8 (5.71)**
M22	5	5	**25 (20.46)**
M23	3	1	**3 (2.5)**
M33	1	2	**2 (2)**

2 Поређење оствареног броја М-бодова са минималним условима потребним за избор у звање научни сарадник:

Минималан број М бодова потребан за избор у звање научни сарадник		Остварено (нормирано)
Укупно	16	**48 (39)**
M10+M20+M31+M32+M33+M41+M42	10	**48 (39)**
M11+M12+M21+M22+M23	6	**46 (37)**

Списак објављених радова и других публикација које се бодују

Радови у међународним часописима изузетних вредности (М21а)

1. **B. Satarić,** V. Slavnić, A. Belić, A. Balaž, P. Murugandam, S. K. Adhikari, *Hybrid OpenMP/MPI programs for solving the time-dependent Gross-Pitaevskii equation in a fully anisotropic trap*, Computer Physics Communications 200, 411 (2016). DOI: 10.1016/j.cpc.2015.12.006; IF(2016)=3.936

Радови у врхунским међународним часописима (М21)

1. Sekulić Dalibor L, **B. Satarić**, Zdravković Slobodan M, Bugay Aleksandr N, Satarić Miljko V, *Nonlinear dynamics of C-terminal tails in cellular microtubules,* CHAOS, vol. 26 no. 7 (2016), DOI: 10.1063/1.4959802; IF(2016) = 2.283

Радови у истакнутим међународним часописима (М22)

1. Satarić Miljko V, Nemeš Tomas I, **B. Satarić**, Sekulić Dalibor L, Zdravković Slobodan M, *Calcium ions tune the beats of cilia and flagella,* Biosystems, vol. 196 (2020), DOI: 10.1016/j.biosystems.2020.104172; IF(2020) = 1.623
2. Tuszynski Jack Adam, Satarić Miljko V, Sekulić Dalibor L, **B. Satarić,** Zdravković Slobodan M, *Nonlinear calcium ion waves along actin filaments control active hair-bundle motility,* Biosystems, vol. 173. 181-190, (2018), DOI: 10.1016/j.biosystems.2018.08.006; IF(2020) = 1.623
3. Satarić Miljko V, Sekulić Dalibor L, **B. Satarić**, Zdravković Slobodan M, *Role of nonlinear localized Ca2+ pulses along microtubules in tuning the mechano-sensitivity of hair cells,*Progress in Biophysics & Molecular Biology, vol. 119, no. 2, 162-174, (2015), DOI: 10.1016/j.pbiomolbio.2015.07.009; IF(2015) = 2.581
4. Satarić Miljko V, Sekulić Dalibor L, **B. Satarić**, *Actin filaments as the fast pathways for calcium ions involved in auditory processes,* Journal of Biosciences, vol. 40 no. 3, 549-559, (2015), DOI: 10.1007/s12038-015-9547-z; IF(2015) = 1.419
5. Sekulić Dalibor L, **B. Satarić,** Tuszynski Jack Adam, Satarić Miljko V, *Nonlinear ionic pulses along microtubules*, European Physical Journal E, vol. 34 no. 5, (2011), DOI: 10.1140/epje/i2011-11049-0; IF(2011) = 1.944

Радови у међународним часописима (М23)

1. Satarić Miljko V, Bednar Nikola, **B. Satarić,** Stojanović Goran M, *Actin Filaments As Nonlinear Rlc Transmission Lines,* International Journal Of Modern Physics B, vol. 23 no. 22, 4697-4711, (2009), DOI: 10.1142/S021797920905331X; IF(2009) = 0.408

Саопштења са међународних скупова штампана у целини (М33)

1. Satarić Miljko **B. Satarić,** *Ionic Pulses along Cytoskeletal Protophilaments***,** 9th International Frohlich's Symposium: Electrodynamic Activity Of Living Cells (Including Microtubule Coherent Modes And Cancer Cell Physics) Book Series: Journal of Physics Conference Series Volume: 329 Article Number: 012009 Published: 2011
2. Satarić Miljko V**,** **B. Satarić,** Tuszynski Jack Adam, *Nonlinear model of microtubule dynamics, Conference:* International Symposium on Coherence and Electromagnetic Fields in Biological Systems Location: Prague, Czech Republic Date: JUL 01-04, 2005

Computer Physics Communications 200 (2016) 411–417

Contents lists available at ScienceDirect

Computer Physics Communications

journal homepage: www.elsevier.com/locate/cpc

Hybrid OpenMP/MPI programs for solving the time-dependent Gross–Pitaevskii equation in a fully anisotropic trap

Bogdan Satarić [a,*], Vladimir Slavnić [b], Aleksandar Belić [b], Antun Balaž [b], Paulsamy Muruganandam [c], Sadhan K. Adhikari [d]

[a] Faculty of Technical Sciences, University of Novi Sad, Trg Dositeja Obradovića 6, 21000 Novi Sad, Serbia
[b] Scientific Computing Laboratory, Institute of Physics Belgrade, University of Belgrade, Pregrevica 118, 11080 Belgrade, Serbia
[c] School of Physics, Bharathidasan University, Palkalaiperur Campus, Tiruchirappalli – 620024, Tamil Nadu, India
[d] Instituto de Física Teórica, UNESP – Universidade Estadual Paulista, 01.140-70 São Paulo, São Paulo, Brazil

ARTICLE INFO

Article history:
Received 30 November 2015
Accepted 11 December 2015
Available online 22 December 2015

Keywords:
Bose–Einstein condensate
Gross–Pitaevskii equation
Split-step Crank–Nicolson scheme
Real- and imaginary-time propagation
C program
MPI
OpenMP
Partial differential equation

ABSTRACT

We present hybrid OpenMP/MPI (Open Multi-Processing/Message Passing Interface) parallelized versions of earlier published C programs (Vudragović et al. 2012) for calculating both stationary and non-stationary solutions of the time-dependent Gross–Pitaevskii (GP) equation in three spatial dimensions. The GP equation describes the properties of dilute Bose–Einstein condensates at ultra-cold temperatures. Hybrid versions of programs use the same algorithms as the C ones, involving real- and imaginary-time propagation based on a split-step Crank–Nicolson method, but consider only a fully-anisotropic three-dimensional GP equation, where algorithmic complexity for large grid sizes necessitates parallelization in order to reduce execution time and/or memory requirements per node. Since distributed memory approach is required to address the latter, we combine MPI programming paradigm with existing OpenMP codes, thus creating fully flexible parallelism within a combined distributed/shared memory model, suitable for different modern computer architectures. The two presented C/OpenMP/MPI programs for real- and imaginary-time propagation are optimized and accompanied by a customizable makefile. We present typical scalability results for the provided OpenMP/MPI codes and demonstrate almost linear speedup until inter-process communication time starts to dominate over calculation time per iteration. Such a scalability study is necessary for large grid sizes in order to determine optimal number of MPI nodes and OpenMP threads per node.

New version program summary

Program title: GP-SCL-HYB package, consisting of: (i) imagtime3d-hyb, (ii) realtime3d-hyb.

Catalogue identifier: AEDU_v3_0

Program Summary URL: http://cpc.cs.qub.ac.uk/summaries/AEDU_v3_0.html

Program obtainable from: CPC Program Library, Queen's University of Belfast, N. Ireland.

Licensing provisions: Apache License 2.0

No. of lines in distributed program, including test data, etc.: 26397.

No. of bytes in distributed program, including test data, etc.: 161195.

Distribution format: tar.gz.

Programming language: C/OpenMP/MPI.

Computer: Any modern computer with C language, OpenMP- and MPI-capable compiler installed.

Operating system: Linux, Unix, Mac OS X, Windows.

* Corresponding author.
E-mail addresses: bogdan.sataric@uns.ac.rs (B. Satarić), vladimir.slavnic@ipb.ac.rs (V. Slavnić), aleksandar.belic@ipb.ac.rs (A. Belić), antun.balaz@ipb.ac.rs (A. Balaž), anand@cnld.bdu.ac.in (P. Muruganandam), adhikari@ift.unesp.br (S.K. Adhikari).

http://dx.doi.org/10.1016/j.cpc.2015.12.006

RAM: Total memory required to run programs with the supplied input files, distributed over the used MPI nodes: (i) 310 MB, (ii) 400 MB. Larger grid sizes require more memory, which scales with Nx*Ny*Nz.

Number of processors used: No limit, from one to all available CPU cores can used on all MPI nodes.

Number of nodes used: No limit on the number of MPI nodes that can be used. Depending on the grid size of the physical problem and communication overheads, optimal number of MPI nodes and threads per node can be determined by a scalability study for a given hardware platform.

Classification: 2.9, 4.3, 4.12.

Catalogue identifier of previous version: AEDU_v2_0.

Journal reference of previous version: Comput. Phys. Commun. 183 (2012) 2021.

Does the new version supersede the previous version?: No.

Nature of problem: These programs are designed to solve the time-dependent Gross–Pitaevskii (GP) nonlinear partial differential equation in three spatial dimensions in a fully anisotropic trap using a hybrid OpenMP/MPI parallelization approach. The GP equation describes the properties of a dilute trapped Bose–Einstein condensate.

Solution method: The time-dependent GP equation is solved by the split-step Crank–Nicolson method using discretization in space and time. The discretized equation is then solved by propagation, in either imaginary or real time, over small time steps. The method yields solutions of stationary and/or non-stationary problems.

Reasons for the new version: Previous C [1] and Fortran [2] programs are widely used within the ultracold atoms and nonlinear optics communities, as well as in various other fields [3]. This new version represents extension of the two previously OpenMP-parallelized programs (imagtime3d-th and realtime3d-th) for propagation in imaginary and real time in three spatial dimensions to a hybrid, fully distributed OpenMP/MPI programs (imagtime3d-hyb and realtime3d-hyb). Hybrid extensions of previous OpenMP codes enable interested researchers to numerically study Bose–Einstein condensates in much greater detail (i.e., with much finer resolution) than with OpenMP codes. In OpenMP (threaded) versions of programs, numbers of discretization points in X, Y, and Z directions are bound by the total amount of available memory on a single computing node where the code is being executed. New, hybrid versions of programs are not limited in this way, as large numbers of grid points in each spatial direction can be evenly distributed among the nodes of a cluster, effectively distributing required memory over many MPI nodes. This is the first reason for development of hybrid versions of 3d codes. The second reason for new versions is speedup in the execution of numerical simulations that can be gained by using multiple computing nodes with OpenMP/MPI codes.

Summary of revisions: Two C/OpenMP programs in three spatial dimensions from previous version [1] of the codes (imagtime3d-th and realtime3d-th) are transformed and rewritten into a hybrid OpenMP/MPI programs and named imagtime3d-hyb and realtime3d-hyb. The overall structure of two programs is identical. The directory structure of the GP-SCL-HYB package is extended compared to the previous version and now contains a folder scripts, where examples of scripts that can be used to run the programs on a typical MPI cluster are given. The corresponding readme.txt file contains more details. We have also included a makefile with tested and verified settings for most popular MPI compliers, including OpenMPI (Open Message Passing Interface) [4] and MPICH (Message Passing Interface Chameleon) [5].

Transformation from pure OpenMP to a hybrid OpenMP/MPI approach has required that the array containing condensate wavefunction is distributed among MPI nodes of a computer cluster. Several data distribution models have been considered for this purpose, including block distribution and block cyclic distribution of data in a 2d matrix. Finally, we decided to distribute the wavefunction values across different nodes so that each node contains only one slice of the X-dimension data, while containing the complete corresponding Y- and Z-dimension data, as illustrated in Fig. 1. This allows central functions of our numerical algorithm, calcluy, calcuz, and calcnu to be executed purely in parallel on different MPI nodes of a cluster, without any overhead or communication, as nodes contain all the information for Y- and Z-dimension data in the given X-sub-domain. However, the problem arises when functions calclux, calcrms, and calcmuen need to be executed, as they also operate on the whole X-dimension data. Thus, the need for additional communication arises during the execution of the function calcrms, while in the case of functions calclux and calcmuen also the transposition of data between X- and Y-dimensions is necessary, while data in Z dimension have to stay contiguous. Transposition provides nodes with all the necessary X-dimension data to execute functions calclux and calcmuen. However, this needs to be done in each iteration of numerical algorithm, thus necessarily increasing communication overhead of the simulation.

Transposition algorithms that were considered where the ones that account for greatest common divisor (GCD) between number of nodes in columns (designated by N) and rows (designated by M) of a cluster configured as 2d mash of nodes [6]. Two of such algorithms have been tested and tried for implementation: the case when GCD $= 1$ and the case when GCD > 1. The trivial situation $N = M = 1$ is already covered by the previous, purely OpenMP programs, and therefore, without any loss of generality, we have considered only configurations with number of nodes in X-dimension satisfying N > 1. Only the former algorithm (GCD $= 1$) was found to be sound in case where data matrix is not a 2d, but a 3d structure. Latter case was found to be too demanding implementation-wise, since MPI functions and data-types are bound to certain limitations. Therefore, the algorithm with $M = 1$ nodes in Y-dimension was implemented, as depicted by the wavefunction data structure in Fig. 1.

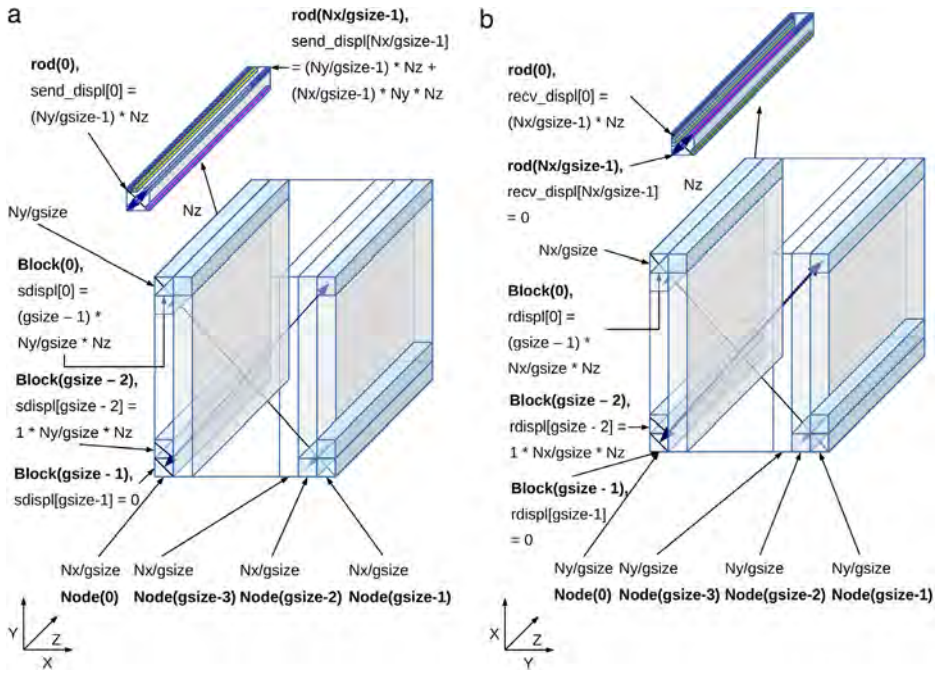

Fig. 1. BEC wavefunction data structure in the employed algorithm. Data are sliced so that the complete Y- and Z-dimension data reside on a single node for a given range of data in X-dimension, while data in X-dimension are distributed over N = gsize nodes. Figures show data transposition and MPI indexed datatype creation parameters for the case of: (a) sending side and (b) receiving side.

Implementation of the algorithm relies on a sliced distribution of data among the nodes, as explained in Fig. 2. This successfully solves the problem of large RAM consumption of 3d codes, which arises even for moderate grid sizes. However, it does not solve the question of data transposition between the nodes. In order to implement the most effective (GCD = 1) transposition algorithm according to Ref. [6], we had to carry out block distribution of data within one data slice contained on a single node. This block distribution of data was done implicitly, i.e. data on one node have been put in a single 1d array (psi) of contiguous memory, in which Z-dimension has stride 1, Y-dimension has stride Nz, and X-dimension has stride Ny*Nz. This is different from previous implementation of the programs, where the wavefunction was represented by an explicit 3d array. This change was also introduced in order to more easily form user MPI datatypes, which allow for implicit block distribution of data, and represent 3d blocks of data within 1d data array. These blocks are then swapped between nodes, effectively performing the transposition in X–Y and Y–X directions.

Together with transposition of blocks between the nodes, the block data also have to be redistributed. To illustrate how this works, let us consider example shown in Fig. 1(a), where one data block has size (Nx/gisze)*(Ny/gsize)*Nz. It represents one 3d data block, swapped between two nodes of a cluster (through one non-blocking MPI_Isend and one MPI_Ireceive operation), containing (Nx/gsize)*(Ny/gsize) 1d rods of contiguous Nz data. These rods themselves need to be transposed within the transposed block as well. This means that two levels of transpositions need to be performed. At a single block level, rods have to be transposed (as indicated in upper left corner of Fig. 1(a) for sending index type and in Fig. 1(b) for receiving index type). Second level is transposition of blocks between different nodes, which is depicted by blue arrows connecting different blocks in Fig. 1.

The above described transposition is applied whenever needed in the functions calclux and calcmuen, which require calculations to be done on the whole range of data in X-dimension. When performing renormalization of the wavefunction or calculation of its norm, root-mean-square radius, chemical potential, and energy, collective operations MPI_Gather and MPI_Bcast are also used.

Figs. 3 and 4 show the scalability results obtained for hybrid versions of programs for small and large grid sizes as a function of number of MPI nodes used. The baseline for calculation of speedups in the execution time for small grid sizes is previous, purely OpenMP programs, while for large grid sizes, which cannot fit onto a single node, the baseline is hybrid programs with minimal configuration runs on 8 nodes. The figures also show efficacies, defined as percentages of measured speedups compared to the ideal ones. We see that an excellent scalability (larger than 80% compared to the ideal one) can be obtained for up to 32 nodes. The tests have been performed on a cluster with nodes containing 2 × 8-core Sandy Bridge Xeon 2.6 GHz processors with 32 GB of RAM and Infiniband QDR (Quad Data Rate, 40 Gbps) interconnect. We stress that the scalability depends greatly on the ratio between the calculation and communication time per iteration, and has to be studied for a particular type of processors and interconnect technology.

Additional comments: This package consists of 2 programs, see Program title above. Both are hybrid, threaded and distributed (OpenMP/MPI parallelized). For the particular purpose of each program, see descriptions below.

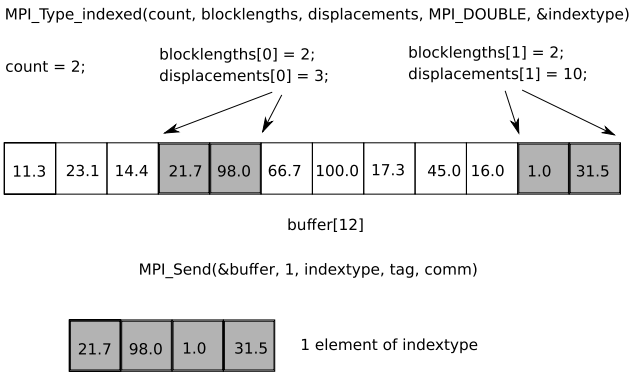

Fig. 2. Creation of a user-defined MPI datatype indextype with the function MPI_Type_indexed. Here, count represents the number of blocks, blocklengths array contains lengths of each block, and displacements array contains the displacement of each block from the beginning of the corresponding data structure. For example, if an array of double precision numbers (designated as buffer in the figure) is sent by MPI_Send with the datatype set to indextype, it is interpreted as a block-distributed data structure, as specified when indextype was created.

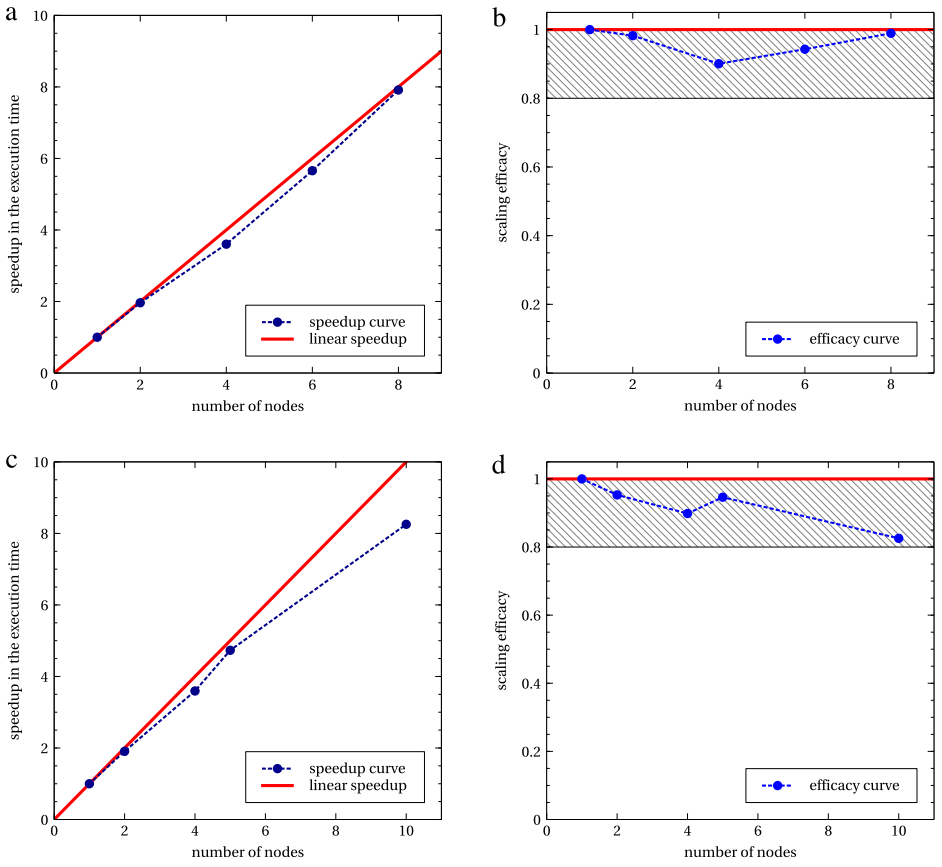

Fig. 3. Speedup in the execution time and efficacy curves of imagtime3d-hyb and realtime3d-hyb programs as a function of the number of MPI nodes used for small grid sizes. The results are obtained on a cluster with nodes containing 2 × 8-core Sandy Bridge Xeon 2.6 GHz processors with 32 GB of RAM and Infiniband QDR interconnect: (a) speedup of imagtime3d-hyb on a 240 × 200 × 160 grid; (b) efficacy of imagtime3d-hyb on a 240 × 200 × 160 grid; (c) speedup of realtime3d-hyb on a 200 × 160 × 120 grid; (d) efficacy of realtime3d-hyb on a 200 × 160 × 120 grid. Shaded areas in graphs (b) and (d) represent high-efficacy regions, where speedup is at least 80% of the ideal one.

Running time: All running times given in descriptions below refer to programs compiled with OpenMPI/GCC compiler and executed on 8–32 nodes with 2 × 8-core Sandy Bridge Xeon 2.6 GHz processors with 32 GB of RAM and Infiniband QDR interconnect. With the supplied input files for small grid sizes, running wallclock times of several minutes are required on 8–10 MPI nodes.

Special features: (1) Since the condensate wavefunction data are distributed among the MPI nodes, when writing wavefunction output files each MPI process saves its data into a separate file, to avoid I/O issues. Concatenating the corresponding files from all MPI processes will create the complete wavefunction file. (2) Due to a known bug in OpenMPI up to version 1.8.4, allocation of memory for indexed datatype on a single node for large grids (such as 800 × 640 × 480) may fail. The fix for this bug is already in 3c489ea branch and is fixed in OpenMPI as of version 1.8.5.

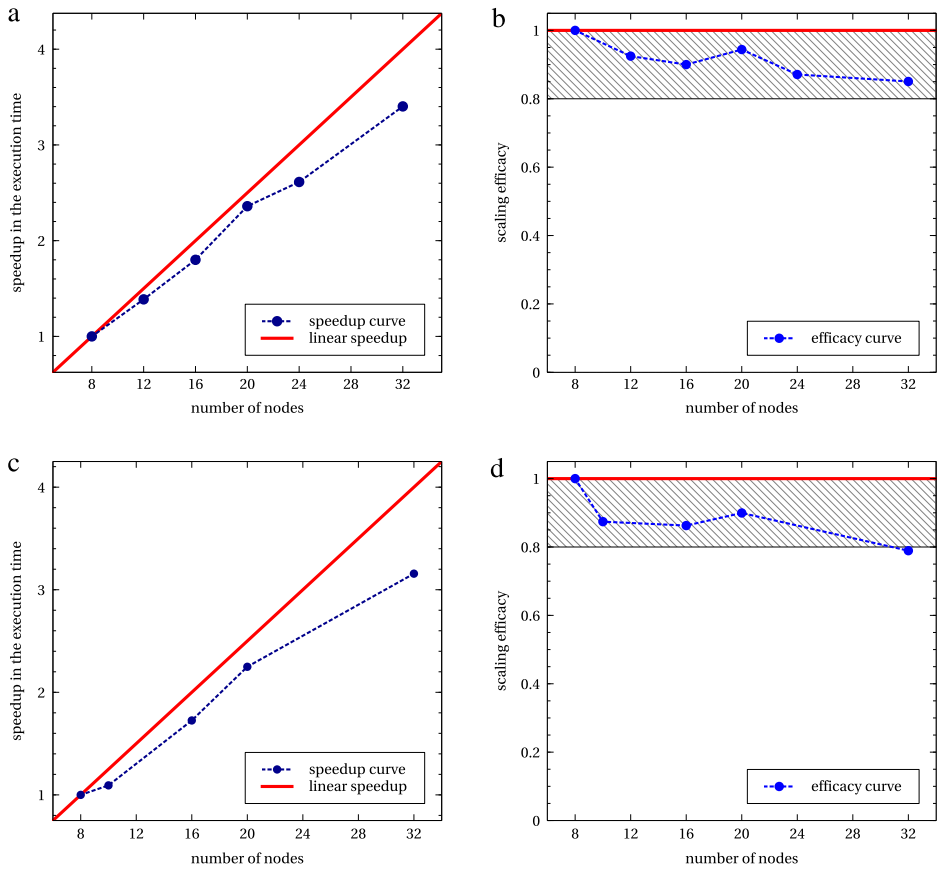

Fig. 4. Speedup in the execution time and efficacy curves of imagtime3d-hyb and realtime3d-hyb programs as a function of the number of MPI nodes used for large grid sizes. The results are obtained on a cluster with nodes containing 2 × 8-core Sandy Bridge Xeon 2.6 GHz processors with 32 GB of RAM and Infiniband QDR interconnect: (a) speedup of imagtime3d-hyb on a 1920 × 1600 × 1280 grid; (b) efficacy of imagtime3d-hyb on a 1920 × 1600 × 1280 grid; (c) speedup of realtime3d-hyb on a 1600 × 1280 × 960 grid; (d) efficacy of realtime3d-hyb on a 1600 × 1280 × 960 grid. Shaded areas in graphs (b) and (d) represent high-efficacy regions, where speedup is at least 80% of the ideal one.

Program summary (i)

Program title: imagtime3d-hyb.

Title of electronic files: imagtime3d-hyb.c, imagtime3d-hyb.h.

Computer: Any modern computer with C language, OpenMP- and MPI-capable compiler installed.

RAM memory requirements: 300 MBytes of RAM for a small grid size 240 × 200 × 160, and scales with Nx*Ny*Nz. This is total amount of memory needed, and is distributed over MPI nodes used for execution.

Programming language used: C/OpenMP/MPI.

Typical running time: Few minutes with the supplied input files for a small grid size 240 × 200 × 160 on 8 nodes. Up to one hour for a large grid size 1920 × 1600 × 1280 on 32 nodes (1000 iterations).

Nature of physical problem: This program is designed to solve the time-dependent GP nonlinear partial differential equation in three space dimensions with an anisotropic trap. The GP equation describes the properties of a dilute trapped Bose–Einstein condensate.

Method of solution: The time-dependent GP equation is solved by the split-step Crank–Nicolson method by discretizing in space and time. The discretized equation is then solved by propagation in imaginary time over small time steps. The method yields solutions of stationary problems.

Program summary (ii)

Program title: realtime3d-hyb.

Title of electronic files: realtime3d-hyb.c, realtime3d-hyb.h.

Computer: Any modern computer with C language, OpenMP- and MPI-capable compiler installed.

RAM memory requirements: 410 MBytes of RAM for a small grid size 200 × 160 × 120, and scales with Nx*Ny*Nz. This is total amount of memory needed, and is distributed over MPI nodes used for execution.

Programming language used: C/OpenMP/MPI.

Typical running time: 10–15 min with the supplied input files for a small grid size 200 × 160 × 120 on 10 nodes. Up to one hour for a large grid size 1600 × 1280 × 960 on 32 nodes (1000 iterations).

Nature of physical problem: This program is designed to solve the time-dependent GP nonlinear partial differential equation in three space dimensions with an anisotropic trap. The GP equation describes the properties of a dilute trapped Bose–Einstein condensate.

Method of solution: The time-dependent GP equation is solved by the split-step Crank–Nicolson method by discretizing in space and time. The discretized equation is then solved by propagation in real time over small time steps. The method yields solutions of stationary and non-stationary problems.

Acknowledgments

B.S., V.S., A.B., and A.B. acknowledge support by the Ministry of Education, Science, and Technological Development of the Republic of Serbia under projects ON171017, III43007, ON171009, ON174027 and IBEC, and by DAAD - German Academic and Exchange Service under project IBEC. P.M. acknowledges support by the Science and Engineering Research Board, Department of Science and Technology, Government of India under project No. EMR/2014/000644. S.K.A. acknowledges support by the CNPq of Brazil under project 303280/2014-0, and by the FAPESP of Brazil under project 2012/00451-0. Numerical simulations were run on the PARADOX supercomputing facility at the Scientific Computing Laboratory of the Institute of Physics Belgrade, supported in part by the Ministry of Education, Science, and Technological Development of the Republic of Serbia under project ON171017.

References

[1] D. Vudragović, I. Vidanović, A. Balaž, P. Muruganandam, S. K. Adhikari, C programs for solving the time-dependent Gross–Pitaevskii equation in a fully anisotropic trap, Comput. Phys. Commun. **183** (2012) 2021.

[2] P. Muruganandam and S. K. Adhikari, Fortran programs for the time-dependent Gross–Pitaevskii equation in a fully anisotropic trap, Comput. Phys. Commun. **180** (2009) 1888.

[3] R. K. Kumar and P. Muruganandam, J. Phys. B: At. Mol. Opt. Phys. **45** (2012) 215301;

L. E. Young-S. and S. K. Adhikari, Phys. Rev. A **86** (2012) 063611;

S. K. Adhikari, J. Phys. B: At. Mol. Opt. Phys. **45** (2012) 235303;

I. Vidanović, N. J. van Druten, and M. Haque, New J. Phys. **15** (2013) 035008;

S. Balasubramanian, R. Ramaswamy, and A. I. Nicolin, Rom. Rep. Phys. **65** (2013) 820;

L. E. Young-S. and S. K. Adhikari, Phys. Rev. A **87** (2013) 013618;

H. Al-Jibbouri, I. Vidanovic, A. Balaz, and A. Pelster, J. Phys. B: At. Mol. Opt. Phys. **46** (2013) 065303;

X. Antoine, W. Bao, and C. Besse, Comput. Phys. Commun. **184** (2013) 2621;

B. Nikolić, A. Balaž, and A. Pelster, Phys. Rev. A **88** (2013) 013624;

H. Al-Jibbouri and A. Pelster, Phys. Rev. A **88** (2013) 033621;

S. K. Adhikari, Phys. Rev. A **88** (2013) 043603;

J. B. Sudharsan, R. Radha, and P. Muruganandam, J. Phys. B: At. Mol. Opt. Phys. **46** (2013) 155302;

R. R. Sakhel, A. R. Sakhel, and H. B. Ghassib, J. Low Temp. Phys. **173** (2013) 177;

E. J. M. Madarassy and V. T. Toth, Comput. Phys. Commun. **184** (2013) 1339;

R. K. Kumar, P. Muruganandam, and B. A. Malomed, J. Phys. B: At. Mol. Opt. Phys. **46** (2013) 175302;

W. Bao, Q. Tang, and Z. Xu, J. Comput. Phys. **235** (2013) 423;

A. I. Nicolin, Proc. Rom. Acad. Ser. A-Math. Phys. **14** (2013) 35;

R. M. Caplan, Comput. Phys. Commun. **184** (2013) 1250;

S. K. Adhikari, J. Phys. B: At. Mol. Opt. Phys. **46** (2013) 115301;

Ž. Marojević, E. Göklü, and C. Lämmerzahl, Comput. Phys. Commun. **184** (2013) 1920;

X. Antoine and R. Duboscq, Comput. Phys. Commun. **185** (2014) 2969;

S. K. Adhikari and L. E. Young-S, J. Phys. B: At. Mol. Opt. Phys. **47** (2014) 015302;

K. Manikandan, P. Muruganandam, M. Senthilvelan, and M. Lakshmanan, Phys. Rev. E **90** (2014) 062905;

S. K. Adhikari, Phys. Rev. A **90** (2014) 055601;

A. Balaž, R. Paun, A. I. Nicolin, S. Balasubramanian, and R. Ramaswamy, Phys. Rev. A **89** (2014) 023609;

S. K. Adhikari, Phys. Rev. A **89** (2014) 013630;

J. Luo, Commun. Nonlinear Sci. Numer. Simul. **19** (2014) 3591;

S. K. Adhikari, Phys. Rev. A **89** (2014) 043609;

K.-T. Xi, J. Li, and D.-N. Shi, Physica B **436** (2014) 149;

M. C. Raportaru, J. Jovanovski, B. Jakimovski, D. Jakimovski, and A. Mishev, Rom. J. Phys. **59** (2014) 677;

S. Gautam and S. K. Adhikari, Phys. Rev. A **90** (2014) 043619;

A. I. Nicolin, A. Balaž, J. B. Sudharsan, and R. Radha, Rom. J. Phys. **59** (2014) 204;

K. Sakkaravarthi, T. Kanna, M. Vijayajayanthi, and M. Lakshmanan, Phys. Rev. E **90** (2014) 052912;

S. K. Adhikari, J. Phys. B: At. Mol. Opt. Phys. **47** (2014) 225304;

R. K. Kumar and P. Muruganandam, Numerical studies on vortices in rotating dipolar Bose–Einstein condensates, Proceedings of the 22nd International Laser Physics Workshop, J. Phys. Conf. Ser. **497** (2014) 012036;

A. I. Nicolin and I. Rata, Density waves in dipolar Bose–Einstein condensates by means of symbolic computations, High-Performance Computing Infrastructure for South East Europe's Research Communities: Results of the HP-SEE User Forum 2012, in Springer Series: Modeling and Optimization in Science and Technologies **2** (2014) 15;

S. K. Adhikari, Phys. Rev. A **89** (2014) 043615;

R. K. Kumar and P. Muruganandam, Eur. Phys. J. D **68** (2014) 289;

J. B. Sudharsan, R. Radha, H. Fabrelli, A. Gammal, and B. A. Malomed, Phys. Rev. A **92** (2015) 053601;

S. K. Adhikari, J. Phys. B: At. Mol. Opt. Phys. **48** (2015) 165303;

F. I. Moxley III, T. Byrnes, B. Ma, Y. Yan, and W. Dai, J. Comput. Phys. **282** (2015) 303;

S. K. Adhikari, Phys. Rev. E **92** (2015) 042926;

R. R. Sakhel, A. R. Sakhel, and H. B. Ghassib, Physica B **478** (2015) 68;

S. Gautam and S. K. Adhikari, Phys. Rev. A **92** (2015) 023616;

D. Novoa, D. Tommasini, and J. A. Nóvoa-López, Phys. Rev. E **91** (2015) 012904;

S. Gautam and S. K. Adhikari, Laser Phys. Lett. **12** (2015) 045501;

K.-T. Xi, J. Li, and D.-N. Shi, Physica B **459** (2015) 6;

R. K. Kumar, L. E. Young-S., D. Vudragović, A. Balaž, P. Muruganandam, and S. K. Adhikari, Comput. Phys. Commun. **195** (2015) 117;

S. Gautam and S. K. Adhikari, Phys. Rev. A **91** (2015) 013624;

A. I. Nicolin, M. C. Raportaru, and A. Balaž, Rom. Rep. Phys. **67** (2015) 143;

S. Gautam and S. K. Adhikari, Phys. Rev. A **91** (2015) 063617;

E. J. M. Madarassy and V. T. Toth, Phys. Rev. D **91** (2015) 044041.

[4] Open Message Passing Interface (OpenMPI), http://www.open-mpi.org/ (2015).

[5] Message Passing Interface Chameleon (MPICH), https://www.mpich.org/ (2015).

[6] J. Choi, J. J. Dongarra, D. W. Walker, Parallel matrix transpose algorithms on distributed memory concurrent computers, Parallel Comput. **21** (1995) 1387.

Nonlinear dynamics of C–terminal tails in cellular microtubules

Dalibor L. Sekulic, Bogdan M. Sataric, Slobodan Zdravkovic, Aleksandr N. Bugay, and Miljko V. Sataric

Citation: Chaos **26**, 073119 (2016); doi: 10.1063/1.4959802
View online: http://dx.doi.org/10.1063/1.4959802
View Table of Contents: http://scitation.aip.org/content/aip/journal/chaos/26/7?ver=pdfcov
Published by the AIP Publishing

Nonlinear dynamics of C–terminal tails in cellular microtubules

Dalibor L. Sekulic,[1,a)] Bogdan M. Sataric,[1] Slobodan Zdravkovic,[2] Aleksandr N. Bugay,[3] and Miljko V. Sataric[1]
[1]*University of Novi Sad, Faculty of Technical Sciences, Novi Sad, Serbia*
[2]*University of Belgrade, Institute of Nuclear Sciences Vinca, Belgrade, Serbia*
[3]*Laboratory of Radiation Biology, Joint Institute for Nuclear Research, Dubna, Russia*

(Received 14 April 2016; accepted 13 July 2016; published online 29 July 2016)

The mechanical and electrical properties, and information processing capabilities of microtubules are the permanent subject of interest for carrying out experiments *in vitro* and *in silico*, as well as for theoretical attempts to elucidate the underlying processes. In this paper, we developed a new model of the mechano–electrical waves elicited in the rows of very flexible C–terminal tails which decorate the outer surface of each microtubule. The fact that C–terminal tails play very diverse roles in many cellular functions, such as recruitment of motor proteins and microtubule–associated proteins, motivated us to consider their collective dynamics as the source of localized waves aimed for communication between microtubule and associated proteins. Our approach is based on the ferroelectric liquid crystal model and it leads to the effective asymmetric double-well potential which brings about the conditions for the appearance of kink–waves conducted by intrinsic electric fields embedded in microtubules. These kinks can serve as the signals for control and regulation of intracellular traffic along microtubules performed by processive motions of motor proteins, primarily from kinesin and dynein families. On the other hand, they can be precursors for initiation of dynamical instability of microtubules by recruiting the proper proteins responsible for the depolymerization process. *Published by AIP Publishing*. [http://dx.doi.org/10.1063/1.4959802]

Microtubules are highly dynamic cellular biopolymers assembled from tubulin heterodimers consisting of a compact globular core and very flexible C–terminal tails. These tubulin tails represent the critical parts of the binding sites of different molecular motors and microtubule–associated proteins, which are major regulators of microtubule dynamics. In the present paper, we have established a nonlinear model which offers a new insight into the mechano–electrical kink–wave propagation mediated by C–terminal tails in the direction of microtubule protofilaments. This original and quite new idea offers the plausible way to feel the gap in understanding the signalling mechanism responsible for the tuning of cellular traffic performed by kinesin or dynein motor proteins. The velocity of kinks excited within the framework of the proposed model is very reasonable (of the order of a few cm/s) and it meets the findings of the very recent experiments with regard to cellular signals.

I. INTRODUCTION

Microtubules (MTs) are major cytoskeletal protein polymers assembled from two slightly different proteins called α– and β–tubulin, first fused in tubulin $\alpha\beta$–heterodimers[1] and then polymerized in MTs. Polymerizing MTs create a helical lattice pattern which always has left–handed chirality, but it is still not known why. In fact, this chirality is also important for the dynamical model developed in this paper. It was contemplated by the leading experts in the field[2] that this intrinsic helicity of MTs solves "the problem of blind mason," thus explaining how the chiral wedgelike shape of tubulin heterodimers has the decisive role in building the correct cylindrical architecture of every MT. These MTs form an important part of the cellular scaffold and provide a network of "rails" for active intracellular transport by kinesin and dynein motor proteins,[3] as illustrated in Fig. 1(a). They also play a crucial role during cell division, by forming a dynamic structure that spatially separates duplicated chromosomes. MTs are very dynamic polymers, and when tubulin dimers are in straight conformation a MT is in the assembling process, while the curved conformations of constituent dimers lead to MT disassembly.[4] These dynamical processes are mainly governed and controlled by the hydrolysis of exchangeable nucleotides GTP (guanosine triphosphate), incorporated in β–tubulines within a MT matrix. The single act of GTP hydrolysis releases the energy quantum of 0.25 eV (Refs. 5 and 6) and makes the remarkable conformation of pertaining tubulin dimer. Depending on the roles that different MTs play in cellular activities, their lifetimes in the permanent recycling processes span from hours to months and even years.[7] Several types of proteins called MAPs efficiently stabilize MTs against depolymerization. This fact will be taken into account within the framework of the model developed here. On the other hand, there are MAP proteins which are responsible for MT dynamics regulation such as kinesin–13 MCAK that depolymerizes MTs acting on their tips.[8]

MTs are polar cylinders from a biochemical point of view in the sense that they are typically radially organized in

[a)]Author to whom correspondence should be addressed. Electronic mail: dalsek@uns.ac.rs. Tel.: +381 21 48 52 538. Fax: +381 21 47 50 572.

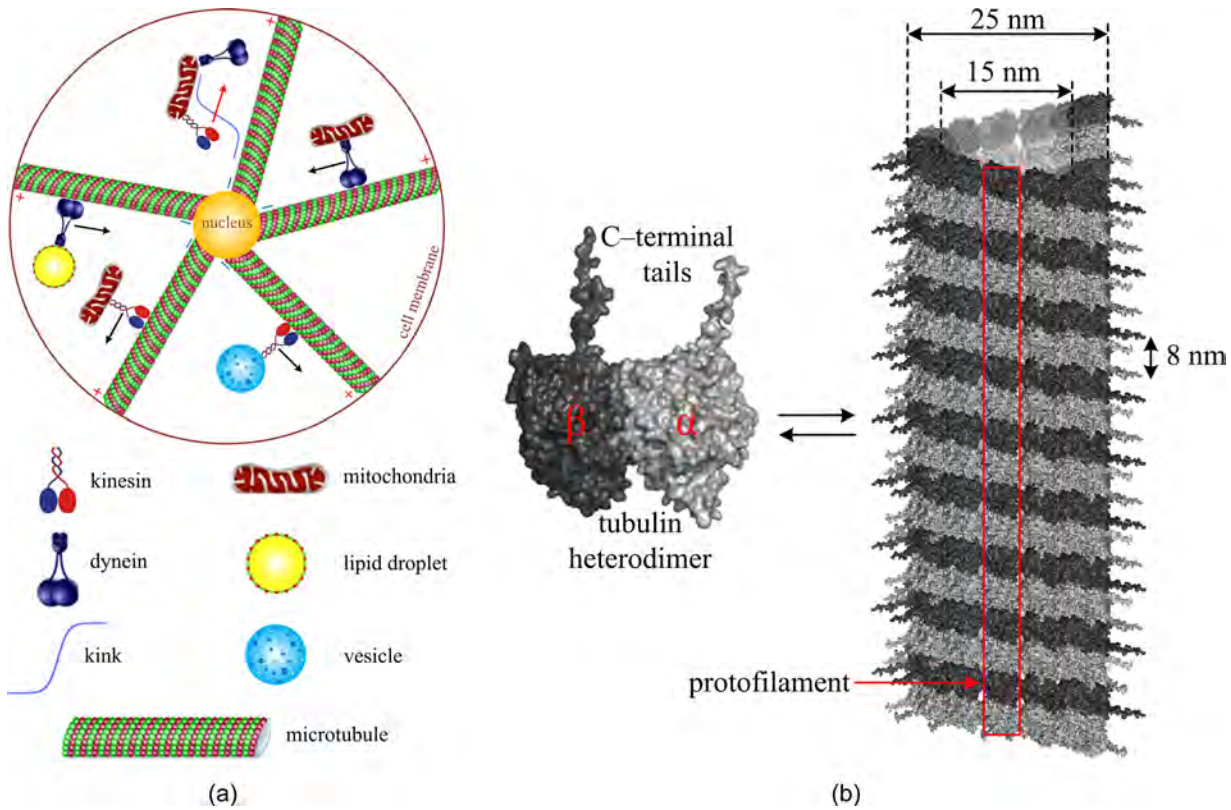

FIG. 1. (a) The radial distribution of MTs within a globular cell. The kinesin and dynein motors carrying cargos are clearly depicted. The kink signal is also shown and its action will attach the proper motor to MT. (b) The three-dimensional structure of a MT as a hollow polymer with the characteristic dimensions of the outer and the inner diameters of 25 nm and 15 nm, respectively. It is made up of 13 protofilaments, the vertical linear rows that are formed by head-to-tail association of $\alpha\beta$–heterodimers with the lengths of 8 nm. The C–terminal tails are localized at the surface of MTs and they are all exposed at the interaction sites of many microtubule–associated proteins (MAPs) and motor proteins.

globular cells, see Fig. 1(a). Their less active minus ends are situated close to the cell nucleus, while the more active plus ends point toward the cell membrane. The lengths of MTs span dimensions from the order of micrometer in globular cells to the order of milimeter in neurons. They represent hollow cylinders formed by protofilaments aligned in directions that are parallel to their axes.[1,3,5] In globular cells, MTs are radially distributed from the cell nucleus towards the cell membrane. Fig. 1(a) shows the MTs decorated with motor proteins involved in busy cellular traffic.

There are *in vivo* usually 13 longitudinally ordered parallel protofilaments covering the cylindrical walls of MTs, as shown in Fig. 1(b). The outer and the inner radii of a MT cylinder are 25 nm and 15 nm, respectively. Each tubulin heterodimer within a MT is effectively an electric dipole.[5,6] The relevant dimension of the dimer length is $l = 8$ nm. Tuszynski *et al.*[6] calculated the dipole moment of a tubulin heterodimer to be $p = 1740$ D (1 D = 1 Debye $= 0.33 \times 10^{-29}$ Cm). Components of the dipole moment are represented in Fig. 2 with the following values: $p_x = 337$ D, $p_y = p_r = -1669$ D, and $p_z = 198$ D. It is remarkable that the radial component p_r is dominant and oriented towards the lumen of MT. While radial components mutually cancel due to cylindrical symmetry, the longitudinal ones (p_x) are cumulative giving a resultant dipole moment which makes MT a giant dipole with an intrinsic electric field aligned along MT axis. This fact is of significance for the model developed here. Notice that the positive electrically charged MT end corresponds to the biologically less dynamically active minus end, and vice versa. For example, a biologically positive end, but electrically negative, is the more intensive growing end of a MT during its polymerization.[9]

We will now concentrate our attention on the essential ingredients of MTs relevant for the model considered here. Each tubulin monomer on the MT lattice has a short C–terminal alpha–helix H_{12} followed by a highly acidic amino acid sequence projecting out of the MT surface, which is referred to as the carboxy–terminal tail or tubulin tail (TT) in the literature.[10,11] Geometrically, these TTs are hair–like projections of 4–6 nm length depending on their structure and the effective charge present, see Fig. 3. Their approximate molecular masses are 5.5 kD and 6.7 kD for the α– and β–tubulin tail, respectively. The TT domains of the α– and β–tubulin are functionally very important because they

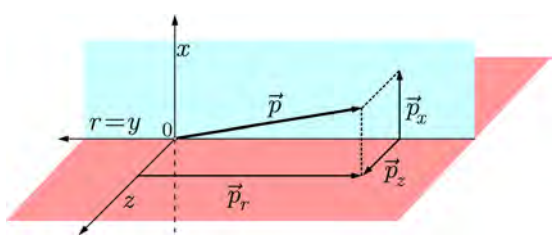

FIG. 2. The components of dipole moment of a tubulin heterodimer with the following values: $p_x = 337$ D, $p_y = p_r = -1669$ D, and $p_z = 198$ D in accordance with Ref. 6.

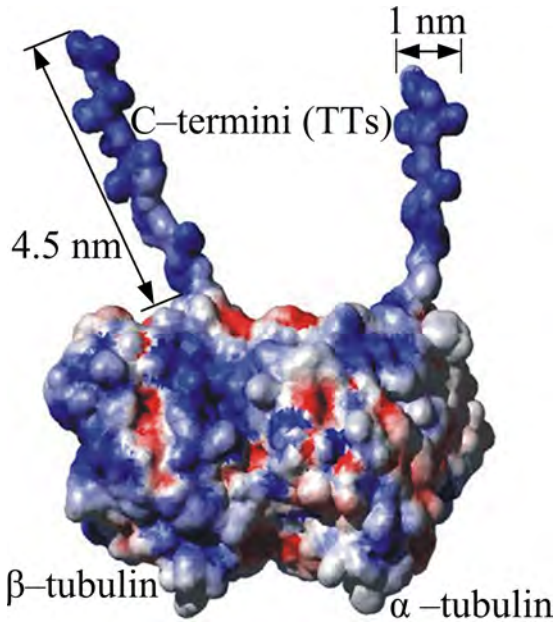

FIG. 3. Charge distribution on the surface of the tubulin $\alpha\beta$–heterodimer with pertaining tubulin tails (TTs) and their characteristic dimensions. Blue and red denote the negative and positive charges, respectively.

support the binding of proteins through which MTs interact with other cells' ingredients, including motor proteins and microtubule associated proteins.[12–14] The very recent biochemical experimental evidences revealed that so–called tubulin post–translational modifications are predominantly expressed on the structures of TTs. Such changes appear to play the crucial roles in tuning different MT functions.[15–17] These new insights give us the strong motivation to establish a new nonlinear model for collective excitations of TTs, which can be implicated in regulation of very diverse functions of MTs.

We here suggest that localized waves of tilting TTs, which could be excited both mechanically and electrically within a MT, could serve as the signals suitable for the initiation and the control of cellular traffic performed by the mentioned kinesin and dynein motor proteins. Importantly, these TTs have a high proportion of negatively charged residues; for example, TT of β–tubulin has 9 Glu residues and 2 Asp residues. As much as 40% of the total tubulun monomer charge can be attributed to a C–terminus.[6] This needs an adequate number of positive counterions for charge compensation in cellular cytosol. The fluctuations of TT domains are certainly associated with accompanying currents of positive counterions.[18,19] The intrinsic negative charge of β–TT is on average $-11e$ (e is elementary charge equal to 1.602×10^{-19} C) and that of the α–TT is $-7e$. Although the remainder of the tubulin heterodimer is also dominantly negatively charged with approximately $-50e$, each tubulin has patches of positively charged clusters of residues which may interact with TTs of the neighboring dimers.[20,21] A detailed map of the charge distribution on the surface of the tubulin dimer at physiological pH is illustrated in Fig. 3. The circumstance that TTs are negatively charged but these charges are partially compensated by positive counterions enables that besides the dipole moment of tubulin heterodimer body the additional one associated with pertaining TTs should be taken into account in the forthcoming modeling. This is the reason why the collection of TTs within a MT can be considered as a cylindrical layer of ferroelectric smectic liquid crystal.[22]

Some ten years ago, Sataric and Tuszynski[23] used a liquid crystal framework to model the dynamics of complete heterodimers within the protofilaments of MTs. Earlier Das and Schwartz[24] followed an analogous strategy in order to elaborate the excitation of solitons in cell membranes. The conspicuous flexibility of TTs,[20] which enables that their respective polar tilt angles could vary in the broad interval $(-\frac{\pi}{2} < \theta < \frac{\pi}{2})$, suggests that the dynamics of their oscillations should be essentially nonlinear leading to the formation of topological kink–waves.

The paper is organized as follows:

In Section II, we introduce the liquid crystal framework of TTs dynamics based on the fact that the latest experimental evidence and computational simulations reveal how tubulin's chirality and dipolar charge distribution fully justify the validity of such an approach. Section III presents the analytical solutions of the nonlinear equation of motion for tilt degrees of freedom for TTs all together with the estimation of pertaining parameters of the model. In line with this, the numerical solution of the corresponding nonlinear differential equation is given. In Section IV, we discuss the possible relationship between the kinks which arise in TT tilting dynamics and the signaling communications between intra cell's compartments in the context of cellular traffic and dynamical instability of MTs.

II. THE FERROELECTRIC LIQUID CRYSTAL FRAMEWORK FOR THE DYNAMICS OF TTs

We now consider the collection of TTs within a MT to be a two–dimensional smectic–C ferroelectric liquid crystal folded into a cylinder so that TTs are pointing radially outwards, see Fig. 4. The detailed map of the electric charge distribution on the surface of the tubulin dimer elaborated in Ref. 25 is here presented in Fig. 3. Tubulin's electrostatic properties, including its surface potential energy, were calculated with the aid of the molecular dynamics package TINKER.[26]

The tubulin dimers within a MT cylinder are incorporated in a way that the inner parts of the dimer are

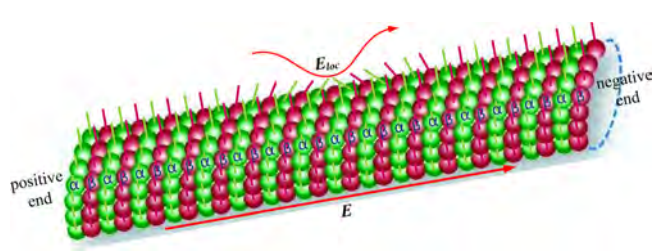

FIG. 4. The set of TTs within a MT can be considered as a two–dimensional smectic–C ferroelectric liquid crystal folded into a cylinder so that TTs are pointing radially outwards. MT represents a giant dipole with one positive and the opposite negative end, thus creating intrinsic electric field E in between. The localized wave is also indicated with accompanying electric field.

compressed, while the outer ones are stretched creating the wedgelike conformation, see Fig. 5. It causes a significant piezoelectric effect due to the additional redistribution of excess negative charges in the dimer's body. It is the main reason for strong transverse tubulin polarization. This conspicuous local dielectric anisotropy is here expressed in terms of parameter μ_p which has the dimensions of electric field (V/m). This parameter will be used in the expression for total polarization energy. The outer surface of a tubulin is pretty highly negatively charged at physiological pH, but much of this negative charge is concentrated on the TT, as it was already mentioned. At neutral pH, the negative charge on the TT causes it to remain extended due to the electrostatic repulsion within the tail. So in the following, we will consider the TTs as the collection of thin rigid rods capable to swing around fixed ends embedded in tubulin's body.

Every TT has its own dipole moment which is superimposed with the resultant dipole moment of heterodimer's body. When a TT tilts about its fixed base, its dipole accordingly swings, causing that the total dipole moment of a tubulin with its TT has a dynamical character. We stress again that the components along x-axis and transversal one (along radius r) are given as follows:

$$p_x = p\sin\gamma; \quad p_r = p\cos\gamma, \tag{2.1}$$

where γ is the angle between the total dimer's moment $\vec{p}$ and the radial axis. This geometry is illustrated in Fig. 6(a). The exact numerical values of parameters from Eq. (2.1) are not measured, but their values for tubulin without TTs are already mentioned on the basis of an *in silico* experiment.[26] The contribution of TTs should further increase the transversal component $\vec{p}_r$ providing that the angle γ must be small.

We should pay attention that along a MT the intrinsic electric field exists in parallel with the x-axis. This is the result of superimposing of $\vec{p}_x$ components of every tubulin dimer within a MT. The transversal components $\vec{p}_r$ mutually cancel; so that the resultant mesoscopic field $\vec{E}$ is aligned along MT's x-axis, see Fig. 6(a). Let us suppose that a TT is tilted at a polar angle θ, see Fig. 6(b), and consider the corresponding components of the polarization vector (dipole moments per unit volume in C/m^2) denoted with capital letters P_r and P_x. Then the density of polarization energy of a MT can be written as follows:

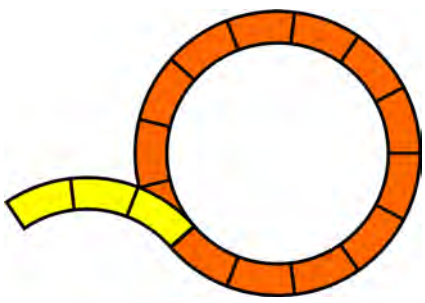

FIG. 5. The cross section of a MT that indicates the wedgelike conformations of 13 tubulin heterodimers. It illustrates the importance of proper orientation of wedgelike tubulin heterodimers in completing the cylindrical architecture of a MT. These chiral forms are the reason for strong anisotropy of dipolar properties of MT. The compression of the inner part of tubulin dimers within this topology contributes to the high value of the radial projection of dimer's dipolar moment.

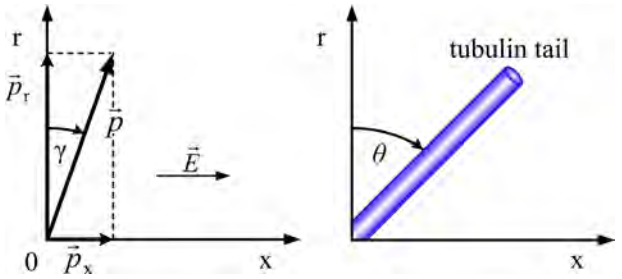

FIG. 6. (a) The components of the total dipole moment of a tubulin. The p_x components of all heterodimers within a protofilament contribute to the creation of the resultant intrinsic electric field E. The characteristic angle γ is indicated. (b) The tilt of a TT with polar angle θ. The angle γ is fixed, while θ changes remarkably.

$$W_{pol}\left[\frac{\mathcal{J}}{m^3}\right] = \frac{P_r^2}{2\chi_r} + \frac{P_x^2}{2\chi_x} - EP_x - \mu_p P_r \sin\theta, \tag{2.2}$$

where the corresponding longitudinal and transversal dielectric susceptibilities are denoted as χ_x and χ_r. When a TT is tilted at the angle θ, so is $\vec{P}_r$, and its projection on the x-axis can be expressed as $\mu_p P_r \sin\theta$. The parameter μ_p reflects the local dielectric anisotropy and the chirality of TTs and it will be elaborated later in more details.

It is now possible to treat the problem in the framework of the smectic–C liquid crystal model in accordance with the seminal approach proposed by Carlsson.[27] For more details see the Appendix. We have already stressed that many MAPs are associated with MTs in order to stabilize their structure against depolymerisation. For example, each MAP–tau is an extended molecule possessing MT–binding domains and one N–terminal "projection" domain that extends from the outer surface of MT[28] as shown in Fig. 7. Also, it can be noticed that every MAP–tau is extended along pertaining protofilament. The size of its "projection" domain provides spacing between MTs containing MAPs in a way that they repel instead of crosslink the neighbouring MTs. But these protofilaments occupied by MAP–tau are insurmountable obstacles for any propagation of tilt waves of TTs as well as for progressive walking of motor proteins. Thus, only the protofilaments free of MAPs provide true conditions for the collective TT's swings keeping the angle $\varphi_1 = 0$ as a favouring option. The angle $\varphi_3 = \frac{\pi}{4}$ could lead to strong asymmetric impact of neighbouring MAPs preventing the survival of a pertaining wave. These angles were elaborated and determined in the Appendix. Similar conclusions were presented in Ref. 29, where Georgiev and Glazebrook have stated that "it is clear that only visibly interacting TT neighbours are those lying in the same protofilament." Such an approach has been recently outlined by us,[30] but here our goal is to elaborate the complete concept through detailed modelling including concrete estimations of relevant parameters. This enables us to determine the velocity of pertaining kink–waves. It is expected that these velocities have the order of centimetre per second which

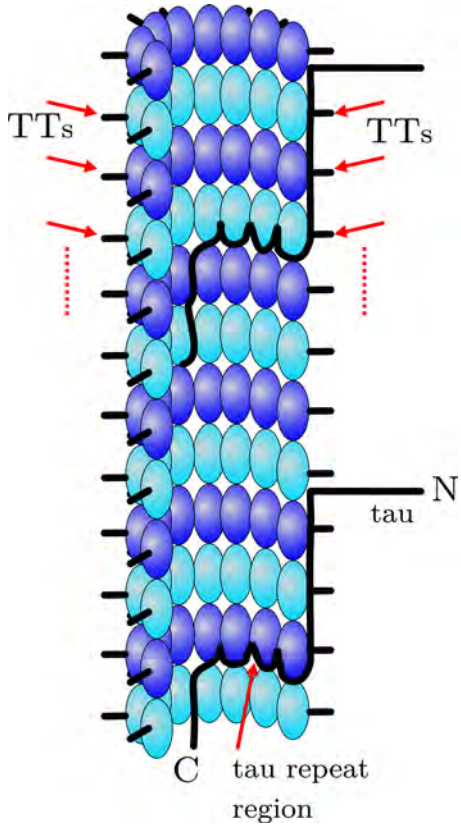

FIG. 7. Model of MAPs from the tau protein family interacting with a MT. Illustration represents the N–terminal domains of tau molecules whose C–terminal segments, including the repeat motifs, bind strongly to the inside of the MT. On the left hand side are the protofilaments free of tau proteins and as such they are suitable for swing waves of TTs. The protofilaments occupied by MAPs are not suitable for signaling by TTs wave.

would mean that kink may serve as a fast and efficient signalling mechanism suitable for in the regulation of intracellular traffic performed by kinesin and dynein motor proteins.

In accordance with the above arguments, the next step is to introduce the density of the splay energy of TTs denoted by $W_{\rm sp}$, along with the elastic layer energy $W_{\rm lay}$ elaborated in the Appendix

$$W_{\rm sp}=\frac{1}{2}K_{11}\left(\frac{\partial\theta}{\partial x}\right)^2,\quad W_{\rm lay}=\frac{K_{11}}{2r^2}+\frac{1}{4r^2}(A\theta^2+B\theta^4), \tag{2.3}$$

and the density of the kinetic energy of tilting TTs

$$W_{\rm k}=\frac{1}{2}\mathcal{J}\left(\frac{\partial\theta}{\partial t}\right)^2, \tag{2.4}$$

where $\mathcal{J}$ stands for the density of rotational inertia of TTs when they rotate around their fixed ends joined with MT body. Importantly, on the basis of the possible large tilt angles θ and taking an appropriate expansion of the function $\sin\theta$, the density of polarization energy, Eq. (2.2) now reads

$$W_{\rm pol}=\frac{P_{\rm x}^2}{2\chi_{\rm x}}+\frac{P_{\rm r}^2}{2\chi_{\rm r}}-EP_{\rm x}-\mu_{\rm p}P_{\rm r}\theta+\frac{1}{6}\mu_{\rm p}P_{\rm r}\theta^3. \tag{2.5}$$

If we use Eq. (2.1), this expression involves the angle γ between the total polarization vector and the radial axis, thus giving

$$W_{\rm pol}=\frac{P^2\sin^2\gamma}{2\chi_{\rm x}}+\frac{P^2\cos^2\gamma}{2\chi_{\rm r}}-EP\sin\gamma-(\mu_{\rm p}P\cos\gamma)\theta+\left(\frac{1}{6}\mu_{\rm p}P\cos\gamma\right)\theta^3. \tag{2.6}$$

The polarization energy density given by Eq. (2.6) can now be minimized with respect to P, thus enabling the elimination of this unknown total polarization vector in terms of the polar angle θ

$$\frac{\partial W_{\rm pol}}{\partial P}=0, \tag{2.7}$$

which leads to the expression

$$P=\left[E\sin\gamma+(\mu_{\rm p}\cos\gamma)\theta-\left(\frac{1}{6}\mu_{\rm p}\cos\gamma\right)\theta^3\right]\Lambda(\gamma),$$
$$\Lambda(\gamma)=\left(\frac{\cos^2\gamma}{\chi_{\rm r}}+\frac{\sin^2\gamma}{\chi_{\rm x}}\right)^{-1}. \tag{2.8}$$

Inserting P from Eq. (2.8) into Eq. (2.6), we finally get

$$W_{\rm pol}=\Lambda\left[\left(\frac{1}{6}\mu_{\rm p}^2\cos^2\gamma\right)\theta^4+\left(\frac{1}{12}E\mu_{\rm p}\sin2\gamma\right)\theta^3-\left(\mu_{\rm p}^2\cos^2\gamma\right)\theta^2-\left(\frac{1}{2}E\mu_{\rm p}\sin2\gamma\right)\theta-\frac{1}{2}E^2\sin^2\gamma\right]. \tag{2.9}$$

This is the complete polynomial of the fourth power. Even in the case where electric field E is small enough making three corresponding terms negligible, the remaining two terms with even powers of the angle θ assure the existence of double–well potential, which enables the existence of kink excitations.

We now gather together all the elastic and polarization energy terms along with kinetic energy, Eqs. (2.3), (2.4) and (2.9), thus creating the total free energy for the complete collection of TTs within a MT of the length (x_2-x_1)

$$F=2\pi\int_R^{R+h}rdr\int_{x_1}^{x_2}dx\left[\frac{K_{11}}{2}\left(\frac{\partial\theta}{\partial x}\right)^2+\frac{\mathcal{J}}{2}\left(\frac{\partial\theta}{\partial t}\right)^2+\frac{K_{11}}{r^2}+\frac{1}{4r^2}(A\theta^2+B\theta^4)+\left(\frac{1}{6}\Lambda\mu_{\rm p}^2\cos^2\gamma\right)\theta^4+\left(\frac{1}{12}\Lambda\mu_{\rm p}E\sin2\gamma\right)\theta^3-\left(\Lambda\mu_{\rm p}^2\cos^2\gamma\right)\theta^2-\left(\frac{1}{2}\Lambda\mu_pE\sin2\gamma\right)\theta-\frac{1}{2}\Lambda E^2\sin^2\gamma\right]. \tag{2.10}$$

Here, $R=12.5$ nm stands for the outer radius of a MT and $h=4.5$ nm is the average length of a TT, thus indicating the bounds for radial integration. Performing the integration with respect to the radial degree of freedom r, the last expression becomes

$$F=\int_{x_1}^{x_2}dx\Bigg\{\pi(2Rh+h^2)\left[\frac{K_{11}}{2}\left(\frac{\partial\theta}{\partial x}\right)^2+\frac{\mathcal{J}}{2}\left(\frac{\partial\theta}{\partial t}\right)^2\right]+\pi K_{11}\ln\left(1+\frac{h}{R}\right)+\frac{\pi}{2}\ln\left(1+\frac{h}{R}\right)(A\theta^2+B\theta^4)$$
$$+\left[\frac{\pi}{6}(2Rh+h^2)\Lambda\mu_p^2\cos^2\gamma\right]\theta^4+\left[\frac{\pi}{12}(2Rh+h^2)\Lambda\mu_pE\sin(2\gamma)\right]\theta^3-\left[\pi(2Rh+h^2)\Lambda\mu_p^2\cos^2\gamma\right]\theta^2$$
$$-\left[\frac{\pi}{2}(2Rh+h^2)\Lambda\mu_pE\sin(2\gamma)\right]\theta-\left[\frac{\pi}{2}(2Rh+h^2)\Lambda E^2\sin^2\gamma\right]\Bigg\}. \tag{2.11}$$

There are two terms with odd powers of θ expressing the direct coupling of mechanical deformation θ with the electric field E.

In order to complete the model, it is important to know the viscous torque density of a TT. Starting from the illustration given in Fig. 8, we see that elementary torque at distance z from TT's fixed end for a small segment dz amounts

$$d\mathcal{M}_{\text{visc}}=-zdF;\quad dF=\eta\upsilon dz$$
$$\nu=z\omega;\quad \omega=\frac{d\theta}{dt}$$
$$d\mathcal{M}_{\text{visc}}=-\eta\omega z^2dz$$
$$\mathcal{M}_{\text{visc}}=-\eta\omega\int_0^h z^2dz;\quad \mathcal{M}_{visc}=-\frac{1}{3}\eta h^3\left(\frac{d\theta}{dt}\right). \tag{2.12}$$

The volume of a TT is given by $V_{\text{TT}}=R_{\text{TT}}^2\pi h$, so that the viscous torque density reads

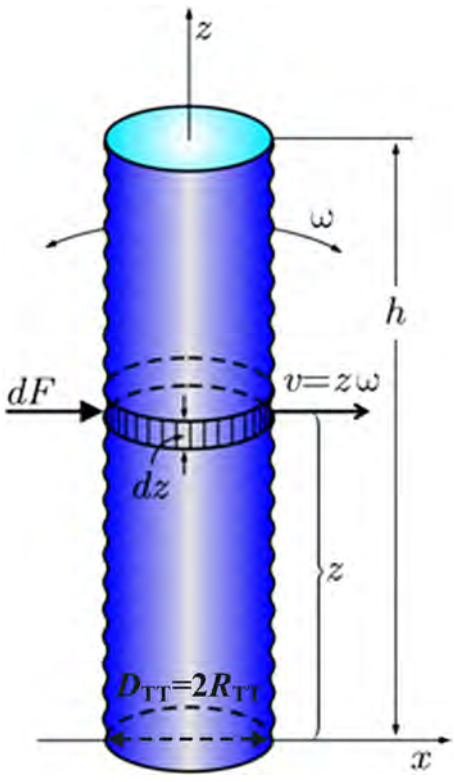

FIG. 8. The display of the geometry for the determination of the viscous torque $\mathcal{M}_{visc}$ pertaining to single TT. Parameter z represents the distance of the small element from the fixed base, ω is the angular velocity related with the local translation velocity ν, h is the length, and R_{TT} is the radius of a TT. The elementary force dF acting at distance z causes local velocity $\nu=z\omega$.

$$\mathcal{D}_{\text{visc}}=-\frac{1}{3}\frac{\eta h^3}{R_{\text{TT}}^2\pi h}\left(\frac{d\theta}{dt}\right)=-\Gamma\frac{d\theta}{dt};\quad \Gamma=\frac{1}{3}\frac{\eta h^2}{\pi R_{\text{TT}}^2}. \tag{2.13}$$

Here, η stands for the viscosity coefficient of cytosol in (Pa s), $h=4.5$ nm is the length of a TT while $R_{\text{TT}}=0.5$ nm is the radius of TT.

Eventually, we can minimize F from Eq. (2.11) with respect to θ and equate it to the damping term (2.13), thus arriving to the Euler–Lagrange equation for the polar angle θ which expresses the swings of TTs

$$\frac{\partial^2\theta}{\partial x^2}-\frac{\mathcal{J}}{K_{11}}\left(\frac{\partial^2\theta}{\partial t^2}\right)-\delta\frac{\partial\theta}{\partial t}-a\theta^3-b\theta^2+c\theta+d=0, \tag{2.14}$$

where we have established the set of abbreviations

$$\delta=\frac{\Gamma}{\pi K_{11}};\quad a=\frac{1}{K_{11}}\left[\frac{2B\ln\left(1+\frac{h}{R}\right)}{(2Rh+h^2)}+\Lambda\mu_p^2\cos^2\gamma\right];$$
$$b=\left[\frac{\Lambda\mu_p}{6K_{11}}\sin(2\gamma)\right]E;$$
$$c=\frac{1}{K_{11}}\left[2\Lambda\mu_p^2\cos^2\gamma-\frac{2A\ln\left(1+\frac{h}{R}\right)}{(2Rh+h^2)}\right];$$
$$d=\left[\frac{\Lambda\mu_p}{2K_{11}}\sin(2\gamma)\right]E. \tag{2.15}$$

III. THE ANALYTICAL SOLUTIONS

In order to determine the analytical solutions of Eq. (2.14), we are going to introduce a set of dimensionless variables transforming the pertinent derivatives in this equation

$$\xi=\sqrt{a}x;\quad \tau=\frac{t}{T_0};\quad T_0=\left(\frac{\mathcal{J}}{K_{11}a}\right)^{\frac{1}{2}};$$
$$\frac{\partial^2\theta}{\partial x^2}=a\frac{\partial^2\theta}{\partial\xi^2};\quad \frac{\partial^2\theta}{\partial t^2}=\frac{1}{T_0^2}\left(\frac{\partial^2\theta}{\partial\tau^2}\right)=\left(\frac{K_{11}a}{\mathcal{J}}\right)\frac{\partial^2\theta}{\partial\tau^2};$$
$$\frac{\partial\theta}{\partial t}=\left(\frac{K_{11}a}{\mathcal{J}}\right)^{\frac{1}{2}}\left(\frac{\partial\theta}{\partial\tau}\right). \tag{3.1}$$

Further, we define the characteristic velocity of undamped linear swing wave of TTs

$$\upsilon_0=\left(\frac{K_{11}}{\mathcal{J}}\right)^{\frac{1}{2}}, \tag{3.2}$$

which along with the actual damped velocity of nonlinear mechanoelectric wave υ arising from Eq (2.14) leads to the dimensionless velocity s

$$s = \frac{\upsilon}{\upsilon_0}. \tag{3.3}$$

Eventually by choosing the dimensionless traveling–wave form for the function $\theta(\xi, \tau)$,

$$\theta = \theta(\xi - s\tau) = \theta(\zeta). \tag{3.4}$$

Eq. (2.14) becomes the nonlinear ordinary differential equation suitable for the analytical as well as numerical explorations

$$\frac{d^2\theta}{d\zeta^2}(1 - s^2) + \lambda s\frac{d\theta}{d\zeta} - \theta^3 - \beta\theta^2 + \rho\theta + \sigma = 0, \tag{3.5}$$

with the set of redefined parameters

$$\lambda = \delta\left(\frac{K_{11}}{\mathcal{J}a}\right)^{\frac{1}{2}}; \quad \beta = \frac{b}{a}; \quad \rho = \frac{c}{a}; \quad \sigma = \frac{d}{a}. \tag{3.6}$$

The explicit forms of the newly introduced parameters read

$$\lambda = \frac{\Gamma}{\pi K_{11}}\left(\frac{K_{11}}{\mathcal{J}a}\right)^{\frac{1}{2}}; \quad \beta = \frac{1}{4}\nu E; \quad \rho = \left(\frac{1 - Aw}{1 + Bw}\right);$$
$$\sigma = \frac{1}{2}\nu E = 2\beta, \quad \nu = \sin(2\gamma)\left[\frac{2B\ln\left(1 + \frac{h}{R}\right)}{\Lambda\mu_p(2Rh + h^2)} + \mu_p\cos^2\gamma\right];$$
$$w = \left[\frac{2\ln\left(1 + \frac{h}{R}\right)}{\Lambda\mu_p^2(2Rh + h^2)\cos^2\gamma}\right]. \tag{3.7}$$

Obviously, Eq. (3.5) involves an asymmetric double–well potential of the form

$$\Pi(\theta) = \frac{1}{4}\theta^4 + \frac{1}{3}\beta\theta^3 - \frac{1}{2}\rho\theta^2 - \sigma\theta. \tag{3.8}$$

We stress that two terms in Eq. (2.14) contain the strength of the local electric field E (terms with b and d) indicating that the shape of double–well potential is influenced by this field. Thus, the positions of the two energy minima can be adjusted by changing the strength of the intrinsic electric field E, or the angle γ which also slightly depends on E. The local values of E could depend on local concentration of present ions, but this aspect is not treated in this stage of model.

We have made at least the rough estimates of the above parameters on the basis of some known data and other pretty uncertain data. We first estimate the characteristic velocity of waves spreading in terms of swings of TTs. In that respect, we take that the elastic constant has the order of magnitude as in the case of the cell membrane $K_{11} = 6 \times 10^{-12}$ N.[31] Otherwise, the elastic constants in higher order terms of expansion in Eq. (A10), due to the lack of experimental evidence, are reasonably approximated as follows:

$$A \sim 1 \times 10^{-12}\,\text{N} \text{ and } B \sim 0.5 \times 10^{-12}\,\text{N}. \tag{3.9}$$

The density of rotational inertia of a single TT can be estimated on a quite reliable basis. If a TT is being considered as a rod of the length $h = 4.5$ nm and with the average mass of $m = 6\,\text{kDa} = 6 \times 10^3 \cdot 1.67 \times 10^{-27}\,\text{kg} = 10.02 \times 10^{-24}\,\text{kg}$, one obtains its rotational inertia as

$$I = \frac{1}{3}mh^2 = 64.8 \times 10^{-42}\,\text{kg}\,\text{m}^2. \tag{3.10}$$

Since the diameter of the TT is $D_{TT} = 1$ nm, then its volume is determined by

$$V_{TT} = \frac{{D_{TT}}^2\pi}{4} \cdot h = 3.5 \times 10^{-27}\text{m}^3. \tag{3.11}$$

Consequently the density of rotational inertia is

$$\mathcal{J} = \frac{I}{V_{TT}} = 18.4 \times 10^{-15}\frac{\text{kg}}{\text{m}}. \tag{3.12}$$

Eventually, the characteristic velosity of the wave in undamped regime is

$$\upsilon_0 = \sqrt{\frac{K_{11}}{\mathcal{J}}} = \sqrt{\frac{6 \times 10^{-12}}{18.4 \times 10^{-15}}} = 17\frac{\text{m}}{\text{s}}. \tag{3.13}$$

Surprisingly, this order of magnitude is very close to the velosity of the so–called action potential propagating along the nerve axon cells. This fact could have some profound consequences in cellular signaling and other functional activities.

In order to estimate the most uncertain parameter μ_p, we start from the request that the term $\rho\theta$ in Eq. (3.5) must assure the existence of the double–well potential if the inequality $\rho > 0$ holds. Based on Eq. (3.7), it implies $Aw < 1$ or

$$\mu_p > \left[\frac{2A\ln\left(1 + \frac{h}{R}\right)}{\Lambda(2Rh + h^2)\cos^2\gamma}\right]^{\frac{1}{2}}. \tag{3.14}$$

We first need to calculate the parameter Λ defined by Eq. (2.8). We rely onto the still unique experimental evidence[32] for the dielectric permittivity of a tubulin dimer $\varepsilon_{red} = 8.4$. This value can be considered as the reduced parameter defined by the expression,

$$\varepsilon_{red} = \frac{\varepsilon_r\varepsilon_x}{\varepsilon_r + \varepsilon_x}. \tag{3.15}$$

On the basis of the fact that the radial component of polarization is very dominant over the longitudinal one,[32] we can conclude that the inequality $\varepsilon_r \gg \varepsilon_x$ holds, thus giving

$$\varepsilon_{red} \approx \varepsilon_x = 8.4. \tag{3.16}$$

If we take that the radial component of polarization is closer to the value of polarization of water, for instance $\varepsilon_r = 50$, we can estimate the parameter Λ on the basis of Eq. (2.8). Prior to this,

we should estimate the angle γ in terms of the components $p_r = 1669$ D and $p_x = 336$ D

$$\gamma = arctg\left(\frac{337}{1669}\right) = 11.4^\circ. \tag{3.17}$$

Consequently, $\sin^2\gamma = 0.039$ and $\cos^2\gamma = 0.96$, thus yielding

$$\Lambda \equiv \frac{\varepsilon_0}{\left(\frac{\sin^2\gamma}{\varepsilon_x} + \frac{\cos^2\gamma}{\varepsilon_r}\right)} = \frac{8.85 \times 10^{-12}}{\left(\frac{0.039}{8.4} + \frac{0.96}{50}\right)} = 3.7 \times 10^{-10}\left(\frac{\mathrm{F}}{\mathrm{m}}\right). \tag{3.18}$$

Then the restriction from Eq. (3.14) leads to the estimation

$$\mu_p > \left[\frac{2 \times 10^{-12} \cdot 0.31}{3.7 \times 10^{-10} \cdot 1.32 \times 10^{-16} \cdot 0.96}\right]^{\frac{1}{2}} = 3.6 \times 10^6\left(\frac{\mathrm{V}}{\mathrm{m}}\right). \tag{3.19}$$

This value indicates very strong local intrinsic field within the dipolar heterodimer. Taking arbitrary,

$$\mu_p = 5 \times 10^6\left(\frac{\mathrm{V}}{\mathrm{m}}\right), \tag{3.20}$$

we are finally in the position to calculate the set of parameters from Eq. (3.7). Inserting $\gamma = 11.4^\circ$, $R = 12.5$ nm; $h = 4.5$ nm, $\Lambda = 3.7 \times 10^{-10}\left(\frac{\mathrm{F}}{\mathrm{m}}\right)$ and $\mu_p = 5 \times 10^6\left(\frac{\mathrm{V}}{\mathrm{m}}\right)$, we obtain

$$\nu = 0.35 \times 10^{-7}\left(\frac{\mathrm{m}}{\mathrm{V}}\right); \quad w = 0.53 \times 10^{12}\,\mathrm{N}^{-1}. \tag{3.21}$$

Now one can calculate the important parameter ρ from Eqs. (3.7), (3.9), and (3.21) as follows:

$$\rho = \frac{1 - 10^{-12} \cdot 0.53 \times 10^{12}}{1 + 0.5 \times 10^{-12} \cdot 0.53 \times 10^{12}} = 0.37. \tag{3.22}$$

It is evident that the parameters β and σ from Eq. (3.5) could survive just in the case of the very strong field E as being of the order of mega–Volts per meter. If we take $E = 5 \times 10^6\left(\frac{\mathrm{V}}{\mathrm{m}}\right)$, which holds for the presence of the action potential in neurons, it yields

$$\beta = \frac{1}{4}\nu E = 0.043; \quad \sigma = \frac{1}{2}\nu E = 0.086. \tag{3.23}$$

The viscous term is the last one that remains to be assessed numerically

$$\lambda = \frac{1}{3\pi}\eta\left(\frac{h}{r}\right)^2\left[\mathcal{J}\left(\frac{2B\ln\left(1+\frac{h}{R}\right)}{2Rh+h^2} + \Lambda\mu_p^2\cos^2\gamma\right)\right]^{-\frac{1}{2}}. \tag{3.24}$$

Inserting respective data already estimated, and taking the viscosity of $\eta = 10^{-3}$ Pa s, we finally get

$$\lambda = 0.17 \times 10^3. \tag{3.25}$$

It suggests that for reasonable value of the factor $s\lambda$ in Eq. (3.5) s must be of the order

$$s \sim 10^{-3}. \tag{3.26}$$

In that case the inertial term $s^2\frac{d^2\theta}{d\zeta^2}$ can be safely neglected while the term $\lambda s\frac{d\theta}{d\zeta}$ is still not overdamped. On that basis, the velocity of the localized wave described by Eq. (3.5) in terms of Eq. (3.13) should be on the order of

$$\upsilon \sim 10^{-3}\upsilon_0 \sim 1.7\left(\frac{\mathrm{cm}}{\mathrm{s}}\right). \tag{3.27}$$

The reason for the dominancy of drag force over inertial force is a very small Reynolds number for TT which is on the order of 10^{-7}. Slower waves are less damped within the framework of our model. If we take into account that the diffusive processes in living cells take place with typical velocities of the order of a few micrometers per second, the velocity given by Eq. (3.27) is much beyond and it has the advantage for cell's signaling.

In order to further transform Eq. (3.5), we introduce new variables as follows:

$$\theta = \frac{f}{\left(\rho + \frac{\beta^2}{3}\right)^{\frac{1}{2}}} - \frac{1}{3}\beta; \quad u = \left(\frac{\rho + \frac{\beta^2}{3}}{1 - s^2}\right)^{\frac{1}{2}}\zeta. \tag{3.28}$$

From the evaluated data, Eqs. (3.22) and (3.23), the condition $\rho + \frac{\beta^2}{3} > 0$ is safely fulfilled. Thus, Eq. (3.5) is converted in the final compact version

$$\frac{d^2f}{du^2} + g\frac{df}{du} - f^3 + f + q = 0, \tag{3.29}$$

where the new redefined parameters read

$$g = \frac{\lambda s}{\left[(1 - s^2)\left(\rho + \frac{\beta^2}{3}\right)\right]^{\frac{1}{2}}}; \quad q = \left(\rho + \frac{\beta^2}{3}\right)^{-\frac{1}{2}}\left(\sigma - \frac{\rho\beta}{3} - \frac{8\beta^2}{27}\right). \tag{3.30}$$

Inserting $\lambda s = 0.17$, $\rho = 0.37$, $\beta = 0.043$, and $\sigma = 0.086$, one readily obtains

$$g = 0.28; \quad q = 0.14, \tag{3.31}$$

which brings about the very concrete form of our equation

$$\frac{d^2f}{du^2} + 0.28\frac{df}{du} - f^3 + f + 0.14 = 0. \tag{3.32}$$

Since we want to consider the potential well with two minima, it is required that the inequality

$$q^2 \le \frac{4}{27}, \tag{3.33}$$

must be fulfilled. This condition in our case conspicuously holds as follows $0.02 < 0.148$.

The kink solution of Eq. (3.29) now can be easily found by the tanh–method.[33,34] Taking

$$f = \mathcal{A} + \mathcal{B}\tanh(\mathcal{H}u), \tag{3.34}$$

and inserting in Eq. (3.29), we obtain the system of algebraic equations

$$\begin{aligned} 2\mathcal{B}\mathcal{H} - \mathcal{B}^3 &= 0 \\ -g\mathcal{B}\mathcal{H} - 3\mathcal{A}\mathcal{B}^2 &= 0 \\ -2\mathcal{B}\mathcal{H}^2 - 3\mathcal{A}^2\mathcal{B} + \mathcal{B} &= 0 \\ g\mathcal{B}\mathcal{H} - \mathcal{A}^3 + \mathcal{A} + q &= 0. \end{aligned} \tag{3.35}$$

The solutions of this system are as follows:

$$\begin{aligned} &\mathcal{H} = \pm\frac{1}{\sqrt{2}}\mathcal{B}; \quad g = -3\sqrt{2}\mathcal{A}; \quad \mathcal{B} = \pm(1-3\mathcal{A}^2)^{\frac{1}{2}}; \\ &-2\mathcal{A} = \{f_{\mathrm{H}}, f_{\mathrm{M}}, f_{\mathrm{L}}\}, \end{aligned} \tag{3.36}$$

where three possible values of the parameter $\mathcal{A}$ are defined through the higher minimum f_{H}, the maximum f_{M}, and the lower minimum f_{L} of pertinent double–well potential

$$\Pi(f) = \frac{1}{4}f^4 - \frac{1}{2}f^2 - qf. \tag{3.37}$$

The shape of this double–well potential for estimated parameter $q = 0.14$ is illustrated in Fig. 9.

These values strictly depend on the parameter q through the angle F defined by

$$F = \frac{1}{3}\arccos\left(\frac{3\sqrt{3}}{2}q\right), \tag{3.38}$$

thus giving

$$\begin{aligned} f_H &= \frac{2}{\sqrt{3}}\cos F; \\ f_M &= -\frac{1}{\sqrt{3}}\left(\cos F - \sqrt{3}\sin F\right); \\ f_L &= -\frac{1}{\sqrt{3}}\left(\cos F + \sqrt{3}\sin F\right). \end{aligned} \tag{3.39}$$

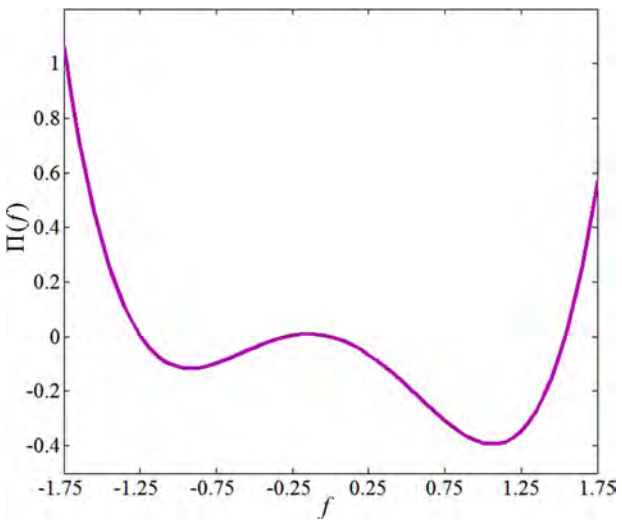

FIG. 9. The shape of double–well potential given by Eq. (3.37) for estimated parameter $q = 0.14$.

For $q = 0.14$, we have $F = 0.4\,\mathrm{rad} = 22.96°$, $f_{\mathrm{H}} = 1.07$, $f_{\mathrm{M}} = -0.14$, and $f_{\mathrm{L}} = -0.92$. From Eq. (3.36), it turns out that the viscous parameter g can define all of the three above characteristic points of pertaining double–well potential. Since this parameter involves the relative velocity s which is adjustable, it appears that for three different values of s_i we have the equalities

$$\lambda s_i = g_i = \frac{3f_i}{\sqrt{2}}; \qquad i = \mathrm{H}, \mathrm{M}, \mathrm{L}, \tag{3.40}$$

where the additional relations hold

$$s_i = \left[1 + \frac{\lambda^2}{g_i f_i^2\left(\rho + \frac{\beta^2}{3}\right)}\right]^{-\frac{1}{2}} < 1. \tag{3.41}$$

Inserting parameters $\lambda = 170$; $\rho = 0.37$; $\beta = 0.043$ and estimated values of f_i, we easily get three characteristic relative velocities of corresponding kinks

$$s_H = 8 \times 10^{-3}; \quad s_M = 1.1 \times 10^{-3}; \quad s_L = 7.1 \times 10^{-3}. \tag{3.42}$$

Using the estimated characteristic velocity $\upsilon_0 = 17\left(\frac{\mathrm{m}}{\mathrm{s}}\right)$, we readily determined the velocities for above three kink configurations as follows:

$$\upsilon_H = 14\left(\frac{\mathrm{cm}}{\mathrm{s}}\right); \quad \upsilon_M = 1.87\left(\frac{\mathrm{cm}}{\mathrm{s}}\right); \quad \upsilon_L = 12\left(\frac{\mathrm{cm}}{\mathrm{s}}\right). \tag{3.43}$$

These values are remarkably greater than the typical diffusion velocities in cells which are of the order of $\left(\frac{\mu\mathrm{m}}{\mathrm{s}}\right)$, but, on the other hand, much lower than the cut off velocity of sound in undamped regime $17\left(\frac{\mathrm{m}}{\mathrm{s}}\right)$. It is clear that viscosity diminishes remarkably the kink's velocity while ρ, β, and f_{i} increase its value. The option $f = f_{\mathrm{H}}$ gives the maximal speed s_{H}, if all remaining parameters from Eq. (3.40) are held fixed. All the possible kink–like functions arising from Eq. (3.39) are

$$\begin{aligned} f_{\mathrm{LM}} &= \frac{f_{\mathrm{L}} + f_{\mathrm{M}}}{2} \pm \left(\frac{f_{\mathrm{L}} - f_{\mathrm{M}}}{2}\right)\tanh(\mathcal{H}_{\mathrm{H}}\zeta); \\ f_{\mathrm{HM}} &= \frac{f_{\mathrm{H}} + f_{\mathrm{M}}}{2} \pm \left(\frac{f_{\mathrm{H}} - f_{\mathrm{M}}}{2}\right)\tanh(\mathcal{H}_{\mathrm{L}}\zeta); \\ f_{\mathrm{HL}} &= \frac{f_{\mathrm{H}} + f_{\mathrm{L}}}{2} \pm \left(\frac{f_{\mathrm{H}} - f_{\mathrm{L}}}{2}\right)\tanh(\mathcal{H}_{\mathrm{M}}\zeta), \end{aligned} \tag{3.44}$$

with

$$\begin{aligned} \mathcal{H}_{\mathrm{H}} &= \frac{3f_{\mathrm{H}}(f_{\mathrm{L}} - f_{\mathrm{M}})\left(\rho + \frac{\beta^2}{3}\right)}{4\lambda s_{\mathrm{H}}}; \\ \mathcal{H}_{\mathrm{L}} &= \frac{3f_{\mathrm{L}}(f_{\mathrm{H}} - f_{\mathrm{M}})\left(\rho + \frac{\beta^2}{3}\right)}{4\lambda s_{\mathrm{L}}}; \\ \mathcal{H}_{\mathrm{M}} &= \frac{3f_{\mathrm{M}}(f_{\mathrm{H}} - f_{\mathrm{L}})\left(\rho + \frac{\beta^2}{3}\right)}{4\lambda s_{\mathrm{M}}}. \end{aligned} \tag{3.45}$$

Corresponding functions θ for the tilt angles can be easily calculated using transformations in Eq. (3.28). Numerical solution of boundary value problem associated with Eq. (3.29) shows excellent fit of the exact solutions given by Eqs. (3.44) and (3.45), see Fig. 10.

It is important to emphasize that in the performed numerical calculations we did not take into account an additional component of tubulin dipolar moment provided by negatively charged tubulin tails. This was caused by the circumstance that, depending on the specific role played by MT, the different amount of counterions can surround TTs thus changing remarkably their effective charge.[18,19] Generally, the role of TTs is to mostly increase the radial component of total tubulin polarization p_r, leading to the decrease of the angle γ, see Fig. 6(a) and Eq. (2.1). The decrease in γ has an impact on the parameters given by Eq. (3.7) in a way that parameters ν and w decrease, while the parameter ρ increases. The resulting effect of all these changes is that the final model parameter q defined by Eq. (3.30) goes down. This yields the weakening of asymmetry of double–well potential, see Eq. (3.37) and Fig. 9. On the other hand, the influx of cations, such as Ca^{2+} and Mg^{2+}, could strongly affect the effective charge of TTs, thus decreasing p_r and consequently increasing the angle γ. In that way, the amplitude and the velocity of the kink are affected by the change of concentration of counterions. The nano–pores present in MT wall[21] also have some role in controlling the flow of these cations. This will be the subject of our future studies which will consider the impact of nano–pores in detail.

Finally, we can discuss at least qualitatively how the so–called posttranslational modification of TTs[14,15] can impact our model due to the change of pertaining parameters. For example, in the TT polyglutamilation by adding one or several glutamate residues, the mass (rotational inertia) of a TT is increased and so is the viscosity drag. At the same time, the radial component of dipolar moment is also increased because of the additional negative charges. All these changes are incorporated in our model described by Eq. (3.27). It enables the excitation of appropriate signaling kink progressing with a specific velocity defined by Eq. (3.41). We rely on the very recent biochemical experimental evidences about the roles of TTs in activities of motors and MAPs.[15,16] We presume that excitation of appropriate kinks of TTs should be the precursor for initiation of attachment of proper motor for MT acting as "cellular GPS" and guiding the motor protein along protofilament by increasing its processivity. In accordance with this fact, the proteolytic removal of TTs decreases the processivity of the molecular motor dynein and kinesin, making cellular traffic impeded or even stopped.

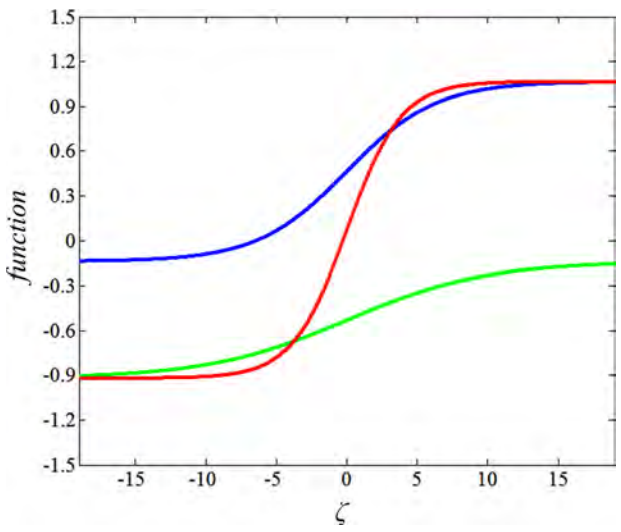

FIG. 10. Exact solutions given by Eq. (3.44) for estimated parameters $g = 0.28$ and $q = 0.14$. Green is f_{LM}, blue is f_{HM}, and red is f_{HL}.

IV. THE BIOPHYSICAL IMPLICATIONS OF THE MODEL

Using a two–dimensional cylindrical smectic liquid crystal model, we have demonstrated the plausibility of mechano–electrical kink–wave propagation mediated by TTs in the direction of MT protofilaments. We obtained a Landau–de Gennes like free energy which consists of elastic, kinetic, and polarization terms together with a ferroelectric term, showing a direct coupling between the electric field and the mechanical deformation variable. Minimizing the free energy given by Eq. (2.11) and equating to a viscous damping term Eq. (2.12) leads to the central equation, Eq. (2.14). Interestingly, this equation in the overdamped regime is very similar to the leading equation of the Fitzhugh–Nagumo[35] coupled set of equations describing the action potential in nerve axon cells. The basic idea developed in this paper has been recently outlined by us,[30] but the goal was to elaborate on the concept in detail by performing concrete estimates of the relevant parameters of the established model and pertaining analysis.

The propagation of kinks arising from our model requires a switching electric field. This field could originate from dipolar character of MTs or can be additionally supplied by the action potential sweeping along a MT within the nerve axon cell. But the propagation of these kinks is slower than the action potential and it is reasonably expected that kink's velocity is maintained by the weaker electric field intrinsically present in MTs, which are basically the mesoscopic electric dipoles.

Let us explain how these kinks could be launched. We suggest that at least two triggers can be implicated in it. First one is the chemo–mechanical event. The hydrolysis of GTP nucleotide from β–subunit brings about the conformation of pertaining tubulin dimer. Earlier, Sataric *et al.*[36] proposed how the core relay helix H7 could be the means for communication from the bottom to the top of such tubulin dimer. This relay helix may shift, tilt, or even shorten, thus making the impact onto the tilt of TTs. This fact is of crucial importance for the model developed here. Consequently, after GTP hydrolysis the whole body of tubulin dimer exibits remarkable conformation. This conformation amounts up to 13° bend at intra–dimer contact and up to 32° bend at inter–dimer contact.[37] It must cause adequate tilts of TTs of up to 45° in the extreme case. In the paper,[37] the authors state that "The stochastic events (responsible for changes in dynamical MT assembly and disassembly) may be initiated by

conformational changes that are propagated along either individual protofilament or small group of protofilaments." To our knowledge, the established model offers a unique and very plausible scenario which can explain these events. The velocity of kinks excited within the framework of this model is very reasonable (of the order of a few cm/s) and it meets the findings of the very recent experiments with regard to cellular signals.[38] The kink progresses along the protofilament which is free of the tau proteins or other MAPs. These proteins decorate parts of protofilaments and thus stabilizing MT against depolymerization, but they are also the obstacles either for kink or motor protein motion. The advancing kink along free protofilament can initiate attachment of a proper motor (kinesin or dynein) to the same MT protofilament and then may serve as a precursor for its stepping in the proper direction carrying the necessary cargo. This could be the reason why these motors always move past tau proteins without switching aside or changing the line, which is the typical case for the transport of mitochondria or chromosomes during cell division.

The second origin of kink excitation may be the local influx of ions through cellular ionic channels. It acts by pushing TTs to swing in terms of Coulomb interactions through strong local fields, like wind pushing the straws of a grass field, just to use easy to grasp analogy. Recently, the experimental essay[39] indicated that MTs exhibit the multi–level memory–switching properties. The scanning tunneling microscope imaging reveals the memory states which correspond to the tilted dipole orientations, see Fig. 4 from there. These tilts and pertaining double–well potential are totally in accordance with the conjugated conformations of TTs implicated in the kinks arisen from our model.

It is of great importance to mention that the characteristics of TTs could be changed by adding or removing some pertaining amino–acids by the action of corresponding enzymes. For example, the so–called tubulin tyrosination/detyrosination cycle has important consequences on MT functions. The product of the detyrosination of pertaining TT residue of α–tubulin is prevalent in a stable MT that displays little dynamicity having lifetime of the order of 20 h. Tyrosinated TTs are present in very dynamic MTs with lifetimes on the order of 3–5 min.[8,40] The change of this constituent amino–acid of TT changes the mechanical and polarization properties of TTs. It has implication on the parameters of our dynamical model presented here, see Eqs. (3.6) and (3.29). It is expected that tyrosinated TTs, in terms of increased length h, rotational inertia J, and dipole moment p, sustain the kink of adjusted velocity and increased amplitude suitable for recruitment of MT dynamics regulators.[15,40] The remarkable proofs of importance of TTs in regulation of motors traffic along MT offer the experimental studies where TTs are cleaved by subtilisin drug. In this case, the MTs are unable to sustain the motor traffic.[41] We firmly expect that the improved resolution of dynamical imaging can serve to detect these kinks and confirm such mechanism as one of the key signaling processes guided by MTs and being responsible for important cellular activities, such as in cell division,[42] and in cognitive and memory functions in the brain.

ACKNOWLEDGMENTS

This research was financially supported by the Provincial Secretariat of Science and Technological Development of AP Vojvodina (Project No. 114–451–2708/2016–03) and also by the Ministry of Education, Science and Technological Development of the Republic of Serbia (Projects Nos. OI171009, III43008, and III45010). The work of A. N. Bugay was supported by Russian Foundation for Basic Research (Project No. 16–02–00453a). The authors also acknowledge the support from Project within the Cooperation Agreement between the Joint Institute for Nuclear Research, Dubna, Russian Federation and Ministry of Science, Education and Technological Development of the Republic of Serbia.

APPENDIX: CYLINDRICAL SMECTIC–C LAYER APPROACH

According to the seminal approach by Carlsson *et al.*,[27] the cylindrical smectic–C liquid crystal thin layer has the density of elastic energy represented in cylindrical coordinates as follows:

$$W_{\text{lay}} = \frac{1}{2r^2}\left[A_{12}(\theta)\sin^4\varphi + A_{21}(\theta)\cos^4\varphi - 2A_{11}(\theta)\sin^2\varphi\cos^2\varphi\right], \tag{A1}$$

where r, θ, and φ are radial, polar and azimuthal degrees of freedom reflecting the symmetry of this system. Elastic coefficients $A_{ij}(\theta)$ are polynomials of even powers of the polar angle θ. In the basic paper,[27] the expansions were of quadratic order due to the relatively small changes of the angle θ. Inasmuch as the angle θ within our model can be of the order of 30°, we should safely expand the pertinent coefficients up to the fourth power of the polar angle θ as follows:

$$\begin{aligned} A_{12}(\theta) &= K_{11} + L_{12}\theta^2 + M_{12}\theta^4 \\ A_{21}(\theta) &= K_{11} + L_{21}\theta^2 + M_{21}\theta^4 \\ A_{11}(\theta) &= -K_{11} + L_{11}\theta^2 + M_{11}\theta^4. \end{aligned} \tag{A2}$$

The parameters K_{11}, L_{ij}, and M_{ij} have the dimensions of force expressed in Newtons.

Inserting the expansions given by Eq. (A2) in Eq. (A1), we get the density of the layer energy in $\left(\frac{\mathcal{J}}{\text{m}^3}\right)$ reads

$$W_{\text{lay}} = \frac{K_{11}}{2r^2} + \frac{1}{2r^2}\left[(L_{12}+L_{11})\sin^4\varphi + (L_{21}+L_{11})\cos^4\varphi - L_{11}\right]\theta^2 + \frac{1}{2r^2}\left[(M_{12}+M_{11})\sin^4\varphi + (M_{21}+M_{11})\cos^4\varphi - M_{11}\right]\theta^4. \tag{A3}$$

Looking for the stable configuration regarding the azimuthal angle φ, we should minimize the layer energy, Eq. (2.5), with respect to $\varphi\left(\frac{\partial W_{\text{lay}}}{\partial\varphi} = 0\right)$, thus obtaining

$$\sin\varphi\cos\varphi\{(L_{12}+L_{11})\sin^2\varphi - (L_{11}+L_{21})\cos^2\varphi + [(M_{11}+M_{12})\sin^2\varphi - (M_{11}+M_{21})\cos^2\varphi]\theta^2\} = 0. \tag{A4}$$

The first two solutions of the above equation are $\varphi_1 = 0$ and $\varphi_2 = \frac{\pi}{2}$. If we select $\varphi_1 = 0$ for symmetry reasons, the expression (A3) is simplified taking the form

$$W_{\text{lay}} = \frac{K_{11}}{2r^2} + \frac{1}{2r^2}\left[L_{12}\theta^2 + M_{21}\theta^4\right]. \tag{A5}$$

The solution $\varphi_2 = \frac{\pi}{2}$ has no physical meaning because it prevents any oscillation of TTs. The remaining factor of Eq. (A4) leads to the identity

$$\begin{aligned}&[(L_{12}+L_{11}) + (M_{12}+M_{11})\theta^2]\sin^2\varphi \\ &\quad = [(L_{21}+L_{11}) + (M_{21}+M_{11})\theta^2]\cos^2\varphi.\end{aligned} \tag{A6}$$

The expressions in the squared brackets must have the same sign, so it is plausible to take them as being positive

$$\begin{aligned}&(L_{12}+L_{11}) + (M_{11}+M_{12})\theta^2 > 0, \\ &(L_{21}+L_{11}) + (M_{11}+M_{21})\theta^2 > 0.\end{aligned} \tag{A7}$$

Apparently, the other stable azimuthal angle is being defined by the formula

$$\varphi_3 = arctg\left[\frac{(L_{11}+L_{21}) + (M_{11}+M_{21})\theta^2}{(L_{11}+L_{12}) + (M_{11}+M_{12})\theta^2}\right]^{\frac{1}{2}}. \tag{A8}$$

If the symmetry conditions $L_{12} = L_{21}$ and $M_{12} = M_{21}$ hold, one obtains $\varphi_3 = \frac{\pi}{4}$. Solving for $\sin^2\varphi$ and $\cos^2\varphi$ from Eq. (A6) and inserting in Eq. (A3), one obtains

$$\begin{aligned}W_{lay} = \frac{K_{11}}{2r^2} + \frac{1}{2r^2}\Bigg\{&\Bigg[(L_{11}+L_{12})\frac{(L_{11}+L_{21})^2}{(L_{12}+L_{21}+2L_{11})^2} \\ &+(L_{11}+L_{12})\frac{(M_{11}+M_{12})^2}{(M_{12}+M_{21}+2M_{11})^2} - L_{11}\Bigg]\theta^2 \\ &+\Bigg[(M_{11}+M_{12})\frac{(L_{11}+L_{12})^2}{(L_{12}+L_{21}+2L_{11})^2} \\ &+(M_{11}+M_{21})\frac{(M_{11}+M_{12})^2}{(M_{12}+M_{21}+2M_{11})^2} - M_{11}\Bigg]\theta^4\Bigg\}.\end{aligned} \tag{A9}$$

If the above symmetry conditions were fulfilled, the reduced version of Eq. (A9) now reads

$$\begin{aligned}&W_{\text{lay}} = \frac{K_{11}}{2r^2} + \frac{1}{4r^2}\left(A\theta^2 + B\theta^4\right), \quad \text{with} \\ &\quad A = L_{21}; \quad B = M_{21} \quad \text{for} \quad \varphi_0 = 0, \quad \text{and otherwise} \\ &\quad A = L_{12} - L_{11} > 0; \quad B = M_{12} - M_{11} > 0 \quad \text{for} \quad \varphi_3 = \frac{\pi}{4}.\end{aligned} \tag{A10}$$

All elastic coefficients (K_{11}, A and B) are expressed in Newtons.

[1] P. Dustin, *Microtubules* (Springer, Berlin, 1984).
[2] V. Hunyadi, D. Chretien, H. Flyvbjerg, and I. M. Janosi, Biol. Cell **99**, 117 (2007).
[3] E. Mandelkow and J. Johnson, Trends Biochem. Sci. **23**, 429 (1998).
[4] H. W. Wang and E. Nogales, Nature **435**, 911 (2005).
[5] J. A. Tuszynski, S. Hameroff, M. V. Sataric, B. Trpisova, and M. L. A. Nip, J. Theor. Biol. **174**, 371 (1995).
[6] J. A. Tuszynski, J. A. Brown, E. Crawford, E. J. Carpenter, M. L. A. Nip, J. M. Dixon, and M. V. Sataric, Math. Comput. Modell. **41**, 1055 (2005).
[7] Y. Fukuda, A. Luchniak, E. R. Murphy, and M. L. Gupta, Curr. Biol. **24**, 1826 (2014).
[8] L. Peris, M. Wagenbach, L. Lafanechère, J. Brocard, A. T. Moore, F. Kozielski, D. Job, L. Wordeman, and A. Andrieux, J. Cell Biol. **185**, 1159 (2009).
[9] L. J. Gagliardi, Phys. Rev. E **66**, 011901 (2002).
[10] E. Nogales, S. G. Wolf, and K. H. Downing, Nature **391**, 199 (1998).
[11] M. A. Jimenez, J. A. Evangelio, C. Aranda, A. Lopez–Brauet, D. Andreu, M. Rico, R. Lagos, J. M. Andreu, and O. Monasterio, Protein Sci. **8**, 788 (1999).
[12] J. E. Schoutens, J. Biol. Phys. **31**, 35 (2005).
[13] U. Z. Littauer, D. Giveon, M. Thierauf, I. Ginzburg, and H. Ponstingl, Proc. Natl. Acad. Sci. U.S.A. **83**, 7162 (1986).
[14] C. P. Garnham and A. Roll-Mecak, Cytoskeleton **69**, 442 (2012).
[15] C. Janke, J. Cell Biol. **206**, 461 (2014).
[16] M. Sirajuddin, L. M. Rice, and R. D. Vale, Nat. Cell Biol. **16**, 335 (2014).
[17] I. Yu, C. P. Garnham, and A. Roll-Mecak, J. Biol. Chem. **290**, 17163 (2015).
[18] M. V. Sataric, D. I. Ilic, N. Ralevic, and J. A. Tuszynski, Eur. Biophys. J. **38**, 637 (2009).
[19] D. L. Sekulic, B. M. Sataric, J. A. Tuszynski, and M. V. Sataric, Eur. Phys. J. E **34**, 49 (2011).
[20] A. Priel, J. A. Tuszynski, and N. J. Woolf, Eur. Biophys. J. **35**, 40 (2005).
[21] H. Freedman, V. Rezania, A. Priel, E. Carpenter, S. Y. Noskov, and J. A. Tuszynski, Phys. Rev. E **81**, 051912 (2010).
[22] J. W. Goodby, *Ferroelectric Liquid Crystals: Principles, Properties and Applications* (Gordon and Breach Science Publishers, New York, 1991).
[23] M. V. Sataric and J. A. Tuszynski, Phys. Rev. E **67**, 011901 (2003).
[24] P. Das and W. H. Schwarz, Phys. Rev. E **51**, 3588 (1995).
[25] J. A. Tuszynski, J. A. Brown, E. J. Carpenter, E. Crawford, and M. L. A. Nip, in *Proceedings of the ESA–IEJ Joint Meeting, Chicago, 2002*, p. 41.
[26] J. A. Brown, Ph.D. thesis, University of Alberta, Edmonton, 1994.
[27] T. Carlsson, I. W. Stewart, and F. M. Leslie, Liq. Cryst. **11**, 49 (1992).
[28] L. Cassimeris and C. Spittle, Int. Rev. Cytol. **210**, 163 (2001).
[29] D. Georgiev and J. F. Glazebrook, Neuroquantology **5**, 62 (2007).
[30] M. Sataric, Bull. Acad. Serbe Sci. Arts, Cl. Sci. Math. Nat. **39**, 1 (2014).
[31] F. Brochard and J. F. Lennon, J. Phys. **36**, 1035 (1975).
[32] A. Mershin, A. A. Kolomenski, H. A. Schuessler, and D. V. Nanopoulos, Biosystems **77**, 73 (2004).
[33] A.-M. Wazwaz, Appl. Math. Comput. **154**, 713 (2004).
[34] D. L. Sekulic, M. V. Sataric, M. B. Zivanov, and J. S. Bajic, Elektron. Elektrotech. **121**, 53 (2012).
[35] R. FitzHugh, Biophys. J. **1**, 445 (1961).
[36] M. V. Sataric, L. Matsson, and J. A. Tuszynski, Phys. Rev. E **74**, 051902 (2006).
[37] L. A. Amos and D. Schlieper, Adv. Protein Chem. **71**, 257 (2005).
[38] B. Fichtl, S. Shrivastava, and M. F. Schneider, Sci. Rep. **6**, 22874 (2016).
[39] S. Sahu, S. Ghosh, K. Hirata, D. Fujita, and A. Bandyopadhyay, Appl. Phys. Lett. **102**, 123701 (2013).
[40] Y. Konishi and M. Setou, Nat. Neurosci. **12**, 559 (2009).
[41] A. Roll-Mecak, Semin. Cell Dev. Biol. **37**, 11 (2015).
[42] L. Matsson, J. Phys.: Condens. Matter **21**, 502101 (2009); **26**, 155102 (2014).

BioSystems 196 (2020) 104172

Contents lists available at ScienceDirect

BioSystems

journal homepage: http://www.elsevier.com/locate/biosystems

Calcium ions tune the beats of cilia and flagella

Miljko V. Satarić [a], Tomas Nemeš [b,*], Bogdan Satarić [b], Dalibor Sekulić [b], Slobodan Zdravković [c]

[a] Serbian Academy of Science and Arts, Belgrade, Serbia
[b] Faculty of Technical Sciences, University of Novi Sad, Serbia
[c] University of Belgrade, Vinca Institute of Nuclear Sciences, Serbia

ARTICLE INFO

Keywords:
Microtubule
Axoneme
Nonlinear electric transmission line
Ionic cloud

ABSTRACT

The cytoskeleton of cilia and flagella is so called axoneme a stable cylindrical architecture of nine microtubule doublets. Axoneme performs periodic bending motion by utilizing specific dynein motor family powered by ATP hydrolysis. It is still unclear how this highly organized "ciliary beat" is being initiated and strongly coordinated by the combined action of hundreds dynein motors. Based on the experimental evidences we here elaborate a plausible scenario in which actually calcium ions play the roles of catalytic activators and coordinators of dynein attachments doing it in superposition with already known mechanical control tools of "ciliary beat". Polyelectrolyte properties of microtubules incorporated in axoneme doublets enable the formation and propagation of soliton-like "ionic clouds" of Ca^{2+} ions along these "coaxial nanocables". The sliding speed of such Ca^{2+} "clouds" along microtubule doublets is comparable with the speed of propagation of "ciliary beat" itself. We elaborated the interplay between influx of Ca^{2+} ions in ciliary based body and the sliding of microtubule triplets therein. In second segment we considered how the dynein motors activated by Ca^{2+} ions contained within solitonic "ionic clouds" in competition with axoneme curvature regulate ciliary and flagellar beating.

1. Introduction

Cilia and flagella are long, thin appendages of some living cells, whose oscillatory bending waves enable cells to be propelled through viscous fluid or to drive fluid flows across the surface of cells. Motile cilia and flagella are capable of complex subtly coordinated movements and can play versatile roles in fertilization and embryonic development (Satir and Christiansen (2007)).

Cilia are especially important for their windshield wiper-like action. It is seen in the trachea where they perform the clearing mucus out of lungs. On the outer hand a flagellum forms the "tail" on sperm cell that propels it in order to swim. The hallmark structure of cilia and flagella is the axoneme. It consists of a cylindrical arrangement of nine doublets of parallel microtubules and a pair of microtubules in the cylinder's center called the central apparatus, see Fig. 1.

Microtubules are long hollow cylinders mostly containing 13 parallel protofilaments of $\alpha - \beta$ tubulin heterodimers. There exist the nanopores in microtubule wall between neighboring tubulins connecting microtubule lumen with external part of microtubule. These nanopores are important for axoneme signaling by Ca^{2+} ions.

In axoneme is a significant number of associated proteins, such as nexin and radially distributed links named radial spokes (Nicastro et al. (2006)), responsible for axoneme integrity and stability, see Fig. 1.a. Each microtubule doublet is connected to its nearest-neighbors by crosslinkers called nexin. They provide mechanical resistance to the relative sliding of doublets and prevent the change in spacing between them. The doublets are parallel to each other with inter spacing of about 30 nm which is comparable with diameter of microtubule (25 nm).

Every doublet is composed of one A-microtubule and one B-microtubule. The A-microtubule has standard 13 protofilaments while B-microtubule has only 10 protofilaments, and is merged with A-microtubule, Fig. 1.b. Radial spokes have the role to keep the diameter of the axoneme of approximately 200 nm thus maintaining cross-section to be constant.

The axoneme is inherently active. A remarkable number of dynein molecular motors are distributed in rows between neighboring microtubule doublets, and they produce active forces in terms of chemical energy provided by ATP hydrolysis. Dynein is a gigantic motor protein family with approximately $4.5{\cdot}10^3$ amino acids. Dyneins are rigidly attached to the A-microtubule and their stalks are briefly in contact with the adjacent B-microtubule during the active power strokes processes. For example, *Chlamydomonas* axoneme contains 14 different types of

* Corresponding author.
E-mail address: nemes.tomas@uns.ac.rs (T. Nemeš).

https://doi.org/10.1016/j.biosystems.2020.104172
Received 4 April 2020; Received in revised form 13 May 2020; Accepted 13 May 2020
Available online 10 June 2020

dyneins and has a total of 10^4 of these motors over its whole length of about $10\mu m$, (Witman (2009)).

All these constituent elements (nexin links, radial spokes and dynein motors) have periodically distributed locations along the axis of axoneme cylinder with a period of about 96 nm. There is also some asymmetry in dynein distribution (Edwards et al. (2018)).

Dynein motors generate forces and torques that slide and bend pertaining microtubule doublets. The variability of sliding velocity is the basis of bend formation. Most notably the different dynein types undergo microtubule translocation at different speeds.

Outer arms dyneins consist of a single type species. But different inner-arm dyneins have significantly diverse intrinsic sliding velocities.

It appears that axoneme is equipped with two qualitatively different, largely independent system for active bending, pertaining to specific cilia and flagella.

First one consists of outer-arm dyneins and the other one includes inner-arm dyneins cooperating with radial spokes and the central-pair of microtubules.

Bending of the axoneme originates from the imbalance of dynein motor forces on the opposite sides of the bending plane.

During their power stroke dyneins produce force that tends to slide the attached axonemal microtubule doublets with respect to each other, thus regulating the beat pattern of the axonemal microtubule doublets. Accordingly, the ciliary and flagellar beat is enabled by alternating episodes of activation of opposing sets of dynein. It is believed that these beats are self-organized processes in such a way that dyneins regulate the beat, and conversely, the beat tunes the dyneins. When activated dyneins on one side of axoneme win the tug-of-war, this leads to relative motion between the microtubule doublets. Passive nexin linkers constrain sliding and convert it into bending (Li et al. (2009); Mukhopadhyay and Dey (2016); Satir and Christiansen (2007); King and Sale (2018); King (2018)).

So far the following four mechanisms of dynein regulation within an axoneme have been elucidated (Sartori et al. (2016)):

a) Sliding control, which produces a load force that triggers dynein detachment. This mechanism has shown the good fit to experimental data for beating of the bull sperm (Riedel-Kruse et al. (2007), Fig. 2. a.
b) Normal force regulation, or geometric clutch control, where the increase in the distance between doublets creates a normal force that tends to detach dynein from B-microtubules (Lindemann (2007)), see Fig. 2.b.
c) Third mechanism is controlled by the curvature of the axoneme (Brokaw (2002)), see Fig. 2.c. We will combine this mechanism in competition with dynein activation by the "ionic cloud" of Ca^{2+} ions.
d) The flagellar beat patterns seem to be partially determined by an interplay of the basal properties of the axoneme and the mechanical feed back of dynein motors (Vernon and Woolley (2004), Riedel-Kruse (2007)). We will pay attention on this aspect of control.

It was stressed (Brokaw (2009)) that major questions about cilia and flagella, beating initiation events still remain unsolved; First is what determines when, where and how a dynein sliding initiations appear? Second dilemma is what mechanism allows sliding to be initiated synchronously over an extended region?

The four concepts dealing with above-mentioned mechanisms of dynein regulation do not consider the doubtless importance of calcium signaling. On the outer hand, there are the abundant experimental evidences indicating how important and even essential roles the Ca^{2+} ions play in the beating dynamics of axoneme (Smith (2002), skato and King (2003), Sakato et al. (2007), DeCaen et al. (2013), Bannai et al. (2000), Doerner et al. (2015)).

Calcium ions impact nearly every aspect of cellular life. During neurons firing, the concentration of Ca^{2+} ions was reported to increase significantly around the microtubules (Clapham (2007)).

Theoretically just qualitative significance of Ca^{2+} ions in increasing of attachment probability of dyneins in axoneme is underlined in (Bayly and Wilson (2014)).

1. In this article we explain how this issue could be addressed quantitatively based on the fast soliton-like signals of Ca^{2+} ions launched through ciliary ionic channels and then being propagated along microtubule doublets within the axoneme, or triplets in basal body.
2. In addition we consider the sliding of microtubule triplets in ciliary basal body as being initiated by sliding controlled influx of Ca^{2+} ions therein.

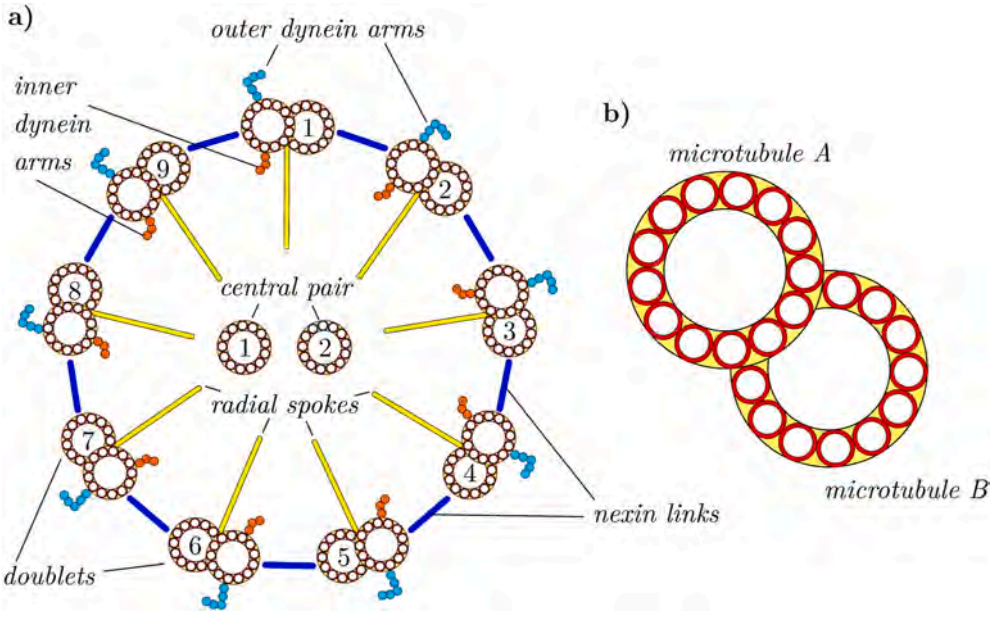

Fig. 1. a) Schematic of an axonemal cross section of radius d_0. The nine doublets are numbered. Nexin links radial spokes, central pair, outer and inner dyneins are indicated. b) Complete A microtubule has 13 protofilaments and B is incomplete with 10 protofilaments. Outer dynein arms are rigidly attached to A-microtubule and are ready to greep B-microtubule of neighboring microtubule pair.

3. Then we elaborate the concept in which dynein attachment within axoneme doublets is initiated by catalytic action of Ca^{2+} ions while the detachment rate during the "ciliary beat" is governed by curvature control mechanism. We obtained numerically exact spatial temporal pattern of bending curvature of axoneme.
4. Finally we present the discussion and conclusion.

2. Cellular microtubules as real polyelectrolytes and the consequences for Ca^{2+} signaling in cilia and flagella

Hundreds of cellular proteins have been adopted to bind Ca^{2+} over a million-fold range of affinities (nM to mM, Burgoyne (2007)).

The abilities of Ca^{2+} and negative phosphate ions to alter local electrostatic fields and protein conformations are the two universal tools of cellular signal transduction.

Cells spend a lot of their energy to effect changes in Ca^{2+} concentration maintaining the difference between their intracellular ($0.1\mu M$ free) and extracellular (mM) concentration. In contrast, the ion concentration of calcium's cousin Mg^{2+} barely differs across plasma membrane.

We earlier established the polyelectrolyte approach aimed to explain how Ca^{2+} ions albeit present in very low concentrations in cytosol, use microtubules and actin filaments to concentrate around and propagate along these filaments faster than it could be achieved by ordinary three-dimensional diffusion (Satarić et al. (2009, 2010; 2019); Sekulić et al. (2011, 2016); Tuszynski et al. (2018); Hunley et al. (2018)). Additionally a series of experimental assays (Minoura and Muto (2006); Priel et al. (2006, 2008); Cantero et al. (2016, 2019)) indicated that microtubule present in cytosolic solution increased its ionic conduction remarkably.

Microtubules are mostly negatively charged on their outer surface since there are numerous amino acids forming tubulin protein with negatively charged residues under physiological conditions.

Each tubulin monomer of the microtubule lattice has a C-terminal helix H12 followed by a highly acidic amino acid sequence protruding out of the microtubule surface called C-terminal tail (TT), with a length when completely outstretched, $\ell_{TT} = 4.5nm$ and with radius of $\mathscr{R}_{TT} = 0.5nm$, Fig. 3a,b.

These TTs are very important for the interactions of microtubules with motor proteins and other associated proteins (MAPs).

We argue that TTs could help the actions of dynein motors in "ciliary beat" by increasing the tubulin capacitance in collecting Ca^{2+} ions.

The α_{TT} is 19 amino acid long and has 10 negatively charged residues in the absence of post-translational modifications, primarily polyglutamylation.

It was revealed (Ikegami et al. (2010)) that for beating asymmetry which is fundamental for airway ciliary action the tubulin polyglutamylation modification is concentrated on TTs and is highly abundant in cilia and flagella, see Fig. 3.c.

This additionally increases the net negative charges of respective TTs elevating the total electrical capacitance of tubulin dimers within microtubule doublets in axoneme.

The fact that microtubules together with their TTs are dominantly negatively charged with high enough charge density brings about that they can be safely referred as typical polyelectrolyte polymers in the context of Manning's concept (Manning (2008, 2011)). As example for a TT without post-translational glutamynation the average linear spacing of elementary charges is on the order of

$$\delta = \frac{4.5nm}{10} = 0.45nm \tag{1}$$

For glutamynated TT this parameter should have smaller value due to greater number of negative charges. The fundamental parameter for electrolytes is the Bjerrum length ℓ_B, expressing the competition of Coulomb interaction between ions and the energy of their thermal agitation:

$$\frac{Ze^2}{4\pi\varepsilon_0\varepsilon_r\ell_B} = k_BT \tag{2}$$

Taking $Z = 2$ for Ca^{2+}, $e = 1.6\cdot10^{-19}C$, $\varepsilon_0 = 8.85\cdot10^{-12}F/m$, $\varepsilon_r = 80$, $k_B = 1.38\cdot10^{-23}J/K$, and at physiological temperature $T = 310K$, one obtains

$$\ell_B = 1.4nm \tag{3}$$

The necessary condition for a polymer to be polyelectroyite is that inequality $\frac{\ell_B}{\delta} > 1$ holds. In actual case we have

$$\frac{\ell_B}{\delta} \approx 3 > 1 \tag{4}$$

and the above condition is safely met.

Negatively charged surface of a microtubule and the associated TTs attracts positively charged counter-ions from cytosol acting as charge-storage devices.

Very recently was elaborated (Shen and Guo (2018)) how these cations are arranged around microtubules in neurons. It was inferred that these microtubules can generate instant response to a Ca^{2+} pulse because of specific permeability for cations due to four types of nanopores in the microtubule wall, see Fig. 4.b.

The cations are absorbed to the surface of microtubule wall with affinity highly dominated by Ca^{2+} ions. As a result when the concentration of Ca^{2+} increases outside of the microtubule during neuronal excitations K^+ and Na^+ ions will be pushed into microtubule lumen through pertaining nanopores, triggering subsequent axial ion redistribution along the microtubule, Fig. 4.a. We think that similar scenario safely holds for microtubule doublets within the axoneme and for microtubule triplets in ciliary basal body. The point is that attracted Ca^{2+} ions are not bound but allowed to slide along microtubules following local electric field and the concentration gradient. This is similar concept as in the case of propagation of action potential in nerve axons (Poznanski et al. (2017)). Polyelectrolyte properties of microtubules per se are not enough to drive Ca^{2+} signal into transmission. We here stress that described pushing of Na^+ and K^+ ions inside microtubule lumen creates local gradient of potential which drives Ca^{2+} "ionic cloud" to progress along pertaining doublet. We also clarify that "ionic clouds" are supposed to be initiated along the doublets of active side of axoneme. They are additionally supported by the ionic channels juxtaposed along ciliary membrane, (for example, Cat-sper, Sun et al. (2017)). Inasmuch microtubule doublets are adorned with radial spokes and nexin linkers, which are a kind of periodic cascade, it should have some impact on the

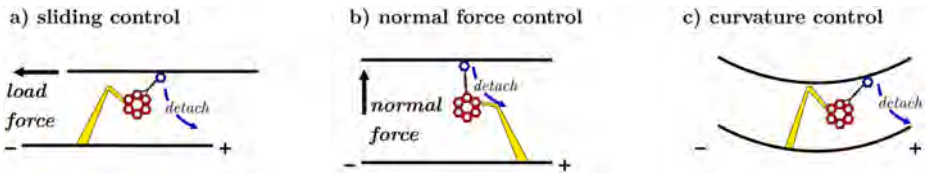

Fig. 2. Schematic of dynein regulation mechanism. a) In sliding control detachment is caused by a tangential loading force. b) In normal force control the normal force tends to separate the filaments enhancing dynein attachment. c) In curvature control the dynein detaches from B-microtubule due to an increase in axoneme curvature.

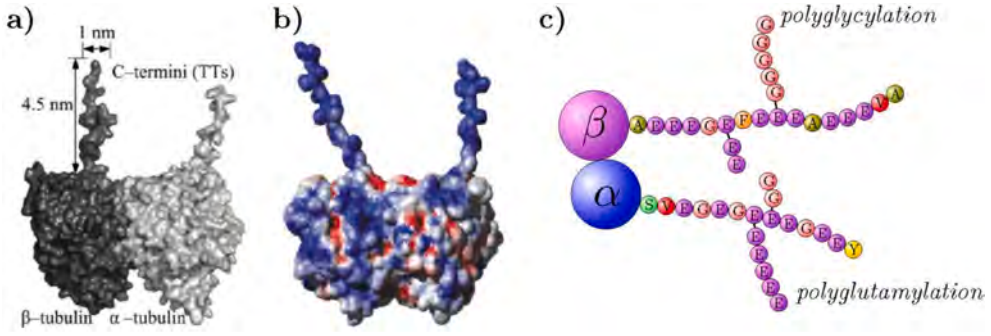

Fig. 3. a) The magnified topology of a tubulin heterodimer with tubulin tails whose dimensions are: the maximum length of 4.5 nm and the diameter of 1 nm. b) Charge distribution on the surface of a tubulin heterodimer. Blue and red denote the negative and positive charges, respectively. c) Polyglutamylation and polyglycylation post-translational modifications of TTs. (For interpretation of the references to colour in this figure legend, the reader is referred to the Web version of this article.)

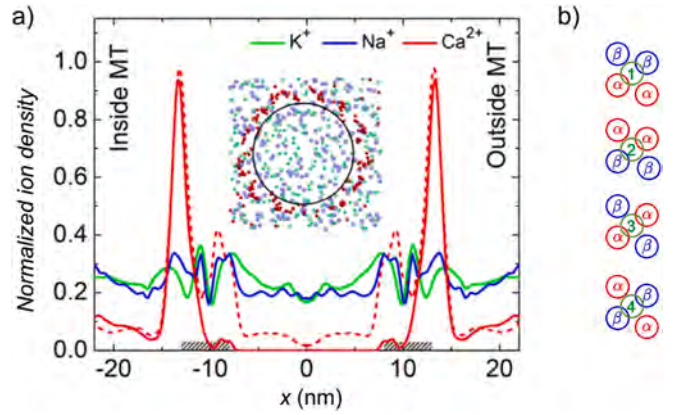

Fig. 4. a) Normalized ion density of K^+, Na^+, and Ca^{2+} ions along the radical orientation of the microtubule. Inset shows equilibrated distribution of K^+ (green), Na^+ (blue), and Ca^{2+} (red) ions. The radius of the black circle is 10 nm. The dashed line is the distribution of Ca^{2+} ions in a system with Ca^{2+} ions initially added inside and outside the microtubule. b) There are four types of nanopores of the α and β tubulins. Used by permission of Shen and Guo (2018). (For interpretation of the references to colour in this figure legend, the reader is referred to the Web version of this article.)

propagation of "ionic clouds". It may influence their speed and the run length, in analogy with myelinated segments in nerve axons, which impact the propagation of action potential.

From our model, the central pair microtubules are not candidates for described Ca^{2+} signaling scenario. They could be the pathways for kinesin motors recruited in transport of some specified proteins involved in ciliary development. We should emphasize that radial spokes play the role of mechanical constrains as being embedded in axoneme architecture and their role in Ca^{2+} signaling in ciliary beat is not clear.

Intra-cilium lumen and extra-axonemal compartment are more important for some other signaling pathways responsible for developmental roles in primary cilia (Bisgrove and Yost (2006)).

The details of establishing the nonlinear transmission line model of microtubule aimed to explain the concept of propagation of soliton-like bell shaped "ionic clouds" of Ca^{2+} ions are freshly elaborated in (Satarić et al. (2019)). We have just remind that a microtubule can be viewed as a lumped serie of elementary rings (ER), possessing nonlinear capacity $C_n(v_n, t)$ of tubulin dimers along with TTs, as well as nonlinear admittance $G_n(v_n, t)$ which arises from negative incremental resistance of nanopores (Siwy et al. (2006)). Our earlier estimations for elementary ring parameters gave the right orders of magnitude for resistance (order of $G\Omega$) and capacitance (order of fF).

This is the rough estimation in comparison with the recent exact results by (Kalra et al. (2019)) revealing for a microtubule $2\mu m$ long the cumulative amounts for resistivity and capacity as follows (the case without post-translational modifications):

$$R_{MT} = 1.07{\cdot}10^{12}\Omega \; C_{MT} = 1.86{\cdot}10^{-12}F \tag{5}$$

Dividing these values with pertaining $2.5{\cdot}10^3$ dimer (ER) rings one gets proper estimations as follows

$$R_{ER} = 4.28 \cdot 10^{9}\Omega \;\; C_{ER}(pg) = 9.3{\cdot}10^{-15}F \tag{6}$$

But if we consider heavily polyglutamylated TTs of cilia and flagella we can assume that the capacitance of such ER is at least doubled and we will have

$$C_{ER} = 15{\cdot}10^{-15}F \tag{7}$$

Let us analyze the significance of cylindrical geometry of cilia and flagella on Ca^{2+} influx through pertaining ionic channels in cell membrane. These play the very important role in regulation of Ca^{2+} levels around microtubule doublets in axoneme.

Now we consider a $10\mu m$ long cylindrical geometry with a diameter of $0.4\mu m$ yielding a $9.56\mu m^2$ surface area and $0.7\mu m^3 = 0.7f\ell$ volume. This is two orders of magnitude smaller volume than that of typical globular cell of radius of $5\mu m$. In comparison with such a cell itself the above cilium has approximately 20-fold larger surface-area-to-volume ratio.

It implies that the same surface density of ion channels should change the Ca^{2+} concentration within such small cilium volume notably faster than that it occurs in the volume of globular cell.

Consequently in primary cilium the resting concentration of Ca^{2+} ions is seven fold ($0.7\mu M$) greater than in cellular cytoplasm ($0.1\mu M$), per liter (Delling et al. (2013)).

In order to estimate the local concentration of Ca^{2+} ions accumulated within an "ionic cloud" we consider a single TT with radius $\mathscr{R}_{TT} = 0.5nm$ and length $\mathscr{L}_{TT} = 4.5nm$. Taking that the thickness of "ionic cloud" is of the order of Bjerrum length, $\ell_B = 1.44nm$ and with only four Ca^{2+} ions occupying the space of pertaining cylindrical shell with respective volume:

$$\Delta V = \pi\left[(\mathscr{R}_{TT} + \ell_B)^2 - \mathscr{R}_{TT}^2\right]\mathscr{L}_{TT} \tag{8}$$

we get

$$n_{Ca^{2+}} = \frac{\Delta n}{\Delta V} = \frac{4}{\pi\left(2^2 - 0.5^2\right)\cdot 4.5{\cdot}10^{-27}m^3} = 125\frac{mM}{\ell} \tag{9}$$

This is the same order of magnitude as the total ion concentration in the intercellular fluid and is about 10^2-fold greater than global Ca concentration in cytosol. Inside the cell usual ratio of total atomic calcium [Ca] to free calcium ions [Ca^{2+}] generally differs by about three to four orders of magnitude (Berridge et al. (2003)).

The presence of fixed and mobile buffers and extruding pumps in cilia additionally diminish the number of bulky diffusing Ca^{2+} ions thus lowering their affordability for control of action of dyneins in axoneme.

Why presented estimations are so important? Because all these arguments clarify the significance of the polyelectrolyte concept of microtubules and the role of "ionic cloud" which enables an efficient

mechanism for fast enough elevation of attachment rate of dyneins associated with microtubules of axoneme.

It is well known that lipid bi-layers increase the speed of interaction of pertaining proteins reducing their diffusion from three dimensions to two (Clapham (2007)).

Analogously, Ca^{2+} ions accumulated around microtubules in axoneme are confined to one dimension thus further increasing the speed of diffusion (Shen and Guo (2018)).

Let us remind to the solution of transmission line equation which describes the bell-shaped "ionic-cloud" of Ca^{2+} ions around microtubule (Satarić et al. (2019), Eq. (22) therein).

We express the concentration of Ca^{2+} ions $C(\xi)$ within "ionic cloud" in traveling wave form with maximal concentration C_0 which depends on the intensity of Ca^{2+} influx through pertaining channels

$$C(\xi)=\frac{C_0}{(\cosh\xi)^2};\ \xi=\frac{s}{\ell}-\frac{v}{v_0}\frac{t}{T_d}=\frac{s}{\ell}-\frac{t}{\tau_d};\ \tau_d=\frac{v_0}{v}T_d \tag{10}$$

Here s is the coordinate along axoneme axis, ℓ is the length of a tubulin dimer (elementary ring-ER), v is the speed of sliding of "ionic cloud" along microtubule, v_0 is cut off velocity. The characteristic time τ_d is related with discharging time T_d of a single ER capacitor.

The speed of "ionic cloud" depends on the characteristic discharge time of elementary ring as nanocapacitor and nanoresistor, Eqs. (6) and (7). We have estimated the speed of discharging of ERs to be the ratio of the elementary ring length $\ell = 8nm$ and above discharge time, Eqs. (6) and (7)

$$v_0=\frac{\ell}{T_d}=\frac{\ell}{R_{ER}C_{ER}(pg)}=200\frac{\mu m}{s} \tag{11}$$

In the case of *Chlamydomonas* cilia with the length $L = 12\mu m$ its axoneme can be traversed by such "ionic cloud" for the time interval of

$$\Delta t=\frac{\ell}{v_0}=0.06s \tag{12}$$

Therefore the time interval in Eq. (12) indicates that a single Ca^{2+} "ionic cloud" can span along an entire microtubule doublet length within the axoneme during three *Chlamydomonas* beating period $T_b \approx 0.02s$ (Sartori (2015)).

The mechanical relaxation time of a *Chlamydomonas* axoneme seen as a slender beam fixed at one end, with the length $L = 12\mu m$, including bending stiffness $\kappa = 6{\cdot}10^{-22}Nm^2$ and drag coefficient $\beta = 0.003\frac{Ns}{m^2}$ is given by

$$\tau_{rel}=(0.8)^4\beta\frac{L^4}{\kappa}=0.04s \tag{13}$$

This shows that an "ionic cloud", Eq. (8) with estimated speed has enough time to activate pertaining dyneins prior to the "ciliary beat" is being relaxed.

Later we will use the assumption that the active motor force during "ciliary beat" will have the same space-time function as the Ca^{2+} concentration within "ionic cloud", Eq. (8).

$$f(s,t)=\frac{f_0}{\left(\cosh\left(\frac{s}{L}-\frac{t}{\tau_d}\right)\right)^2} \tag{14}$$

f_0 is the maximal motor force linear density (N/m). It is additionally important to pay attention on the issue of propagation of Ca^{2+} signals along cilia of Paramecium where was found out that the time for achieving maximal concentration of Ca^{2+} ions after induced ionic spill-over, is of the order of 0.008s, (Husser et al. (2004); Plattner and Hentschel (2006)). Having in mind that the length of these cilia is of the order of $20\mu m$ it implies that the expected speed of "ionic cloud" in this case has the same order of magnitude as arises from Eq. (11).

The circumstance that Ca^{2+} "ionic clouds" have speeds of the order as the beating waves in cilia and flagella is of basic importance. It provides fast initiation of enough number of dyneins, making the imbalance in dynein forces from the opposite sides in proximal part of axoneme. When dyneins on active side of axoneme win the tag-of-war, this leads to sliding of neighboring doublets. Basal body, nexin linkers and radial spokes convert sliding into bending. The Ca^{2+} ions from "ionic cloud" are partly chelated by Calmodulin, but this initial bending enables pertaining cat-sper channels to open. Thus a new Ca^{2+}ions leak into axoneme and replace missing ones allowing "ionic cloud" to resume progression along beating wave.

From the biological point of view, it should be emphasized that the chemical properties of Ca^{2+} had uniquely permitted the lowering of its concentration in flagella to levels that would avoid the precipitation of phosphate salt. This is crucial because the phosphates was to be used as the fundamental cellular energetic currency (ATP, GTP). That is the strong reason why the confinement and drift of Ca^{2+} ions along microtubule doublets in axoneme is favorable in two respects: It has a greater speed of drift than 3D diffusion of ions and it protects ubiquitous ATP molecules (needed for dynein energy supply) against precipitation.

It was strongly stressed by Gatenby and Frieden (2017) that Ca^{2+} ions, and cations in general, form the cellular information circuits that detect, process and respond environmental signals imparted to living cells. It appears that the signal transmission through trans-membrane ion flow (Ca^{2+} and others) form an optimal Shanon information channel that minimizes loss of information and maximizes transmission speed. This is in very accord with our concept.

The extremely important experimental evidences, regarding intrinsic electrical properties of microtubules, were revealed by Cantero et al. (2016, 2018). The emphasize is on the role of microtubule wall and nanopores therein in eliciting the self-sustained electrical oscillations. Very interestingly, the fundamental frequency of these oscillations is 29Hz, for two-dimensional microtubule sheets. In the case of bundles of brain microtubules the self-sustained electrical oscillations have the fundamental frequency of 39Hz. As the argument for central roles of nanopores in maintaining of these oscillations was the impact of adding taxol drag which interacts with nanopores thus changing their ionic propulsion. The result is gradual decrease in amplitude of oscillations and eventually their stops at critical taxol concentration. Both of above frequencies are of the order of magnitude of inverse time for propagation of "ionic clouds", Eq. (12). This order is also close to the beating frequency of different cilia (30–50)Hz. It suggests that two mechanisms could have something in common.

So, it would be interesting to examine how taxol influences the ciliary microtubules during drag treatment. The possible scenario would be that the reduction of nanopore size impairs the distribution of cations in a way that Na^+ and K^+ dominate Ca^{2+} concentration around microtubule decreasing its presence in the "ionic cloud", which would result in less efficient control of dynein sliding. It may have harmful effects for cilia in lungs and in renal complex.

3. Model which combines Ca^{2+} initiation with basal sliding

The part inside the cell that anchors cilia or flagella is called basal body. Basal body and cilia are joined by a transition zone. These three regions are connected continuously with microtubule cytoskeleton; normally as triplet microtubules in the basal body and doublets in axoneme as well as in transition zone.

It has been shown (Vernon and Wooley (2004)) by light microscope that in flagella of the spermatozoa from the Chinchila the sliding within cell basal body doubtlessly occurs. This fact brought about an idea that the beat frequency is controlled by some property of basal flagellar region and this region could be considered as a pacemaker for beating patterns.

The experiment by Iwadate (2003) has shown that iontophoretic application of Ca^{2+} to the ciliary base of a permeabilized P. caudatum cell induces ciliary reversal beat, though the application to the ciliary tip does not!

We here suggest that the influx of Ca^{2+} ions in basal body through ion channels (Cat-Sper) and from internal Ca^{2+} stores (mitochondria) tune basal sliding and vice versa, the sliding regulates the probability of channels opening in a feedback manner.

The corresponding mechanical equation governing the interplay of sliding displacement δ in flagellar basal body and the action of dynein motors along axoneme has the form

$$\gamma_b \frac{d\delta}{dt} = -k_b\delta + \int_0^L f(s,t)dx \tag{15}$$

Here γ_b is the basal friction coefficient and k_b is a basal stiffness; $f(s,t)$ is the linear density $\left(\frac{N}{m}\right)$ of net force along axoneme length L with axial coordinate s as follows

$$f(s,t) = f_m - K\Delta - \gamma\frac{\partial\Delta}{\partial t} \tag{16}$$

f_m is the density of active dynein motor-force, Δ is the sliding displacement of microtubule doublets within the axoneme; K is the axoneme sliding stiffness and γ is corresponding friction coefficient.

$\frac{\partial\Delta}{\partial t}$ is the outer dynein arms sliding velocity which is load dependent.

The inertial term $m_b\frac{d^2\delta}{dt^2}$ in Eq. (15) is safely ignored due to the very small Reynolds number for basal body.

We first assume that the total active force along axoneme is constant in time during the flagellar beat:

$$\int_0^L f(s,t)ds = F_0 \tag{17}$$

Thus we can solve Eq. (15) turning it in dimensionless form by defining non-dimensional variables and model parameters as follows

$$x = \frac{\delta}{\delta_0};\ \tau = \frac{t}{\tau_b};\ \tau_b = \frac{\gamma_b}{k_b};\ \delta_0 = 50nm \tag{18}$$

where δ_0 is the amplitude and τ_b is the mechanical relaxation time of basal sliding of microtubule triplets. It gives the equation:

$$\frac{dx}{d\tau} + x = \sigma_1;\ \sigma_1 = \frac{\tau_b F_0}{\delta_0\gamma_b} = \frac{F_0}{\delta_0 k_b} \tag{19}$$

with solution for initial condition $x = 0;\ \tau = 0$,

$$x = \sigma_1(1 - e^{-\tau}) \tag{20}$$

or explicitly

$$\delta(t) = \frac{\tau_b F_0}{\gamma_b}\left(1 - e^{-\frac{t}{\tau_b}}\right) = \delta_0\sigma_1\left(1 - e^{-\frac{t}{\tau_b}}\right) \tag{21}$$

This is the point where we should include the control role of Ca^{2+} ions in initiating and sustaining of such basal sliding in flagellary beating scenario.

We introduce similar concept as was previously used for kinocilia in auditory cells (Camalet et al. (2000)). Namely it could be feasible that Ca^{2+} influx and sliding displacements catalyze each other through a feedback mechanisms (Husser et al. (2004); Plattner and Hentschel (2006)).

If the concentration of Ca^{2+} ions in basal body is $C(t)$, the rate of its change is described by the equation in which basal body sliding influences the probability of opening of pertaining ionic channels as follows:

$$\frac{dC}{dt} = -\frac{C}{\tau_c} + \frac{C_0}{\tau_c}\left[\frac{1}{1 + Ae^{-\frac{\delta}{\delta_0}}}\right] \tag{22}$$

First term on the right hand side reflects the decay of Ca^{2+} influx due to buffers and extruding pumps. The second one includes the impact of sliding $\delta(t)$ on the opening probability of ionic channels. C_0 is the maximal concentration of Ca^{2+} ions brought about by influx through pertaining channels in basal body and τ_c is the relaxation time for equilibration. A is the dimensionless constant.

By doing the usual non-dimensionality steps

$$\Theta = \frac{C}{C_0};\ \tau = \frac{t}{\tau_c} \tag{23}$$

and replacing $\delta(t)$ from Eq. (21) into Eq. (22), we get

$$\frac{d\Theta}{d\tau} + \Theta = \frac{1}{1 + Ae^{-\sigma_1(1-e^{-\tau})}} \tag{24}$$

It is important to estimate the parameters involved in this concept. We here relay on the assay by (Riedel-Kruse et al. (2007)) where the shape of bull sperm flagella beat is treated experimentally and fitted theoretically. For the case of these flagella planar swimming the values of basal parameters are

$$\gamma_b = 2{\cdot}10^{-4}\frac{Ns}{m};\ k_b = 9.62{\cdot}10^{-2}\frac{N}{m} \tag{25}$$

The amplitude of basal sliding is estimated therein to be $\delta_0 = 0.05\mu m$.

The total active force F_0, Eq. (17), can be found from relation

$$F_0 = \frac{\kappa\Omega_{av}}{d_0} \tag{26}$$

where the flexural rigidity κ, the average curvature Ω_{av} and the radius of flagella d_0 have the following values

$$\kappa = 1.73{\cdot}10^{-21}Nm^2\ \ \Omega_{av} = 10^5 m^{-1}\ \ d_0 = 1.85{\cdot}10^{-7}m \tag{27}$$

It gives

$$F_0 = 9.35{\cdot}10^{-10}N \tag{28}$$

so that Eq. (19) yields

$$\sigma_1 = \frac{9.35{\cdot}10^{-10}}{5{\cdot}10^{-8}{\cdot}9.62{\cdot}10^{-2}} = 0.194 \approx 0.2 \tag{29}$$

The basal mechanical relaxation time, from Eq. (18) reads

$$\tau_b = \frac{\gamma_b}{k_b} \approx 2.1ms \tag{30}$$

If the dimension of basal body is of the order of $0.05\mu m$ and the speed of "ionic cloud" along microtubule triplets is $v = 250\frac{\mu m}{s}$, Eqs. (11) and (12) it appears that τ_c is of the same order as τ_b in Eq. (30)

$$\tau_c \approx 2ms \tag{31}$$

Calcium signals in deed sweep into the basis of cilia very rapidly. Voltage gated Ca^{2+} selective channels are the fastest Ca^{2+} signaling proteins. Each channel conducts roughly 10^6 Ca^{2+} ions per second (Qi et al. (2007)). A few thousand channels can affect 10 fold changes in intracellular Ca^{2+} levels within milliseconds. This is in agreement with our estimation, Eq. (31).

Eventually Eq. (24) for $A = 1$ has the explicit form

$$\frac{d\Theta}{d\tau} + \Theta = \frac{1}{1 + e^{-0.2(1-e^{-\tau})}} \tag{32}$$

while the numerical solution for initial condition $\Theta = 0$ is presented in Fig. 5.

The second option is if we take that the total active force along axoneme during "ciliary beats" is the time dependent.

In the context of our polyelectrolyte model of microtubules, Eq. (10), where the "ionic cloud" in bell shaped form is being responsible for dynein activation we will use Eqs. 14 and 17 to obtain the time dependent version of the total force

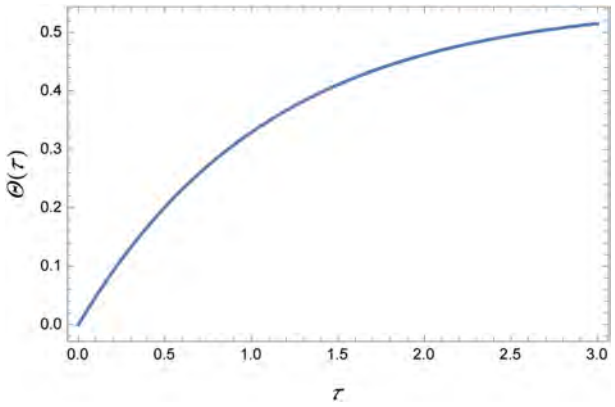

Fig. 5. This figure shows the evolution of Ca^{2+} concentration in basal body which is responsible for basal body sliding and initiating the axoneme bending.

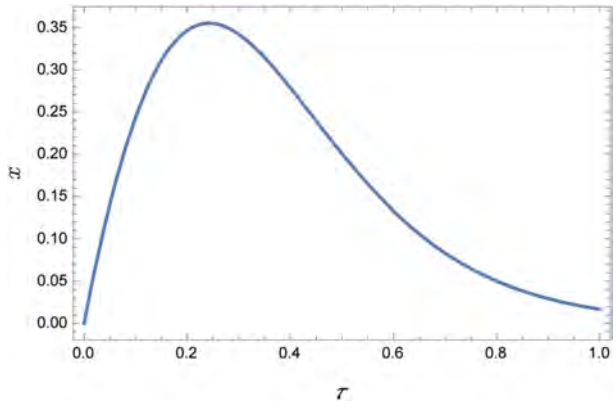

Fig. 6. This figure shows the time evolution of "recoil-like" basal body sliding as a result of sliding of microtubule doublets in axoneme caused by progressing bell shaped Ca^{2+} "ionic cloud". Corresponding maximal basal sliding appears at the time $\frac{1}{4}\tau_b = 0.5ms$ and it amounts approximately.$17nm$

$$F_0 = \int_0^L \frac{f_0 ds}{\left(\cosh\left(\frac{s}{L} - \frac{t}{\tau_d}\right)\right)^2} \tag{33}$$

Going over to non-dimensional length variable $z = s/\ L$ in above integration, and returning back to Eq. (15) we have

$$\gamma_b \frac{d\delta}{dt} + k_b\delta = f_0 L\left[\tanh\left(1 - \frac{t}{\tau_d}\right) + \tanh\left(\frac{t}{\tau_d}\right)\right] \tag{34}$$

$$\frac{dx}{d\tau} + x = \sigma_2[\tanh(1-\alpha t) + \tanh(\alpha\tau)] \tag{35}$$

where the abbreviations include:

$$x = \frac{\delta}{\delta_0};\ \tau = \frac{t}{\tau_b};\ \sigma_2 = \frac{f_0 L\tau_b}{\gamma_b\delta_0};\ \alpha = \frac{\tau_b}{\tau_d} \tag{36}$$

The dimensionless version of Eq. (34) reads

The solution of Eq. (35) with the initial condition $\tau = 0; x = 0$ has the form

$$x(\tau) = \sigma_2 e^{-\alpha\tau}\left\{\ln 2 - e\,\ln(e+1) + \ln\left[\frac{(e+e^{\alpha\tau})^e}{1+e^{\alpha\tau}}\right]\right\} \tag{37}$$

We use the capacitance of polyglutamylated microtubule Eq. (6), and estimate the relaxation time of "ionic cloud" discharge as follows:

$$\tau_d = \frac{v_0}{v}T_d = \frac{v_0}{v}R_{ER}C_{ER}(pg) = \frac{v_0}{v}30\cdot 10^{-6}s \tag{38}$$

for $\frac{v}{v_0} = 10$ one obtains

$$\tau_d = 0.3ms \tag{39}$$

Replacing the numerical values from Eqs. 30 and 38 into the last non-dimensional term in Eq. (36), we get

$$\alpha = \frac{2.1}{0.3} = 7 \tag{40}$$

Taking the density of amplitude force f_0 to be of the order of $f_0 = 2\cdot 10^{-4}N/m$, Eq. (36) gives $\sigma_2 \approx 2$ and Eq. (37) finally reads

$$x = 2e^{-7\tau}\left\{\ln 2 - e\cdot\ln(e+1) + \ln\left[\frac{(e+e^{7\tau})^e}{1+e^{7\tau}}\right]\right\} \tag{41}$$

The shape of this function Eq. (41) is presented in Fig. 6.

4. How the interplay between dynein activation by Ca^{2+} ions and axoneme curvature regulate flagellar beating

Let us first shortly elaborate the biochemical experimental evidences regarding the importance of Ca^{2+} signaling in regulation of dynamics of cilia and flagella paying attention on the roles of ionic channels in such scenario.

It is well-known that cilia in the node drive left-right asymmetry in vertebrate embryo. It was revealed by (Babu and Roy (2013)) that Ca^{2+} signaling in the node is very dynamic in those occasions. Takao et al. (2013) realized that protein PKD2 which is 6-pass trans-membrane protein of 968 amino acids regulates the influx of Ca^{2+} ions into cilia axonemes. It appears that PKD2 controls the dynamics of Ca^{2+} signals so that the frequency and not just the spatial distribution of Ca^{2+} ions is critical for initiating and maintaining left-right asymmetry in an embryo. It refers to the frequency of successive "puffs" of Ca^{2+} ions caused by channel openings. Alternatively Wood et al. (2005) concluded that the flagellum may be very sensitive to the rate of change of Ca^{2+} concentration increasing its beating asymmetry in response to the rapid elevation in Ca^{2+} concentration performed by activation of nimodipine sensitive pathway.

Importantly in mammalian sperm cells Ca^{2+} currents were ubiquitously detected in the Cat-Sper channels.

Cat-Sper is in the plasma membrane on the flagellar principal part (Sun et al. (2017)). Besides the presence of the other ionic channels only the Cat-Sper directly modulate the physiological processes of sperm hyper-activation, sperm capacitation, chemotaxis toward the egg and acrosome reaction.

A few more details about how Ca^{2+} ion indirectly modulates the activity of axonemal dyneins. It is known that Ca^{2+} activates ATP-sensitive microtubule binding by a *Chlamydomonas* outer arm dynein comprising the α, β and γ heavy chains (HC). The γ–HC associated LC4 (light chain 4) is a member of Calmodulin family with the molar mass of 18 kDa. Calmodulin LC4 binds 1–2 Ca^{2+} ions with binding affinity $K_{Ca^{2+}} = 30\mu M$ in vitro. This binding changes the Calmodulin conformation in order to catalyze the dynein arm attachment to B microtubule of neighboring doublet.

It indicates that Calmodulin LC4 acts as Ca^{2+} sensor and catalyzer for outer arm dyneins sliding. This Calmodulin can bind Ca^{2+} within milliseconds as being tightly associated with flagellary membrane and to axoneme itself (Sakato and King (2003); Sakato et al. (2007)). All above suggest that dynein with an associated LC4 Calmodulin play a pivotal role in Ca^{2+} regulation of flagellar motility.

It is important to note that the nexin link, the central pair-radial spoke and inner arm dyneins all contain proteins that bind Ca^{2+}. It means that Ca^{2+} may indirectly regulate dynein activation by binding to multiple-bridging axonemal structures and thus modulating inter doublet spacing (Kamiya and Yagi (2014)). Let us now make the quantitative analysis of implications of Ca^{2+} signaling on axonemal beating dynamics. In Mukundan et al. (2014) it was elaborated how dynamic axoneme curvature regulation has a basic role in tuning ondulatory

beats of *Chlamydomonas* flegella. The flagellar beat is provided by dynein motors powered by ATP hydrolysis thus generating the sliding forces between adjacent microtubule doublets. In this case of partially disintegrated *Chlamydomonas* axoneme the authors have shown that the curvature control mechanism can explain the circular bent form of pertaining pair of microtubule doublets.

But their conclusion was that this bend arises as the consequence of the fact that only dynein motors at short distal end of axoneme are active releasing forces of the order of 5–10 pN per motor. This is obviously highly exaggerated value.

We here follow general mechanical approach (Sartori (2015)) in which planar beat of a flagella can be modeled considering an axoneme as a pair of opposing inextensible filaments A and B, see Fig. 8.

These filaments are separated by a spacing $d(s)$ which can depend on the arc length s. The relative sliding of these filaments $\Delta(s)$ is superimposed with basal sliding δ_0, Eq. (18). Opposing motors in filaments A/B (denoted) by triangles) produce forces $F_{A,B}$ and reactions-$F_{A,B}$. Sliding compression and normally oriented compression are limited by nexin links and radial spokes and corresponding stiffnesses are denoted by springs K (green) and K_n (blue) while a basal body spring k_b Eq. (16) is red. The pertaining tangent angle $\psi(s)$ is the bending measure. Total mechanical energy of the axoneme-motors system is presented by the following integral along the filament length L:

$$U = \int_0^L \left\{ \frac{\kappa}{2}[\Omega(s)]^2 + \frac{K}{2}[\Delta(s)]^2 + \frac{K_n}{2}[d(s) - d_0]^2 - f_m \Delta(s) \right\} ds \tag{42}$$

The sliding stiffness K and the active motor force per unit length f_m (Eq. (16)), as well as the flexural rigidity κ (Eq. (27)), are already introduced.

First three terms in Eq. (42) stand for binding, sliding and geometric clutch effect and the last one represents the active dynein motor forces.

The curvature of filaments $\Omega(s)$ is defined through the tangent angle $\psi(s)$, Fig. 7, with its first derivative

$$\Omega(s) = \frac{\partial \psi}{\partial s} \tag{43}$$

$d(s)$ is generally variable of inter filament spacing.

The straightforward variation of total energy U, Eq. (42), with respect to the ψ was given in Mukundan et al. (2014).

Under stationary condition $\frac{\delta U}{\delta \psi} = 0$ along with the inter-filament spacing being fixed ($d(s) = d_0$), Eq. (42) yields the basic equation which serves us to establish the interplay between Ca^{2+} "ionic cloud" along the axoneme and pertaining curvature in process of ciliary (flagellary) bends.

$$\kappa \frac{d\Omega}{ds} = -d_0 \mathscr{F}(s) \tag{44}$$

We are now in the position to make the quantitative assessment of the influence of Ca^{2+} "ionic-cloud", Eq. (10), in control of axoneme curvature.

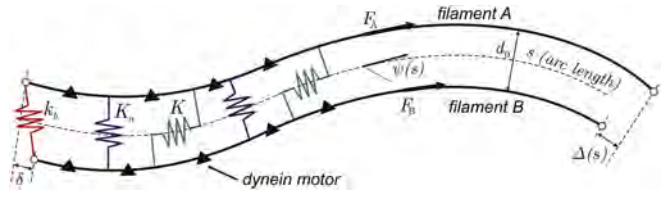

Fig. 7. The scheme of axoneme represented with two filaments A/B. The dynein motors are black triangles. The sliding K and normal stiffness K_n are springs (green and blue) and basal body k_b is red. The sliding displacement are δ and $\Delta(s)$. Tangent angle is $\psi(s)$ and tangent forces F_A and F_B. d_0 is the equilibrium spacing, (diameter) of axoneme. (For interpretation of the references to colour in this figure legend, the reader is referred to the Web version of this article.)

Dynein motors attach to a neighboring doublet due to the activation initiated by Ca^{2+} ions contained within "ionic cloud" and mediated by LC4 Calmodulin molecules. Oppositely they detach from B microtubules of adjacent doublet due to pertaining curvature of axoneme.

A single attached motor exerts the positive force $f > 0$. The probability that a motor at position s is being attached is $p(s)$. The net linear density of motor forces may be written as follows:

$$\mathscr{F}(s) = \rho f p(s) \tag{45}$$

We assume that the linear density ρ of the same dynein isoforms is uniform along microtubule doublets, which is not always the case.

For stationary configuration the motor attachment probability, according to \cite{bell}, expressed through attachment and detachment rates, can be written as

$$p(s) = \left[1 + \frac{K_{off}}{K_{on}}\right]^{-1} \tag{46}$$

Smith (2002) performed seminal assays which revealed that dynein attachments increase in a linear response to the elevation of Ca^{2+} concentration.

We now assume that the attachment rate $K_{on}(s)$ is enabled by Calmodulin LC4 activated by Ca^{2+} ions which are carried and distributed, along microtubule doublets within bell-shaped "ionic-clouds" described by the function following from Eq. (10):

$$\left.\begin{aligned} K_{on}(s,t,t_d) &= K_{10}\{\mathrm{sech}[\alpha(s,t,t_d)]\}^2 \\ \alpha(s,t,t_d) &= \left(\frac{s}{L} - v\frac{t-t_d}{L}\right) \end{aligned}\right\} \tag{47}$$

Here K_{10} means the maximum of attachment rate which depends on ATP concentration, while t_d stands for the time delay caused by chemical inertia of this process (Li et al. (2009)). Namely it is the delay between the chelating attachment of Ca^{2+} ions to Calmodulin LC4 causing its conformation which activates the targeted γ-heavy chain of pertaining dynein motor. The maximum of the attachment rate is on the order of a characteristic ATP cycling rate

$$K_{10} = 10^3 s^{-1} \tag{48}$$

The detachment rate of motors does comply to the curvature control scenario in accordance with the fact that it follows the Bell's low, (Bell (1978)):

$$K_{off} = K_{20} e^{\Omega/\Omega_C} \tag{49}$$

where Ω_C represents the characteristic curvature which indicates the onset of motor detachment. We can use Eq. (44) combining it with Eqs. (45)–(47), (49) to obtain the implicit nonlinear differential equation for curvature $\Omega(s,t)$

$$\kappa \frac{\partial \Omega}{\partial s} = \frac{-d_0 \rho f}{\left\{1 + \frac{K_{20}}{K_{10}}[e^{\Omega/\Omega_C}](\cosh[\alpha(s,t,t_d])^2\right\}} \tag{50}$$

Again we are going over to dimensionless version using appropriate abbreviations

$$x = \frac{s}{L};\ y = \frac{\Omega}{\Omega_C};\ \tau = v_0 \frac{t - t_d}{L};\ \lambda = \frac{d_0 \rho f L}{\kappa \Omega_C} \tag{51}$$

which yields

$$\frac{\partial y}{\partial x} = -\lambda \left\{1 + \frac{K_{20}}{K_{10}} e^y [\cosh(x - \tau)]^2\right\}^{-1} \tag{52}$$

If we use the set of parameters estimated for the bull-sperm flagella (Riedel-Kruse et al. (2007))

$$\left.\begin{array}{ll} d_0 = 1.85{\cdot}10^{-7}m & \rho = 2{\cdot}10^{8}m^{-1} \\ L = 5.8{\cdot}10^{-5}m & \kappa = 1.73{\cdot}10^{-21}Nm^{2} \\ f = 10^{-12}N & \Omega_C = 10^{5}m^{-1} \end{array}\right\} \quad (53)$$

from Eq. (51) we readily get

$$\lambda_{bs} = 10.7 \quad (54)$$

The numerical graphical solution of Eq. (52) is presented in Fig. 8 and it shows the space-time evolution of bending curvature of bull-sperm axoneme in the context of our model. It exhibits how the beat initiated by "ionic cloud" relaxes during characteristic time $\tau = 1$.

Fig. 8.a. is with balanced rates ($K_{20} = K_{10}$). In Fig. 8.b is shown the option ($K_{20}/K_{10} = 0.5$) which concerns the case where the "ionic cloud" is with amplitude K_{10} arising when high Ca^{2+} influx and maximal ATP concentration are present. It brings about the greatest curvature with the greatest time derivatives of curvature. Oppositely in Fig. 8.c the smaller K_{10} with the same K_{20} causes a band pattern with smaller curvature.

It is also interesting to see the solution of Eq. (52) in the case of *Chlamydomonas* flagella. Accordingly we adopted the pertaining parameters $L = 12\mu m$, $\kappa = 0.6{\cdot}10^{-21}Nm^{2}$, $\Omega_C = 0.25{\cdot}10^{6}m^{-1}$, retaining the parameters d_0, ρ, f the same as in Eq. (53). It yields:

$$\lambda_{Ch} = 6.2 \quad (55)$$

Corresponding spatio-temporal evolutions are presented in Fig. 9 (a, b, c).

The propagation of Ca^{2+} "ionic clouds" with estimated speeds is bringing about the activation of dyneins which is followed by axoneme curvature. It is well in accord with the concept of dynamic curvature control (Sartori et al. (2016)), where it appears that the motor force depends only on the time derivative of the curvature.

Let us now consider qualitatively the feasible roles of post-translational polyglutamylation of microtubule TTs within axoneme in here elaborated control scenario. It was proven (Redeker (2010)) that polyglutamylation critically affects the function of inner arm dyneins. In cilia more than 10 glutamates per single TT are common reaching up to 28 residues.

In one aspect the microtubule doublets with highly acidic (negatively charged) polyglutamylated side chains elicit stronger attractive long-range electrostatic interaction between positive segments of dynein and negative TTs raising the level of precision to one otherwise noisy dynein sliding process (Li et al. (2016)). Second aspect is that more negatively charged TTs attract more Ca^{2+} ions thus increasing capacitance of ER (elementary ring of transmission line, Eqs. (6) and (7)) adequately controlling the speed of "ionic cloud", Eq. (11).

Also these Ca^{2+} ions posed along the TTs extensions are more accessible by LC4 Calmodulin molecules which need Ca^{2+} ions to enhance the motor activity underlying the bending curvature of axoneme.

5. Discussion

Let us recall that concentrations of Ca^{2+} ions in cells, including cilia and flagella is of the order of nano-mol (nM). Cellular bioenergetics is prevailingly based on phosphate salts (mostly ATP and GTP). This phosphate based energetics would be impossible in the mM Ca^{2+} concentration within bulk cytosol because calcium phosphate salts, unlike those of magnesium have poor solubility.

Deviations from Ca^{2+} resting nM concentration in the cytosol do actually occur in response to physiological demands but they should appear in a spatially and thermally strongly controlled manner. In that context the central point of this article is our original approach explaining how Ca^{2+} ions injected by appropriate ionic channels are being spatially and temporally located around microtubule doublets and how they initiate and control the beating dynamics of cilia and flagella. These Ca^{2+} ions in association with LC4 Calmodulin enzyme tune the activities of dynein motors in the axoneme.

The essential importance for this concept has the polyelectrolyte character of microtubules within the axoneme which exhibits the properties of nonlinear electric transmission lines. It enables positive ions, mostly Ca^{2+} (Shen and Guo (2018)) to form the localized movable bell shaped "ionic clouds" around microtubules (Eqs. 10 and 13). The speed and stability of these "ionic clouds" provides a much more precise and efficient way for Ca^{2+} distribution compared with three-dimensional diffusion itself. At the same time such confined distribution of Ca^{2+} ions yields avoiding the precipitation of ATP molecules.

Earlier Riedel-Kruse et al. (2007) stressed that "The activity of the motors along the axoneme could be regulated directly via a spatio-temporal traveling wave in the form of biochemical or electrical signal". Similar mechanisms for localized ionic currents were utilized by Poznanski et al. (2017) as well as by Hunley et al. (2018), for action filaments.

We were firstly elaborated the process of sliding within the basal body of axoneme associated with Ca^{2+} influx thus initiating the ciliary (flagellary) beats. The main results is Eq. (41) which express the time evolution of basal sliding which is experimentally evidenced to play a significant role in the initiation of reversal bends in ciliary dynamics (Vernon and Woolley (2004)), Fig. 6.

Second important contribution here is the scenario in which bell-shaped Ca^{2+} "ionic clouds" activate dyneins indirectly through the engagement of LC4 Calmodulin molecules. According to Bell's law (Bell (1978)) we obtained the significant nonlinear equation, Eq. (52) which express the axoneme relative curvature $y = \Omega/\Omega_C$ as a function of axial position x and time τ. The numerical solutions of this equation are shown graphically in Figs. 8 and 9. We could compare it with the results of Mukundan et al. (2014), which concern the dynamics of disintegrated axoneme exhibiting the constant curvature of a pair of microtubule doublets except at very distal end where the dyneins are only attached by exerting unreasonably strong forces.

Our results, Figs. 8 and 9, show the gradual change of axoneme

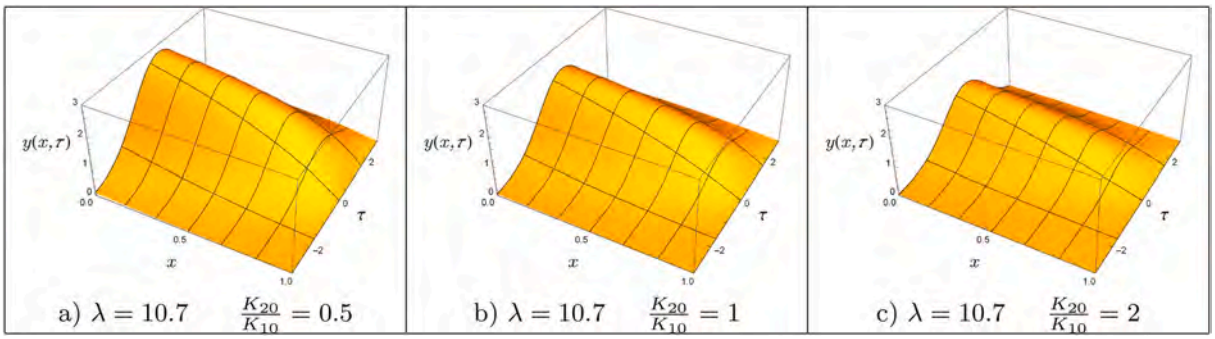

Fig. 8. The numerical graphical solution of Eq. (52) for boundary condition $y(1,\tau) = 0$, obtained and plotted with Mathematica (*Wolfram Research*) software.

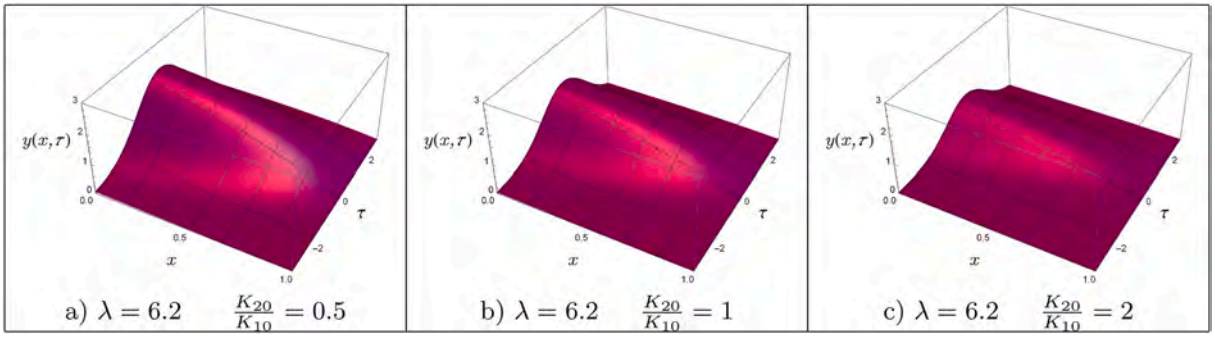

Fig. 9. The numerical graphical solution of Eq. (52) for boundary condition $y(1,\tau) = 0$, obtained and plotted with Mathematica (*Wolfram Research*) software.

curvature which for both bull-sperm and *Chlamydomonas* sublinearly decreasing from proximal to distal end of axoneme, indicating that active motors are distributed in progressing bell-shaped form caused by "ionic clouds".

Experimental assay by Smith (2002) has shown that dynein activities in axoneme increased in a linear manner with an increasing Ca^{2+} concentration. But further increasing Ca^{2+} concentration causes somewhat abruptly a switch from an asymmetric to a symmetric beat wave form.

According to our concept, at lower Ca^{2+} influx, involving smaller and slower "ionic clouds", the binding of Ca^{2+} to LC4, than LC4 to β/γ dynein heavy chains causes increasing activities of these dynein arms enhancing pertaining bend. An additional increase of Ca^{2+} concentration (in terms of bigger and faster "ionic clouds") brings about a partial neutralization of negatively charged polyglutamylated TT chains. It causes the weakening of motor-B microtubule interaction within an incoming bell-shaped Ca^{2+} "ionic cloud".

In literature was criticized the curvature control mechanism with regard to the controversy that negligible small tubulin strains are associated with the observed amount of axoneme curvatures (Mukundan et al. (2014)). But the time derivative of curvature which follows the dynamics of fastly progressing Ca^{2+} "ionic clouds" can be more appropriate answer for this controversy. We also guess that instead of tubulin bodies the pertaining glutamynated, flexible TTs can sense axoneme curvature more effectively (Sekulić et al. (2016)).

In conclusion, we should stress the fact that this article represents remarkably upgraded version compared with Satarić et al. (2019). First aspect in that respect is our original approach in considering the role of Ca^{2+} ions in tuning the sliding of microtubule triplets in basal body of cilia. This has strong experimental support in Vernon and Wooley (2004), and our concept uniquely explains the temporal evolution of this segment of ciliary dynamics. Secondly, the scenario in which Ca^{2+} "ionic clouds" are being initiators and coordinators of ciliary beat is now applied for curvature control of complete native flagella of *Chlamydomonas* and Bull sperm. The former option concerns the beat of demembranated and partially disintegrated axoneme to just two doublets of *Chlamydomonas*, viewed in the context of experiment by Mukundan et al. (2014). At last, but not the least, in this version the expanded spatio-temporal pattern of beating curvature is solved exactly numerically without approximation applied in the former case.

Declaration of competing interest

The authors declare that they have no known competing financial interests or personal relationships that could have appeared to influence the work reported in this paper.

Acknowledgements

This research was financially supported by the Provincial Secretariat for Higher Education and Scientific Research of AP Vojvodina (Project No. 1144512708/201603), also by the Ministry of Education, Science and Technological Development of the Republic of Serbia (Project No. OI171009, III43008, and III45010) and by project of Serbian Academy of Sciences and Arts.

References

Babu, D.E., Roy, S.K., 2013. Left-right asymmetry: cilia stir up new surprises in the node. Open Biol. 3 (130052).
Bannai, H., Yoshimura, M., Takahashi, K., Shingyoji, C., 2000. Calcium regulation of microtubule sliding in reactivated sea urchin sperm flagella. J. Cell Sci. 113, 831–839.
Bayly, P.V., Wilson, K.S., 2014. Equations of interdoublet separation during flagella motion reveal mechanisms of wave propagation and instability. Biophys. J. 107, 1756–1772.
Bell, G.I., 1978. Models for the specific adhesion of cells to cells. Science 200, 618–627.
Berridge, M.J., Bootman, M.D., Roderick, H.L., 2003. Calcium signalling: dynamics, homeostasis and remodelling. Nat. Rev. Mol. Cell Biol. 4, 517–529.
Bisgrove, B., Yost, H., 2006. The roles of cilia in developmental disorders and disease. Development 133, 4131–4143.
Brokaw, C.J., 2002. Computer simulations of flagellar movement viii: coordination of dynein by local curvature control can generate helical bending waves. Cell Motil Cytoskeleton 53, 103–124.
Brokaw, C.J., 2009. Thinking about flagellar oscillations. Cell Motil Cytoskeleton 66, 425–436.
Burgoyne, R.D., 2007. Neuronal calcium sensor proteins: generating diversity in neuronal Ca^{2+} signalling. Nat. Rev. Neurosci. 8, 182–193.
Camalet, S., Duke, T., Jülicher, F., Prost, J., 2000. Auditory sensitivity provided by self-tuned critical oscillations of hair cells. Proc. Natl. Acad. Sci. Unit. States Am. 97, 3183–3188.
Cantero, M.D.R., Perez, P.L., Scarinci, N., Cantiello, H.F., 2019. Two-dimensional brain microtubule structures behave as memristive devices. Sci. Rep. 9, 12398.
Cantero, M.D.R., Perez, P.L., Smoler, M., Villa Etchegoyen, C., Cantiello, H.F., 2016. Electrical oscillations in two-dimensional microtubular structures. Sci. Rep. 6, 27143.
Cantero, M.D.R., Villa Etchegoyen, C., Perez, P.L., Scarinci, N., Cantiello, H.F., 2018. Bundles of brain microtubules generate electrical oscillations. Sci. Rep. 8, 11899.
Clapham, D.E., 2007. Calcium signaling. Cell 131, 1047–1058.
DeCaen, P.G., Delling, M., Vien, T.N., Clapham, D.E., 2013. Direct recording and molecular identification of the calcium channel of primary cilia. Nature 504, 315–318.
Delling, M., DeCaen, P.G., Doerner, J.F., Febvay, S., Clapham, D.E., 2013. Primary cilia are specialized calcium signalling organelles. Nature 504, 311–314.
Doerner, J.F., Delling, M., Clapham, D.E., 2015. Ion channels and calcium signaling in motile cilia. eLife 4, e11066.
Edwards, B.F.L., Wheeler, R.J., Barker, A.R., Moreira-Leite, F.F., Gull, K., Sunter, J.D., 2018. Direction of flagellum beat propagation is controlled by proximal/distal outer dynein arm asymmetry. Proc. Natl. Acad. Sci. Unit. States Am. 31, E7341–E7350.
Gatenby, R.A., Frieden, B.R., 2017. Cellular information dynamics through transmembrane flow of ions. Sci. Rep. 7, 15075.
Hunley, C., Uribe, D., Marucho, M., 2018. A multi-scale approach to describe electrical impulses propagating along actin filaments in both intracellular and in vitro conditions. RSC Adv. 8, 12017–12028.
Husser, M.R., Blanchard, M.P., Hentschel, J., Klauke, N., Plattner, H., 2004. One-way calcium spill-over during signal transduction in paramecium cells: from the cell cortex into cilia, but not in the reverse direction. Cell Calcium 36, 349–358.
Ikegami, K., Sato, S., Nakamura, K., Ostrowski, L.E., Setou, M., 2010. Tubulin polyglutamylation is essential for airway ciliary function through the regulation of beating asymmetry. Proc. Natl. Acad. Sci. Unit. States Am. 107, 10490–10495.
Iwadate, Y., 2003. Photolysis of caged calcium in cilia induces ciliary reversal in paramecium caudatum. J. Exp. Biol. 206, 1163–1170.
Kalra, A., Patel, S., Bhuiyan, A., Preto, J., Scheuer, K., Mohammed, U., Lewis, J., Rezania, V., Shankar, K., Tuszynski, J.A., 2019. On the Capacitive Properties of Individual Microtubules and Their Meshworks. arXiv, 1905.02865.
Kamiya, R., Yagi, T., 2014. Functional diversity of axonemal dyneins as assessed by in vitro and in vivo motility assays of chlamydomonas mutants. Zool. Sci. 31, 633–644.

King, S., 2018. Turning dyneins off bends cilia. Cytoskeleton 75, 372–381.
King, S., Sale, W., 2018. Fifty years of microtubule sliding in cilia. Mol. Biol. Cell 29, 698–701.
Li, L., Alper, J., Alexov, E., 2009. Mechanical signaling in networks of motor and cytoskeleton proteins. Annu. Rev. Biophys. 38, 217–234.
Li, L., Alper, J., Alexov, E., 2016. Cytoplasmic dynein binding, run length, and velocity are guided by long-range electrostatic interactions. Sci. Rep. 6, 31523.
Lindemann, C., 2007. The geometric clutch as a working hypothesis for future research on cilia and flagella. Ann. N. Y. Acad. Sci. 1101, 477–493.
Manning, G.S., 2008. Approximate solutions to some problems in polyelectrolyte theory involving nonuniform charge distributions. Macromolecules 41, 6217–6227.
Manning, G.S., 2011. A counterion condensation theory for the relaxation, rise and frequency dependence of the parallel polarization of rodlike polyelectrolytes. Eur. Phys. J. E 34, 1–7.
Minoura, J., Muto, E., 2006. Dielectric measurement of individual microtubules using the electroorientation method. Biophys. J. 90, 3739–3748.
Mukhopadhyay, A., Dey, C., 2016. Reactivation of flagellar motility in demembranated leishmania reveals role of camp in flagellar wave reversal to ciliary waveform. Sci. Rep. 6, 37308.
Mukundan, V., Sartori, P., Geyer, V.F., Jülicher, F., Howard, J., 2014. Motor regulation results in distal forces that bend partially disintegrated *Chlamydomonas* axonemes into circular arcs. Biophys. J. 106, 2434–2442.
Nicastro, D., Schwartz, C., Pierson, J., Gaudette, R., Porter, M.E., McIntosh, J.R., 2006. The molecular architecture of axonemes revealed by cryoelectron tomography. Science 313, 944–948.
Plattner, H., Hentschel, J., 2006. Sub-second cellular dynamics: time-resolved electron microscopy and functional correlation. Int. Rev. Cytol. 255, 133–176.
Poznanski, R.R., Cacha, L.A., Al-Wesabi, Y.M.S., Ali, J., Bahadoran, M., Yupapin, P.P., Yunus, J., 2017. Erratum: solitonic conduction of electrotonic signals in neuronal branchlets with polarized microstructure. Sci. Rep. 7, 10675.
Priel, A., Ramos, A.J., Tuszynski, J.A., Cantiello, H.F., 2006. A biopolymer transistor: electrical amplification by microtubules. Biophys. J. 90, 4639–4643.
Priel, A., Ramos, A.J., Tuszynski, J.A., Cantiello, H.F., 2008. Effect of calcium on electrical energy transfer by microtubules. J. Biol. Phys. 34, 475–485.
Qi, H., Moran, M.M., Navarro, B., Chong, J.A., Krapivinsky, G., Krapivinsky, L., Kirichok, Y., Ramsey, I.S., Quill, T.A., Clapham, D.E., 2007. All four cat-sper ion channel proteins are required for male fertility and sperm cell hyperactivated motility. Proc. Natl. Acad. Sci. Unit. States Am. 104, 1219–1223.
Redeker, V., 2010. Mass spectrometry analysis of c-terminal posttranslational modifications of tubulins. Methods Cell Biol. 95, 77–103.
Riedel-Kruse, I.H., Hilfinger, A., Howard, J., Jülicher, F., 2007. How molecular motors shape the flagellar beat. HFSP J. 1, 192–208.
Sakato, M., King, S.M., 2003. Calcium regulates atp-sensitive microtubule binding by chlamydomonas outer arm dynein. JBC 278, 43571–43579.
Sakato, M., Sakakibara, H., King, S.M., 2007. Chlamydomonas outer arm dynein alters conformation in response to Ca^{2+}. Mol. Biol. Cell 18, 3620–3634.
Sartori, P., 2015. Effect of Curvature and Normal Forces on Motor Regulation of Cilia. PhD Thesis. Technische Universität Dresden, Germany.
Sartori, P., Geyer, V., Scholich, A., Jülicher, F., Howard, J., 2016. Dynamic curvature regulation accounts for the symmetric and asymmetric beats of chlamydomonas agella. eLife 5, e13258.
Satarić, M.V., Ilić, D.I., Ralević, N., Tuszynski, J.A., 2009. A nonlinear model of ionic wave propagation along microtubules. Eur. Biophys. J. 38, 637–647.
Satarić, M.V., Nemeš, T., Sekulić, D., Tuszynski, J.A., 2019. How signals of calcium ions initiate the beats of cilia and flagella. Biosystems 182, 42–51.
Satarić, M.V., Sekulić, D., Živanov, M., 2010. Solitonic ionic currents along microtubules. J. Comput. Theor. Nanosci. 7, 1–10.
Satir, P., Christiansen, S.T., 2007. Overview of structure and function of mammalian cilia. Annu. Rev. Physiol. 69, 377–400.
Sekulić, D.L., Satarić, B.M., Tuszynski, J.A., Satarić, M.V., 2011. Nonlinear ionic pulses along microtubules. Eur. Phys. J. E 34, 45–49.
Sekulić, D.L., Satarić, B.M., Zdravković, S., Bugay, A.N., Satarić, M.V., 2016. Nonlinear dynamics of c-terminal tails in cellular microtubules. Chaos 26, 073119.
Shen, C., Guo, W., 2018. Ion permeability of a microtubule in neuron environment. J. Phys. Chem. Lett. 9, 2009–2014.
Siwy, Z.S., Powell, M.R., Petrov, A., Kalman, E., Trautman, C., Eisenberg, R.S., 2006. Calcium induced voltage gating in single conical nanopores. Nano Lett. 8, 1729–1734.
Smith, E.F., 2002. Regulation of flagellar dynein by calcium and a role of an axonemal calmodulin dependent kinase. Mol. Biol. Cell 13, 3303–3313.
Sun, X.H., Zhu, Y.Y., Wang, L., Liu, H.L., Ling, Y., Li, Z.L., Sun, L.B., 2017. The catsper channel and its roles in male fertility: a systematic review. Reprod. Biol. Endocrinol. 15, 65.
Takao, D., Nemoto, T., Abe, T., Kiyonari, H., Kajiura-Kobayashi, H., Shiratori, H., Nonaka, S., 2013. Asymmetric distribution of dynamic calcium signals in the node of mouse embryo during left-right axis formation. Dev. Biol. 376, 23–30.
Tuszynski, J.A., Satarić, M.V., Sekulić, D.L., Satarić, B.M., Zdravković, S., 2018. Nonlinear calciumion waves along actin filaments control active hair-bundle motility. Biosystems 173, 181–190.
Vernon, G., Woolley, D.M., 2004. Basal sliding and the mechanics of oscillation in a mammalian sperm flagellum. Biophys. J. 87, 3934–3944.
Witman, G.B., 2009. The Chlamydomonas Sourcebook; Cell Motility and Behaviour, second ed., vol. 3. Academic Press.
Wood, C.D., Nishigaki, T., Furuta, T., Baba, S.A., Darszon, A., 2005. Real-time analysis of the role of Ca^{2+} in flagellar movement and motility in single sea urchin sperm. J. Cell Biol. 169, 725–731.

BioSystems 173 (2018) 181–190

Contents lists available at ScienceDirect

BioSystems

journal homepage: www.elsevier.com/locate/biosystems

Nonlinear calcium ion waves along actin filaments control active hair–bundle motility

Jack A. Tuszynski[a,b,c], Miljko V. Sataric[d], Dalibor L. Sekulic[d,*], Bogdan M. Sataric[d], Slobodan Zdravkovic[e]

[a] Department of Physics, University of Alberta, Edmonton, Alberta, Canada
[b] Department of Experimental Oncology, Cross Cancer Institute, Edmonton, Alberta, Canada
[c] Department of Mechanical and Aerospace Engineering, Politecnico di Torino, Torino, Italy
[d] University of Novi Sad, Faculty of Technical Sciences, Novi Sad, Serbia
[e] University of Belgrade, Institute of Nuclear Sciences Vinca, Belgrade, Serbia

ARTICLE INFO

Keywords:
Actin filament
Calcium ion dynamics
Myosin motor
Hair cells
Nonlinear model

ABSTRACT

Calcium ions (Ca^{2+}) tune and control numerous diverse aspects of cochlear and vestibular physiological processes. This paper is focused on the Ca^{2+} control of mechanotransduction in sensory hair cells in the context of polyelectrolyte properties of actin filaments within the hair–bundles of inner ear. These actin filaments appear to serve as efficient pathways for the flow of Ca^{2+} ions inside stereocilia. We showed how this can be utilized for tuning of force–generating myosin motors. In an established model, we unified the Ca^{2+} nonlinear dynamics involved in the control of myosin adaptation motors with mechanical displacements of hair–bundles. The model shows that the characteristic time scales fit reasonably well with the available experimental data for spontaneous oscillations in the inner ear. This scenario promises to fill a gap in our understanding of the role of Ca^{2+} ions in the regulation of processes in the auditory cells of the inner ear.

1. Introduction

Actin filaments are highly dynamic and negatively charged polymers, which are the most abundant proteins in living cells, especially the inner ear apparatus and in neural cells. In this paper we present a new concept based on the polyelectrolyte properties of actin filaments within the stereocilia of inner ear. These cytoskeletal filaments serve as guides or pathways for directed flows of Ca^{2+} ions implicated in the adaptation of biomolecular unconventional motors, such as myosin Ic, myosin IIIa and myosin VIIa. These motors interact in a Ca^{2+} dependent manner with actin filaments at the core of stereocilia. This is a faster and more efficient mechanism for controlling the movement of Ca^{2+} ions when compared with simple diffusion process. Following the introduction of the biophysical model, we apply it to a quantitative analysis of slow motor adaptation and to establish a relationship between Ca^{2+} tuned myosin activities and spontaneous oscillations of hair–bundles.

Neighbouring stereocilia in hair–bundles of the inner ear are connected by tip links, which are joined to transduction channels and whose stiffness is remarkably Ca^{2+} dependent. The deflection of the stereocilia by sound waves change tip link tension and brings about opening and closing of transduction channels permitting or preventing the entrance of K^+ and Ca^{2+} ions into stereciolia, respectively. The role of Ca^{2+} ions is to detach myosin motors in order to ease increased tip link tension. Conversely, if the tension is reduced the myosin motors reattach and ascend along actin filaments restoring the resting tension in tip links. In this paper, specific emphasis is placed on the ability of hair–bundles in the bullfrog's sacculus to produce oscillations that might underlie spontaneous otoacoustic emissions. The reason for this is due to the fact that the experimental data for this species are very reliable.

The paper is organized as follows. In Section 1, we explain the polyelectrolyte character of actin filaments within stereocilia. Our biophysical model that describes the mechanism of localized Ca^{2+} ion pulse propagation along actin filaments is presented in Section 2. Further, in Section 3 we discuss in detail the Ca^{2+} ions dependent myosin–based adaptation of hair–bundle motility. Finally, our model's application to the spontaneous oscillations of hair–bundles is presented and discussed in Section 4. In Section 5 we present main conclusions and discuss the obtained results.

* Corresponding author.
E-mail address: dalsek@uns.ac.rs (D.L. Sekulic).

https://doi.org/10.1016/j.biosystems.2018.08.006
Received 1 July 2018; Received in revised form 15 August 2018; Accepted 16 August 2018
Available online 01 September 2018
0303-2647/

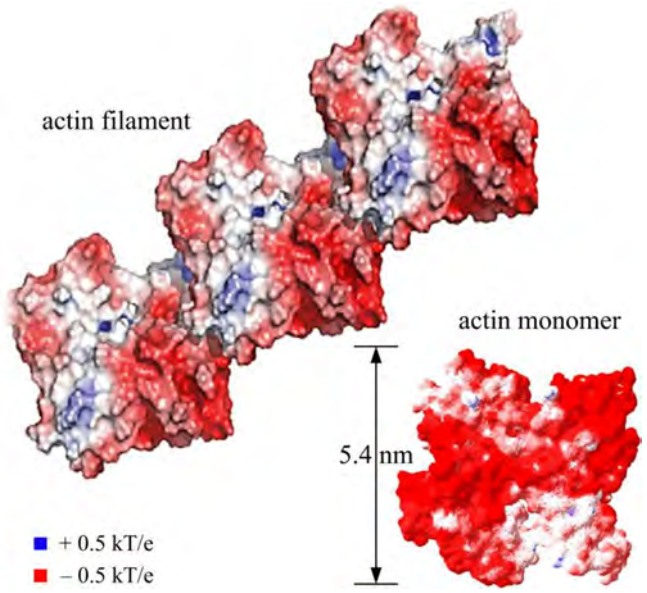

Fig. 1. Structural model of an actin filament consisting of two intertwined long–pitch right–handed helices showing an electrostatic charge distribution on the surface of an actin monomer and a segment of the actin filament (red color indicates negative charges, blue positive charges and white neutral regions) (For interpretation of the references to colour in this figure legend, the reader is referred to the web version of this article).

2. Actin filaments as polyelectrolyte guidelines for Ca^{2+} ions within stereocilia

We first explain how actin filaments within the hair–bundles can serve as conduits for Ca^{2+} ion flows, which are implicated in myosin motor adaptation. Recently, in a separate paper we have described why and how actin filaments can be considered as linear polyelectrolytes (Sataric et al., 2015), which is in accordance with the approach of Manning (2008). It is well known that these globular actin proteins have a diameter r = 5.4 nm and spontaneously polymerize to form double stranded filaments referred to as F–actin, see Fig. 1. Also, it is well established that the negatively charged surface of actin protein attracts positive cations to different extents (Strzelecka–Gołaszewska et al., 1978, 1989). For example, besides single high-affinity bound site at actin polymers of skeletal muscle, it also contains multiple sites that loosely bind divalent cations with an equilibrium dissociation constant on the order of 0.1 mM for Ca^{2+} and Mg^{2+} ions. There is also ample evidence for the presence in actin of binding sites for divalent cations with a still lower affinity. These sites underlie the polyelectrolyte nature of actin filaments at physiological conditions that was discovered some twenty years ago and corresponding crucial empirical parameters were presented by Tang and Janmey (1996). The various theoretical and experimental results available today provide an explanation why actin filaments are true polyelectrolytes, which play functional roles in the signalling pathways for Ca^{2+} ions within the cells (Gartzke and Lange, 2002). In this study we quantitatively elaborate on this concept and demonstrate that it is exactly true. Further, it has been shown that actin filaments support ionic conductance and transmit electrical currents in the form of localized counterionic waves around the filament's surface (Cantiello et al., 1991; Lin and Cantiello, 1993; Janmey et al., 2014). These experimental results also motivated us to establish a model, which is present in the text below.

The basic idea relies on the fact that the negatively charged surface of an actin filament attracts positive counterions from cytosol, mainly in terms of divalent ions such as Ca^{2+}. Each actin monomer carries an excess of 11 negative elementary charges $e = 1.6 \times 10^{-19}$ C, and counting two strands with two monomers one easily finds that the linear charge density is approximately 4 e/nm. This gives the average linear spacing of elementary charges along the filament axes to be $\delta = 0.25$ nm. This should be compared with a characteristic Bjerrum length l_B, which defines the distance at which thermal fluctuations are equal to the electrostatic attraction or repulsion between ions and negative sites on the actin filament. For divalent Ca^{2+} ions ($z = 2$) at $T = 310$ K, the Bjerrum length is determined by

$$\frac{ze^2}{4\pi\varepsilon_r\varepsilon_0 l_B} = k_B T \Rightarrow l_B = \frac{ze^2}{4\pi\varepsilon_r\varepsilon_0 k_B T} = 1.38\text{nm}, \tag{2.1}$$

where $\varepsilon_r = 78$, $\varepsilon_0 = 8.85 \times 10^{-12}$ F/m and $k_B = 1.38 \times 10^{-23}$ J/K is the Boltzmann's constant. In accordance with this value, the characteristic dimensionless parameter ξ for an actin filament is found as

$$\xi = \frac{l_B}{\delta} = 5.4 >> 1, \tag{2.2}$$

which is a very important factor for electrolytic free energy of Ca^{2+} ions around an actin filament. Since this value is significantly greater than unity, the necessary condition for the creation of a polyelectrolyte is clearly satisfied supporting our argument about the polyelectrolyte character of actin filaments at physiological conditions. This also confirms that the attractive Coulomb force brings Ca^{2+} ions very close to the filament's surface forming a cylindrical condensed "ionic cloud" with a thickness on the order of $d = 1$ nm and an inner radius equal approximately to $r = 5.4$ cm, see Fig. 2. Around this "ionic cloud" there is a layer depleted of ions of both signs with a thickness equal to the Bjerrum length l_B. Consequently, an actin filament can be considered as a transmission line with a nano–capacitor that is capable of storing and transporting an "ionic cloud" of attracted Ca^{2+} ions along the filament's length (Sataric et al., 2009).

In order to properly apply the theory of polyelectrolytes (Manning, 2011), the screening Debye length Δ in the hair cell's endolymph must first be estimated. Since the average ionic concentration in a typical endolymph is on the order of $n_s = 9 \times 10^{25}\,\text{m}^{-3}$, the Debye length amounts to (Israelachvili, 1992)

$$\Delta = \left(\frac{\varepsilon_r\varepsilon_0 k_B T}{2e^2 n_s}\right)^{1/2} = 0.81\text{nm} \tag{2.3}$$

An electrolytic free energy G of the actin filament with N condensed Ca^{2+} counterions is defined as follows (Manning, 2011)

$$G = -Nk_B T(1 - z\theta)^2\xi \ln\left(\frac{\delta}{\Delta}\right) + Nk_B T\theta \ln\left(\frac{\theta}{\Omega}\right). \tag{2.4}$$

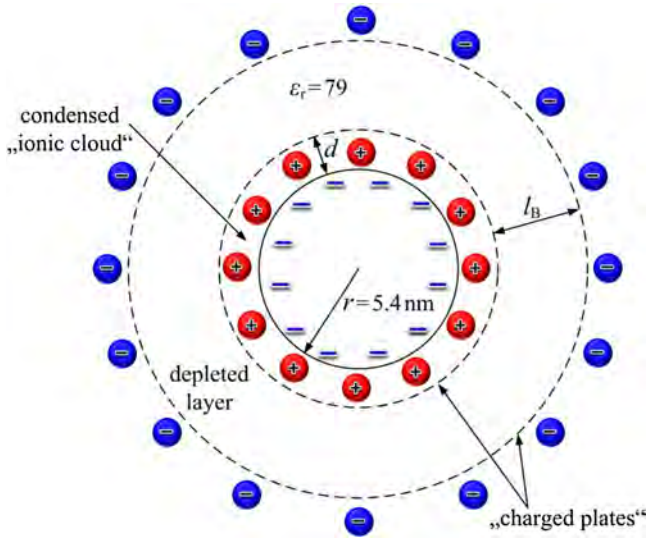

Fig. 2. Schematic representation of the counterion charge distributions surrounding an actin filament.

The first term in the above expression reflects the Debye–screened repulsions between all pairs of negative sites on the charged filament considered. With the already determined parameters $\Delta = 0.81$ nm and $\delta = 0.25$ nm, the first term in Eq. (2.4) is positive as required because ln $(\delta/\Delta) = -1.176$. The dimensionless quantity θ represents the relative concentration of Ca^{2+} with respect to the negative sites of the filament. If every negative site is covered by one counter ion, then the total coverage is $\theta = 1$. Under a lower ionic concentration around the filament, the condition $\theta < 1$ holds and it leads to the inequality

$$\frac{\theta}{\delta} \leq \frac{1}{\delta}. \tag{2.5}$$

For this reason, the effective charge of a site is reduced to the following fraction for Ca^{2+} counterions

$$1 - z\theta = 1 - 2\theta. \tag{2.6}$$

The second term in Eq. (2.4) involves an internal partition function Ω, which reflects the short–range interactions between Ca^{2+} counterions and the corresponding actin filament in accordance with the concept of an ideal gas of particles.

By using the free energy given in Eq. (2.4) we define the free energy per Ca^{2+} ion expressed in units of thermal energy as

$$g = \frac{G}{Nk_BT} = -(1 - z\theta)^2\xi \ln\left(\frac{\delta}{\Delta}\right) + \theta \ln\left(\frac{\theta}{\Omega}\right). \tag{2.7}$$

It is then possible to calculate the electrochemical potential μ_c for a condensed "ionic cloud" as follows:

$$\mu_c = k_BT\frac{\partial g}{\partial \theta} = 2k_BTz(1 - z\theta)\xi \ln\left(\frac{\delta}{\Delta}\right) + k_BT\left[\ln\left(\frac{\theta}{\Omega}\right) + 1\right]. \tag{2.8}$$

The equilibrium concentration of counterions on an actin filament can be adequately estimated by equalizing the first term of the above–defined chemical potential μ_c with the potential of free counterions μ_{free} for a stationary endolymph concentration ($n_s = 9 \times 10^{25}\,m^{-3} = 0.15$ mol/l). Since

$$\mu_{free} = 2k_BT \ln(n_s), \text{ and } \ln(n_s) = \ln(0.15) = -1.897, \tag{2.9}$$

the equality will hold if we balance the multipliers of $2k_BT$ in Eqs. (2.8) and (2.9)

$$z(1 - z\theta_0)\xi \cdot 1.176 = 1.897. \tag{2.10}$$

This resulting equality determines the equilibrium concentration of a partial covering of an actin filament by Ca^{2+} counterions as

$$\theta_0 = 0.425. \tag{2.11}$$

The fraction of remaining negatively charged sites on an actin filament is equivalently expressed as:

$$1 - \theta_0 = 0.575. \tag{2.12}$$

This number defines the available space such that with an increased influx of Ca^{2+} ions through transduction channels, the additional ions can be accommodated on the filament creating a denser "ionic cloud". The ions from the "ionic cloud" are free to slide along the corresponding actin filament but are inhibited from diffusing away. This delocalized loosely binding is more preferable for counterions of higher valence such as Ca^{2+} ions, in which case the charged filament is neutralized to a higher degree.

Let us estimate the concentration of Ca^{2+} ions within an "ionic cloud" under thermodynamic equilibrium conditions. Using a well–known fact that one elementary unit of an actin filament has $2 \times 11e = 22e$ charges with an estimated fractional covering of $\theta_0 = 0.425$, the number of Ca^{2+} ions is approximately n = 9. Taking dimensions from Fig. 2, we obtain the ionic density within the thin hollow cylinder with base area A, length L = 5.4 nm and the thickness $d = 1$ mm as:

$$n_s^{Ca^{2+}} = \frac{n}{A \cdot L} = \frac{n}{\pi((r + d)^2 - r^2) \cdot L} = 4.5 \times 10^{25} m^{-3}. \tag{2.13}$$

This is very close to an equilibrium ionic concentration in an endolymph, namely $n_s = 9 \times 10^{25}\,m^{-3}$. It is obvious that with a doubled number of Ca^{2+} ions within an "ionic cloud", we find $n_s^{Ca^{2+}} = n_s = 9 \times 10^{25} m^{-3}$, a number, which is equal to the global ionic concentration in an endolymph. Why is this result so important? Despite the fact that Ca^{2+} ions play a crucial role in controlling myosin motors in stereocilia, their concentration is marginally small in an endolymph compared with those of the dominant K^+ and Na^+ ions. The experimental assay by Beurg et al. (2010) revealed that when the influx current through channels of a hair–bundle is 3.4 nA, just 0.2% of this current is carried by Ca^{2+} ions with a corresponding peak of 7 pA. Moreover, some experimental data show that the total concentration of neutral Ca atoms in these processes is by one order of magnitude higher than its ionized fraction. Moreover, Gartzke and Lange (2002) pointed out that the bundles of actin filaments in stereocilia form strong diffusion barrier for ionic propagation. Additionally the presence of fixed and mobile buffers and extruding pumps also diminishes the number of diffusing Ca^{2+} ions in an endolymph, thus lowering their affordability for myosin control. Taking into account all these observations, we are convinced that this newly proposed mechanism of polyelectrolyte pathways can describe how to efficiently distribute Ca^{2+} ions along actin filaments in order to provide highly concerted hair cell's response to fast and complex auditory signals.

Over the last two decades or so, signalling along actin filaments has been studied using both experimental and theoretical approaches. The experimental results in the early stages (Cantiello et al., 1991; Lin and Cantiello, 1993) revealed how the ionic currents in the presence of actin filaments were amplified in comparison with actin–free solution. Accordingly, we earlier proposed a biophysical model based on the polyelectrolyte properties of actin filament, which emulates the nonlinear electric transmission line (Sataric et al., 2009). Below, we briefly discuss the main estimates arising from that model. Since an "ionic cloud" can be approximated by a cylindrical layer shown in Fig. 2, we could first assess the elementary capacitance of one actin dimer of length L = 5.4 nm with radius $r = 5.4$ nm and the distance between "charged plates" assumed to be $l_B = 1.38$ nm as follows

$$C_0 = \frac{2\pi\varepsilon_r\varepsilon_0 L}{\ln\left(1 + \frac{l_B}{r}\right)} = 1.08 \times 10^{-16} F. \tag{2.14}$$

Otherwise, the resistance of this same electric elementary unit of the "transmission line" can be calculated using the formula

$$R_0 = \frac{1}{\sigma}\frac{L}{A} = \frac{1}{\sigma}\frac{L}{\pi((r + d)^2 - r^2)}. \tag{2.15}$$

If we use two different values for the electrical conductivity experimentally revealed by Minoura and Muto (2006) $\sigma^{MM} = 0.15$ S/m and by Uppalapati et al. Uppalapati et al. (2008) $\sigma^U = 0.25$ S/m, respectively, we obtain two estimates for the elementary resistance of an "ionic cloud", namely

$$R_0^{MM} = 0.97 \times 10^9 \Omega \text{ and } R_0^U = 0.58 \times 10^9 \Omega. \tag{2.16}$$

Based on the above results, we determine the characteristic times of discharging an elementary electric unit of an actin filament

$$T_0^{MM} = R_0^{MM}C_0 = 1.05 \times 10^{-7} s \text{ and } T_0^U = R_0^U C_0 = 0.61 \times 10^{-7} s. \tag{2.17}$$

As a result, the order of magnitude estimate for the velocity of an "ionic cloud" propagating along an actin filament is

$$v_0^{MM} = \frac{L}{T_0^{MM}} = 5.1\frac{cm}{s} \text{ and } v_0^U = \frac{L}{T_0^U} = 8.8\frac{cm}{s}. \tag{2.18}$$

A similar order of magnitude was obtained in a very recent experimental study of ionic conductivity along microtubules (Cantero et al., 2016).

3. Equation of motion for propagation of Ca^{2+} ions along actin filament

Although the magnitude of the velocity of "ionic cloud" propagation given in Eq. (2.18) seems to be overestimated due to the simplified geometry, it surprisingly fits very well with the results of more sophisticated calculations, which have been published recently (Hunley et al., 2018). Thus, the velocity of localized ionic pulses along actin filaments is much greater than the velocity of pure diffusion of ions in bulk endolymph, which is on the order of μm/s. This advantage is an additional motivation for introducing the concept of fast and efficient control of adaptation of myosin motors involved in the mechanoelectrical transduction in stereocilia, which we postulate is performed by the action of Ca^{2+} "ionic clouds" propagating along corresponding actin filaments.

The influx of Ca^{2+} ions through a transduction channel is mainly distributed along closely arranged actin filaments in the form of "ionic clouds". The particular influx involves a voltage gradient in the form of a localized field E, which may depend on space and time. Accordingly, the local concentration of Ca^{2+} ions within an "ionic cloud" becomes a function of both time t and position x along the actin filament. The excess Ca^{2+} ions due to channel influx propagate along an actin filament with drift velocity v_d provided by the force F defined by a negative gradient of electrochemical and electrical potential as follows

$$F = -\frac{\partial}{\partial x}(\mu_c - zeEx), \tag{3.1}$$

where the electrochemical potential μ_c for a condensed "ionic cloud" satisfies Eq. (2.8). This force acting on Ca^{2+} ions is balanced by the viscosity damping characterized by the parameter λ and drift velocity v_d

$$F = \lambda v_d. \tag{3.2}$$

The ionic flux can be expressed as

$$J(x,t) = \frac{\theta}{\delta}v_d = \frac{\theta}{\delta}\left(\frac{F}{\lambda}\right). \tag{3.3}$$

Combining the expressions given in Eqs. (2.8), (3.1) and (3.2) one finds

$$J(x,t) = \frac{ze}{\delta\lambda}E\theta - \frac{k_B T}{\delta\lambda}\left[1 - 2z^2\xi\theta\ln\left(\frac{\delta}{\Delta}\right)\right]\frac{\partial\theta}{\partial x}. \tag{3.4}$$

On the other hand, the relative concentration of condensed Ca^{2+} counterions θ must obey the continuity condition

$$\frac{\partial J}{\partial x} = -\frac{1}{\delta}\frac{\partial\theta}{\partial t}. \tag{3.5}$$

Thus, on the basis of Eqs. (3.4) and (3.5) the master equation of motion for the concentration of counterions within a mobile "ionic cloud" has the following shape:

$$\frac{\partial\theta}{\partial t} = -\frac{ze}{\lambda}E\frac{\partial\theta}{\partial x} + \frac{k_B T}{\lambda}\frac{\partial^2\theta}{\partial x^2} - \frac{k_B T}{\lambda}2z^2\xi\ln\left(\frac{\delta}{\Delta}\right)\left(\frac{\partial\theta}{\partial x}\right)^2 - \frac{k_B T}{\lambda}2z^2\xi\ln\left(\frac{\delta}{\Delta}\right)\left(\theta\frac{\partial^2\theta}{\partial x^2}\right). \tag{3.6}$$

Instead of linearizing the above master equation as Manning did earlier (Manning, 2011), we have exactly solved this problem by using a traveling wave approach, which is widely exploited in the theory of soliton waves (Sekulic et al., 2016). This makes sense keeping in mind that in Eq. (3.6) the dispersive term $\frac{\partial^2\theta}{\partial x^2}$ competes with the nonlinear terms $\left(\frac{\partial\theta}{\partial x}\right)^2$ and $\theta\left(\frac{\partial^2\theta}{\partial x^2}\right)$ resulting in a kind of balance, which leads to a moving shape of the underlying "ionic pulse".

Using a detailed derivation presented in Appendix 1, we have obtained the following implicit function $\theta(\varphi)$ determining time–space evolution of "ionic cloud":

$$\alpha\varphi = [\Omega_M - \theta - (\theta_0 + \beta)\ln(\theta - \theta_0)];\ \Omega_M = \theta_M + (\theta_0 + \beta)\ln(\theta_M - \theta_0), \tag{3.7}$$

where the parameters are determined by the following expressions

$$\alpha = \left(s\frac{L^2}{T_0} - \frac{zeLE}{\lambda}\right)\left[-\frac{k_B T}{\lambda}2z^2\xi\ln\left(\frac{\delta}{\Delta}\right)\right]^{-1},$$
$$\beta = \left[-2z^2\xi\ln\left(\frac{\delta}{\Delta}\right)\right]^{-1}. \tag{3.8}$$

Additionally, θ_M represents the local maximum concentrations of Ca^{2+} along an actin filament, while θ_0 has the equilibrium value given in Eq. (2.11). Furthermore, the total covering of negative charges of an actin filament with Ca^{2+} ions could lead to $\theta_T = 1$ which gives the maximal ratio

$$\frac{\theta_T}{\theta_0} = 2.35. \tag{3.9}$$

Finally, we estimate the parameters of Eq. (3.7) in order to obtain a final equation for numerical analysis. It is very easy to calculate parameter β on the basis of its definition given by Eq. (3.8) and using previously obtained parameters involved therein. Hence

$$\beta = [-2\cdot4\cdot5.4\cdot(-1.176)]^{-1} = 0.02. \tag{3.10}$$

In order to calculate the parameter α from Eq. (3.8), it is necessary to first estimate the ratio

$$\frac{L^2}{T_0} = \frac{(5.4\times10^{-9})^2}{1.05\times10^{-7}} = 2.8\times10^{-10}\frac{m^2}{s}, \tag{3.11}$$

which is expressed in the units of a diffusion constant. In an attempt to see how the applied field E affects the above propagation process, the viscous damping coefficient λ should be specified. Viscosity acting on a single Ca^{2+} ion can be roughly estimated by using the well–known Stokes'law

$$\lambda = 6\pi\eta r. \tag{3.12}$$

Taking water as solvent, its viscosity coefficient is $\eta \sim 10^{-3}$ Pas. Using this value with an effective radius of Ca^{2+} ions of $r = 2\times10^{-10}$ m, one obtains $\lambda = 3.7\times10^{-12}$ Ns/m. This is a very approximate underestimation since Dhont and Kang (2010) revealed that this parameter should be 20 times greater according to an experiment with Ca^{2+} ions moving around an fd virus. We adopt their estimation, which leads to $\lambda_{DK} = 0.74\times10^{-10}\frac{Ns}{m}$. By using both of the above parameters, the second term in Eq. (3.8) is on the order of

$$\frac{zeLE}{\lambda_{DK}} \le 10^{-16}E, \tag{3.13}$$

and can compete with the first one for very strong fields of the order of 10^6 V/m. In fact, the transmembrane field is known to reach this order of magnitude (Ashmore et al., 2010), but here we disregard such cases using just the first term in Eq. (3.8) thus calculating the value of parameter α as

$$\alpha = 0.17. \tag{3.14}$$

As an illustration, if we take $\theta_M = 2\theta_0 = 0.85$, we find that

$$\Omega_M = \theta_M + (\theta_0 + \beta)\ln(\theta_M - \theta_0) = 0.85 + 0.445\ln(0.425) = 0.47, \tag{3.15}$$

and accordingly the explicit function for Ca^{2+} ions distribution within an "ionic cloud" has the following form

$$\varphi = 2.76 - 5.88\theta - 2.51\ln(\theta - 0.425)\text{for}\theta_0 \le \theta \le \theta_M. \tag{3.16}$$

If $\theta_M = 0.7$ the function given in Eq. (3.7) reads

$$\varphi = 0.88 - 5.88\theta - 2.51\ln(\theta - 0.425)\text{for}\theta_0 \le \theta \le \theta_M. \tag{3.17}$$

The graphical shape of the above functions representing the ionic pulses is shown in Fig. 3. We stress here that our approach is based on a chemical thermodynamics leading to nonlinear differential equation

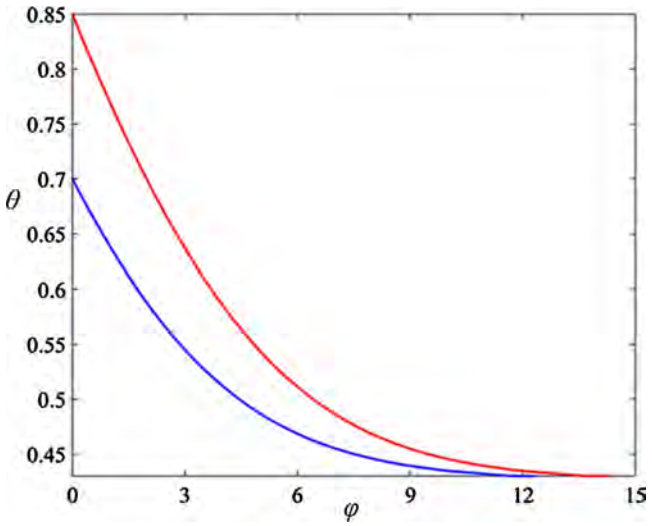

Fig. 3. The numerical representation of functions of the model for charge distribution of Ca^{2+} counterions within a localized pulse, which propagates along an actin filament.

Eq. (A.4), describing the relative concentration of condensed ions. The essential original contribution of this paper is the general solution of nonlinear master equation, Eq. (3.6), which describes motion of counterions within a mobile "ionic cloud" in the form of a traveling wave. This enables the localized ionic pulses to exist and propagate with a velocity on the order of cm/s (Sataric et al., 2015) which is substantially higher than the velocity of ionic diffusion in cytosol. Particularly important is the fact that a channel's denser influx of Ca^{2+} ions leads to faster pulses in stereocilia. Our earlier studies dealing with polyelectrolyte properties of actin filaments and microtubules were based on the electrical transmission line approach and their results showed a possible appearance of localized ionic pulses with a velocity of similar magnitude (Sataric et al., 2009).

Very recently Hunley et al. (2018) published the results of an alternative multi–scale approach based on the polyelectrolyte nature of actin filaments, which describe electrical cationic impulses propagating along these cytoskeletal filaments. In this study the detailed molecular characterization including the amino acid sequences and the number and type of residues exposed to the surrounding electrolyte (i.e. cytosol) is provided and utilized. In terms of a mean field Poisson–Boltzmann theory along with a suitable modification of Nernst–Planck theory, these authors performed a quantitative description of conductive properties and capacitance of actin filaments, similar to that we did earlier (Sataric et al., 2009). They further applied a lossy nonlinear dispersive transmission line model and in terms of Kirchhoff's laws and a perturbed Korteweg–de Vries equation was derived within the framework of the model. The main result is that the actin filament is able to support localized ionic pulses propagation. These waves in the form of the solitons are narrower and travel faster at a higher voltage input in the intracellular conditions. They display a deceleration with soliton peak attenuation, which is more pronounced for faster solitons. Very importantly, the time averaged propagation velocity of these soliton pulses is on the order of a few centimetres per second, which is on the same order of magnitude as in our approach presented here. Accordingly, these results additionally corroborate the validity of our concept present here.

4. Ca^{2+} dependent myosin based adaptation of hair–bundle motility

In hair cells of the inner ear mechanical stimulation supplies the energy sufficient to open transduction channels responsible for the influx of positive ions. In non–mammalian vertebrates Ca^{2+} ions entering the mechanosensitive ion channels drive adaptation, but it has been questioned whether this mechanism applies to mammals. Corns et al. (2014) have shown that adaptation in mammalian cochlear hair cells is, as in other vertebrates, driven by Ca^{2+} entry demonstrating the importance of this process as a fundamental mechanism in all vertebrate hair cells. When an incoming sound wave excites the cochlea's basilar membrane into resonant oscillation, the tectorial membrane impairs force to the mechano–sensitive hair–bundle (Benser et al., 1993). Each hair cell is adorned with its hair–bundles, which comprise hexagonal arrays of so–called stereocilia, and play the role of mechanosensory antenna and force generator for amplificatory processes. Every stereocilium is a bundle of parallel actin filaments interconnected with some specific lateral links. The tip links are of basic importance since they serve for opening and closing of ionic transduction channels of the hair cell membrane. Tip links are mechanically in series with a yet unidentified gating–spring element, which pulls on transduction channels and whose stiffness can be Ca^{2+} dependent. Under the action of the Ca^{2+} chelator BAPTA to the hair–bundle disrupts the tip links and stops mechanotransduction currents (Ceriani and Mammano, 2012). It appears that proteins cadherin 27 and protocadherin 15 are part of tip links and Ca^{2+} binding to them determine the robustness of tip links. The hair–bundle is arranged like a harp or the back acoustic compartment of a piano in rows of increasing height, see Fig. 4. As an illustrative example, in a striolar hair–bundle of chicks the longest

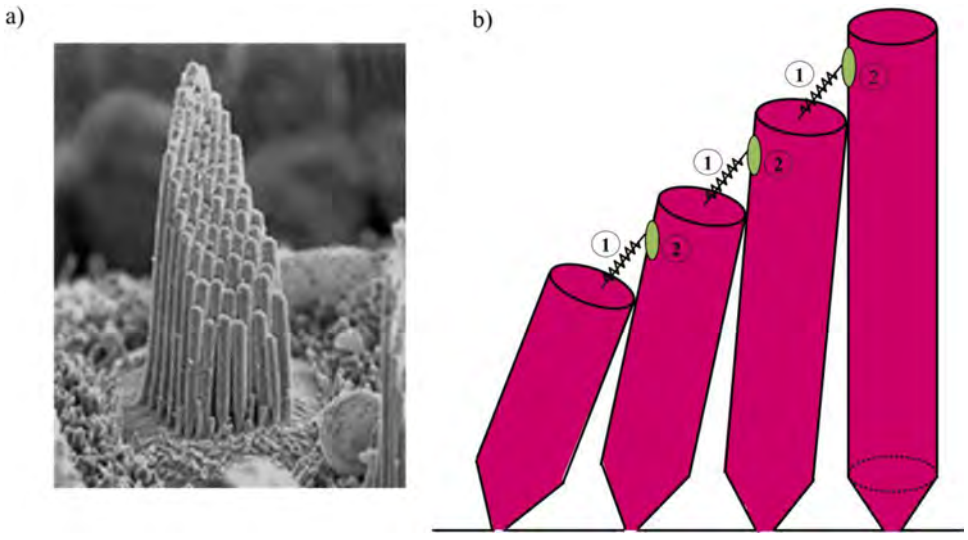

Fig. 4. (a) Morphology of a hair–bundle of a vestibular hair cell. In this organ, each bundle consists of approximately 50 stereocilia arranged into several rows with variable heights. (b) Schematic illustrating a single row of stereocilia with tip links–1 and corresponding transduction channels–2, which are responsible for ionic currents.

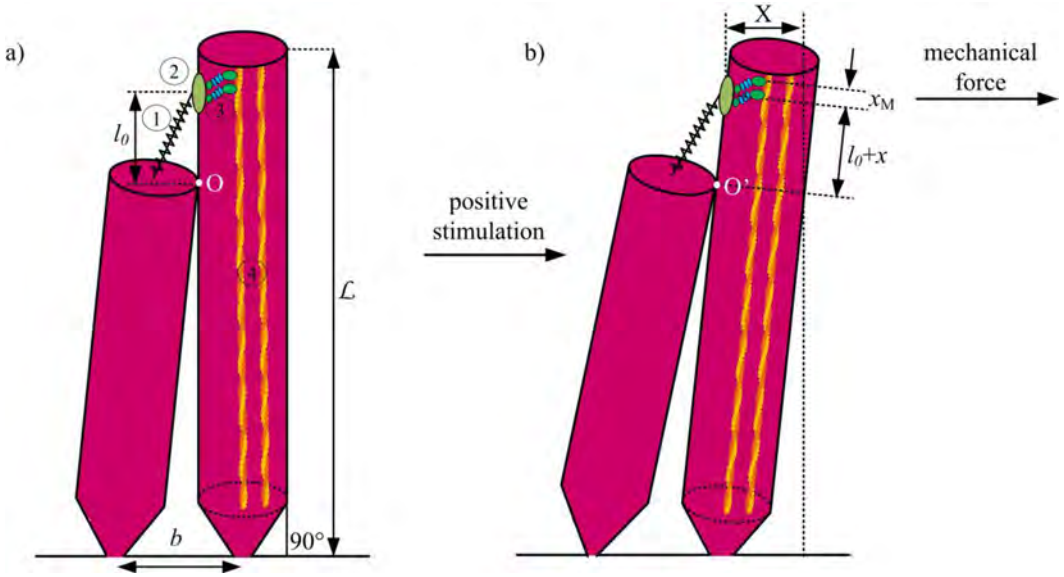

Fig. 5. (a) The tallest stereocilia of a hair–bundle in equilibrium (1–tip link; 2–transduction channel; 3–myosin adaptation motors; 4–actin filaments). L is the height of the tallest stereocilia, b is the distance between the roots of neighboring stereocilia, and l_0 represents the distance between the touching point O and the channel in an equilibrium position of the bundle. (b) Transversally displaced bundle by distance X shifts the stereocilia contact point O to new position O' so that its distance is now l_0+x with respect to the channel, where x stands for channel's shift due to bundle's displacement X. This leads to relation $Xb/L = x–x_M$.

stereocilia are 9.2 μm and the shortest are 2.4 μm. The number of stereocilia in that bundle is N = 51. The diameter of a single stereocilium is about 0.42 μm and the number of tip links in this bundle is 42. Generally, if a hair–bundle comprises N stereocilia, which slope up against each other and the longest of them has the length L, Holt and Corey (2000) noted that there is an inverse relation between N and L in a way that N spans 20–300 stereocilia whose lengths L are in the inverse range, i.e. 30–2 μm.

In response to an external force, a hair–bundle pivots at its base. Let us consider a free standing hair–bundle with highest stereocilia of length L and with b being the distance between roots of the nearest stereocilia, see Fig. 5a. The position where the tallest stereocilium touches its neighbor is the point O. The distance between the tallest channel and attached motors relative to O is $l_0 + x_M$, where l_0 is the length of a tip link without extension and x_M represents the extension under the action of myosin motors. If the tip of the bundle is laterally displaced with distance X, see Fig. 5a, all stereocilia pivot at their bases and neighboring ones are sheared by the displacement $b/L \cdot X = \gamma X$. The new location of the touching point between the sterecilia is displaced to O' making the distance between O' and the same channel to be $l_0 + x$. Thus, the sheared distance O–O' is

$$\gamma X = l_0 + x - (l_0 + x_M) = x - x_M. \tag{4.1}$$

This horizontal displacement of the bundle is countered by the elastic restoring force, which consists of two components. The first one arises from the fact that pivoting around roots stereocilia provides effective bundle stiffness given by

$$k_{SP} = \kappa \frac{N}{L^2}, \tag{4.2}$$

with κ being the pivotal stiffness of a single stereocilium. Hudspeth et al. (2000) provided an experimental value $\kappa = 1.5 \times 10^{-16}$ Nm/rad indicating that the range of k_{SP} is between 0.03 pN/nm for the longest bundles and 11 pN/nm for the shortest ones. The second contribution for the restoring force comes from the tension in the tip links themselves. When the hair–bundle is displaced in positive (right) direction, see Fig. 5b, the gating spring of the tip link exerts a force on the trap door and thus opens the ionic channel. This enables the entry of positive K^+ and Ca^{2+} ions inside stereocilia. Not only are Ca^{2+} ions essential for preserving the stability of tip links, but significantly contribute to the mechanotransduction processes. Fast adaptation is caused by the direct binding of Ca^{2+} ions to an intracellular site of mechanotransduction channel which closes the channel itself. On the other hand, slow adaptation is linked to the activity of unconventional myosin motors (Ceriani and Mammano, 2012) and that mechanism is the main point here. The tip link force consists of two parts in the following form

$$F_{TL} = k_{TL}x + f(x - x_s(\theta)) = k_{TL}x + f(x, \theta), \tag{4.3}$$

where $x_s(\theta)$ is an effective shift in the channel gating point dependent on the local Ca^{2+} ion concentration θ according to Eq. (2.4). The first term represents the passive linear elastic force with tip link stiffness k_{TL}, while the second one is the nonlinear active force of the transduction channel often called the gating force. Vilfan and Duke (2003) established that the transduction channel protein incorporates a lever arm segment acting as an amplifier for small structural changes as being present when the channel switches its state. It turns out that a minimally sufficient model includes just two switching states. In line with that, the open state has a probability $p_O(x, \theta)$ and its corresponding lever arm position is d_O, while the closed state has a probability $p_C(x, \theta)$ and lever arm position d_C. The gating force is related to the channel opening probability of a single open state $p_O(x, \theta)$ by definition (van Netten and Kros, 2000) whereby

$$f(x, \theta) = k_B T \frac{\partial}{\partial x}[\ln p_O(x, \theta)] - k_{TL} d_O. \tag{4.4}$$

In the steady state, the probability for an open state is given in accordance with Boltzmann's distribution (Hudspeth et al., 2000)

$$p_O = \frac{W_O}{W_O + W_C} = \frac{1}{1 + \frac{W_C}{W_O}}, \tag{4.5}$$

where the weighting functions for open and closed states read:

$$W_{O(C)} = \exp\left\{\frac{1}{k_B T}\left[-\left(\frac{1}{2}k_{TL}(x - x_s(\theta) - d_{O(C)})\right)^2 - G_{O(C)}\right]\right\}. \tag{4.6}$$

G_O and G_C are the free energies of an open and closed state of the transduction channel protein, respectively. They depend on the local Ca^{2+} ion concentration, which is regulated by the entry of Ca^{2+} ions through corresponding channels and by being primarily distributed along actin filaments in the form of mobile "ionic clouds" given by Eq.

(3.15).

Based on experimental results (Corey and Hudspeth, 1983), the impact of the Ca^{2+} ion concentration on the active force $f(x, \theta)$ can be accounted for by an effective shift in the channel gating point, which is related to the local Ca^{2+} ion concentration actually attributed to an incoming "ionic pulse" imparted by channel's opening. The shift $x_s(\theta)$ in the context of our proposed model, see Eq. (3.7), reads:

$$x_s(\theta) = D\varphi = \frac{D}{\alpha}[\Omega_M - \theta - (\theta_0 + \beta)\ln(\theta - \theta_0)], \tag{4.7}$$

where the constant D was empirically estimated as $D \sim 4$ nm in the bullfrog's saculus (Corey and Hudspeth, 1983). On the basis of the above Eqs. (4.4), (4.5) and (4.6), the explicit form of the gating force for a single channel is

$$f(x, \theta) = \frac{k_{TL}(d_O - d_C)}{1 + \exp\{F(x, x_s(\theta))\}} - k_{TL}d_O, \tag{4.8}$$

where

$$F(x, x_s(\theta)) = \frac{1}{k_B T}\left\{k_{TL}(d_O - d_C)(x - x_s(\theta)) - \frac{1}{2}(d_O^2 - d_C^2) - (G_O - G_C)\right\}. \tag{4.9}$$

If we use the following set of parameters from the data available in the literature (Martin et al., 2000, 2003)

$$d_O = 8.5\text{nm};\ \ G_O = 70 \times 10^{-21}\text{J};\ \ k_{TL} = 4 \times 10^{-3}\text{N/m}$$
$$d_C = 7\text{nm};\ \ G_C = 60 \times 10^{-21}\text{J};\ \ k_{SP} = 2 \times 10^{-4}\text{N/m}$$
$$k_B T = 4.28 \times 10^{-21}\text{J at physiological temperatu re}, \tag{4.10}$$

we obtain

$$\exp F(x, x_s(\theta)) = \frac{1}{40}\exp\left\{\frac{k_{TL}(d_O - d_C)(x - x_s(\theta))}{k_B T}\right\}. \tag{4.11}$$

Changing $(x - x_s(\theta))$ from zero to infinity, $f(x, \theta)$ changes in the narrow interval $(-k_{TL}d_C, -k_{TL}d_O)$. Thus we can take the average gating force to be

$$\langle f(x, \theta)\rangle = -7.75 \times 10^{-9} \cdot 4 \times 10^{-3}\ \text{N} = -31\text{pN}. \tag{4.12}$$

It is also necessary to know the gradient of the gating force, which can be determined from Eqs. (4.8) and (4.9)

$$\frac{df(x, \theta)}{dx} = -\frac{k_{TL}^2(d_O - d_C)^2}{k_B T}\frac{\exp F(x, x_s(\theta))}{[1 + \exp F(x, x_s(\theta))]^2}. \tag{4.13}$$

In the similar way as above, and on the basis of the set of parameters given by Eq. (4.10), we estimate the maximum value of Eq. (4.13) taking the maximal value of the exponential factor that amounts to

$$\left\{\frac{\exp F(x, x_s(\theta))}{[1 + \exp F(x, x_s(\theta))]^2}\right\}_{\max} = 0.25.$$

We thus obtain

$$\left\{\frac{df(x, \theta)}{dx}\right\}_{\max} = -\frac{0.84 \times 10^{-3}}{4}\text{N/m} = -0.21 \times 10^{-3}\text{N/m}. \tag{4.14}$$

Eventually the movement of the displaced bundle is also opposed by the viscous drag of the surrounding fluid. The corresponding friction coefficient for the bundles of maximal height of sterecilia L is

$$\lambda = \eta L, \tag{4.15}$$

where η is the endolymph viscosity.

We stress that the inertial force $M_b\frac{d^2x}{dt^2}$, where M_b is the bundle's mass, is much smaller than the force of viscous damping $\lambda\frac{dx}{dt}$ and thus can be safely discarded in the Newtonian equation of motion. By combining Eqs. (4.1), (4.2) and (4.3) including the damping term, the equation of motion for the transduction channel reads

$$\lambda\frac{dx}{dt} = -\{N\gamma^2[k_{TL}x + f(x, \theta)] + k_{SP}(x - x_M)\}. \tag{4.16}$$

This equation will be exploited in the next section as the basis for establishing a relation between the dynamics of transduction channels and adaptation motors in the stereocilia of a hair–bundle. Eventually, we can make the estimate of the damping parameter λ. Vilfan and Duke used the value $\lambda = 0.65 \times 10^{-6}$Ns/m, which is based on dynamical viscosity of water (Vilfan and Duke, 2003). This is much underestimated and we believe that this value should be multiplied by the factor 20 proposed by Dhont and Kang (2010). Consequently, we adopt $\lambda = 13 \times 10^{-6}$Ns/m for the following calculations.

5. The coupled dynamics of adaptation motors and transduction channels of stereocilia

Experimental results (Wu et al., 1999) revealed that when a vertebrate hair–bundle is suddenly twitched, it exhibits a slow adaptation of the channel current on the order of tens of milliseconds. The transduction channel is linked to the actin filaments of a stereocilium by a number of adaptation motors of myosin 1c, IIIa and VIIa families. It was strongly confirmed that these myosin motors maintain the adequate tension in the tip link thus mediating slow adaptation of a hair bundle (Ceriani and Mammano, 2012; Holt et al., 2002).

We start from a linear force–velocity relation for these adaptation motors (Vilfan and Duke, 2003)

$$\frac{dx_M}{dt} = v_0\left[1 - \frac{k_{TL}x + f(x, \theta)}{F_M n_M(t)}\right], \tag{5.1}$$

where x_M is the position of adaptation motors along actin filaments, see Eq. (4.1), v_0 is the zero–load motor velocity, x represents the displacement of pertaining transduction channel, see Eq. (4.1), $f(x, \theta)$ is the gating force according to Eq. (4.8), F_M is the stall force of a single motor and $n_M(t)$ is the number of attached adaptation motors.

In order to solve Eq. (5.1), it is first necessary to consider the dynamics of motors detaching from an actin filament governed by the influence of Ca^{2+} ions. Adamek et al. (2008) showed that Ca^{2+} ions cause a 7–fold inhibition of ATP hydrolysis within a myosin–1c and inversely a 10–fold acceleration of ADP release from it. These effects lead to the increase of the detachment rate of the motor–filament cross–bridge and increase the lifetime of the motors' detached state. The detachment dynamics $n_M(t)$ of initially present $N_M = 20$ motors bound to an actin filament (Vilfan and Duke, 2003) is governed by the following linear equation

$$\frac{dn_M}{dt} = \omega_M[-n_M g(\theta) + (N_M - n_M)]. \tag{5.2}$$

Here $\omega_M = 200\ s^{-1}$ stands for the myosin binding rate, while $g(\theta)$ is a nonlinear function describing how the concentration of Ca^{2+} ions impacts the motor's detachment rate. Following the method used by Vilfan and Duke (2003) we assume that $g(\theta)$ has the cubic nonlinear form with respect to the dimensionless excess concentration θ of Ca^{2+} ions in the mobile "ionic pulse" around actin filaments

$$g(\theta) = \left(\frac{\theta}{\theta_0}\right)^3;\ \theta_0 = 0.425. \tag{5.3}$$

Then, Eq. (5.2) can be solved exactly and we obtain the number of remaining attached motors as the function of time, with the initial condition $n_M(t = 0) = N_M$,

$$n_M(t) = \frac{N_M}{g(\theta) + 1}[1 + g(\theta)e^{-At}],\ A = [g(\theta) + 1]\omega_M. \tag{5.4}$$

The characteristic detachment time τ_d is represented in Fig. 6 and it is given by

$$\tau_d = \frac{1}{A} = \{[g(\theta) + 1]\omega_M\}^{-1}. \tag{5.5}$$

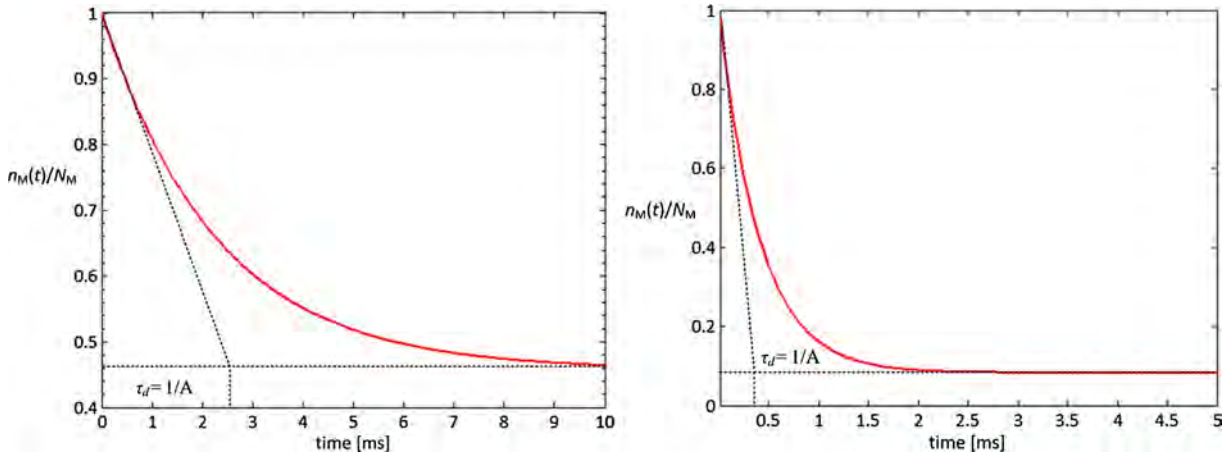

Fig. 6. Characteristic detachment time τ_d for $\theta = 0.45$ (left) and $\theta = 0.95$ (right).

Since within the different ionic pulses the concentration θ could change in the range $\theta_0 < \theta \leq 2.35\theta_0$, it implies that the following inequality is valid

$$1 \leq g(\theta) \leq 13, \tag{5.6}$$

and the range of the detachment rate is, respectively

$$\tau_d \approx (0.38 - 2.5)\text{ms}. \tag{5.7}$$

This is in sharp contrast with the statements given by Vilfan and Duke (2003) in which they pointed out that the motors operate on a slower timescale than mechanical relaxation of a bundle. Hence, in their description of bundle's dynamics the motor position x_M was taken as being fixed. Here we respect the fact that motors move during adaptation process.

This new assumption allows us to safely link the dynamics of adaptation motors given by Eq. (5.1) with the Eq. (4.16) that describes the motion of the transduction channels. In order to combine these equations, we first differentiate the channel's equation with respect to time as follows

$$\frac{d}{dt}\left(\lambda\frac{dx}{dt}\right) = -\frac{d}{dt}(N\gamma^2[k_{TL}x + f(x,\theta)]) - \frac{d}{dt}(k_{SP}(x - x_M)). \tag{5.6}$$

Then using Eq. (5.1), we get the following second order differential equation with respect to $x(t)$

$$\frac{d^2x}{dt^2} + \frac{1}{\lambda}\left(N\gamma^2\frac{df(x,\theta)}{dx} + N\gamma^2k_{TL} + k_{SP}\right)\frac{dx}{dt} + \frac{1}{\lambda}\left(\frac{v_0k_{SP}k_{TL}}{F_Mn_M(t)}\right)x = \frac{v_0k_{SP}}{\lambda}\left(1 - \frac{f(x,\theta)}{F_Mn_M(t)}\right). \tag{5.7}$$

Strictly speaking, this equation is nonlinear due to the presence of exponential functions $f(x, \theta)$ and $df(x, \theta)/dx$ as well as $n_M(t)$. However, using the previously found numerical estimates of the narrow ranges of these functions given in Eqs. (4.12) and (4.14), nonlinearity in the above equation can be ignored within a first order approximation. Also, it is suitable, instead of the explicit function $n_M(t)$ defined by Eq. (5.4), to keep here just a characteristic number of motors remaining after the detachment time τ_d, namely $n_M = N_M/14 = 10/7$ for the largest influx giving the fastest "ionic pulse" arising in the open channel state, and $n_M = N_M/2 = 10$ for the smallest influx of Ca^{2+} ions and the slowest "ionic pulse".

Further, we can use the following abbreviations in Eq. (5.7)

$$a = \frac{1}{\lambda}\left(N\gamma^2\frac{df(x,\theta)}{dx} + N\gamma^2k_{TL} + k_{SP}\right);$$
$$b = \frac{1}{\lambda}\left(\frac{v_0k_{SP}k_{TL}}{F_Mn_M}\right);$$
$$c = \frac{v_0k_{SP}}{\lambda}\left(1 - \frac{f(x,\theta)}{F_Mn_M}\right), \tag{5.8}$$

so that the compact form of the equation of motion now reads

$$\frac{d^2x}{dt^2} + a\frac{dx}{dt} + bx = c. \tag{5.9}$$

The solution of the homogeneous part of the above equation is:

$$x_h(t) = A\exp(r_1t) + B\exp(r_2t);\ r_{1,2} = \frac{1}{2}[-a \pm (a^2 - 4b)^{1/2}], \tag{5.10}$$

where the integration constants A and B are defined by the initial conditions.

Of particular interest here is to determine the coefficients a, b and c defined by Eq. (5.8). Using the specified set of the experimentally determined and numerically estimated parameters given by Eqs. (4.10), (4.12), and (4.14) completed with $F_M = 1.25\,\text{pN}$, $v_0 = 0.3\,\mu\text{m/s}$, $N_M = 20$, and $n_M = 10/7$ (Vilfan and Duke, 2003), the following values are obtained for bullfrog saculus hair–bundles

$$a = 154\text{s}^{-1};\ b = 10300\text{s}^{-2};\ c = 0.8 \times 10^{-4}\frac{\text{m}}{\text{s}^2}. \tag{5.11}$$

This leads to the explicit parameter $r_{1,2} = (-77 \pm \sqrt{5929 - 10300})\text{s}^{-1}$ which describes the damped oscillations with the decay rate

$$\tau_d = \frac{1}{77}\ \text{s} = 13\text{ms}, \tag{5.12}$$

This is well in accordance with the experiment of Wu et al. (1999). Also, this value is one order of magnitude greater than the detachment time of adaptation motors, Eq. (5.7). The corresponding angular velocity of these oscillations is $\omega = (4371)^{1/2}\text{s}^{-1} = 66.1$ rad/s, giving the frequency

$$f = \frac{\omega}{2\pi} = 10.5\text{Hz}. \tag{5.13}$$

This value is in good agreement with the available experimental results (Martin et al., 2003; Tinevez et al., 2007); Tinevez et al. (2007) demonstrated that a hair–bundle from bullfrog saculus exhibits spontaneous oscillations at a frequency of ~ 12 Hz and a round–mean–squared magnitude of 22 nm.

Finally, a particular solution of Eq. (5.9) is found as

$$x_p = \frac{c}{b} = \frac{0.8 \times 10^{-4}}{1.03 \times 10^4} \cong 8\text{ nm}. \tag{5.14}$$

This value is very close to $d = 7$ nm, which is the distance of gating

spring relaxation on channel opening (Martin et al., 2000). From Eq. (5.1) it follows that the condition for the emergence of the bundle's spontaneous oscillations is given by

$$a^2 - 4b \leq 0, \tag{5.15}$$

which yields

$$\frac{n_M}{N_M} \geq \frac{9}{20}. \tag{5.16}$$

It means that the number of attached motors must be above 45% in order to self–tune such an active process. Increasing Ca^{2+} ions concentration θ increases the value of parameter b, which leads to an increase in the frequency of oscillations. This frequency also depends on the elastic properties of hair–bundle and tip links as well as on the viscosity damping. Sinusoidal oscillations defined by Eq. (5.10) that are specified by parameters given in Eqs. (5.12) and (5.13) correspond to the leading harmonic. The higher harmonics reflecting the real experimental bundle movement in bullfrog sacculus (Martin et al., 2003) manifest the basically nonlinear character of Eq. (5.7) due to the functions $f(x, \theta)$, $df(x, \theta)/dx$ and $n_M(t)$. These harmonics have not been considered here and will be the subject of future studies. All these arguments clearly corroborate the validity of our concept in establishing a strong correlation between the dynamics of transductions channels and active movements of myosin adaptation motors in hair–bundles mediated by Ca^{2+} ions carried by propagating localized "ionic pulses" described by our model in Eq. (3.7).

6. Discussion and conclusions

Experimental and theoretical studies have shown that both non–mammalian and mammalian stereociliary hair–bundles of inner ear can produce a force due to the interaction of Ca^{2+} ions with myosin motors (Corns et al., 2014). This active force production is connected to the slow adaptation of the transduction Ca^{2+} currents. We have shown in this paper that a collection of myosin motor proteins within a hair–bundle can generate oscillations at a frequency that depends on the elastic properties of the bundle as well as on the gating force and the number of attached myosin motors controlled by the localized waves of Ca^{2+} ions. Tension-gated transduction channels, which detect the motion of hair–bundles regulate these processes by admitting an ionic influx of Ca^{2+} ions that tune motor activities. Most of the essential cellular functions involve directional movement and transport of chemical species. The main interest of this paper has been centered on the specific mechanism of directional propagation of Ca^{2+} ions from transduction channels of hair cells of the vertebrate inner ear along corresponding actin filaments. The polyelectrolyte properties of actin filaments explain the reasons why Ca^{2+} ions can form dense "ionic clouds" around these protein filaments with local concentrations of contained ions much higher than in the bulk solution. These Ca^{2+} ions propagate along actin filaments with a velocity proportional to the density of the "ionic cloud", which is substantially greater than the diffusion velocity of free ions on the order of magnitude of cm/s. Importantly, another approach based on polyelectrolyte properties of actin filaments (Hunley et al., 2018) leads to the localized pulses with the velocities on the same order of magnitude. Our concept leads to a mechanism with the detachment rate of adaptation myosin motors in the range of milliseconds as given in Eq. (5.7), which is faster than the rate obtained in the context of the theory established by Vilfan and Duke (2003). Consequently, we have been able to unify the dynamics of adaptation myosin motors and the corresponding transduction channels. This leads to damped oscillations of the transduction channels according to Eqs. (5.10), (5.11), and (5.13). The relaxation rate of these oscillations is on the order of ten milliseconds, which is one order of magnitude longer than the motor's detachment time. This fact justifies our replacement of the explicit function $n_M(t)$ defined by Eq. (5.4) with a characteristic number of motors remaining after rapid partial detachment caused by a fast sweeping movement of the "ionic cloud". On the basis of well–established parameters from experimental data (Martin et al., 2003; Tinevez et al., 2007), we calculated the frequency of these oscillations to be on the order of ten Hertz, which is very close to the available experimental data on the spontaneous oscillations of a hair–bundle in bullfrog saculus (Tinevez et al., 2007).

Finally, we emphasize that in addition to this case where actin filaments guide ionic signals in stereocilia, similar mechanisms can be present in other cellular processes. Namely, calcium signalling plays a very important role in different biological activities. For example, cilia and flagella contain a cylindrical axoneme composed of "9 + 2″ microtubule doublets with dynein motors responsible for relative sliding of adjacent doublets. This process is also regulated by Ca^{2+} ion influx, which might be guided by the correspoding microtubules (Smith, 2002; Doerner et al., 2015). It was also demonstrated that long–range electrostatic interactions between positive segments of dynein motors and negative carboxyl terminal tails of microtubule bring a level of precision to an otherwise noisy dynein stepping process (Li et al., 2016). The influx of Ca^{2+} ions along these microtubules can regulate the amount of dynein sliding and thus control the beating waves of cilia and flagella.

Acknowledgments

This research was financially supported by the Provincial Secretariat for Higher Education and Scientific Research of AP Vojvodina (Project No. 114–451–2708/2016–03), also by the Ministry of Education, Science and Technological Development of the Republic of Serbia (Projects No. OI171009, III43008, and III45010), and by the Serbian Academy of Sciences and Arts. JAT acknowledges funding from NSERC (Canada).

Appendix 1

We consider the case that the influx of Ca^{2+} ions provides locally elevated concentration $\theta(x,t) > \theta_0$, which flows along actin filament in the traveling wave form

$$\theta(x, t) = \theta\left(\frac{x}{L} - v\frac{t}{L}\right), \tag{A.1}$$

where L = 5.4 nm stands for the length of filament's unit and $v \leq v_0$ is the wave velocity. In order to make the master equation dimensionless, it is convenient to introduce new variables and parameters as follows

$$\zeta = \frac{x}{L}; \tau = \frac{t}{T_0}; s = \frac{v}{v_0}; v_0 = \frac{L}{T_0}. \tag{A.2}$$

By analogy with solitonic waves, we postulate that the velocity v of "ionic pulse" is proportional to its density, namely the number of involved Ca^{2+} ions, which is provided by the intensity of the permitted ionic influx through pertaining transduction channel and expressed by θ_M, the maximum of relative concentration of Ca^{2+} ions within "ionic pulse". Further, the form of the traveling wave enables that time and space can be unified with single dimensionless variable φ

$$\theta = \theta(\varphi);\ \varphi = \zeta - s\tau. \tag{A.3}$$

After performing the straightforward transformation as defined above, partial differential equation given by Eq. (3.6) becomes ordinary differential equation of the following form

$$\alpha\frac{d\theta}{d\varphi} + (\beta + \theta)\frac{d^2\theta}{d\varphi^2} + \left(\frac{d\theta}{d\varphi}\right)^2 = 0, \tag{A.4}$$

where the two abbreviations were introduced

$$\alpha = \left(s\frac{\mathrm{I}_0^2}{\eta_0} - \frac{ze\mathrm{LE}}{\lambda}\right)\left[-\frac{k_\mathrm{B}T}{\lambda}2z^2\xi\ln\left(\frac{\delta}{\Delta}\right)\right]^{-1};$$
$$\beta = \left[-2z^2\xi\ln\left(\frac{\delta}{\Delta}\right)\right]^{-1}. \tag{A.5}$$

The order of Eq. (A.4) can be reduced by the standard substitution:

$$\frac{d\theta}{d\varphi} = y(\theta),\ \frac{d^2\theta}{d\varphi^2} = y\frac{dy}{d\theta}. \tag{A.6}$$

This leads to the linear differential equation of first order in the following form

$$(\beta + \theta)\frac{dy}{d\theta} + y = -\alpha. \tag{A.7}$$

The next step is to solve this equation in terms of the following improved boundary conditions in comparison with our previous calculation (Sataric et al., 2015)

$$\text{for}\theta = \theta_0;\ \frac{d\theta}{d\varphi} = 0,$$
$$\text{for}\varphi = 0;\ \theta = \theta_\mathrm{M},$$

where θ_M represents the local maximum of concentration of injected Ca^{2+} ions within "ionic pulse", while θ_0 has the meaning in accordance with Eq. (2.11). After a straightforward calculation and finding the constants of integration from the above conditions, the solution of Eq. (A.7) in the form of an implicit function $\theta(\varphi)$ is found as

$$\alpha\varphi = [\Omega_\mathrm{M} - \theta - (\theta_0 + \beta)\ln(\theta - \theta_0)],\ \Omega_\mathrm{M}{=}\theta_\mathrm{M} + (\theta_0 + \beta)\ln(\theta_\mathrm{M} - \theta_0). \tag{A.8}$$

References

Adamek, N., Coluccio, L.M., Geeves, M.A., 2008. Calcium sensitivity of the cross–bridge cycle of Myo1c, the adaptation motor in the inner ear. Proc. Natl. Acad. Sci. U. S. A. 105, 5710–5715.

Ashmore, J., Avan, P., Brownell, W.E., Dallos, P., Dierkes, K., Fettiplace, R., Grosh, K., Hackney, C.M., Hudspeth, A.J., Jülicher, F., Lindner, B., Martin, P., Meaud, J., Petit, C., Santos Sacchi, J.R., Canlon, B., 2010. The remarkable cochlear amplifier. Hearing Res. 266, 1–17.

Benser, M.E., Issa, N.P., Hudspeth, A.J., 1993. Hair–bundle stiffness dominates the elastic reactance to otolithic–membrane shear. Hear. Res. 68, 243–252.

Beurg, M., Nam, J.H., Chen, Q., Fettiplace, R., 2010. Calcium balance and mechanotransduction in rat cochlear hair cells. J. Neurophysiol. 104, 18–34.

Cantero, M.R., Perez, P.L., Smoler, M., Etchegoyen, C.V., Cantiello, H.F., 2016. Electrical oscillations in two–dimensional microtubular structures. Sci. Rep. 6, 27143.

Cantiello, H.F., Patenaude, C., Zaner, K., 1991. Osmotically induced electrical signals from actin filaments. Biophys. J. 59, 1284–1289.

Ceriani, F., Mammano, F., 2012. Calcium signaling in the cochlea–Molecular mechanisms and physiopathological implications. Cell Commun. Signal 10, 20.

Corey, D.P., Hudspeth, A.J., 1983. Kinetics of the receptor current in bullfrog saccular hair cells. J. Neurosci. 3, 962–976.

Corns, L.F., Johnson, S.L., Kros, C.J., Marcotti, W., 2014. Calcium entry into stereocilia drives adaptation of the mechanoelectrical transducer current of mammalian cochlear hair cells. Proc. Natl. Acad. Sci. U. S. A. 111, 14918–14923.

Dhont, J.K.G., Kang, K., 2010. Electric–field–induced polarization and interactions of uncharged colloids in salt solutions. Eur. Phys. J. E 33, 51–68.

Doerner, J.F., Delling, M., Clapham, D.E., 2015. Ion channels and calcium signaling in motile cilia. eLife 4, 11066.

Gartzke, J., Lange, K., 2002. Cellular target of weak magnetic fields: ionic conduction along actin filaments of microvilli. Am. J. Physiol., Cell Physiol. 283, C1333–C1346.

Holt, J.R., Corey, D.P., 2000. Two mechanisms for transducer adaptation in vertebrate hair cells. Proc. Natl. Acad. Sci. U. S. A. 97, 11730–11735.

Holt, J.R., Gillespie, S.K.H., Provance, D.W., Shah, K., Shokat, K.M., Corey, D.P., Mercer, J.A., Gillespie, P.G., 2002. A chemical–genetic strategy implicates myosin–1c in adaptation by hair cells. Cell 108, 371–381.

Hudspeth, A.J., Choe, Y., Mehta, A.D., Martin, P., 2000. Putting ion channels to work: Mechanoelectrical transduction, adaptation, and amplification by hair cells. Proc. Natl. Acad. Sci. U. S. A. 97, 11765–11772.

Hunley, C., Uribe, D., Marucho, M., 2018. A multi–scale approach to describe electrical impulses propagating along actin filaments in both intracellular and in vitro conditions. RSC Adv. 8, 12017–12028.

Israelachvili, J.N., 1992. Intermolecular and Surface Forces: With Applications to Colloidal and Biological Systems. Academic Press, London.

Janmey, P.A., Slochower, D.R., Wang, Y.H., Wen, Q., Cebers, A., 2014. Polyelectrolyte properties of filamentous biopolymers and their consequences in biological fluids. Soft Matter 10, 1439–1449.

Li, L., Alper, J., Alexov, E., 2016. Cytoplasmic dynein binding, run length and velocity are guided by long–range electrostatic interactions. Sci. Rep. 6, 31523.

Lin, E.C., Cantiello, H.F., 1993. A novel method to study the electrodynamic behavior of actin filaments. Evidence for cable–like properties of actin. Biophys. J. 65, 1371–1378.

Manning, G.S., 2008. Approximate solutions to some problems in polyelectrolyte theory involving nonuniform charge distributions. Macromolecules 41, 6217–6227.

Manning, G.S., 2011. A counterion condensation theory for the relaxation, rise, and frequency dependence of the parallel polarization of rodlike polyelectrolytes. Eur. Phys. J. E 34, 39.

Martin, P., Mehta, A.D., Hudspeth, A.J., 2000. Negative hair–bundle stiffness betrays a mechanism for mechanical amplification by the hair cell. Proc. Natl. Acad. Sci. U. S. A. 97, 12026–12031.

Martin, P., Bozovic, D., Choe, Y., Hudspeth, A.J., 2003. Spontaneous oscillation by hair bundles of the bullfrog's sacculus. J. Neurosci. 23, 4533–4548.

Minoura, I., Muto, E., 2006. Dielectric measurement of individual microtubules using the electroorientation method. Biophys. J. 90, 3739–3748.

Sataric, M.V., Bednar, N., Sataric, B.M., Stojanovic, G., 2009. Actin filaments as nonlinear RLC transmission lines. Int. J. Mod. Phys. B 23, 4697–4711.

Sataric, M.V., Sekulic, D.L., Sataric, B.M., 2015. Actin filaments as the fast pathways for calcium ions involved in auditory processes. J. Biosciences 40, 549–559.

Sekulic, D.L., Sataric, B.M., Zdravkovic, S., Bugay, A.N., Sataric, M.V., 2016. Nonlinear dynamics of C–terminal tails in cellular microtubules. Chaos 26, 073119.

Smith, E.F., 2002. Regulation of flagellar dynein by calcium and a role for an axonemal calmodulin and calmodulin–dependent kinase. Mol. Biol. Cell 13, 3303–3313.

Strzelecka–Gołaszewska, H., Prochniewicz, E., Drabikowski, W., 1978. Interaction of actin with divalent cations. The effect of various cations on the physical state of actin. Eur. J. Biochem. 88, 219–227.

Strzelecka–Gołaszewska, H., Boguta, G., Zmorzynski, S., Moraczewska, J., 1989. Biochemical and theoretical approach to localization of metal–ion–binding sites in the actin primary structure. Eur. J. Biochem. 182, 299–305.

Tang, J.X., Janmey, P.A., 1996. The polyelectrolyte nature of F–actin and the mechanism of actin bundle formation. J. Biol. Chem. 271, 8556–8563.

Tinevez, J.Y., Jülicher, F., Martin, P., 2007. Unifying the various incarnations of active hair–bundle motility by the vertebrate hair cell. Biophys. J. 93, 4053–4067.

Uppalapati, M., Huang, Y.M., Jackson, T.N., Hancock, W.O., 2008. Microtubule alignment and manipulation using AC electrokinetics. Small 4, 1371–1381.

van Netten, S.M., Kros, C.J., 2000. Gating energies and forces of the mammalian hair cell transducer channel and related hair bundle mechanics. Proc. R. Soc. Lond. B 267, 1915–1923.

Vilfan, A., Duke, T., 2003. Two adaptation processes in auditory hair cells together can provide an active amplifier. Biophys. J. 85, 191–203.

Wu, Y.C., Ricci, A.J., Fettiplace, R., 1999. Two components of transducer adaptation in auditory hair cells. J. Neurophysiol. 82, 2171–2181.

Progress in Biophysics and Molecular Biology xxx (2015) 1–13

Contents lists available at ScienceDirect

Progress in Biophysics and Molecular Biology

journal homepage: www.elsevier.com/locate/pbiomolbio

Role of nonlinear localized Ca^{2+} pulses along microtubules in tuning the mechano–sensitivity of hair cells

Miljko V. Sataric [a], Dalibor L. Sekulic [a, *], Bogdan M. Sataric [a], Slobodan Zdravkovic [b]

[a] Faculty of Technical Sciences, University of Novi Sad, Trg Dositeja Obradovica 6, Novi Sad, Serbia
[b] Institute of Nuclear Sciences Vinca, University of Belgrade, Belgrade, Postanski fah 522, Serbia

ARTICLE INFO

Article history:
Received 29 December 2014
Received in revised form
10 July 2015
Accepted 19 July 2015
Available online xxx

Keywords:
Microtubule
Polyelectrolyte
Calcium ions
Hair cells
Nonlinear ionic pulse

ABSTRACT

This paper aims to provide an overview of the polyelectrolyte model and the current understanding of the creation and propagation of localized pulses of positive ions flowing along cellular microtubules. In that context, Ca^{2+} ions may move freely on the surface of microtubule along the protofilament axis, thus leading to signal transport. Special emphasis in this paper is placed on the possible role of this mechanism in the function of microtubule based kinocilium, a component of vestibular hair cells of the inner ear. We discuss how localized pulses of Ca^{2+} ions play a crucial role in tuning the activity of dynein motors, which are involved in mechano–sensitivity of the kinocilium. A prevailing notion holds that the concentration of Ca^{2+} ions around the microtubules within the kinocilium represents the control parameter for Hopf bifurcation. Therefore, a key feature of this mechanism is that the velocities of these Ca^{2+} pulses be sufficiently high to exert control at acoustic frequencies.

1. Introduction

The conspicuous difference between the cochlear and the other hair cells is the presence of kinocilium in the hair bundle on the vestibular and lateral line organ receptor cells, and its absence in the cochlear hair cells (Duvall et al., 1966). Yet the cochlear hair cells always possess the centriole which is the structural equivalent to the basal body of the kinocilium in vestibular hair cells. These centrioles are also present in the human cochlea and this fact raises the generality of the strategy developed for kinocilium.

In most vertebrates the active process originates from active motility of hair cells (Lewis et al., 1985). We here concentrate on the inner ear cells of non–mammalians vertebrates. Each such cell is decorated with a collection of organelle known as the hair–bundle which is a cluster of (20–300) actin filament–filled rods called stereocilia. Stereocilia are arranged in rows of gradually increasing height, like harp or the back plane of piano, and finished with a single cylindrical kinocilium at the tall edge of the hair–bundle, see Fig. 1. Collectively stereocilia and kinocilium form the "hairs" of the hair–bundle (Xue and Peterson, 2006). On the top of each stereocilia there is the transduction channel with a pertinent tension–gated tip links responsible for opening and closing of transduction channels. If a hair–bundle is deflected in the direction towards the kinocilium with stereocilia pivoting at their bases, the tip links get stretched and being connected directly to transduction channels, open them admitting the influx of K^+ and Ca^{2+} ions which penetrate inside stereocilia and kinocilium. This is the crucial mechanism of the process of mechano–sensing in hair cells. The influx of Ca^{2+} ions inside kinocilium and stereocilia is important for subtle regulation of hair cell sensitivity (Beurg et al., 2010; Manley et al., 2004). It was found that molecular motors, such as dyneins in the kinocilium or myosins in the stereocilia, are responsible for the force generations taking part in the amplification of hair–bundle motion (Lumpkin and Hudspeth, 1998). Basically the control of the dynamics of these motors is governed by ATP hydrolysis cycle which is catalyzed by the very local concentration of calcium ions around motors. The kinocilia erect from basal bodies in the vestibular hair cell's epithelial layer through a column of gelatinous layer and stuck in the overlaying otoconical layer, see Fig. 1. Every kinocilium acts as a mechanical relay–lever that transfers movements of the otholitic layer to the stereocilia, whose consecutive deflection modulate mechano–transduction performed by hair cells.

The topological arrangement and polarization of kinocilia within each hair bundle is related to the direction of mechanical displacement of the hair bundle in the course of acoustic

* Corresponding author.
E-mail address: dalsek@uns.ac.rs (D.L. Sekulic).

http://dx.doi.org/10.1016/j.pbiomolbio.2015.07.009
0079-6107/

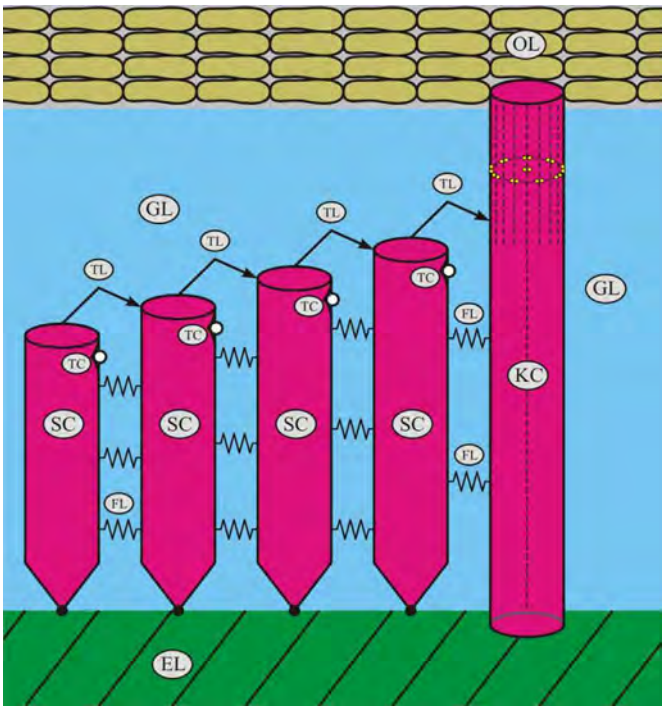

Fig. 1. The sketch of a hair bundle of vestibular hair cell consists of a row of stereocilia (SC) interconnected by filamentous links (FL) and finished with a single kinocilium (KC). The tip links (TL) and pertaining transduction channels (TC) are responsible for ionic currents. Epithelial layer (EL), otholitic layer (OL) and gelatinous layer (GL) are also depicted.

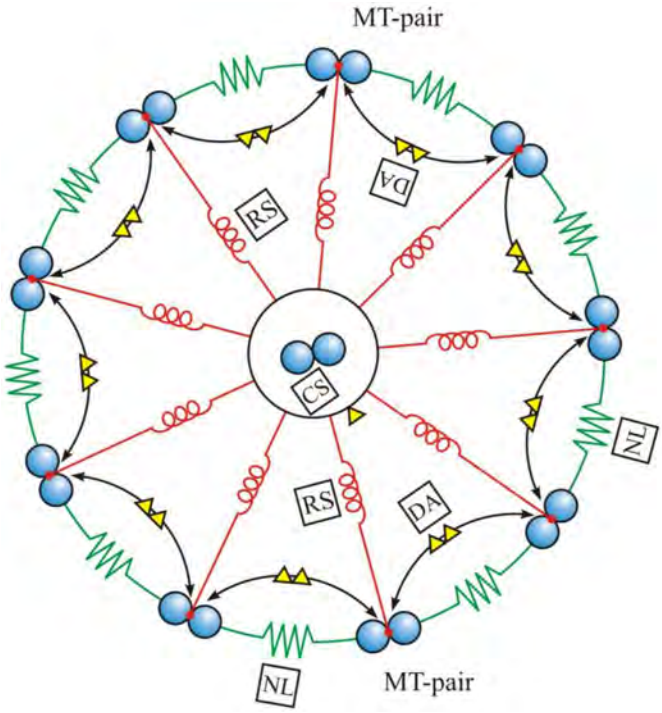

Fig. 2. The cross–sectional view of a kinocilium with "9 + 2" axoneme tightened with 9 radial spokes (RS), 9 nexin links (NL) and changeable number of dynein arms (DA) and two central single MT (CS).

stimulation of the auditory cell (Lowenstein et al., 1964). It was found that primary cilia and planar cell polarity proteins both essentially contribute to auditory cell polarization (Axelrod, 2008). In the process of embryonic developing phase of cochlea in mouse, it was revealed that the kinocilium migrates by Brownian motion probably using the treadmilling dynamics of constituent microtubules (Lepelletier et al., 2013). The uniform orientation of auditory hair cells is the consequence of mentioned planar cell polarity which is microtubule–mediated development (Sipe et al., 2013).

The kinocilium is composed of a microtubular cylindrical scaffold, a "9 + 2" axoneme, comprising nine peripheral doublet microtubules (MTs) connected with two central single MT by radial spokes, see Fig. 2. Importantly for the model considered here, the peripheral MT doublets link to each other through fixed nexin links, and are additionally tightened by the set of movable dynein motor proteins called dynein arms, arranged in a pretty uniform way when a kinocilium is in equilibrium. These dynein arms play the central role in response to calcium ions considered here as catalyzers. Radial spokes consist of some 17 different proteins still not completely characterized, but important part of them are the calmodulin and ubiquitous dynein light chain LC8 (Yang et al., 2001). The deflection of kinocilium pulls complete hair–bundle of stereocilia, since they are interconnected by structures called filamentous links, see Fig. 1. Five types of these links have been identified and described in that context (Bashtanov et al., 2004). Biomechanics of kinocilium fundamentally depends on the elastic properties of constituent MTs and the controlling role of dynein arms. Both of these factors are catalyzed by the impact of Ca^{2+} ions, which dynamics was elaborated by Kis et al. (2002).

The historical path in understanding of subtle interplay between MTs and Ca^{2+} ions is pretty long. The oldest seminal paper concerning the role of ions in dynamics of long polymers (Kuhn, 1949) indicated that three–dimensional network containing ordered filaments of polyacrylic acid would shrink or stretch reversibly upon alternating addition of negative and positive ions in water solution in which they are suspended. This effect was later exploited in explaining the electric capacity of α–β tubulin heterodimers, the basic structural units of MTs. Also, the roles of MTs in sensory transductions were examined in early stages (Moran and Varela, 1971; Atema, 1973). These experimental evidences revealed that MTs are indispensable components in the processes of mechano–transductions. Thus, the ciliary and microtubular apparatus in sensory cells receive the environmental information (signal) and transmit it via collectively excited conformational changes in MTs. It has been demonstrated (Sataric et al., 1993; Sataric and Tuszynski, 2003) that MTs can play such transduction roles as being capable of specific type of wave propagation. It was shown that both gross mechanical deformation and local chemical distortion (conformation) caused by GTP hydrolysis can act as a trigger to launch a soliton wave along pertinent MT.

In microtubule theory of sensory transduction (Atema, 1973), it was emphasized that the receptor cells of the sensory systems such as olfactory receptors, photoreceptors, mechanoreceptors (hair cells) all contain ciliary structure with "9 + 2" arrangement of MTs, which is also the characteristics of motile cilia and flagella. Earlier experimental studies (Solomon, 1977) indicated that Ca^{2+} ions have high– and low–affinity sites on tubulin heterodimers. It was noticed that Ca^{2+} ions inhibit MT polymerization and also cause destabilization of MT. Low–affinity sites play an important role for polyelectrolyte model of MT, which was established several decades later (Sataric et al., 2009b; Sekulic et al., 2011). Karr et al. (1980) pointed out that Ca^{2+} ions induce rapid depolymerization of MTs, but it was stressed that this is primarily the endwise depolymerization. If the ends of MTs are protected from Ca^{2+} ions by the end–binding proteins (Grimaldi et al., 2014), it is expectable

Please cite this article in press as: Sataric, M.V., et al., Role of nonlinear localized Ca^{2+} pulses along microtubules in tuning the mechano–sensitivity of hair cells, Progress in Biophysics and Molecular Biology (2015), http://dx.doi.org/10.1016/j.pbiomolbio.2015.07.009

that these ions involved in localized pulses should not destabilize the MTs within a kinocilium. But instead their catalytic role seems to have decisive impact for the tuning of mechano–sensitivity of hair cells. Later, Serrano et al. (1986) revealed that two Ca^{2+} strong–binding sites are located in the tubulin tails of both tubulin subunits. This finding also had the significance for establishment of the biophysical model which mimics the signaling behavior of a MT in solution.

Over the last two decades or so, the electrical signaling along MTs has been studied using both experimental and theoretical approaches. The initial motivation for the theoretical modeling of signaling function of the MT was based on the fact that direct experimental observations (Priel et al., 2006; Lin and Cantiello, 1993) revealed that MTs, as well as actin filaments, act as electrical transmission lines for ion flows along their lengths. In the context of these findings, it was suggested (Tuszynski et al., 2004; Sataric et al., 2009b) that so called condensed ionic clouds around these filaments could serve as the conductive medium for stronger electrical coupling. The derivative calculations of this biophysical model are consistent with the experimental observations for ionic conduction along MTs. Interestingly the experimental data demonstrated that the number of localized ionic waves along actin filament (Lin and Cantiello, 1993) is increased with increasing of their velocities as the input voltage pulse increases. Even more important in the case of MTs (Priel et al., 2006), the ionic current is being amplified exhibiting some kind of transistor effect!

On the other hand, the main reason for the establishing of the discussed biophysical model was the fact that the impact of Ca^{2+} ions on the striking sensitivity and frequency selectivity by the mechano–receptive hair cells is hardly to be justified by simple diffusion mechanism. Experimental results (Beurg et al., 2010) clearly showed that the largest current through mechano–-transducer channel in rat cochlear hair cell is of the order of 4.2 nA. But the most part of it is carried by K^+ ions and only 0.2% of total amount is carried by calcium ions, so the peak Ca^{2+} current is just of about 7 pA. If such a small current should cover all volume of hair–bundle below this channel, it should take a few seconds since the bulk diffusion of ions has the velocity of the order of 2 μm/s. If the time for Ca^{2+} extrusion from hair–bundle is added, it is hardly to expect that this could control the fast acoustic frequencies that should be detected. But mentioned experimental assay (Beurg et al., 2010) reveals that mechano–transduction currents displayed fast adaptation with submillisecond time constant. These fast local pulses confined along MTs and actin filaments could meet the posed tasks. It is reasonable to expect that negatively charged surface of MTs and actin filaments primarily attract divalent Ca^{2+} ions. Therefore Ca^{2+} ions dominate ionic clouds and on the basis of nonlinear polyelectrolitic features of MTs, it was possible to establish an adequate biophysical model which follows. The scenario arising from recently proposed model of MTs as nonlinear transmission lines (Sekulic et al., 2011), as well as from similar models developed for actin filaments (Tuszynski et al., 2004; Sataric et al., 2009a), is very appealing and offers a plausible option to fill the gap in still uncompleted puzzle of hearing mechanism.

The paper is organized as follows:

In Section 2, we discuss the current understanding of polyelectrolyte characteristics of MTs which are the basis for their nonlinear transmission line features. There we describe the origin of the basic nanoscale electric elements and estimate the corresponding parameters, stressing the particular importance of tubulin C–termini in establishing the nonlinear character of ionic conduction along MTs. Further, we provide an overview of biophysical model for Ca^{2+} signaling along kinocilium's MTs. Also, the current knowledge of microtubule–associated proteins is given in outline.

In Section 3, we briefly consider the mathematical details of ionic conductivity along MT. In line with this, the corresponding nonlinear differential equation and its particular solution describing the localized electric current of Ca^{2+} ions and accompanying voltage along a MT are presented.

In Section 4, we analyze how these localized nanocurrents of Ca^{2+} ions can control and tune the dynein motor–driven oscillations of pertaining kinocilium in the context of self–tuned auditory sensitivity.

Section 5 provides discussion and conclusions.

2. Ca^{2+} signaling via kinocilial microtubules

MTs are self–assembling biological nanotubes that have outstanding mechanical properties exhibiting high resilience and stiffness, which allow them to accomplish multiple tasks in living cells (Amos and Amos, 1991). They are hollow cylinders with respective external and internal diameters of 25 nm and 15 nm, composed of mostly 13 parallel loosely connected protofilaments, built of series of α–β tubulin heterodimers (TD), see Fig. 3. The tubular shape of the MT is an economical way to make a rigid structure with a minimum protein mass. For example, the mass per unit length of a MT is approximately 10–fold higher than that of actin filament but MT is over 100 times more resistant to bending. Besides MTs which are present in the majority of eukaryotic cells, actin filaments are also important component of cellular cytoskeleton. Polymerizing MT from a helical lattice pattern which always has left–handed chirality, but it is still not known why so.

Experimental observations (Kis et al., 2002; Guo et al., 2007) and theoretical considerations (Shen, 2011) suggest that single MT, as well as bundles of MTs such as kinocilium, under radial loads exhibit buckling into the wavelike shapes, on the basis of shear deformations of constituent protofilaments. These mechanical properties are of great importance in MT performances involved in kinocilium dynamics in active hair–bundle motility. It is important to stress that Ca^{2+} ions also have an impact on these mechanical features of MTs (Kis et al., 2002). In the polyelectrolyte framework, similar role of actin filaments in stereocilia dynamics can be expected.

Each TD is decorated with two highly flexible C–terminal tails (TTs) that are negatively charged and can extend up to 4.5 nm from tubulin dimer surface, see Fig 4. Every TT can stretch or shrink depending on amount of net negative charge on it. Besides, it can tilt under the action of thermal fluctuations or local electric potential. These properties are of basic importance for the model discussed below. Sui and Downing (2010) pointed out that low resistance of MTs to lateral deformation is an intrinsic property which is crucial for keeping their structural integrity during bending or buckling.

2.1. Microtubules and microtubule–associated proteins (MAPs)

Several types of proteins called MAPs efficiently stabilize MTs against depolymerization. They tend to have repeating domains, which allow each MAP molecule to associate with more than one TD from the same protofilament. The binding of these structural MAPs is in turn controlled by kinases and phosphatases (Cassimeris and Spittle, 2001). Each MAP–tau is extended molecule possessing a microtubule–binding domains and one N–terminal “projection” domain that extends from the outer surface of the MT, see Fig 5. The size of this projection domain provides spacing between MTs containing MAPs in a way that they repel instead of crosslink neighboring MTs. In that respect these MAPs assist kinesin and dynein motor traffic by creating enough space around pertaining

Please cite this article in press as: Sataric, M.V., et al., Role of nonlinear localized Ca^{2+} pulses along microtubules in tuning the mechano–sensitivity of hair cells, Progress in Biophysics and Molecular Biology (2015), http://dx.doi.org/10.1016/j.pbiomolbio.2015.07.009

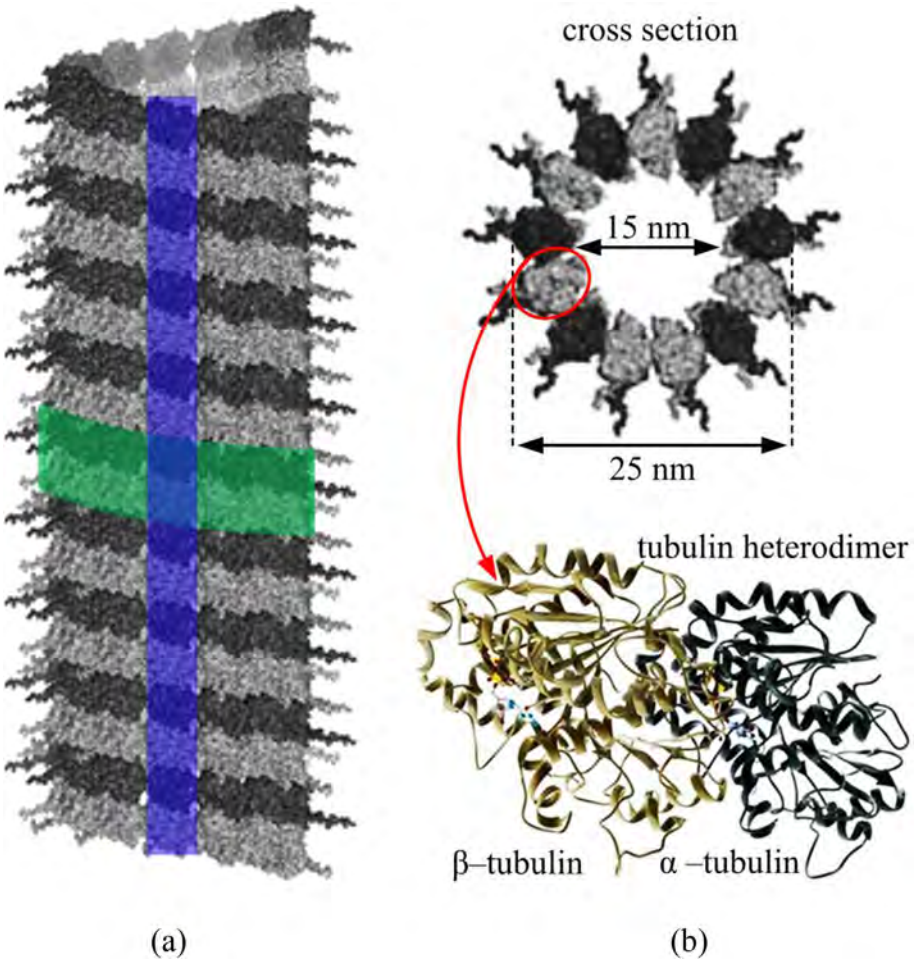

Fig. 3. (a) The MT hollow cylinder of 13 parallel protofilaments in helical left–handed chirality. The protofilament is blue and left–handed chirality is indicated by green color. (b) The cross–sectional view of 13 protofilaments with tubulin tails and denoted characteristics dimension (outer and inner diameters of 25 nm and 15 nm, respectively). The structure of tubulin heterodimer with α–helices which are dominant is displayed down.

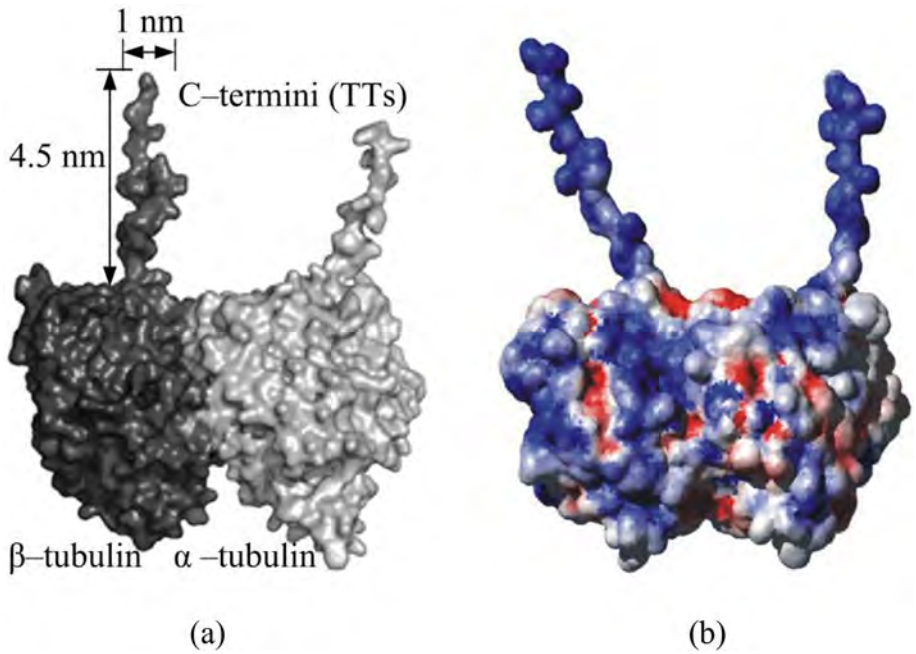

Fig. 4. (a) The magnified topology of a tubulin heterodimer with tubulin tails whose dimensions are: the maximum length of 4.5 nm and the diameter of 1 nm. (b) Charge distribution on the surface of a tubulin heterodimer. Blue and red denote the negative and positive charges, respectively.

Please cite this article in press as: Sataric, M.V., et al., Role of nonlinear localized Ca^{2+} pulses along microtubules in tuning the mechano–sensitivity of hair cells, Progress in Biophysics and Molecular Biology (2015), http://dx.doi.org/10.1016/j.pbiomolbio.2015.07.009

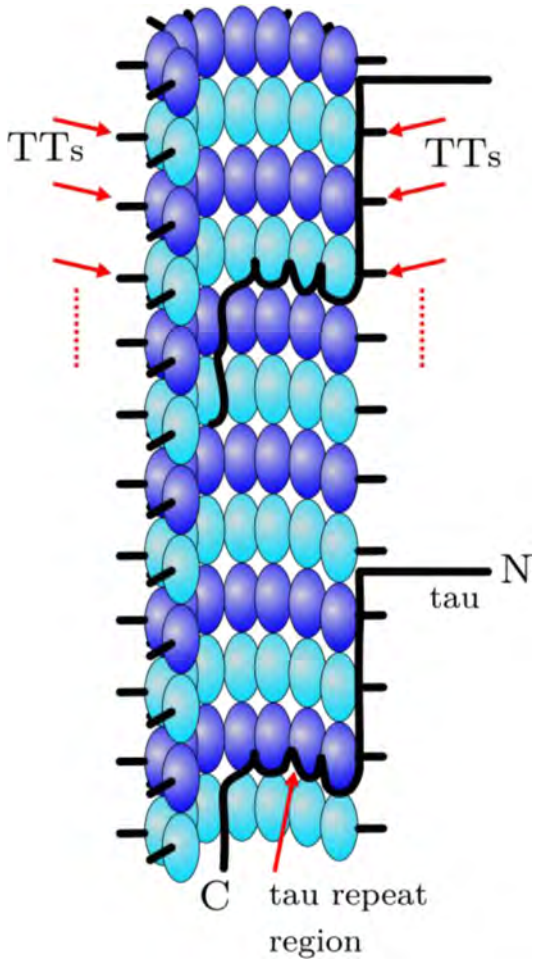

Fig. 5. Model of MAPs from the tau protein family interacting with a MT. Illustration represents the N–terminal domains of tau molecules whose C–terminal segments, including the repeat motifs bind strongly to the inside of the MT. The tubulin tails (TTs) are also depicted. The protofilaments free of MAPs are candidates for Ca^{2+} flow along MT.

MTs (Chen et al., 1992). It seems that these motor proteins move past MAPs projection domain without difficulty choosing path along protofilaments free of MAPs. The same behavior holds for the oscillations of C–terminal tails. In the framework of established model which is discussed further, the presence of MAPs dose not interfere with ionic currents along "clean" protofilaments. These protofilaments are the pathways of the least resistance for this kind of fast distribution of Ca^{2+} ions along MTs.

MAPs are primarily implicated in development and maintenance of stability of neuronal axons and dendrites. To investigate how MAPs stabilize MTs, Al–Bassam et al. (2002) calculated 3D maps of MTs fully decorated with MAP2c or tau proteins. These results provided strong evidence that these proteins lie along the ridges of protofilaments, but not in clefts between them. The MAP2 is not only the microtubule–associated protein but also binds to other structures or molecules through its "projection" domain. It was shown that projection region also contains three calcium–binding sites (Hernfindez et al., 1988). This suggests that a part of Ca^{2+} ions flowing along a MT can be utilized by MAP2 molecules in the context of their implication in MT functions. Two distinct effect of Ca^{2+} on MAP2 are taking place; the first one in the terms of calmodulin affects to the tubulin–binding domain of MAP2, and second one, direct, on the tubulin tail domain as mentioned before. It seems that the complex role of Ca^{2+} ions has the following character (Serrano et al, 1986): if the efflux of Ca^{2+} ions activate calmodulin molecules, which hinder the interactions of MAP2 with MTs, then this lead to exposing tubulin tails to Ca^{2+}. As a result MTs can start to depolymerize endwise. In that respect the association of MAP2 with MTs is very desirable. The role of MAP2 in cochlear inner hair cells of rat was experimentally examined by Ladrech and Lenior (2002). The studies of the role of myosin VIIA motor in sensory hair cells (Todorov et al., 2001) also revealed that its interaction with calmodulin and MAP–2B is regulated by Ca^{2+} ions, which also could be supplied by localized pulses conveyed by actin filaments as polyelectrolytes.

2.2. Polyelectrolyte features of microtubules in the context of Ca^{2+} counterions

Both the outer surface of a tubulin dimer and a tubulin tail are mostly negatively charged due to the lack of protons released from pertaining amino acids. These charged structures are used to be called polyons as being conceived as the huge ions. The overall negatively charged surface for a MT is with an average linear charge density of 52.5 e (e is elementary charge equal to 1.602×10^{-19} C) per dimer or total MT linear charge density of 85 e/nm (Minoura and Muto, 2006). The small radius of surface curvature of tubulin dimers and especially tubulin tails causes strong local electrical fields, implying that MTs could be proper candidates for true polyelectrolytes. They attract a fraction of surrounding primarily divalent cations, forming positive condensed ionic cloud localized around the MT's landscape. This is especially the case with Ca^{2+} ions for which TD has several low–affinity binding sites. In the presence of an applied voltage, the loosely held ionic cloud is free to migrate along MT creating an ionic flow and giving rise to ionic conduction (Priel et al., 2006). We here pay attention on the divalent Ca^{2+} ions as counterions for MTs in kinocilia.

Another very important feature of MTs is ferroelectricity, the ability to spontaneously generate dipole moments (Tuszynski et al., 2008). Using an atomic resolution structure of tubulin dimer in conjunction with molecular dynamics simulations, Tuszynski et al. (2005) discovered that every tubulin dimer represents a mesoscopic dipole with magnitude of electric dipole moment of 1740 Debye. As being the collection of many such dipoles oriented in the same direction, MT represents a giant dipole with one positive and the opposite negative end, thus creating electric field in between. This capability of creating intrinsic electric field serves as a biophysical basis for modeling signaling along MTs.

In accordance with Manning approach (Manning, 1993, 2009, 2011), besides the positive ionic cloud formed around MT, the negative ions of cytosol are repelled beyond the distance called the Bjerrum length (l_B), defined by the balance between Coulomb forces of pertaining counterions and the actual thermal energy:

$$\frac{ze^2}{4\pi\varepsilon_r\varepsilon_0 l_B} = k_B T. \tag{1}$$

At the physiological temperature $T = 310$ K, taking $z = 2$ for Ca^{2+} ions, $e = 1.6 \times 10^{-19}$ C, $\varepsilon_r = 80$, $\varepsilon_0 = 8.85 \times 10^{-12}$ F/m and $k_B = 1.38 \times 10^{-23}$ J/K, one gets

$$l_B = 1.34 \text{ nm}. \tag{2}$$

This is the thickness of "depleted layer" sandwiched between these two "charged plates" around the MT, see Fig. 6. The main criterion for a thin polymer to be polyelectrolyte is that the radius of its surface curvature should be of the same order of magnitude as the Debye length (l_{Db}) defined as follows

Please cite this article in press as: Sataric, M.V., et al., Role of nonlinear localized Ca^{2+} pulses along microtubules in tuning the mechano–sensitivity of hair cells, Progress in Biophysics and Molecular Biology (2015), http://dx.doi.org/10.1016/j.pbiomolbio.2015.07.009

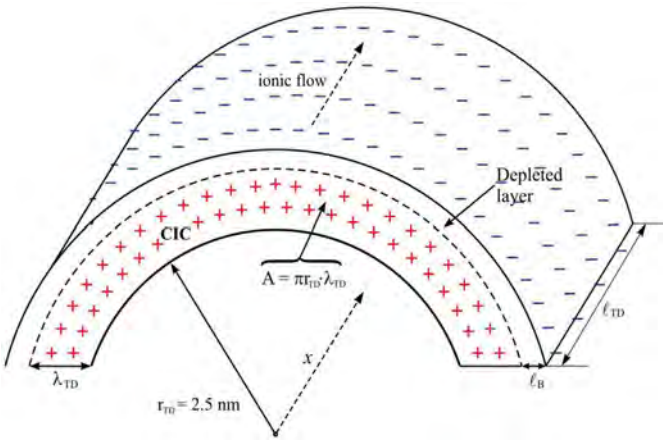

Fig. 6. Schematic illustration of an outer part of tubulin heterodimer with its condensed ionic cloud (CIC), depleted layer and the geometry of a "coaxial cylinder" with the dimensions necessary for calculation of elementary unit capacitance. *A* is the cross section area of a CIC around tubulin dimer.

$$l_{Db} = (8\pi n l_B)^{-1/2}, \tag{3}$$

where n stands for the global concentration of ions in endolymph. In the typical endolymph the concentration of K^+ ions is 160 mM together with 20 μM of Ca^{2+} ions (Beurg et al., 2010). Including these values in concentration n, the corresponding Debye length amounts:

$$l_{Db} \approx 1.4 \text{ nm}. \tag{4}$$

The radius of the outer tubulin dimer curvature is about $r_{TD} = 2.5$ nm, while the radius of a tubulin tail is $r_{TT} = 0.5$ nm, providing that the polyelectrolyte criterion is safely met for both. For example, the DNA with $r_{DNA} = 3.4$ nm is commonly considered as real polyelectrolyte. Also, the important parameter is the polyon charge spacing b which is estimated for one tubulin dimer of the length $l_{TD} = 8$ nm to be:

$$b = \frac{l_{TD}}{52e} = 0.15\ \frac{\text{nm}}{e}. \tag{5}$$

Since the screening length $l_{Db} = 1.4$ nm is much longer than b, it additionally guaranties that MT can be safely treated as true polyelectrolyte. For example, for DNA parameter b is 0.17 nm/e, which is almost the same as in Eq. (5).

In establishing the adequate biophysical model for MTs as ionic conductors, it is necessary to take into account both their geometrical structure and electrostatic properties. As reported (Sataric et al., 2009b), the geometric features of tubulin dimer and C–terminal tails can be reduced to pure cylindrical forms without loss of generality. In this case, the outer part of a tubulin dimer is considered as a half cylinder of radius $r_{TD} = 2.5$ nm and the length $l_{TD} = 8$ nm, see Fig 6. The thickness of condensed ionic cloud around the rodlike filamentous polyon of radius r is given by the expression (Dhont and Kang, 2011)

$$\lambda = \mathscr{A}(r l_{Db})^{1/2}, \tag{6}$$

with the dimensionless parameter $\mathscr{A} \approx 1$. Thus, the corresponding values regarding MT are as follows:

$$\lambda_{TD} = 1.87 \text{ nm}; \quad \lambda_{TT} = 0.83 \text{ nm}. \tag{7}$$

The depleted layer between ionic cloud and repelled anions, in terms of present water molecules, plays the role of a dielectric between charged plates in coaxial cable, see Fig. 6.

Further on, between neighboring tubulin dimers within a MT there are two kinds of nano–pores, which can permit the ions from pertaining condensed ionic cloud to leak into the MT lumen (Freedman et al., 2010), see Fig. 7. These pores also have important role in modeling signalling along MTs.

2.3. Characterization of a microtubule as nonlinear transmission line for Ca^{2+} signaling

Bearing in mind the condensed ionic cloud localized around the MT's cylinder, this macromolecular structure made from polymerized tubulin may act as biological "wire" (Friesen et al., 2015), which can be modeled as nonlinear transmission line (Sataric et al., 2009b; Sekulic et al., 2011). In this section, we discuss the origin and values of electrical components at nanoscale that make up transmission line model which mimics the behavior of MT in solution. Due to its symmetry, it is plausible to consider just one of 13 MT protofilaments directed along x–axis and to introduce the so called elementary unit, which is a single tubulin dimer with its two tubulin tails and two nano–pores, see Figs. 4b and 7.

Both TD and TTs contribute to the capacitance of this elementary unit. The contribution of a tubulin dimer is determined as half–cylindrical capacitor that has the following value:

$$C_{TD} = \frac{\pi \varepsilon_r \varepsilon_0 l_{TD}}{\ln\left(1 + \frac{l_B}{r_{TD}^{CIC}}\right)} = 0.66 \times 10^{-16} \text{ F}, \tag{8}$$

where the parameter is $r_{TD}^{CIC} = r_{TD} + \lambda_{TD} = (2.5 + 1.87)$ nm $= 4.37$ nm, representing the outer radius of respective ionic cloud, see Fig. 6, while the other parameters are already mentioned. Similarly, taking an extended tubulin tail as a smaller cylinder with $r_{TT}^{CIC} = r_{TT} + \lambda_{TT} = (0.5 + 0.83)$ nm $= 1.33$ nm, see Fig. 8, and calculating the corresponding effective length of the part of tubulin tail not plunged in λ_{TD} when tubulin tail stands vertically

$$l_{TT}^{eff} = l_{TT} - \lambda_{TD} = (4.5 - 1.87) \text{ nm} = 2.63 \text{ nm}, \tag{9}$$

and its capacitance is defined by expression

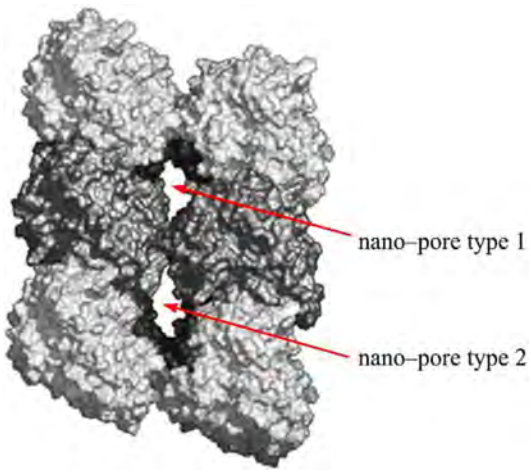

Fig. 7. The magnified view of two short sections of neighboring protofilaments of MT with two pertaining nano–pores penetrating into MT lumen. These pores are pretty different in geometry and structure so their conductances differ remarkably.

Please cite this article in press as: Sataric, M.V., et al., Role of nonlinear localized Ca^{2+} pulses along microtubules in tuning the mechano–sensitivity of hair cells, Progress in Biophysics and Molecular Biology (2015), http://dx.doi.org/10.1016/j.pbiomolbio.2015.07.009

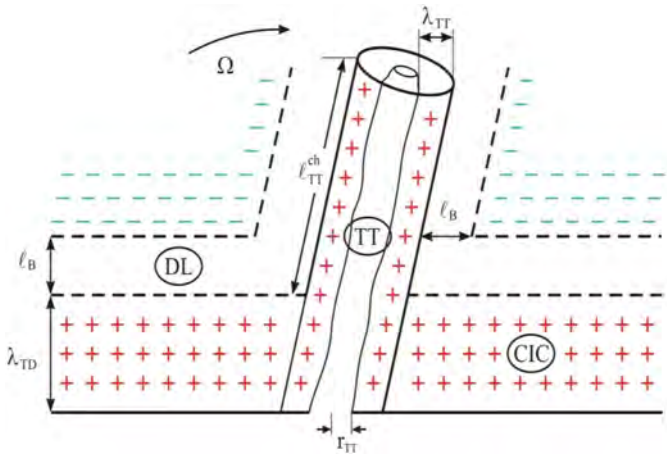

Fig. 8. The cylindrical geometry of charge distribution around a tubulin tail (TT) including the geometry of adjacent tubulin dimer. The dimensions λ_{TD}, λ_{TT} and l_B are clearly depicted. l_{TT}^{eff} is the effective length of a stretched tubulin tail. (DL) is depleted layer and (ClC) condensed ionic cloud. The tilt of a tubulin tail with the frequency Ω causes the change of its effective length due to the plunging of the part of condensed ionic cloud of a tubulin tail into the condensed ionic cloud of tubulin dimer.

$$C_{TT}^{(0)} = \frac{2\pi\varepsilon_r\varepsilon_0 l_{TT}^{eff}}{\ln\left(1+\frac{l_B}{r_{TT}^{ClC}}\right)} = 0.17\times10^{-16}\ \mathrm{F}. \tag{10}$$

Since two tubulin tails pertain to each tubulin dimer, and keeping in mind that the capacitances C_{TD} and $2C_{TT}^{(0)}$ are in parallel arrangement, it implies that total maximal static capacitance of an elementary unit can be estimated as the simple sum of above components

$$C_0 = C_{TD} + 2C_{TT}^{(0)} = 1\times10^{-16}\mathrm{F}. \tag{11}$$

It was emphasized that tubulin tails are negatively charged and very flexible with respect to variation in the amount of their charge. It means that in the case where there is no counterions condensed on it, the tubulin tail is maximally stretched due to the repulsion of intrinsic negative charges on its surface. When the concentration of ionic cloud increases this repulsion weakens and tubulin tail shrinks in proportion with the increase of positive local voltage v at the site of tubulin tail. This effect is in full agreement with early findings presented by Kuhn (1949). Sekulic et al. (2011) have pointed out that these changes are slightly different for structurally different α and β–type of tubulin tails. This circumstance is captured by introducing the reduced parameter of change of tubulin tail capacitance b_r as follows (b_α, b_β have the dimensions of inverse voltage):

$$b_r = \frac{b_\alpha b_\beta}{b_\alpha + b_\beta}. \tag{12}$$

The corresponding change of both tubulin tails capacitance $\Delta C_{TT}^{(1)}$ can accordingly be expressed as linear function of voltage with opposite sign (positive voltage diminishes capacitance and vice versa)

$$\Delta C_{TT}^{(1)} = -2C_{TT}^{(0)} b_r v. \tag{13}$$

The second component of variable capacitance of tubulin tails is caused by their tilt displacement, as shown in Fig. 8. The variation of the effective length of a tubulin tail (l_{TT}^{eff}) depends on its part which is additionally plunged into the ionic cloud of tubulin dimer with the depth λ_{TD}. If two tubulin tails oscillate with frequency Ω according to Marder (2000), the change of effective length has the form:

$$\Delta l_{TT}^{eff} = -2\lambda_{TD}\sin[\Omega(t-t_0)]. \tag{14}$$

This effect can be considered as electro–mechanical ratchet mechanism, since the electrostatic potential around tubulin tails is asymmetric thus causing that the thermal noise is forcing, instead of damping these small oscillations of tubulin tails (Hanggi et al., 2005). Since the frequency Ω is much less than the inverse charging time of the elementary unit capacitor due to damping effect of surrounding cytosol affecting tilt of tubulin tails, then the linearization of expression given by Eq. (14) makes sense

$$\Delta l_{TT}^{eff} = -2\lambda_{TD}\Omega(t-t_0). \tag{15}$$

Thus the pertaining change of capacitance of an elementary unit due to above dynamics of tubulin tails reads

$$\Delta C_{TT}^{(2)} = -2C_{TT}^{(0)}\Gamma\Omega(t-t_0), \tag{16}$$

where dimensionless parameter $\Gamma = \lambda_{TD}/l_{TT}$ represents the relative length.

Including all elaborated contributions of Eqs. (11), (13) and (16), the charge of an elementary unit can be eventually expressed in the following essentially nonlinear shape with respect to the voltage v, and being a linear function of time:

$$Q = C_0[1-\Gamma_0\Omega(t-t_0) - b_0 v]v, \tag{17}$$

where new abbreviations were given in explicit forms

$$\Gamma_0 = \frac{2C_{TT}^{(0)}}{C_0}\Gamma = 0.52\Gamma; \quad b_0 = \frac{2C_{TT}^{(0)}}{C_0}b_r = 0.52 b_r. \tag{18}$$

According to Gauss' law the voltage v depends on the local charge density created by Ca^{2+} counterions restricted around respective elementary unit and superimposed with intrinsic MT voltage as giant dipole.

In analysis of ohmic resistance of an elementary unit (Sataric et al., 2009b), it was determined that the ionic current leaking through the depleted layer is negligible and that it is necessary to consider the main stream in parallel with the MT axis only. This stream is charging elementary unit capacitors and partly leaking through nano–pores into MT lumen. In that respect, *in silico* estimation of respective resistivity published by Freedman (Freedman et al., 2010) is adopted as follows:

$$R_0 = 6.2\times10^7\ \Omega. \tag{19}$$

In the order hand, the conductance of both nano–pores is given as a sum of pretty different components reflecting difference in two types of nano–pores (Freedman et al., 2010)

$$G_p = G_1 + G_2 = (2.93+7.8)\mathrm{nS} = 10.7\times10^{-9}\ \mathrm{S}, \tag{20}$$

with corresponding resistivity

$$R_p = \frac{1}{G_p} = 9.3\times10^7\ \Omega. \tag{21}$$

3. The biophysical model of a microtubule as a nonlinear transmission line for Ca^{2+} signaling

Following the estimations for the components of elementary electric unit, it was possible to establish an ideal periodic electric

Please cite this article in press as: Sataric, M.V., et al., Role of nonlinear localized Ca^{2+} pulses along microtubules in tuning the mechano–sensitivity of hair cells, Progress in Biophysics and Molecular Biology (2015), http://dx.doi.org/10.1016/j.pbiomolbio.2015.07.009

circuit which simulates the single protofilament of a MT as a long ladder network composed of repeating lumped sections of identical elementary units as depicted in Fig. 9. In such scenario the longitudinal ionic current flows through the series of identical resistors each with ohmic resistance R_0. The nonlinear capacitor of an elementary unit at the position n has the charge Q_n expressed by Eq. (17) and is posed in parallel with total resistance R_p of both nano−pores expressed by Eq. (21). The discrete values of current i_n are accompanied by the voltage v_n. Since the bulk cytosol and MT lumen can be considered as grounded, the Kirchhoff's law for this discrete network simply reads (Sekulic et al., 2011)

$$\left.\begin{aligned} i_n - i_{n+1} &= \frac{\partial Q_n}{\partial t} + \frac{v_n}{R_p}, \\ v_{n-1} - v_n &= R_0 i_n. \end{aligned}\right\} \tag{22}$$

Taking the time derivative of Eq. (17) and inserting it in first of Eq. (22), it leads to the system of equations describing the ionic current within the condensed ionic cloud of that way established transmission line

$$\left.\begin{aligned} i_n - i_{n+1} = C_0\frac{\partial v_n}{\partial t} - C_0\Gamma_0\Omega v_n \quad & -C_0\Gamma_0\Omega(t-t_0)\frac{\partial v_n}{\partial t} \\ & -2b_0C_0v_n\frac{\partial v_n}{\partial t} + \frac{v_n}{R_p}, \\ v_{n-1} - v_n = R_0 i_n. & \end{aligned}\right\} \tag{23}$$

Instead of two unknown functions (i_n, v_n), it is convenient to introduce just one auxiliary function $u_n(x, t)$, where x means the distance along transmission line network (the protofilament), and t stands for time

$$u_n(x,t) = Z^{1/2} i_n = Z^{-1/2} v_n. \tag{24}$$

The total impedance of an elementary unit is given by an appropriate expression (Sekulic and Sataic, 2015)

$$Z = R_0 + \left(\frac{R_p}{1+\omega_0^2 C_0^2 R_p^2}\right)\left(1+\omega_0^2 C_0^2 R_p^2\right)^{1/2}. \tag{25}$$

Here, the parallel arrangement of C_0 and R_p coupled in the series with R_0 has taken into account.

3.1. The continuum approximation version leads to localized nonlinear Ca^{2+} pulses

Since the discrete voltage v_n and the current i_n change gradually from an elementary unit to its neighbors, it is plausible to expand the discrete function $u_n(x, t)$ in continuum approximation applying Taylor series with respect to a small parameter l_{TD} (l_{TD} = 8 nm). Then using the traveling−wave form of this function $u_n(x, t) = u(x-vt)$, it is possible to go on to dimensionless space and time variables (ξ, τ), and relative wave's velocity$s = v/v_0 < 1$, on a standard way:

$$\xi = \frac{x}{l_{TD}} - \tau; \quad \tau = s\frac{t}{T_0}; \quad v_0 = \frac{l_{TD}}{T_0}, \tag{26}$$

where v_0 is the characteristic cut−off velocity. The characteristic time of charging (discharging) of an elementary unit capacitor is defined as usual by

$$T_0 = R_0 C_0. \tag{27}$$

By taking the parameters from Eqs. (11) and (19), the following estimations are obtained:

$$T_0 = 6.2\times10^{-9}\text{s}; \quad v_0 = \frac{8\times10^{-9}\text{m}}{6.2\times10^{-9}\text{s}} = 1.29\text{m/s}; \quad \omega_0 = \frac{2\pi}{T_0} = 1.01\times10^{9}\text{s}^{-1}. \tag{28}$$

According to Eq. (25) and in terms of Eqs. (11), (19), (21) and (28), the value of elementary impedance Z is estimated at:

$$Z = 1.55\times10^{8}\Omega. \tag{29}$$

The corresponding phases lag of voltage versus current amounts 1.19 radians.

After completing the mentioned expanding procedure (Sekulic et al., 2011), one eventually gets the nonlinear partial differential equation:

$$\frac{\partial u}{\partial\tau} + \beta\frac{\partial^3 u}{\partial\xi^3} + \alpha u\frac{\partial u}{\partial\xi} + \gamma(\xi)\frac{\partial u}{\partial\xi} + \delta u = 0, \tag{30}$$

where the set of abbreviations are arranged as follows:

$$\left.\begin{aligned} &\alpha = \frac{2Z^{3/2}b_0C_0s}{T_0\left(\frac{ZC_0s}{T_0}-2\right)}; \quad \beta = \frac{1}{3\left(\frac{ZC_0s}{T_0}-2\right)}; \quad \delta = \frac{ZR_p^{-1}+Z^{-1}R_0 - ZC_0\Gamma_0\Omega}{\left(\frac{ZC_0s}{T_0}-2\right)}; \\ &\gamma(\xi) = \frac{ZC_0\Gamma_0\Omega(\xi-\xi_0)}{\left(\frac{ZC_0s}{T_0}-2\right)} = \gamma_0(\xi-\xi_0); \quad \gamma_0 = \frac{ZC_0\Gamma_0\Omega}{\left(\frac{ZC_0s}{T_0}-2\right)}. \end{aligned}\right\} \tag{31}$$

Imposing that the velocity of traveling wave is of the order $v = 0.01v_0$ ($s = 0.01$), it is easily infer the following inequality

$$\frac{ZC_0s}{T_0} = 2.5\times10^{-2} << 2, \tag{32}$$

The choice s = 0.01 is pretty arbitrary. It was based on the fact that viscous damping might cause much more slowly spreading of mechanical tilts than in the ideal case where damping is absent (Fichtl et al., 2015). This circumstance simplifies the above set of parameters and allows that Eq. (30) can be multiplied by factor (−2), thus removing common denominators contained in parameters of Eq. (31). In that respect, for example the dispersion

Please cite this article in press as: Sataric, M.V., et al., Role of nonlinear localized Ca^{2+} pulses along microtubules in tuning the mechano−sensitivity of hair cells, Progress in Biophysics and Molecular Biology (2015), http://dx.doi.org/10.1016/j.pbiomolbio.2015.07.009

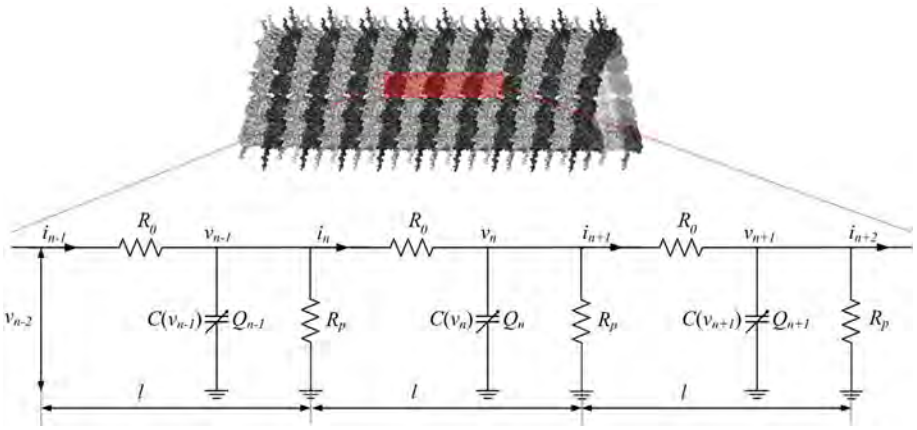

Fig. 9. An effective discrete circuit diagram describing biophysical model which mimics the behavior of MT in solution.

parameter now reads:

$$\beta = \frac{1}{3}, \tag{33}$$

The Eq. (30) can be farther transformed by the change of space–time variables $(\xi, \tau) \rightarrow (\rho, \theta)$ as follows

$$\left.\begin{aligned} \rho(\xi,\tau) &= (\xi - \xi_0)\exp(-\gamma_0\tau), \\ \theta(\tau) &= \frac{1}{3\gamma_0}\exp(-3\gamma_0\tau), \\ u(\xi,\tau) &= W(\rho,\theta)\exp(-2\gamma_0\tau), \end{aligned}\right\} \tag{34}$$

thus achieving the more simplified form

$$\frac{\partial W}{\partial \theta} + \alpha W\frac{\partial W}{\partial \rho} + \beta\frac{\partial^3 W}{\partial \rho^3} + \frac{\kappa}{\theta}W = 0; \quad \kappa = \frac{2}{3} - \frac{\delta}{3\gamma_0}. \tag{35}$$

If we analyze the last equation, it can be easily concluded that just the parameter κ contains ohmic losses. It is plausible that these losses can be balanced by the "electro–mechanical ratchet" term in Eq. (35), in order that κ parameter should vanish

$$\frac{2}{3} - \frac{\delta}{3\gamma_0} = 0; \quad \delta = 2\gamma_0. \tag{36}$$

This implies the following condition in explicit form

$$ZR_p^{-1} + Z^{-1}R_0 = 3ZC_0\Gamma_0\Omega. \tag{37}$$

Here, by inserting the estimated values $Z = 1.55 \times 10^8\ \Omega$, $R_p = 9.3 \times 10^7\ \Omega$, $R_0 = 6.2 \times 10^7\ \Omega$, $C_0 = 1 \times 10^{-16}$ F, it is possible to evaluate mechanical swing frequency of a TT

$$\Gamma_0\Omega \approx 4.43 \times 10^7 \mathrm{s}^{-1}, \tag{38}$$

with corresponding period

$$T_{TT} = \frac{2\pi}{\Gamma_0\Omega} \approx 1.42 \times 10^{-7}\mathrm{s}. \tag{39}$$

This period is twenty times greater of characteristic discharging time of an elementary unit capacitor, $T_0 = 0.062 \times 10^{-7}$ s, from Eq. (27). This fact provides the clear evidence that the approximation of Eq. (14), leading to Eq, (15), is safely justified.

Eventually, the straightforward calculation brings about the localized bell–shaped solution of Eq. (30), which slightly decays in parallel with its deceleration in a way subtly depending on the balance among respective parameters (α, β, γ_0 and δ)

$$u(\xi,\tau) = \frac{u_0\exp(-2\gamma_0\tau)}{\cosh^2\left\{\left[\frac{\alpha u_0}{4\beta}\exp(-2\gamma_0\tau)\right]^{1/2}\left[\xi - \xi_0(1-\exp(\gamma_0\tau)) + \frac{\alpha u_0}{3\beta}(1-\exp(3\gamma_0\tau))\exp(-2\gamma_0\tau)\right]\right\}}. \tag{40}$$

The amplitude u_0 should be proportional to the input current provided by the open transduction channels. It is also realistic that the velocity of above ionic pulse depends on the influx current through corresponding transduction channel. This is suggested by the early experimental evidences for actin filaments (Lin and Cantiello, 1993).

3.2. The numerical solution for Ca^{2+} pulses

In a specific case with the following set of parameters ($\alpha = 2\beta$, $\gamma_0 = \beta/2$, $\xi_0 = \beta$ and $\beta = 1/3$) the numerical solution is presented in Fig. 10. For that case, on the basis of expressions for α and β, Eq. (31), the parameter of nonlinear capacity, Eq. (18), has the value $b_0 = 0.03\ \mathrm{V}^{-1}$ which is pretty reasonable. It appears that the ionic pulse propagates along MT with a highly localized shape exhibiting the slowly decaying amplitude and an almost constant velocity of propagation. Using the values of time and space units and the geometry of Fig. 10, one can easily estimate the average velocity of this localized pulse under these specific circumstances, as follows

$$\begin{aligned} \langle \mathrm{v} \rangle &= \frac{170 l_{TD}}{1000 T_{TD}} = \frac{170 \times 8 \times 10^{-9}\mathrm{m}}{1000 \times 0.72 \times 10^{-7}\mathrm{s}} \approx 1.8\frac{\mathrm{cm}}{\mathrm{s}}; \\ s &= \frac{\mathrm{v}}{\mathrm{v}_0} \approx 1.4 \times 10^{-2}. \end{aligned} \tag{41}$$

Please cite this article in press as: Sataric, M.V., et al., Role of nonlinear localized Ca^{2+} pulses along microtubules in tuning the mechano–sensitivity of hair cells, Progress in Biophysics and Molecular Biology (2015), http://dx.doi.org/10.1016/j.pbiomolbio.2015.07.009

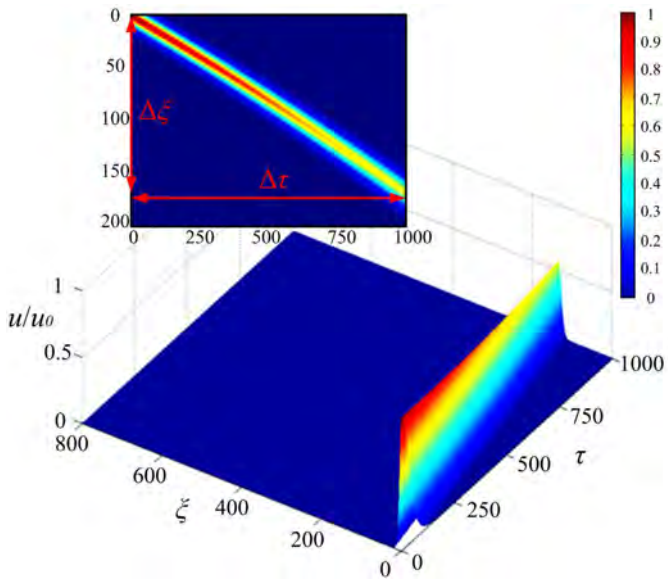

Fig. 10. Numerical solution of the function $u(\xi, \tau)$ for the specific set of parameters: $\alpha = 2\beta$, $\gamma_0 = \beta/2$, $\xi_0 = \beta$ and $\beta = 1/3$. The time space evolution of highly localized ionic pulse with slowly diminishing amplitude. Inset: the top view which shows almost constant velocity of propagation.

It is also possible to estimate that the pulse width is of the order of ten elementary units. This fact supports the validity of continuum approximation leading to Eq. (30).

Having in mind that the typical velocities of ionic diffusion in bulk cytosol are of the order of a few micrometers per second, it seems that here discussed model offers a new mechanism for much faster control of dynein arms activities in kinocilium. It is well known that the transduction channels in hair bundles must open and close even on a microsecond time scale in order to support the transduction in bats for example that hear up to 120 kHz. The dynein arm motors are thought to be coupled to faster transduction channel adaptation, so this fast ionic signaling is the proper candidate for such a coupling.

4. Dynein motor–driven oscillations of kinocilium controlled by Ca^{2+} ions

4.1. The existing evidences about the role of Ca^{2+} in hair cells

It has been revealed that the calcium ions in the hair cells are very important for normal sensory transduction (Crawford et al., 1991; Tinevez et al., 2007). However, it was very difficult to measure the local concentrations of different ionic species in the fluid surrounding the transduction channels as well as around MTs and actin filaments within a hair bundle (Lumpkin and Hudspeth, 1998). Previous studies have shown that the raising Ca^{2+} concentration above hair bundles of the frog's sacculus caused the oscillating movements of hair bundles (Martin and Hudspeth, 1999). Raising Ca^{2+} levels raised the frequency and reduced the amplitude of oscillations, while the lowering Ca^{2+} had the reverse effect. With new advances in more sophisticated measurement techniques it became possible to perform subtle assays and this resulted in an experiment that was conducted *in vivo* in the context of spontaneous otoacoustic emission in Australian bobtail lizards (*Tiliqua rugosa*) (Manley et al., 2004). It also demonstrated the conspicuous influence of calcium concentration into these otoacoustic phenomena.

The idea of how the currents of Ca^{2+} ions could be encompassed by the theoretical description of mechano–sensitivity of hair cells was established by Camalet et al. (Camalet et al., 2000), emphasizing the role of kinocilium. The kinocilium is relay lever that attaches the cell bundles to overlying structures. Sensory stimulation causes vibrations in these structures which than in terms of kinocilium efficiently delivers energy to stereocilia which play the central role in the transduction process. These results follow from experimental assays conducted by the group led by Hudspeth (Lumpkin and Hudspeth, 1998; Martin and Hudspeth, 1999).

Feedback control of the active amplificatory process relies on the influx of Ca^{2+} ions through set of transduction channels of a hair–bundle, regulated by the tension in their tip links. The part of these ions from the closest channel penetrate in interior of kinocilium and tune the generation of force by the dynein motor proteins, even causing the spontaneous oscillations of hair bundle (Julicher and Prost, 1997). This was incorporated in a very appealing scenario in which a hair bundle operates close self–tuned Hopf bifurcation point in order to sustain an active amplification in hair cells. Self–tuning keeps hair bundle in the vicinity of critical point in terms of a feedback mechanism that couples the output signal to the control parameter which does trigger the bifurcation.

It was proposed the simple algorithm for dynamics of control parameter ($\mathscr{P}_c$) responsible to keep hair–bundle system to be precisely balanced at the critical point (Camalet et al., 2000). This defines the time change of control parameter in response to the deflection (y) of the tip of kinocilum as follows

$$\frac{\partial \mathscr{P}_c}{\partial t} = \mathscr{P}_c \frac{1}{\tau_0}\left(\frac{y^2}{y_0^2} - 1\right), \tag{42}$$

with y_0 representing the amplitude of deflection y, and τ_0 the relaxation time of control parameter $\mathscr{P}_c$. Interestingly and very importantly, the control parameter was identified with the concentration of Ca^{2+} ions. The concept of bifurcation point (Camalet et al., 2000) strongly relied on the mechanosensing mechanism in kinocilia controlled by Ca^{2+} concentration.

Recent experimental evidences (Beurg et al., 2010) aimed to monitor calcium balance in mechano–transduction processes in hair cells firmly confirmed that the regulation of active hair bundle motility by Ca^{2+} ions has the decisive role for mechanisms of orientation and hearing. It implies that Ca^{2+} ions are a prime factor in hair cell pathology. It is clear that the proper influx of Ca^{2+} ions trough transduction channels and their successful distribution within the hair bundle and kinocilium is one side of the process. Nonetheless a very important fact is that after being used for functional purposes these ions should be fastly enough extruded from hair bundles. In that respect, we stress the basic role of mitochondria in Ca^{2+} balance. These organelles are producers of ATP which is the fuel for operating of motor proteins. Mitochondria are indeed conspicuously concentrated in hair cells mostly in epithelial layer bellow hair–bundles. In this context, the ATP produced is spent for the action of dynein arms and myosin in stereocilia, as well as for PMCA pumps which extrude ions through plasma membrane of hair cells. Moreover, mitochondria act as a large–capacity calcium store (Beurg et al., 2010), removing the part of ions imparted by the influx through transduction channels and transported by ionic pulses along MTs. The wide complexity of Ca^{2+} pathways casts doubt that only ordinary diffusion of ions can be sufficient for delicate balancing in every stage of subtle mechano–sensitivity action of hair–bundles. Earlier experimental evidences (Lumpkin and Hudspeth, 1998) revealed "that in mechanosensitive processes in hair–bundles there is no smoothly changing concentration of Ca^{2+} ions but rather a staccato rhythm of Ca^{2+} pulses that reflect channel flickering". This statement offers

Please cite this article in press as: Sataric, M.V., et al., Role of nonlinear localized Ca^{2+} pulses along microtubules in tuning the mechano–sensitivity of hair cells, Progress in Biophysics and Molecular Biology (2015), http://dx.doi.org/10.1016/j.pbiomolbio.2015.07.009

strong argument in favour of biophysical model of a MT as a nonlinear transmission line for Ca^{2+} signalling, that has been discussed above.

4.2. Role of Ca^{2+} ions regarding the dynamics of a kinocilium in the context of nonlinear transmission line model of microtubule

What would be the role of Ca^{2+} ions regarding the dynamics of a kinocilium in the context of the discussed biophysical model of ionic pulses? Namely in very essence of model proposed by (Sekulic et al., 2011) is the fact that changing of conformation of tubulin tails causes the nonlinear capacitance of elementary unit, Eq. (17), which changes the current of the Ca^{2+} signalling which then affects dynein arms which finally affect the vibration of kinocilium tuning its frequency and amplitude. Typically dynein arms move along MTs within a kinocilium and elastic elements oppose their motion. There are two possibilities in that respect. First one is that the kinocilium reaches a stable balance between the opposing forces. Second one is to oscillate around the equilibrium state.

If the kinocilium is considered as being isolated with the length L, as fixed at the basal epithelial layer and its tip (otoconical layer), it would vibrate as a standing wave of a string with the wavelength $\lambda = 2L$. In as much dynein arms grip the pairs of MTs at respective positions this circumstance changes the vibrating conditions of the kinocilium. The Ca^{2+} ions contained in localized ionic pulse sweeping along MT, partly bind to the dynein arms causing a fraction of motors to detach from MTs temporarily. It is expectable that Ca^{2+} inhibits the rate of the ATP hydrolysis and accelerates ADP release thus accelerating the cross–bridge detachment of dynein motors. These local concentrations of Ca^{2+} ions close to MTs also cause changes of interactions between neighboring protofilaments thus additionally adjusting the elastic properties of kinocilium (Kis et al., 2002).

The diminishing force exerted by the dynein arms weakens the tension within the kinocilium thus causing the lowering its bending flexural rigidity. This brings about that the tension in tip links also weakens leading that transduction channels are getting closed preventing farther influx of Ca^{2+} ions. Since the ionic pulses are gone fast the previously detached dynein arms grip MTs again and the oscillation of kinocilium starts again. The specific positions of dynein arms along MTs within the kinocilium cause that these points play the role of nodes for different overtone harmonics of standing wave in kinocilium. In an easy to grasp analogy, it could be stated that the repositioning of dynein arms along a kinocilium resembles “the role of fingers touching the strings while playing on a guitar”.

We are strongly convinced that here discussed mechanism, based on polyelectrolyte features of filamentous polymers, primarily MTs and actin filaments, may be amongst the promising candidates for completing still unfinished puzzle of explanation and better understanding of such dazzling sensitivity and frequency selectivity of otoacoustic apparatus (Ashmore et al., 2010).

5. Discussion and conclusion

It was experimentally demonstrated that the condensed ionic clouds surrounding charged nano–rods called polygons are being decoupled, if the longitudinal electric field is applied. Therefore, the ionic cloud gains the mobility in the direction of field's attraction sliding along pertaining polyon. The polyelectrolitic features of DNA are already elaborated, both theoretically and experimentally (Ponomarev et al., 2004; Keyser et al., 2006). These properties have profound impact on DNA dynamics and functioning. In this paper, we provided an overview of current understanding and adequate biophysical model of how to use the polyelectrolitic properties of MTs in explaining their ability to be the pathways for fast and efficient transport of cations participating in the important physiological processes in living cells. The specific attention is focussed on the function of hair cells in that context. There the MTs are ingredients of kinocilium which participate in auditory processes.

It is known that receptor cells of other sensory systems such as olfactory receptors and photoreceptors contain ciliary structures with $9 + 2$ arrangement of MTs. This suggests that similar interplay between pertaining MTs and Ca^{2+} ions must be present in these important biosensors. In that respect the mechanism elaborated in this paper has the more general meaning.

Here, we clearly explained and justified why MTs, and particularly tubulin tails, comply with the criteria for being typical polyelectrolytes. On that basis the geometric symmetry of MTs provides the opportunity that one protofilament of MT can be approximately seen as a “coaxial cable” with the “charged plates” composed of cytosolic counterions with a depleted layer of water molecules in between. It enabled that the row of tubulin dimers with pertaining tubulin tails could be viewed as series of identical elementary units with estimated capacitance and resistance, including the resistance of two nano–pores. The origin of nonlinearity is attributed to the capacitance of tubulin tails in terms of their electro–mechanical flexibility.

Considering a protofilament as a long ladder network of identical lumped sections of elementary units and by applying the Kirchhoff's law, it is possible to construct, in continuum limit, a nonlinear differential equation Eq. (30), describing the localized Ca^{2+} current (with an accompanying voltage). This equation possesses the dissipative term due to the ohmic effects but this energy loss is at least partly compensated by the “electro–mechanical ratchet” action of tubulin tails.

As a consequence the solution of Eq. (30) has the form of Eq. (40) which exhibits a pulse–like shape slowly decelerating and slightly diminishing the amplitude. For different combinations of pertaining parameters from Eq. (30), explicitly given by Eq. (31), localized pulse Eq. (40) can persist for dozens of micrometres with velocities in the range from centimetres to decimetres per second. These velocities are conspicuously greater than the typical velocity of ionic diffusion in cytosol under physiological conditions (a few micrometres per second). Experimental evidences show that the forces elicited within the hair bundles of vestibular hair cells change in a submillisecond time scale. This is expected to be tuned by accordingly fast elevation of local concentration of control parameter (Ca^{2+}) in contact with dynein arms of kinocilium (Camalet et al., 2000). The results obtained from the recently proposed model by Sekulic et al. (2011) clearly elucidate the mentioned “staccato rhythm of Ca^{2+} pulses” within the hair–bundles.

Since the typical length of a kinocilium is of the order of 10 μm, then the ionic pulses with the velocity of the order of 1 cm/s, Eq. (41) implies the time of spanning such a distance to be of the order of

$$\tau_{ep} \approx \frac{10^{-5}\ \mathrm{m}}{0.01\ \mathrm{m/s}} = 10^{-3}\mathrm{s}. \tag{43}$$

This order of magnitude matches the millisecond times characteristic for fast manifestations of active hair bundle motility observed in auditory organs of frog and turtle. The change of pertinent frequencies is brought about by the change of number of dynein arms attached (detached), which is tuned by a number of Ca^{2+} pulses within the framework of biophysical model that has been discussed above. We argue that the velocity and amplitude of ionic pulses of Ca^{2+} depends on the intensity of ionic influx through the transduction channels. This subtle mechanism can offer a new glance at the still unclear complete picture of active hair–bundles motility

Please cite this article in press as: Sataric, M.V., et al., Role of nonlinear localized Ca^{2+} pulses along microtubules in tuning the mechano–sensitivity of hair cells, Progress in Biophysics and Molecular Biology (2015), http://dx.doi.org/10.1016/j.pbiomolbio.2015.07.009

which is characterized by acoustic amplification, frequency tuning, compressive nonlinearity and spontaneous otoacoustic emission (Martin et al., 2003; Manley, 2000). Experimental evidences (Kis et al., 2002) demonstrated that the changes of Ca^{2+} concentration close to MTs reflects in conformational changing of protruding polypeptide loops of tubulin dimers, which are responsible for lateral bonds between protofilaments within MT's matrix. This brings about the change of effective interaction surface between protofilaments, thus changing the pertaining shear modulus. In that way the concentration of Ca^{2+} ions around MT within the kinocilium changes its mechanical parameters, thus additionally tuning its spectra of frequencies.

Acknowledgments

This research was supported by the funds from Serbian Ministry of Education and Science, Grants: III43008, OI171009 and III45010, and Serbian Academy of Sciences and Arts.

References

Al–Bassam, J., Ozer, R.S., Safer, D., Halpain, S., Milligan, R.A., 2002. MAP2 and tau bind longitudinally along the outer ridges of microtubule protofilaments. J. Cell Biol. 157, 1187–1196.

Amos, L.A., Amos, W.B., 1991. Molecules of the Cytoskeleton. Guilford Press, New York.

Ashmore, J., Avan, P., Brownell, W.E., Dallos, P., Dierkes, K., Fettiplace, R., Grosh, K., Hackney, C.M., Hudspeth, A.J., Julicher, F., Lindner, B., Martin, P., Meaud, J., Petit, C., Santos Sacchi, J.R., Canlon, B., 2010. The remarkable cochlear amplifier. Hear. Res. 266, 1–17.

Atema, J., 1973. Microtubule theory of sensory transduction. J. Theor. Biol. 38, 181–190.

Axelrod, J.D., 2008. Basal bodies, kinocilia and planar cell polarity. Nat. Genet. 40, 10–11.

Bashtanov, M.E., Goodyear, R.J., Richardson, G.P., Russell, I.J., 2004. The mechanical properties of chick (*Gallus domesticus*) sensory hair bundles: relative contributions of structures sensitive to calcium chelation and subtilisin treatment. J. Physiol. 559, 287–299.

Beurg, M., Nam, J.H., Chen, Q., Fettiplace, R., 2010. Calcium balance and mechano-transduction in rat cochlear hair cells. J. Neurophysiol. 104, 18–34.

Camalet, S., Duke, T., Julicher, F., Prost, J., 2000. Auditory sensitivity provided by self–tuned critical oscillations of hair cells. Proc. Natl. Acad. Sci. U. S. A. 97, 3183–3188.

Cassimeris, L., Spittle, C., 2001. Regulation of microtubule–associated proteins. Int. Rev. Cytol. 210, 163–226.

Chen, J., Kanai, Y., Cowan, N.J., Hirokawa, N., 1992. Projection domains of MAP2 and tau determine spacings between microtubules in dendrites and axons. Nature 360, 674–677.

Crawford, A.C., Evans, M.G., Fettiplace, R., 1991. The actions of calcium on the mechano–electrical transducer current of turtle hair cells. J. Physiol. 434, 369–398.

Dhont, J.K.G., Kang, K., 2011. Electric–field induced polarization of the layer of condensed ions on cylindrical colloids. Eur. Phys. J. E 34, 1–19.

Duvall, A.J., Flock, A., Wersäll, J., 1966. The ultrastructure of the sensory hairs and associated organelles of the cochlear inner hair cell, with reference to directional sensitivity. J. Cell Biol. 29, 497–505.

Freedman, H., Rezania, V., Priel, A., Carpenter, E., Noskov, S.Y., Tuszynski, J.A., 2010. Model of ionic currents through microtubule nanopores and the lumen. Phys. Rev. E 81, 051912.

Fichtl, B., Shrivastava, S., Schneider, M.F., 2015. Protons at the Speed of Sound: Specific Biological Signaling from Physics. http://arxiv.org/vc/arxiv/papers/1503/1503.00952v2.pdf.

Friesen, D.E., Craddock, T.J.A., Kalra, A.P., Tuszynski, J.A., 2015. Biological wires, communication systems, and implications for disease. BioSystems 127, 14–27.

Grimaldi, A.D., Maki, T., Fitton, B.P., Roth, D., Yampolsky, D., Davidson, M.W., Svitkina, T., Straube, A., Hayashi, I., Kaverina, I., 2014. CLASPs are required for proper microtubule localization of end–binding proteins. Dev. Cell 30, 343–352.

Guo, Y., Liu, Y., Tang, J.X., Valles Jr., J.M., 2007. Polymerization force driven buckling of microtubule bundles determines the wavelength of patterns formed in tubulin solutions. Phys. Rev. Lett. 98, 198103.

Hanggi, P., Marchesoni, F., Nori, F., 2005. Brownian motors. Ann. Phys. Leipz. 14, 51–70.

Hernfindez, M.A., Serrano, L., Avila, J., 1988. Microtubule–associated protein, MAP2, is a calcium–binding protein. Biochimica Biophysica Acta 965, 195–201.

Julicher, F., Prost, J., 1997. Spontaneous oscillations of collective molecular motors. Phys. Rev. Lett. 78, 4510–4513.

Karr, T.L., Kristofferson, D., Purich, D.L., 1980. Calcium ion induces endwise depolymerization of bovine brain microtubules. J. Biol. Chem. 255, 11853–11856.

Keyser, U.F., Koeleman, B.N., van Dorp, S., Krapf, D., Smeets, R.M.M., Lemay, S.G., Dekker, N.H., Dekker, C., 2006. Direct force measurements on DNA in a solid–state nanopore. Nat. Phys. 2, 473–477.

Kis, A., Kasas, S., Babić, B., Kulik, A.J., Benoit, W., Briggs, C.A.D., Schönenberger, C., Catsicas, S., Forro, L., 2002. Nanomechanics of microtubules. Phys. Rev. Lett. 89, 248101.

Kuhn, W., 1949. Reversible Dehnung und Kontraktion bei Änderung der ionisation eines Netzwerks polyvalenter Fadenmolekülionen. Experientia 5, 318–319.

Ladrech, S., Lenior, M., 2002. Changes in MAP2 and tyrosinated α–tubulin expression in cochlear inner hair cells after amikacin treatment in the rat. J. Comp. Neurol. 451, 70–78.

Lepelletier, L., de Monvel, J.B., Buisson, J., Desdouets, C., Petit, C., 2013. Auditory hair cell centrioles undergo confined Brownian motion throughout the developmental migration of the kinocilium. Biophys. J. 105, 48–58.

Lewis, E.R., Leverenz, E.L., Bialek, W.S., 1985. The Vertebrate Inner Ear. CRC Press, Boca Raton, Florida.

Lowenstein, O., Osborne, M.P., Wersall, J., 1964. Structure and innervation of the sensory epithelia of the labyrinth in the thornback ray (*Raja clavata*). Proc. R. Soc. Lond. B Biol. Sci. 160, 1–12.

Lin, E.C., Cantiello, H.F., 1993. A novel method to study the electrodynamic behavior of actin filaments. Evidence for cable–like properties of actin. Biophys. J. 65, 1371–1378.

Lumpkin, E.A., Hudspeth, A.J., 1998. Regulation of free Ca^{2+} concentration in hair–cell stereocilia. J. Neurosci. 18, 6300–6318.

Manley, G.A., 2000. Cochlear mechanisms from a phylogenetic viewpoint. Proc. Natl. Acad. Sci. U. S. A. 97, 11736–11743.

Manley, G.A., Sienknecht, U., Koppl, C., 2004. Calcium modulates the frequency and amplitude of spontaneous otoacoustic emissions in the bobtail skink. J. Neurophysiol. 92, 2685–2693.

Manning, G.S., 1993. A condensed counterion theory for polarization of polyelectrolyte solutions in high fields. J. Chem. Phys. 99, 477–486.

Manning, G.S., 2009. On the apparent saturation of the dipole induced in a rodlike polyion at high electric fields. J. Phys. Chem. B 113, 2231–2233.

Manning, G.S., 2011. Counterion condensation theory of attraction between like charges in the absence of multivalent counterions. Eur. Phys. J. E 34, 1–18.

Marder, M.P., 2000. Condensed Matter Physics. John Wiley & Sons, New York, p. 311.

Martin, P., Hudspeth, A.J., 1999. Active hair–bundle movements can amplify a hair cell's response to oscillatory mechanical stimuli. Proc. Natl. Acad. Sci. U. S. A. 96, 14306–14311.

Martin, P., Bozovic, D., Choe, Y., Hudspeth, A.J., 2003. Spontaneous oscillation by hair bundles of the bullfrog's sacculus. J. Neurosci. 23, 4533–4548.

Minoura, I., Muto, E., 2006. Dielectric measurement of individual microtubules using the electroorientation method. Biophys. J. 90, 3739–3748.

Moran, D.T., Varela, F.G., 1971. Microtubules and sensory transduction. Proc. Nat. Acad. Sci. U. S. A. 68, 757–760.

Ponomarev, S.Y., Thayer, K.M., Beveridge, D.L., 2004. Ion motions in molecular dynamics simulations on DNA. Proc. Natl. Acad. Sci. U. S. A. 101, 14771–14775.

Priel, A., Ramos, A.J., Tuszynski, J.A., Cantiello, H.F., 2006. A biopolymer transistor: electrical amplification by microtubules. Biophys. J. 90, 4639–4643.

Sataric, M.V., Tuszynski, J.A., Zakula, R.B., 1993. Kinklike excitations as an energy–transfer mechanism in microtubules. Phys. Rev. E 48, 589.

Sataric, M.V., Tuszynski, J.A., 2003. Relationship between the nonlinear ferroelectric and liquid crystal models for microtubules. Phys. Rev. E 67, 011901.

Sataric, M.V., Bednar, N., Sataric, B.M., Stojanovic, G., 2009a. Actin filaments as nonlinear RLC transmission lines. Int. J. Mod. Phys. B 23, 4697–4711.

Sataric, M.V., Ilic, D.I., Ralevic, N., Tuszynski, J.A., 2009b. A nonlinear model of ionic wave propagation along microtubules. Eur. Biophys. J. 38, 637–647.

Sekulic, D.L., Sataic, B.M., Tuszynski, J.A., Sataic, M.V., 2011. Nonlinear ionic pulses along microtubules. Eur. Phys. J. E 34, 49.

Sekulic, D.L., Sataic, M.V., 2015. An improved nanoscale transmission line model of microtubule: the effect of nonlinearity on the propagation of electrical signals. Facta Univ. Ser. Electron. Energ. 28, 133–142.

Serrano, L., Valencia, A., Caballero, R., Avila, J., 1986. Localization of the high affinity calcium–binding site on tubulin molecule. J. Biol. Chem. 261, 7076–7081.

Shen, H.S., 2011. Nonlinear vibration of microtubules in living cells. Curr. Appl. Phys. 11, 812–821.

Sipe, C.W., Liu, L., Lee, J., Grimsley–Myers, C., Lu, X., 2013. Lis1 mediates planar polarity of auditory hair cells through regulation of microtubule organization. Development 140, 1785–1795.

Solomon, F., 1977. Binding sites for calcium on tubulin. Biochemistry 16, 358–363.

Sui, H., Downing, K.H., 2010. Structural basis of interprotofilament interaction and lateral deformation of microtubules. Structure 18, 1022–1031.

Tinevez, J.Y., Julicher, F., Martin, P., 2007. Unifying the various incarnations of active hair–bundle motility by the vertebrate hair cell. Biophys. J. 93, 4053–4067.

Todorov, P.T., Hardisty, R.E., Brown, S.D.M., 2001. Myosin VIIA is specifically associated with calmodulin and microtubule–associated protein–2B (MAP–2B). Biochem. J. 354, 267–274.

Tuszynski, J.A., Portet, S., Dixon, J.M., Luxford, C., Cantiello, H.F., 2004. Ionic wave propagation along actin filaments. Biophys. J. 86, 1890–1903.

Tuszynski, J.A., Brown, J.A., Crawford, E., Carpenter, E.J., Nip, M.L.A., Dixon, J.M., Sataric, M.V., 2005. Molecular dynamics simulations of tubulin structure and

Please cite this article in press as: Sataric, M.V., et al., Role of nonlinear localized Ca^{2+} pulses along microtubules in tuning the mechano–sensitivity of hair cells, Progress in Biophysics and Molecular Biology (2015), http://dx.doi.org/10.1016/j.pbiomolbio.2015.07.009

calculations of electrostatic properties of microtubules. Math. Comput. Model 41, 1055–1070.
Tuszynski, J.A., Craddock, T.J.A., Carpenter, E.J., 2008. Bio–ferroelectricity at the nanoscale. J. Comput. Theor. Nanosci. 5, 2022–2032.
Xue, J., Peterson, E.H., 2006. Hair bundle heights in the utricle: differences between macular locations and hair cell types. J. Neurophysiol. 95, 171–186.
Yang, P., Diener, D.R., Rosenbaum, J.L., Sale, W.S., 2001. Localization of calmodulin and dynein light chain LC8 in flagellar radial spokes. J. Cell Biol. 153, 1315–1326.

Please cite this article in press as: Sataric, M.V., et al., Role of nonlinear localized Ca^{2+} pulses along microtubules in tuning the mechano–sensitivity of hair cells, Progress in Biophysics and Molecular Biology (2015), http://dx.doi.org/10.1016/j.pbiomolbio.2015.07.009

Actin filaments as the fast pathways for calcium ions involved in auditory processes

MILJKO V SATARIC, DALIBOR L SEKULIC* and BOGDAN M SATARIC
Faculty of Technical Sciences, University of Novi Sad, Trg Dositeja Obradovića 6, 21000, Novi Sad, Serbia

**Corresponding author (Email, dalsek@uns.ac.rs)*

We investigated the polyelectrolyte properties of actin filaments which are in interaction with myosin motors, basic participants in mechano-electrical transduction in the stereocilia of the inner ear. Here, we elaborated a model in which actin filaments play the role of guides or pathways for localized flow of calcium ions. It is well recognized that calcium ions are implicated in tuning of actin-myosin cross-bridge interaction, which controls the mechanical property of hair bundle. Actin filaments enable much more efficient delivery of calcium ions and faster mechanism for their distribution within the stereocilia. With this model we were able to semiquantitatively explain experimental evidences regarding the way of how calcium ions tune the mechanosensitivity of hair cells.

[Sataric MV, Sekulic DL and Sataric BM 2015 Actin filaments as the fast pathways for calcium ions involved in auditory processes. *J. Biosci.* **40** 549–559] DOI 10.1007/s12038-015-9547-z

1. Introduction

Hair cells are mechanosensitive receptors of vertebrate inner ears that are specialized to transform mechanical motion into the change in membrane potential and to initiate the pertaining ionic currents. Each hair cell is equipped with the hair bundles which comprise the hexagonal arrays of so called stereocilia. Every stereocilium is a bundle of parallel actin filaments interconnected with different lateral links. The tip links are especially important since they serve for opening and closing of ionic channels in cell membrane. The hair bundle is arranged like a harp or the back acoustic compartment of a piano in rows of increasing height (Helmholtz 1954), see figure 1. As an example, in striolar hair bundle from chicks the tallest stereocilia are 9.2 μm height and the shortest are 2.4 μm. The number of stereocilia in that bundle is 51. Diameter of a single stereocilium is 0.4 μm and the number of tip links in this bundle is 42.

When the hair bundle is pushed in positive (right) direction (figure 2A), the spring of tip-link exerts a force on the trap door and thus opens the ionic channel. It enables the influx of positive K^+ and Ca^{2+} ions inside stereocilia endolymph. Deflecting the hair bundle in the opposite direction, the tip-link is getting compressed, thus closing the trap door of channel and preventing the ionic influx (figure 2B) (Nam *et al.* 2006). The number of open channels depends largely on the deflecting position of the bundle and not on its velocity or acceleration of movement. But, opening dynamics should depend on frequency of movement thus enabling the essential selectivity of hair cells.

It is widely recognized that mechano-electrical transduction in hair bundles posits that force-generating myosin motors regulate the elastic properties of the transduction channels as being tuned by the concentration of Ca^{2+} ions. Namely, the cross-bridge cycle of Myo1c motor protein is calcium sensitive (Gillespie and Cyr 2004; Adamek *et al.* 2008). Myosin motors Myo1c are responsible for anchoring the channel's mechanical complex to the actin filament core of the stereocilia forming the cross-bridge. In the relaxed state troponin molecule forms a tropomyosin complex which blocks the attachment site for the actin-myosin cross-bridge. The Ca^{2+} ion attaches to troponin, causing it to change shape thus exposing the binding site for myosin on the actin filament. Such troponin role in stereocilia is widely elaborated by Karkanevatos (2001). Since the channel is permeable to Ca^{2+} ions, its opening tunes the local intrabundle

Keywords. Actin filament; calcium ions; hair cell; polyelectrolyte; stereocilia

Published online: 14 August 2015

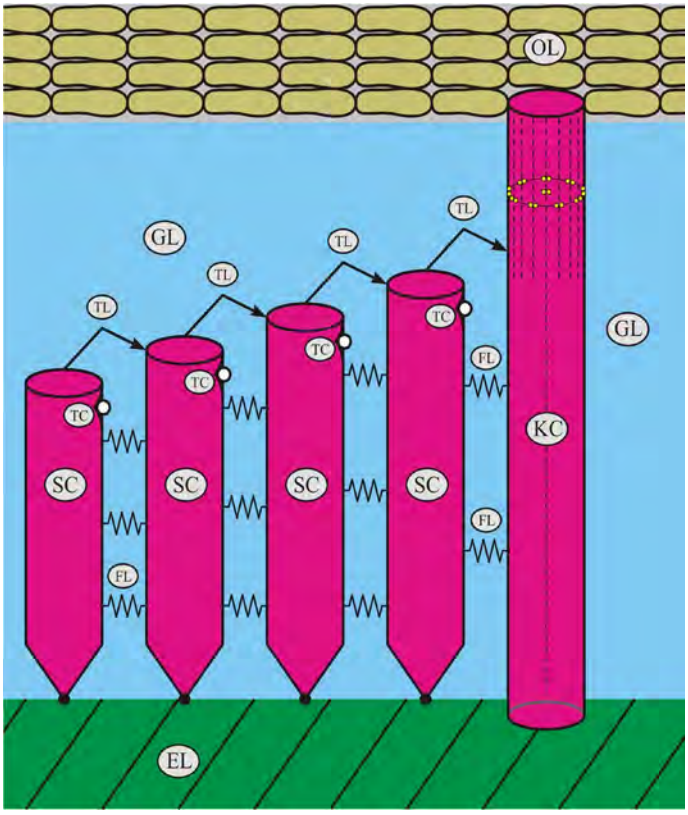

Figure 1. The sketch of single row of stereocilia (SC) within a hair bundle of vestibular hair cell. The row of stereocilia (SC) is interconnected by filamentous links (FL) and finished with a single kinocilium (KC). The tip links (TL) and pertaining transduction channels (TC) are responsible for ionic currents. Epithelial layer (EL), otholitic layer (OL) and gelatinous layer (GL) are also depicted.

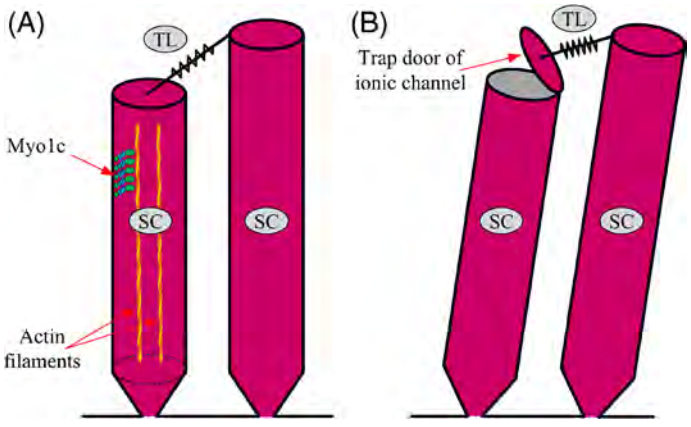

Figure 2. A model of mechano-electrical transduction in hair bundles. (**A**) Schematic illustration of two adjacent stereocilia (SC) with tip-link (TL) joining two ion channels and Myo1c motors in interaction with actin filaments. (**B**) Hair bundle is deflected with a positive stimulus; spring of tip-link exerts a force on the trap door and opens the ionic channel.

Ca^{2+} concentration which in turn regulates the force generated by Myo1c motors and it is manifested through channel reclosure.

There is a sharp but essentially nonlinear mechanical tuning of auditory process within the hair cells with oscillating bundles. Although the bundle's response far from the resonance's center is linear, at the resonance peak the response increases sublinearly, actually logarithmically, compressing almost 80 dB into about 20 dB (Ruggero 1992). It is apparent that auditory sensitivity is developed by an active amplificatory process whose exact nature still remains to be completely explained.

It is the prevailing view that Myo1c motors propel these active oscillations of hair bundles as being powered by the energy supply provided by ATP hydrolysis. Calcium obviously affects the probability of a Myo1c motor to be bound to actin, and more than that, it impacts the stiffness of an actin-myosin cross-bridge controlling the amount of the power stroke of a single motor (Martin *et al*. 2003).

It was shown that the time course of channel activation and motor adaptation were substantially slowed down by decreasing calcium levels from 2.8 mM to 0.05 mM (Ricci *et al*. 2003). Adequately the changes in frequency and amplitude of hair-cell bundle oscillations in the bullfrog sacculus exhibit the property that raising calcium concentration raised the frequency and reduced the amplitude, while lowering calcium exhibits the reverse effect.

The seminal paper by Lumpkin and Hudspeth (1998) presented the experimental assay about regulation of free Ca^{2+} ions in hair-cell stereocilia. The authors used confocal microscopy to detect Ca^{2+} ions entry and distribution within stereocilia of hair cells. They also developed a model of stereociliary Ca^{2+} homeostasis with appropriate regulatory mechanisms. Their theoretical approach is very complex, being described by a system of seven differential equations. They claimed that 'although images were collected from hundreds of stereocilia most were not suitable for fitting with that model'. In the other publication by the same authors (Lumpkin and Hudspeth 1995), it was realized that regulatory mechanism of Ca^{2+} fluxes must be located in stereocilia shaft region which is densely packed with bundled actin filaments. Otherwise in an exhaustive review article, Gartzke and Lange (2002) have stressed that the bundles of microfilaments are forming a diffusion barrier so that the polyelectrolyte nature of actin filaments plays a crucial role in Ca^{2+} signaling in stereocilia.

Interestingly in despite of the fact that Ca^{2+} ions play leading role in controlling the active force generation by Myo1c motors, the concentration of these ions is marginally small compared with that of dominant K^+ ions. The very seminal experimental assay by Beurg *et al*. (2010) performed in rat hair cells revealed that when the influx current through hair bundle channels amounts 3.4 nA, just 0.2% ot this current is carried by Ca^{2+} ions with corresponding peak current of the order of 7 pA. And more than that; little is known about the equilibria between ionized and nonionized calcium fraction in the hair cell's endolymph. Some evidences show that the total calcium concentration is by one order of magnitude higher than the ionized fraction. It opens the question of how this low concentration of Ca^{2+} ions can be properly distributed in order to be on right time at the right places to provide so concerted cell's responses to complex auditory signals.

All these facts motivated us to elaborate a new approach in order to try to explain still uncompleted answer of how calcium mediates so efficiently this active nonlinear mechanism of auditory sensitivity. The approach is strongly relied on the fact that actin filaments within the hair bundles exhibit polyelectrolyte properties in natural endolymph. So the effect of counterion condensation (Manning 1978) could be safely expected to take place for these cytoskeletal filaments. The additional arguments were found in the circumstance that earlier experimental evidences (Lin and Cantiello 1993; Priel *et al*. 2006) and some theoretical contributions (Tuszynski *et al*. 2004; Sataric *et al*. 2009a, b; Sekulic *et al*. 2011) suggested that both microtubules and actin filaments, as being polyelectrolytes in physiological conditions, significantly increase ionic currents even exhibiting conspicuous effects of current amplification.

The paper is organized as follows: In section 2, we explained the polyelectrolyte character of actin filaments and quote some earlier models. In section 3, we applied the standard Manning's model (Manning 1996, 2011) for the condensation of calcium ions on the actin filaments within the stereocilia. Using the trawling-wave approach, the problem is solved exactly. Section 4 provides discussion and conclusions.

2. Actin filaments as polyelectrolytes

It is well known that first conspicuous biological example of typical polyelectrolyte was DNA under physiological conditions. This circumstance has very essential impact on the functional properties of these sophisticated molecules. The phenomenon of DNA condensation has been successfully elaborated by the theory of linear polyelectrolytes (Manning 1978, 1993, 2008). A double stranded DNA at neutral pH has a linear charge spacing b = 0.17 nm, much less than the Bjerrum length.

The Bjerrum length l_B defines the distance at which the thermal fluctuations are equal to the electrostatic attraction or repulsion between ions in solution whose relative dielectric constant is ε. For univalent ions and for a given absolute temperature T it reads (Israelachvili 1992):

$$\frac{e^2}{4\pi\varepsilon_r\varepsilon_0 l_B} = k_B T \quad \Rightarrow \quad l_B = \frac{e^2}{4\pi\varepsilon_r\varepsilon_0 k_B T}, \tag{1}$$

where $e = 1.6\times10^{-19}$ C is the elementary charge, $\varepsilon_0 = 8.85\times10^{-12}$ F/m is the permittivity of the vacuum and $k_B =$

1.38×10^{-23} J/K is Boltzmann's constant. It follows that for $T = 310$ K and $\varepsilon_r = 80$ this parameter has the value

$$l_B = 0.67\,\text{nm}. \tag{2}$$

Actin filaments are abundant cytoskeletal structures that play the important roles in a variety of cell functions including locomotion, cell shape and auditory processes. The globular actin monomers of diameter $d = 5.4$ nm polymerize to double stranded filaments form, so called F-actin, see figure 3. The polyelectrolyte nature of actin filaments was noticed some twenty years ago (Lin and Cantiello 1993), and the adequate values of relevant parameters were estimated (Tang and Janmey 1996). The already mentioned review by Gartzke and Lange (2002) considers different theoretical and experimental concepts of actin filaments as typical polyelectrolytes in providing the signaling pathways for Ca^{2+} ions. Our approach is in accord with this strategy but has originality and plausibility. Each monomer carries an excess of 14 negative charges, three of which are neutralized by protonation of three pertaining histidines per monomer at pH = 7.2. It provides that remaining 11 charges give the linear charge density of approximately 4 *e*/nm. This fact has the fundamental implication that the linear charge spacing along the filament axis b=0.25 nm is sufficiently small compared to the Bjerrum length to make the counterion condensation theory relevant. The corresponding dimensionless parameter ξ for the univalent ions is greater than unity

$$\xi = \frac{l_B}{b} = 2.7 > 1. \tag{3}$$

In our approach related for the stereocilia, we contemplated that pertaining actin filaments should be surrounded primarily by divalent Ca^{2+} ions forming screened 'condensed cloud'. In that shielded layer one could estimate the corresponding local Bjerrum length to be twice greater than in the univalent case, equation (2), since the charge is $z = 2$, giving:

$$l_B = 1.34\,\text{nm}. \tag{4}$$

Accordingly, the parameter that indicates the polyelectrolyte nature of actin filament now reads:

$$\xi = 5.4. \tag{5}$$

Around this 'condensed cloud' there is the layer of thickness equal to Bjerrum length and which is depleted of ions of both signs. This argument brings about that one could consider an actin filament as a capacitor capable to store and transport localized Ca^{2+} counterions along its length (Sataric *et al*. 2009a). The other important parameter relevant for polyelectrolytes is Debye screening length Δ, defined in a way to depend on total ionic concentration in a given solution. For typical hair cell's endolymph (Israelachvili 1992), the average ionic number concentration is of the order of $c_s = 150$ mol/m^3. Taking $N_A = 6\times10^{23}$ 1/mol, we easily get:

$$n_s = N_A c_s = 9 \times 10^{25}\,1/\text{m}^3. \tag{6}$$

In as much the Debye length is defined as

$$\Delta = \left(\frac{\varepsilon_r \varepsilon_0 k_B T}{2e^2 n_s}\right)^{1/2}, \tag{7}$$

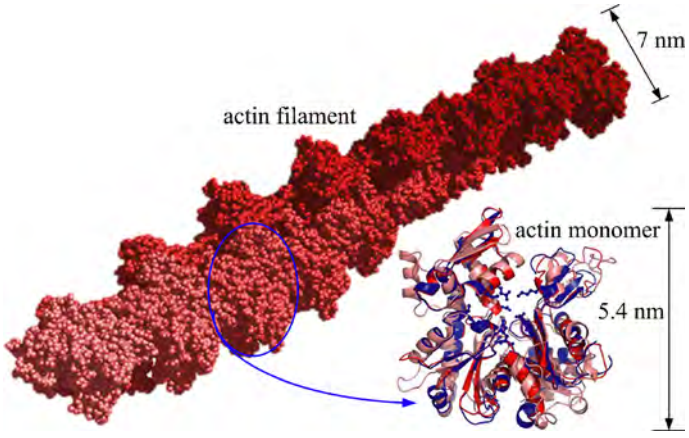

Figure 3. Structure model of actin filament consisting of two intertwined long-pitch right-handed helices is shown on the left. Actin monomer ribbon structure is shown on the right.

using the same set of parameter as in equation (1) along with equation (6), one easily gets

$$\Delta = 0.81 \times 10^{-9}\,\mathrm{m}. \tag{8}$$

We are now able to start from the Manning's polyelectrolyte theory (Manning 2011), introducing electrolytic free energy G of an actin filament with N condensed counterions (in the case of stereocilia the Ca^{2+} ions) and defining the dimensionless density of free energy g:

$$g = \frac{G}{Nk_{\mathrm{B}}T} = -(1-z\theta)^2\xi\ln\left(\frac{\mathrm{b}}{\Delta}\right) + \theta\ln\left(\frac{\theta}{Q}\right). \tag{9}$$

The first term in this expression arises from the sum of Debye-screened repulsions between all pairs of negative sites on the charged filament. Since $\mathrm{b}/\Delta = 0.313$ and $\ln(\mathrm{b}/\Delta) = -1.163$, the first term in equation (9) is positive as required. The quantity θ is the number of Ca^{2+} counterions condensed on the charged actin filament per single charge site (negative). This is the fraction less than unity at low ionic concentration. The parameter b is introduced earlier, but its inverse value $\mathrm{b}^{-1} = 4\times10^{9}$ m^{-1} is the number of negative sites on the filament per unit length, bringing about that the linear concentration of condensed counterions obeys the inequality

$$\frac{\theta}{\mathrm{b}} \le \frac{1}{\mathrm{b}}. \tag{10}$$

From this reason the effective charge of a site is reduced from a former bare unit charge 1 to the following fraction for Ca^{2+} counterions

$$1-z\theta = 1-2\theta. \tag{11}$$

The second term in equation (9) is of ideal-gas type free energy, where Q stands for an internal partition function which contains the short-range interactions between the condensed calcium counterions and actin filament but is assumed to be independent of θ.

The expression given by equation (9) enables us to calculate the electrochemical potential of the condensed counterions as follows:

$$\mu_c = k_{\mathrm{B}}T\frac{\partial g}{\partial\theta} = 2k_{\mathrm{B}}Tz(1-z\theta)\xi\ln\left(\frac{\mathrm{b}}{\Delta}\right) + k_{\mathrm{B}}T\left[\ln\left(\frac{\theta}{Q}\right)+1\right]. \tag{12}$$

If the filament with counterions is subjected to the constant external electric field E, parallel to filament axis x, the corresponding potential energy is

$$E_{\mathrm{p}} = -zeEx. \tag{13}$$

The equilibrium state of counterions on an actin filament can be inferred if above chemical potential μ_{c} is compared with the chemical potential of the free counterions, which at low ionic concentration c_{s} equals

$$\mu_{\mathrm{free}} = 2k_{\mathrm{B}}T\ln(c_{\mathrm{s}}). \tag{14}$$

For already used concentration c_{s} = 150 mol/m^3 for endolymph, we can compare logarithmic factors

$$\ln\left(\frac{\mathrm{b}}{\Delta}\right) \cong \ln(c_{\mathrm{s}}), \tag{15}$$

and it is apparent that equality of both chemical potential, Eqs. (12) and (14), is provided for a discrete positive fractional value θ_0, if the following condition holds:

$$z(1-z\theta_0)\xi = 1; \quad \theta_0 = \frac{1}{z}\left(1-\frac{1}{z\xi}\right). \tag{16}$$

The fractional coverage of bare negative sites along an actin filament θ_0 is the equilibrium value that is constant along the length of the filament in the absence of an applied electric field or equivalently without the influx of Ca^{2+} ions from transduction channels. Substituting in equation (16) the valence of Ca^{2+} ions $z = 2$ and $\xi = 5.4$, we get

$$\theta_0 = 0.45, \tag{17}$$

while for monovalent counterions with $\xi = 2.7$ one obtains $\theta_0 = 0.4$. The fraction of remaining negatively charged sites on an actin filament is adequately expressed as:

$$1-z\theta_0 = 0.1. \tag{18}$$

In the following section, we will use the above approach to analyze the dynamics of calcium ions along actin filaments in the context of hair bundle active adaptation within an auditory process. Shortly we should mention here that some earlier attempts were made in order to clarify the experimental results (Lin and Cantiello 1993) exhibiting the enhanced ionic currents along actin filaments *in vitro*. These models (Tuszynski *et al.* 2004; Sataric *et al.* 2009a) were based on the assumption that actin filaments possess the features of nonlinear electric transmission lines and also by taking into account the polyelectrolyte character of actin filaments. Sequencing a filament into series of elementary units represented by actin monomers and considering them as small capacitors and resistors, we earlier estimated (Sataric *et al.* 2009a) the elementary capacitance to be of the order of $C_0 \sim 10^{-16}$ F and respective ohmic

resistance $R_0 \sim 10^8\ \Omega$. The corresponding characteristic time of discharging such elementary unit is thus given as

$$T_0 = R_0 C_0 \approx 10^{-8}\ \mathrm{s}. \tag{19}$$

Since the length of this elementary unit is the diameter of an actin monomer $d = 5.4$ nm, the velocity of migration of ionic waves along a filament is of the order of a few decimeters per second. This is much more reasonable result compared with very high velocity estimated by Tuszynski *et al.* (2004), which is physically intractable.

3. The nonlinear flux equation for the propagation of Ca^{2+} ions along actin filaments

Let us concentrate on the analysis of how the influx of Ca^{2+} ions through transduction channels can be distributed along actin filaments within the stereocilia. Every single influx is accompanied by the gradient of voltage and the presence of consecutive field E which may depend on time. It brings about that the concentration of the condensed counterions becomes a function both of the time and of the coordinate x directed along the pertinent actin filament. Then the linear concentration of condensed counterions must obey the continuity condition

$$\frac{1}{\mathrm{b}}\frac{\partial \theta}{\partial t} = -\frac{\partial J}{\partial x}, \tag{20}$$

where $J(x,t)$ stands for the Ca^{2+} flux confined along a filament and being the product of linear concentration of Ca^{2+} ions θ/b and their average drift velocity v_d. The drift velocity is provided with the force F acting on an ion and being balanced by the friction of viscosity characterized by the parameter λ

$$F = \lambda v_\mathrm{d}; \quad v_\mathrm{d} = \frac{F}{\lambda}. \tag{21}$$

Thus the ionic flux is expressed as

$$J(x,t) = \frac{\theta}{\mathrm{b}}\left(\frac{F}{\lambda}\right). \tag{22}$$

The force F is primarily the consequence of the presence of the negative gradient of electrochemical potential, given by equation (12), with addition of electric field, Eq (13)

$$F = -\frac{\partial}{\partial x}(\mu_\mathrm{c} - zeEx). \tag{23}$$

In that respect the flux equation (22) becomes

$$J(x,t) = \frac{ze}{\mathrm{b}\lambda}E\theta - \frac{k_\mathrm{B}T}{\lambda}\left[1 - 2z^2\xi\theta\ln\left(\frac{\mathrm{b}}{\Delta}\right)\right]\frac{\partial \theta}{\partial x}, \tag{24}$$

and this implies that on the basis of continuity condition, Eq (20), the equation of motion for concentration of counterions $\theta(x,t)$ has the following shape:

$$\frac{\partial \theta}{\partial t} = -\frac{ze}{\lambda}E\frac{\partial \theta}{\partial x} + \frac{k_\mathrm{B}T}{\lambda}\frac{\partial^2 \theta}{\partial x^2} - \frac{k_\mathrm{B}T}{\lambda}2z^2\xi\ln\left(\frac{\mathrm{b}}{\Delta}\right)\left(\frac{\partial \theta}{\partial x}\right)^2 - \frac{k_\mathrm{B}T}{\lambda}2z^2\xi\ln\left(\frac{\mathrm{b}}{\Delta}\right)\left(\theta\frac{\partial^2 \theta}{\partial x^2}\right). \tag{25}$$

This is obviously the nonlinear partial differential equation of second order. In the case of the presence of the field of small amplitude, Manning (2011) used to linearize the above master equation by neglecting the nonlinear term of gradient squared and also replaced θ in front of second derivative by the equilibrium value θ_0, given by equation (16). It reduced the nonlinear equation to standard diffusion equation. We will return to this option later. Now we will solve equation (25) exactly by the specific procedure applied for solitonic waves. This was motivated by the fact that equation (25) contains the dispersive term $\left(\frac{\partial^2 \theta}{\partial x^2}\right)$ which competes with two nonlinear terms present here.

First, we assume that the influx of Ca^{2+} ions creates the nonequilibrium concentration $\theta(x,t) > \theta_0$, which flows along actin filament in the traveling wave form

$$\theta(x,t) = \theta\left(\frac{x}{l_0} - v\frac{t}{l_0}\right), \tag{26}$$

where $l_0 = 5.4$ nm stands for the length of an actin monomer and v is wave velocity. We should go over to the dimensionless coordinate ζ and time τ with the velocity s, as follows:

$$\zeta = \frac{x}{l_0}; \quad \tau = \frac{t}{T_0}; \quad s = \frac{v}{v_0}; \quad \mathrm{v}_0 = \frac{l_0}{T_0}. \tag{27}$$

The characteristic cut-off velocity v_0 is defined by the time T_0 for what the drift of counterions passes by a single monomer of the length l_0. Therefore expression (26) now reads

$$\theta = \theta(\zeta - s\tau) = \theta(\varphi); \quad \varphi = \zeta - s\tau. \tag{28}$$

On the basis of Eqs. (26) and (28), we have the set of transformations:

$$\frac{\partial\theta}{\partial t}=\frac{\partial\theta}{\partial\tau}\frac{\partial\tau}{\partial t}=\frac{1}{T_0}\frac{\partial\theta}{\partial\tau};\quad \frac{\partial\theta}{\partial x}=\frac{\partial\theta}{\partial\zeta}\frac{\partial\zeta}{\partial x}=\frac{1}{l_0}\frac{\partial\theta}{\partial\zeta};$$
$$\frac{\partial\theta}{\partial\tau}=-s\frac{d\theta}{d\varphi};\frac{\partial\theta}{\partial\zeta}=\frac{d\theta}{d\varphi}. \tag{29}$$

Eventually by taking all exposed transformations given by equation (29) and inserting them in equation (25), instead of partial differential equation, problem is reduced to a nonlinear ordinary differential equation as follows:

$$-\frac{s}{T_0}\frac{d\theta}{d\varphi}=-\frac{ze}{\lambda}\frac{E}{l_0}\frac{d\theta}{d\varphi}+\frac{k_BT}{\lambda l_0^2}\frac{d^2\theta}{d\varphi^2}-\frac{k_BT}{\lambda l_0^2}$$
$$2z^2\xi\ln\left(\frac{b}{\Delta}\right)\left(\frac{d\theta}{d\varphi}\right)^2-\frac{k_BT}{\lambda l_0^2}2z^2\xi\ln\left(\frac{b}{\Delta}\right)\left(\theta\frac{d^2\theta}{\partial\varphi^2}\right). \tag{30}$$

After simple rearrangement this equation can be brought into this compact form:

$$\alpha\frac{d\theta}{d\varphi}+(\beta+\theta)\frac{d^2\theta}{d\varphi^2}+\left(\frac{d\theta}{d\varphi}\right)^2=0, \tag{31}$$

where the two abbreviations were introduced:

$$\alpha=\left(s\frac{l_0^2}{T_0}-\frac{zel_0E}{\lambda}\right)\left[-\frac{k_BT}{\lambda}2z^2\xi\ln\left(\frac{b}{\Delta}\right)\right]^{-1};$$
$$\beta=\left[-2z^2\xi\ln\left(\frac{b}{\Delta}\right)\right]^{-1}. \tag{32}$$

We could reduce the order of equation (31) by the substitutions:

$$\frac{d\theta}{d\varphi}=y(\theta);\quad \frac{d^2\theta}{d\varphi^2}=yy', \tag{33}$$

thus getting the linear differential equation of first order :

$$y'+\frac{1}{\beta+\theta}y=-\frac{\alpha}{\beta+\theta}. \tag{34}$$

After a straightforward calculation and finding the constants of integration from the following conditions

$$\left.\begin{array}{l}\text{for}\quad \theta=\theta_0;\quad y=0,\\ \text{for}\quad \varphi=0;\quad \theta=\theta_0,\end{array}\right\} \tag{35}$$

we obtain the solution in the form of an implicit function $\theta(\varphi)$

$$\theta-\theta_0+(\theta_0-\beta)\ln(\theta-\theta_0)=-\frac{\alpha\beta}{\beta+\theta_0}\varphi. \tag{36}$$

If we introduce the new variable

$$\Delta\theta=\theta-\theta_0=w, \tag{37}$$

the above equation reduces to the simpler version

$$w+(\theta_0-\beta)\ln w=-\frac{\alpha\beta}{\beta+\theta_0}\varphi. \tag{38}$$

Now is the moment to estimate parameters α and β in order to prepare final equation for numerical treatment. It is very easy to calculate β on the basis of definition, see equation (32). Inserting z = 2, ξ = 5.4 and ln(b /Δ) = -1.163, the estimated value of β is

$$\beta=0.02;\quad \beta<<\theta_0=0.45. \tag{39}$$

In the other hand, looking for the parameter α we need to know the viscosity factor λ for a single ion, the order of magnitude of electric field, and the ratio l_0^2/T_0 which has the dimension of the constant of diffusion. The dimensionless wave velocity s could be taken to be exactly one. So, the estimation of parameter α has more uncertainty. Nevertheless we will do it as follows. The viscosity acting on a single Ca^{2+} ion can be roughly estimated for the bulk solution first, starting from Stokes' law of viscous force acting on the sphere

$$F=6\pi\eta rv;\quad \lambda=6\pi\eta r. \tag{40}$$

If the viscosity constant is taken for the water it amounts $\eta \sim 10^{-3}$ Pa·s, while the effective radius of Ca^{2+} ions is $r=2\times10^{-10}$ m. It gives the bulk viscosity:

$$\lambda_b\approx3.7\times10^{-12}\,\frac{\text{Ns}}{\text{m}}. \tag{41}$$

But, this bulk viscosity parameter should be multiplied properly. The increased value is the consequence of the fact that the condensed Ca^{2+} counterions reside quite literally on the surface of filament's landscape which is not smooth. We chose arbitrary to multiple it by five yielding

$$\lambda \approx 1.85 \times 10^{-11} \frac{\mathrm{Ns}}{\mathrm{m}}. \tag{42}$$

Dhont and Kang (2010) mentioned that this parameter was taken to be twenty times greater than the bulk value in order to fit their theoretical model with experimental data collected from fd virus. The ratio l_0^2/T_0 can be evaluated on the basis of a few different approaches. First, we can rely on the characteristic time T_0 from equation (19), thus getting

$$\frac{l_0^2}{T_0} \approx \frac{\left(5.4 \times 10^{-9}\right)^2}{10^{-8}} = 2.9 \times 10^{-9} \frac{\mathrm{m}^2}{\mathrm{s}}. \tag{43}$$

The alternative is to use the expression for the diffusion parameter of bulk solution (Dhont and Kang 2011), $D_0 = 2\times10^{-9}$ m^2/s. Third option is the most realistic one and it represents the effective diffusion parameter elaborated by Manning (2011) for linearized version of master equation (25), and expressed as

$$D_{\mathrm{eff}} = \frac{k_B T}{\lambda}\left[1 - 2z^2 \xi \theta_0 \ln\left(\frac{b}{\Delta}\right)\right], \tag{44}$$

this brings about the numerical value pertinent to Ca^{2+} ions flowing along actin filaments at physiological temperature, yielding:

$$D_{\mathrm{eff}} = 5.4 \times 10^{-9} \frac{\mathrm{m}^2}{\mathrm{s}}. \tag{45}$$

This value is expected to be the best choice because it catches the remarkable features of actin filament as a polyelectrolyte. Very similar results for effective diffusion of counterions were elaborated by Dhont and Kang (2010, 2011). Including above evaluations, we see that for realistic values of intrinsic electric field, which arises from ionic influx through transduction channels and is being in range (10^3–10^4) V/m, the inequality

$$s\frac{l_0^2}{T_0} >> \frac{zel_0E}{\lambda} \tag{46}$$

safely holds. But, if the strong local field of the order of 10^6 V/m is present, then the terms in equation (46) are mutually competitive.

Taking $sl_0^2/T_0 = 6.12\times10^{-9}\mathrm{m}^2/\mathrm{s}$ and $\left[-\frac{k_B T}{\lambda} 2z^2 \xi \ln\left(\frac{b}{\Delta}\right)\right] = 5.7 \times 10^{-9}\mathrm{m}^2/\mathrm{s}$, we eventually get the parameter α posed in front of first derivative in equation (31)

$$\alpha = 1.07 \tag{47}$$

This enables us to complete the specific numerical expression of equation (38) as follows:

$$w + 0.43 \ln w = -0.046\varphi. \tag{48}$$

The graphical shape of above implicite function representing the ionic pulse is shown in figure 4(A). If we take that wave progresses ten times slower ($s = 0.1$)

$$w + 0.43 \ln w = -0.0046\varphi, \tag{49}$$

it leads to the pulse more spread out along filament as shown in figure 4(B). The symbolic view of charge distribution of Ca^{2+} counterions within the localized pulse is given in figure 5.

This nonlinear pulse propagates along actin filament and pertaining counterions do not leak out into solution in despite of the fact that the concentration of bulk counterions Ca^{2+} is much less than the local concentration within the pulse. It seems paradoxical, but it appears that the electrostatic interactions within the ionic cloud remarkably augment the ordinary diffusion providing that actin filaments are the true pathways of the least resistance for Ca^{2+} ionic current. It assures that the propagation of ionic cloud should be faster and protected of leaking out into the bulk endolymph, thus preventing to be caught by calcium buffers. When an incoming ionic pulse sweeps along actin filament, it performs the control role regarding activities of Myo1c motors bridged to this filament. Then this pulse comes to the end position by cuticular plate, the cytoskeletal anchor for the stereocilia bundle, where mitochondria are conspicuously concentrated. The mitochondria are primarily responsible for generating adenosine 5'-triphosphate (ATP) that fuels Myo1c motors. Mitochondria also affect Ca^{2+} balance fueling PMCA pumps that extrude calcium from hair bundle and themselves act as a large-capacity calcium store (Nicholls 2005).

Let us now consider shortly of how Ca^{2+} ions influence the cross-bridge cycle of Myo1c motors in hair bundles. It was shown experimentally (Adamek *et al.* 2008) that calcium inhibits the rate of ATP hydrolysis process which powers the energy for Myo1c strength and at the same time calcium accelerates the release of ADP, the product of hydrolysis. In that way calcium induces the accelerations of cross-bridge detachment enabling Myo1c to slide or climb up along actin filament. The transient increase in calcium concentration should reduce the stiffness of the so called lever arm of

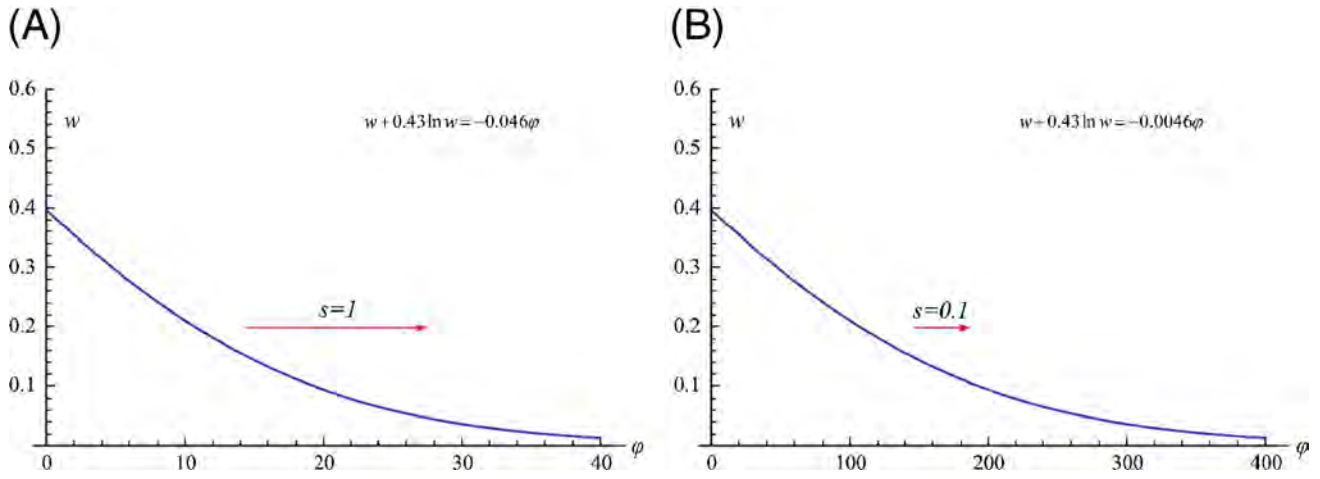

Figure 4. (**A**) Numerical solution of the function $w(\varphi)$ if dimensionless velocity s is equal to 1. (**B**) The shape of the same function for ten time slower pulse ($s = 0.1$). This pulse is spread out remarkably in comparison with first one.

Myo1c. This is lowering the strain in the same motor allowing ADP to escape and motor itself to detach from filament and to slide along. The detachment of motor is followed by the ATP hydrolysis before the cross-bridge to actin filament is reestablished. In the presence of Ca^{2+} ions, the 7-fold reduction in the rate constant for ATP hydrolysis should adequately increase the life time of detached state, allowing longer time for slippage of a motor along the filament (Adamek *et al.* 2008). It was already stressed that troponin molecules are important mediators in this catalytic action of Ca^{2+} ions (Karkanevatos 2001).

In the context of the model presented here, it is reasonable that faster ionic pulse will spend shorter time in the vicinity of operating motors. During that time the motor is detached and adapts its position in order to remove the cause that brought about its deactivation. If we take that the cut-off velocity of ionic pulse

$$v_0 = \frac{l_0}{T_0} = \frac{5.4 \times 10^{-9}}{10^{-8}} \approx 0.54 \frac{\mathrm{m}}{\mathrm{s}}, \tag{49}$$

and the length of that pulse from figure 4(A) is $\Delta L = 20 \times l_0 \approx 0.11\,\mu\mathrm{m}$, the corresponding time of Ca^{2+} impact on Myo1c is of the order of

$$\tau = \frac{\Delta L}{v_0} = \frac{0.11\,\mu\mathrm{m}}{0.54 \frac{\mathrm{m}}{\mathrm{s}}} \approx 0.21 \times 10^{-6}\mathrm{s}. \tag{50}$$

For the case represented in graph from figure 4(B), the time is longer for two orders of magnitude $\tau \approx 2.1 \times 10^{-5}$ s. Generally, the pulses with lower velocity should spend more time in catalyzing the detachment of motors and they tune the processes of lower frequencies. The velocity and the length of a pulse are determined by the opening dynamics of transduction channels, which in turn is dictated by the incoming acoustic signals.

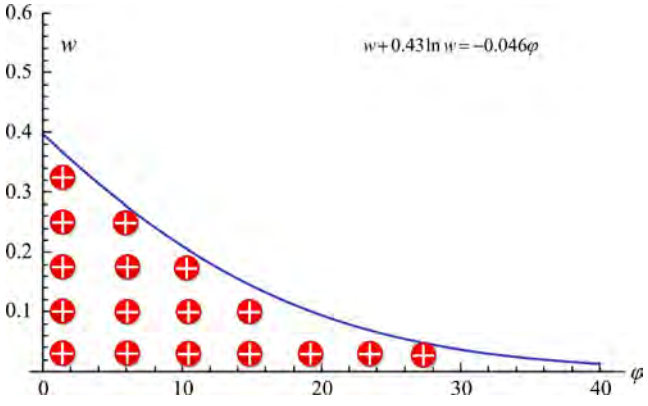

Figure 5. The symbolic view of charge distribution of Ca^{2+} counterions within localized pulse.

4. Discussion and conclusion

At least two motives were the reason for us in an attempt to contribute in resolving the very important problem of how calcium ions efficiently control the activities of Myo1c adaptation motors, implicated in mechanoelectrical transduction in the stereocila of the inner ear. First one is the fact that actin filaments are the true polyelectrolytes *in vivo* conditions and the very profound theory of rodlike polyelectrolytes was systematically developed by Manning (1978, 1993, 1996, 2011). Secondly, we were intrigued by some earlier experiments (Lin

and Cantiello 1993; Priel *et al*. 2006) which indicated that actin filaments and microtubules exhibit the amplifying effect for ionic conduction in dilute solution, *in vitro*.

In the introduction we shortly explained the mechanisms of mechanoelectrical transduction of hair cells emphasizing the role of Ca^{2+} ions in tuning these mechanisms. The polyelectrolytes nature of actin filaments was carefully documented with estimations of relevant parameters as linear charge spacing, the Bjerrum length, Debye length and fractional coverage of a filament with calcium counterions. In parallel, we made a short reminder of our earlier approach based on the electric transmission line model for ionic flow along actin filaments (Sataric *et al*. 2009a).

The main part of paper is dedicated to the application of seminal Manning's model (Manning 2011) for calcium ionic pulse propagation along actin filaments within the stereocilia. Instead of simplifying the master equation (25), we performed an exact solution using the unified space-time variable φ for traveling wave. That was initiated by the fact that nonlinear character of equation (25) suggests that the competition between dispersion, governed by the second derivative term, and nonlinearity, represented by the gradient squared term, should lead to creation of a kind of stable pulse localized enough to persist propagating with gradual distortion due to the friction. Second argument for such expectation was the one-dimensionality of this phenomenon which prevents the spatial dispersion. We obtained the solution which is somewhere between kink-like and usual diffusive profile, and which propagates with roughly estimated velocities bounded with cut off value of the order of decimetres per second. Based on such estimations, we were able to extract the conclusion that this mechanism of calcium distribution within stereocilia must be much more efficient than ordinary bulk diffusion. These shielded pulses of ionic clouds are more suitable to fast reach the Myo1c motors and to control their activities. The general outcome is that Ca^{2+} ions within a pulse accelerate of cross-bridge detachment and increase lifetime of detached cross-bridge. The time scale of this process is dictated by the velocity and the length of a single pulse which is defined by the time course of opening and closing of pertinent ionic channels.

Beurg *et al*. (2010) found that raising the calcium level close to hair-cell transduction channels increases the oscillating frequency of hair bundle and decreases its amplitude. Since increased Ca^{2+} level enables injection of faster pulse along actin filament, this pulse detaches for shortly Myo1c motors and they catch the filament soon again reversing the direction of movement of the bundle. In a word, these short and fast pulses accelerate cross-bridge attachment-detachment dynamics. The opposite is true for slow pulses dictated by small influx through transduction channels.

The quantitative relation of ionic pulses with mechanoelastic performances of hair bundles will be presented in a separated article. In final conclusion, it is very probably that Ca^{2+} ions play similar roles in insulin-mediated glucose uptake in which Myo1c is also basically implicated (Bose *et al*. 2002).

Acknowledgements

This research was supported by the Ministry of Education, Science and Technological Development of the Republic of Serbia through Projects: OI171009 and III43008, and Project of Serbian Academy of Sciences and Arts.

References

Adamek N, Coluccio LM and Geeves MA 2008 Calcium sensitivity of the cross-bridge cycle of Myo1c, the adaptation motor in the inner ear. *Proc. Natl. Acad. Sci. USA* **105** 5710–5715

Beurg M, Nam JH, Chen Q and Fettiplace R 2010 Calcium balance and mechanotransduction in rat cochlear hair cells. *J. Neurophysiol.* **104** 18–34

Bose A, Guilherme A, Robida SI, Nicoloro SMC, Zhou QL, Jiang ZY, Pomerleau DP and Czech MP 2002 Glucose transporter recycling in response to insulin is facilitated by myosin Myo1c. *Nature* **420** 821–824

Dhont JKG and Kang K 2010 Electric-field-induced polarization and interactions of uncharged colloids in salt solutions. *Eur. Phys. J. E.* **33** 51–68

Dhont JKG and Kang K 2011 Electric-field-induced polarization of the layer of condensed ions on cylindrical colloids. *Eur. Phys. J. E.* **34** 40

Gartzke J and Lange K 2002 Cellular target of weak magnetic fields: ionic conduction along actin filaments of microvilli. *Am. J. Physiol. Cell Physiol.* **283** C1333–C1346

Gillespie PG and Cyr JL 2004 Myosin-1c, the hair cell's adaptation motor. *Annu. Rev. Physiol.* **66** 521–549

Helmholtz HLF 1954 *On the sensations of tone as a physiological basis for theory of music* (New York: Dover Publications)

Israelachvili JN 1992 *Intermolecular and surface forces: With applications to colloidal and biological systems* (London: Academic Press)

Karkanevatos A 2001 Ultrastructural localization of cytoskeletal proteins in guinea-pig cochlear hair cells. M. Phil Thesis, Keele University, UK

Lin EC and Cantiello HF 1993 A novel method to study the electrodynamic behavior of actin filaments. Evidence for cable-like properties of actin. *Biophys. J.* **65** 1371–1378

Lumpkin EA and Hudspeth AJ 1995 Detection of Ca^{2+} entry through mechanosensitive channels localizes the site of mechanoelectrical transduction in hair cells. *Proc. Natl. Acad. Sci. USA* **92** 10297–10301

Lumpkin EA and Hudspeth AJ 1998 Regulation of free Ca^{2+} concentration in hair-cell stereocilia. *J. Neurosci.* **18** 6300–6318

Manning GS 1978 The molecular theory of polyelectrolyte solutions with applications to the electrostatic properties of polynucleotides. *Q. Rev. Biophys.* **11** 179–246

Manning GS 1993 A condensed counterion theory for polarization of polyelectrolyte solutions in high fields. *J. Chem. Phys.* **99** 477–486

Manning GS 1996 Counterion condensation theory constructed from different models. *Phys. A.* **231** 236–253

Manning GS 2008 Approximate solutions to some problems in polyelectrolyte theory involving nonuniform charge distributions. *Macromolecules.* **41** 6217–6227

Manning GS 2011 A counterion condensation theory for the relaxation, rise, and frequency dependence of the parallel polarization of rodlike polyelectrolytes. *Eur. Phys. J. E.* **34** 39

Martin P, Bozovic D, Choe Y and Hudspeth AJ 2003 Spontaneous oscillation by hair bundles of the bullfrog's sacculus. *J. Neurosci.* **23** 4533–4548

Nam JH, Cotton JR, Peterson EH and Grant W 2006 Mechanical properties and consequences of stereocilia and extracellular links in vestibular hair bundles. *Biophys. J.* **90** 2786–2795

Nicholls DG 2005 Mitochondria and calcium signaling. *Cell Calcium.* **38** 311–317

Priel A, Ramos AJ, Tuszynski JA and Cantiello HF 2006 A biopolymer transistor: electrical amplification by microtubules. *Biophys. J.* **90** 4639–4643

Ricci AJ, Crowford AC and Fettiplace R 2003 Tonotopic variation in the conductance of the hair cell mechanotransducer channel. *Neuron* **40** 983–990

Ruggero MA 1992 Responses to sound of the basilar membrane of the mammalian cochlea. *Curr. Opin. Neurobiol.* **2** 449–456

Sataric MV, Bednar N, Sataric BM and Stojanovic G 2009a Actin filaments as nonlinear RLC transmission lines. *Int. J. Mod. Phys. B.* **23** 4697–4711

Sataric MV, Ilic DI, Ralevic N and Tuszynski JA 2009b A nonlinear model of ionic wave propagation along microtubules. *Eur. Biophys. J.* **38** 637–647

Sekulic DL, Sataic BM, Tuszynski JA and Sataric MV 2011 Nonlinear ionic pulses along microtubules. *Eur. Phys. J. E.* **34** 49

Tang JX and Janmey PA 1996 The polyelectrolyte nature of F-actin and the mechanism of actin bundle formation. *J. Biol. Chem.* **271** 8556–8563

Tuszynski JA, Portet S, Dixon JM, Luxford C and Cantiello HF 2004 Ionic wave propagation along actin filaments. *Biophys. J.* **86** 1890–1903

MS received 14 October 2014; accepted 23 July 2015

Corresponding editor: Vidita A Vaidya

Eur. Phys. J. E (2011) **34**: 49
DOI 10.1140/epje/i2011-11049-0

THE EUROPEAN PHYSICAL JOURNAL E

Regular Article

Nonlinear ionic pulses along microtubules

D.L. Sekulić[1,a], B.M. Satarić[1], J.A. Tuszynski[2,3], and M.V. Satarić[1]

[1] Faculty of Technical Sciences, University of Novi Sad, Trg D. Obradovića 6, 21000 Novi Sad, Serbia
[2] Department of Oncology, Cross Cancer Institute, University of Alberta, Edmonton, Alberta, Canada
[3] Department of Physics, University of Alberta, Edmonton, Alberta, Canada

Received 27 December 2010 and Received in final form 24 March 2011
Published online: 23 May 2011 –

Abstract. Microtubules are cylindrically shaped cytoskeletal biopolymers that are essential for cell motility, cell division and intracellular trafficking. Here, we investigate their polyelectrolyte character that plays a very important role in ionic transport throughout the intra-cellular environment. The model we propose demonstrates an essentially nonlinear behavior of ionic currents which are guided by microtubules. These features are primarily due to the dynamics of tubulin C-terminal tails which are extended out of the surface of the microtubule cylinder. We also demonstrate that the origin of nonlinearity stems from the nonlinear capacitance of each tubulin dimer. This brings about conditions required for the creation and propagation of solitonic ionic waves along the microtubule axis. We conclude that a microtubule plays the role of a biological nonlinear transmission line for ionic currents. These currents might be of particular significance in cell division and possibly also in cognitive processes taking place in nerve cells.

1 Introduction

Microtubules (MTs) are major cytoskeletal protein polymers assembled from the protein called tubulin that plays a number of crucial biological roles in all eukaryotic cells [1]. The role of MTs in cell division has been extensively discussed in the cell biology literature. In this paper, we focus on the importance of MTs in the process of ionic current regulation within biological cells. Many years ago Matsumoto *et al.* [2] revealed that axoplasmic MTs and 260 K proteins in the structure underlying the axolema play a role in generating Na^+ currents in squid giant axons. Another seminar paper [3] considered the importance of Ca^{++} ionic currents in cell division and emphasized that MTs in the mitotic apparatus might be controlled by the local Ca^{++} concentration which should be tuned by nearby endoplasmic reticulum (ER). Spindle MTs appear to be very sensitive to Ca^{++} concentration increases in such a way that MT depolymerisation occurs when the concentration is raised above $1\,\mu$M. It was suggested that during anaphase Ca^{++} release from ER activates MT depolymerisation and this facilitates movement of chromosomes to the spindle poles [4]. Here, we postulate that localized Ca^{++} ionic currents along MTs serve as triggers for the onset of their depolymerisation. The synchronously regulated separation of sister chromatid pairs in mitotic spindles has been recently described by Matsson [5,6] using an elegant nonlinear theoretical model. We propose that the process of MT depolymerisation involved in cell division is finely orchestrated by Ca^{++} influx from ER which propagates along MTs as a nonlinear wave.

The structure of MTs is cylindrical and it typically involves 13 parallel protofilaments *in vivo*, see fig. 1. The building block of a MT is a tubulin dimer (TD) that contains approximately 900 amino acid residues comprising some 14000 atoms with a combined mass of 110 kDa (1 Da is the atomic unit of mass, $1\,\mathrm{Da} = 1.7 \times 10^{-27}$ kg). The TD is made up of two structurally slightly different monomers called α and β tubulin, respectively. Each TD in the MT has a length of 8 nm along the MT cylinder axis, a width of about 6.5 nm and the radial dimension of 4.6 nm. The inner core of the cylinder, known as the lumen, is approximately 15 nm in diameter. The surface of MTs is mostly characterized by a so-called B-lattice structure [7], see fig. 2.

Between neighboring protofilaments there are two distinct types of nanopores (NP). NP-1, see fig. 2, left panel, is located where an inter-dimer β/α interface of one TD lies next to the inter-dimer β/α interface of the adjacent TD molecule. The so-called NP-2 arises where an intra-dimer interface of one dimer lies next to the intra-dimer interface of an adjacent TD of a neighboring protofilament, see fig. 2, right panel. Freedman *et al.* [8] used HOLE and AMBER programs to estimate the effective radius of the narrowest points within these NPs and found them to be 0.4 nm and 0.47 nm for type-1 and type-2 NPs, respectively.

The biological relevance of NPs in MT is still largely unknown. However, it has been experimentally determined

[a] e-mail: dalsek@yahoo.com

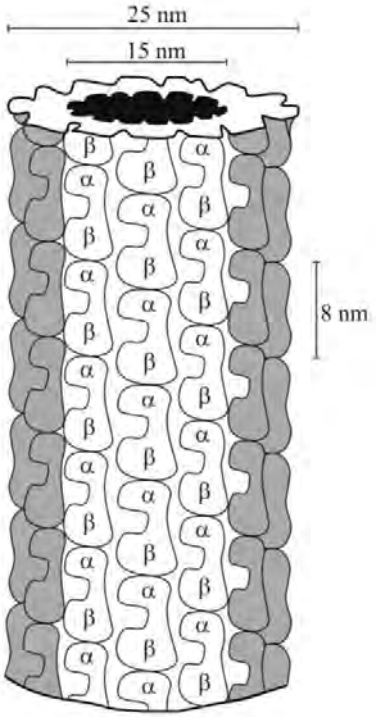

Fig. 1. A MT hollow cylinder of 13 parallel protofilaments with denoted characteristic dimensions: outer and inner diameters of 25 nm and 15 nm, respectively, and tubulin dimer length of 8 nm.

that the molecules of some chemotherapy drugs such as paclitaxel and epothilone diffuse through MT NPs to their corresponding binding sites mostly positioned in the lumen [9]. Thus, it can be safely assumed that these NPs, on the basis of their size, should be quite permeable to the counter-ions from the ionic clouds covering outer and inner sides of the MT wall. This paper will theoretically examine the role of these NPs in the regulation of ionic currents along MTs within the regime comparable to transmission lines used in electric engineering applications. We have earlier made preliminary attempts to evaluate MTs as nonlinear transmission lines. The first stage was a model which disregards the role of NPs but includes the nonlinear electric capacity of MTs [10]. The outcome of this model was the appearance of stable localized kink-like pulses of cations propagating along MTs. The next step was extended by the inclusion of NPs [11]. This approach was based on the simple conical geometry pattern of NPs considered earlier by the group of Eisenberg [12]. This preliminary description of NPs in our model has led to the emergence and propagation of ionic pulses analogous to the celebrated Korteveg de Vries (KdV) solitons and was arrived at using reasonable values of model parameters.

This paper is intended to develop a much more realistic model based on the sophisticated simulations performed by Freedman *et al.* [8]. We briefly state the main results of the simulations reported in [8] which are relevant for the model considered here. Based on the modified version of the Poisson-Boltzmann equation, the conductances of NPs are determined in terms of Brownian dynamics of ions. For the type-1 NP, inner and outer cationic conductances were calculated to be 2.93 nS and 1.22 nS, respectively, while for type-2 NP the respective values of 7.80 nS and 4.98 nS were found. Interestingly, it was demonstrated that both types of NPs are impermeable to anions whose respective conductances are 0.044 nS and 0.012 nS for type-1 and type-2 NPs. Freedman *et al.* [8] also explained in great detail how the constriction zones of NPs, due to the presence of negative ASP and THR residues, prevent the passage of more negative ions through the NPs. Similar asymmetric conductance has been found in various experiments involving ion channels, for example Omp F porin [13].

We now focus on the second, an even more important constituent of MTs in the context of the present model. Each tubulin monomer of the MT lattice has a short C-terminal alpha-helix H12 followed by a highly acidic amino acid sequence projecting out of the MT outer surface which is referred to as a tubulin tail (TT). Geometrically, these TTs are hair-like projections of 4–5 nm length, see fig. 3. Their approximate molecular masses are 5.5 kDa and 6.7 kDa for α and β tubulin, respectively. TTs are of great functional importance because they participate in the binding of proteins through which MT interact with many cellular structures such as motor proteins (kinesin and dynein) and a plethora of microtubule associated proteins (MAPs) [14]. Satarić and Tuszynski [15] developed a model of nonlinear waves created by tilting excitations of TTs emphasizing their possible role in the control of motor protein traffic along MTs. In α tubulin the TT consists of the last 10 residues in their sequence, while in β tubulin the corresponding TT is longer comprising 18 residues. The most common isotype of α tubulin has a TT with 5 Glu and 2 Asp residues, while its β counterpart has 9 Glu and 2 Asp residues. The negative charge on TTs is the reason why they are surrounded by a large number of cations required for overall charge neutrality. The important aspect of the aforementioned modeling [8] is the claim that TTs could contribute to ionic currents flowing along MTs by playing the role of small voltage generators (batteries). This claim is based on their larger time-scale thermal fluctuations which result in an oscillatory transfer of ions between the bulk solution and the cloud of counterions located near the MT surface. Here, we partly rely on the results of the simulations reported in [8] and partly on our earlier transmission line analysis [11], in order to elucidate the possible active role MTs play in ionic signaling throughout cytoskeletal networks.

The paper is organized as follows: In sect. 2 we explain the polyelectrolyte character of MTs. In sect. 3 we describe the basic elements of MTs as a biological nanoscale transmission line. In sect. 4 we analyze a nonlinear differential equation of the modified KdV type for the electric potential accompanying a localized ionic wave along an MT. Then, we solve and analyze the pertaining differential equation which exhibits the common features with spherical and cylindrical solitons arising in ion-acoustic waves in plasma. Section 5 provides conclusions stemming from the results of this paper.

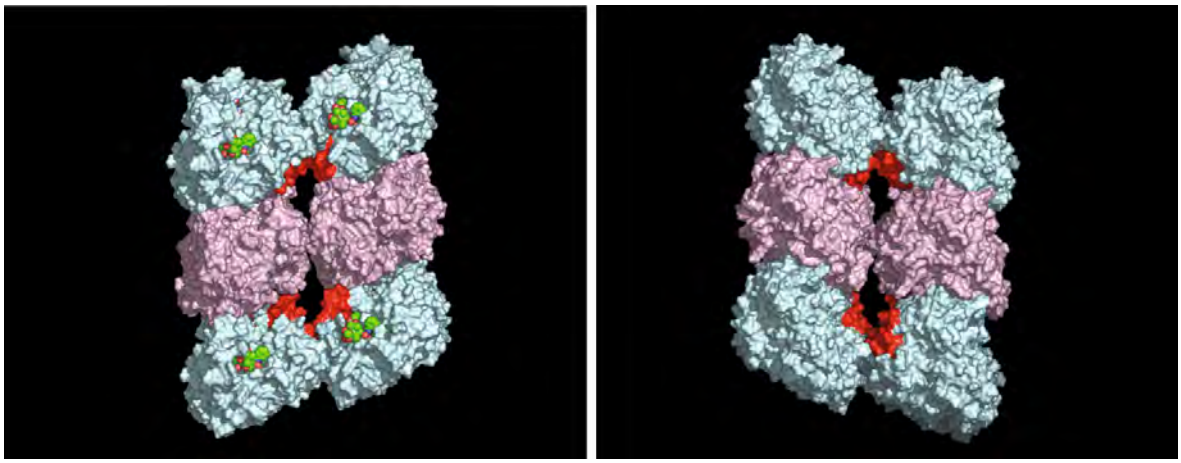

Fig. 2. An illustration of the nanopores in the A and B MT lattices, respectively.

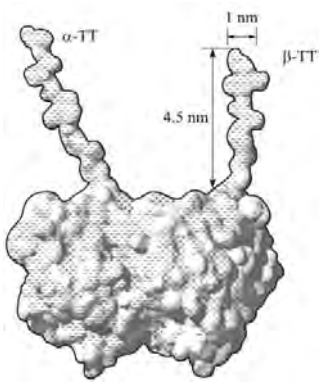

Fig. 3. The topology of a tubulin dimer with TTs whose dimensions are: length of 4.5 nm and diameter of 1 nm. The surface charge distribution is indicated by plus and minus signs.

2 The biophysical basis for the model

Extensive molecular dynamics simulations were performed on the TD structure and MTs [16,17]. Their results indicate the existence of a highly negatively charged solvent exposed surface of the TD with a net electric charge on the order of (20–25)e per monomer, depending on the isotype of tubulin considered. This net charge is distributed preferentially on the outer surface of the MT at an approximate charge ratio of 2:1 between the outer surface and the rest of the protein. Therefore, we conclude that MTs as highly charged polyelectrolytes are expected to attract a fraction of their surrounding counter-ions in the form of a condensed ionic cloud (IC) preferentially localized around the MT surface.

Manning's theory of polyelectrolyte solutions [18] states that ionic condensation occurs along the stretch of a charged polymer, if a sufficiently high linear electric charge density is present on the polymer's surface. On this basis, it can be concluded that the cylindrical sheath of depleted ions outside the ionic cloud surrounding the MT serves as an electrical shield. The "cable-like" behavior of such a structure can be supported by the protein polymer itself and the "condensed" counter-ions, which are physically "bound" to the polymer. The strength of this interaction has been estimated to be such that even under infinite dilution conditions, the counter-ions are still attached to the polymer and do not diffuse out from its vicinity. Although this theory was originally postulated for such polyelectrolytes as DNA, the same applies to highly charged quasi-one-dimensional, or cylindrical polymers such as actin filaments and MTs. These two cases were studied theoretically in more detail in other publications [8,10,19–22] and we adopt this approximation as valid for the case considered in our paper.

Moreover, experimental confirmation of the novel nonlinear amplification of ionic currents by MTs serves as support for this model [23]. Since our model is directly based on the ionic condensation effect around the MT cylinder, we first evaluate the effective charge density around the MT length. The Bjerrum length, denoted l_B, describes the distance beyond which thermal fluctuations are stronger than the electrostatic interactions between charges in solution whose dielectric constant is ε. Specifically, the following equation is satisfied:

$$\frac{e^2}{4\pi\varepsilon_0\varepsilon l_B} = k_B T; \quad \varepsilon_0 = 8.85 \times 10^{-12}\,\mathrm{F/m}. \tag{2.1}$$

At a physiological temperature ($T = 310\,\mathrm{K}$), taking the elementary charge as $e = 1.6 \times 10^{-19}\,\mathrm{C}$, Boltzmann's constant as $k_B = 1.38 \times 10^{-23}\,\mathrm{J/K}$ and the relative dielectric permittivity of the cytosol as $\varepsilon = 80$, one readily obtains

$$l_B = 0.67 \times 10^{-9}\,\mathrm{m} = 0.67\,\mathrm{nm}. \tag{2.2}$$

Accordingly, every MT should attract an IC of positive counter-ions close to its surface and along TTs, while negative ions of the cytosol are repelled away from the MT surface so that a roughly cylindrical ionic depletion area around TDs and TTs emerges. The thickness of such a depleted area is approximately equal to the Bjerrum length.

In addition, counter-ion condensation occurs when the mean distance between two charges, b, is such that

$$S = \frac{l_B}{b} > 1. \tag{2.3}$$

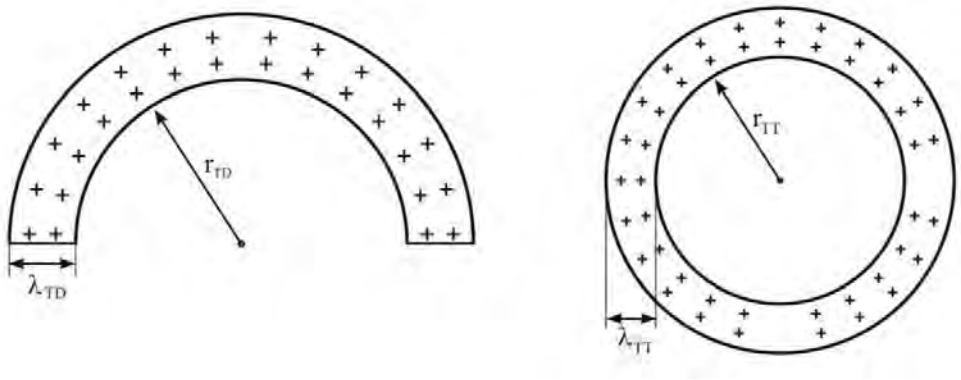

Fig. 4. Schematic representation of the counter-ion charge distributions surrounding a microtubule (left panel) and a C-terminal tail (right panel).

As a reasonable approximation we assume that each β tubulin monomer carries an excess of 24 negative charges in vacuum while each α tubulin monomer carries 22 charges. Moreover, some 30–40% of the net charge is located in areas of tubulin that are not solvent accessible. Therefore, we expect to have 15–18 exposed negative charges per TD, without counting the charges present on the protruding TTs. Since each dimmer is 8 nm long and 13 protofilaments form a MT, we readily find that there is a linear charge of (20–30)e/nm and a linear charge spacing of $b = (0.33\text{–}0.44) \times 10^{-10}$ m which gives S in the range between 16 and 21. As the effective charge q_{eff} is defined as the bare value of net charge divided by S, we estimate it to be $q_{\text{eff}} = (0.43\text{–}0.57)e$/monomer. This quantity has been indirectly measured in experimental assays where MTs were subjected to external electrical fields [23]. However, it should also be noted that this number represents a "far-field" value which could be overly high since it belies additional screening which is achieved by all ions attached to the MT but not all necessarily condensed on it. We conclude that in view of the experimental data, these estimates are acceptable for our continuum model calculations. For this type of model it is important to estimate the thickness of an IC of positive counter-ions around MTs and TTs. This is dictated by the geometry of the surface landscape and by its negative charge distribution.

The occurrence of Manning condensation around the polymer of radius r also depends on the fact that the salt concentration n in the cytosol should be low enough to satisfy the inequality [24]

$$l_{\text{Db}} \gg r, \tag{2.4}$$

where the Debye length l_{Db} is defined by

$$l_{\text{Db}}^{-1} = (8\pi n l_B)^{1/2}. \tag{2.5}$$

Since the radius of a TT is of the order of 0.5 nm and the radius of a TD is of the order of 2.5 nm, while the Debye length for the cytosol is of the order of 10 nm [25], we see that the condition in (2.4) holds for both radii. Thus, we are now able to reliably estimate the respective condensate thickness λ

$$\lambda = A(r l_{\text{Db}})^{1/2}; \quad A < 1, \tag{2.6}$$

where A depends only weakly on the Manning parameter q_0. Taking $A = 1/2$ one finds the corresponding values for the TD (λ_{TD}) and TT (λ_{TT}) as follows:

$$\lambda_{\text{TD}} = 2.5\,\text{nm}; \qquad \lambda_{\text{TT}} = 1.1\,\text{nm}. \tag{2.7}$$

These values will be used in our calculations of the corresponding capacity and resistivity, see fig. 4.

We expect that this IC which is shielded from the cytosol by a depleted layer is an analog of a coaxial cable used in electrical engineering applications, so MTs may effectively act as nonlinear inhomogeneous transmission lines capable of propagating nonlinear dispersive ionic waves within an IC. Independent corroboration of this idea can be found in experimental assays first performed for actin filaments [26] demonstrating that an IC current along a single filament exhibits localized wave patterns similar to solitons in nonlinear electric LC transmission lines. Recently, a similar experiment was conducted on single MTs providing evidence of the amplification of input electrical signals [23]. In our model of IC currents we only consider one of the 13 parallel currents associated with a single protofilament. The elementary unit of this "nanowire" is one tubulin dimer with adjacent NPs (type-1 and type-2) and two associated TTs (α and β). The shape of a tubulin dimer with extended α- and β-TTs is presented in fig. 3, including the charge distribution on its surface. At neutral pH values, the negative charge on each TT causes it to be extended away from the MT surface due to the electrostatic repulsion. When the negative charges of the amino acids within a TT are partly neutralized by counter-ions condensed around, it will cause TTs to contract by folding as shown in fig. 5.

As mentioned earlier, the differences in the structures of α- and β-TTs will cause them to fold differently so that the β-TT is expected to shrink to a greater extent. In addition to these electrostatically generated conformations of TTs, their tilting oscillations due to thermal fluctuations of the environment are also present. Quantitative features of this effect will be presented in the next section. These effects are accompanied by a change in the electrostatic capacity contributed by TTs which inevitably leads

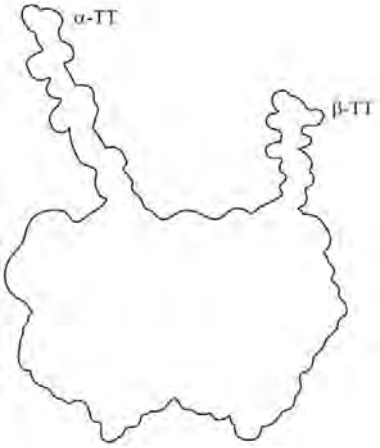

Fig. 5. The shape of TTs, where β-TT is shown to have shrunk due to the surrounding counter-ions, thus diminishing its electrostatic capacity.

to a slightly nonlinear overall capacity of every elementary unit of the ionic current along each filament.

3 The model parameters of an MT as an electric transmission line

Here, we proceed to estimate the electric parameters of an elementary unit of each MT protofilament (EUP). The essential assumption could be that an MT with a condensed IC is separated from the rest of the ions in the bulk solution by a depleted layer which plays the role of a dielectric medium located between the MT and the bulk cytosol. This IC is a conductive medium which dictates the electrical features of MTs. The depleted layer results in the IC and repelled anions playing the roles of "conductive plates" of a cylindrical capacitor. The ions injected from an appropriate cellular compartment are primarily confined to flow along an MT within its IC whose estimated thickness is $\lambda_{\rm TD} = 2.5\,{\rm nm}$.

For example, the opening of inositol (1, 4, 5) triphosphate (IP_3) receptors clustered at specific sites on the ER can lead to large-scale intracellular calcium waves [3,27]. By novel experimental techniques that permit the visualization of subcellular events it has become clear that Ca^{++} dynamics is a highly localized process with respect to these release events and also by the channelling of these waves along cytoskeletal filaments, primarily MTs. We have earlier proposed that such Ca^{++} waves could cause controlled MT depolymerisation during mitosis.

3.1 The capacitance of an EUP

In an earlier paper [10], a detailed Poisson-Boltzmann approach was used to evaluate the capacitance of an elementary ring of an MT which consists of 13 dimers. Here, we

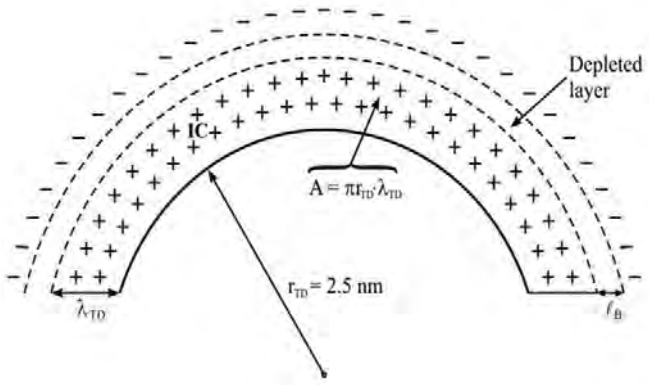

Fig. 6. Schematic illustration of the calculation of the MT capacitance.

adopt the same expression which reads

$$C_0 = \frac{2\pi\varepsilon_0\varepsilon l}{\ln\left(1+\frac{l_B}{R_{\rm IC}}\right)}\,, \tag{3.1}$$

where l stands for the length of a polymer unit and $R_{\rm IC} = r_{\rm TD} + \lambda_{\rm TT}$ for the outer radius of an IC. The other parameters have already been introduced.

We first estimate the EUP capacitance contributed by a TD, see fig. 6. With $l_{\rm TD} = 8\,{\rm nm}$ and $R_{\rm IC} = r_{\rm TD} + \lambda_{\rm TT} = 2.5\,{\rm nm} + 2.5\,{\rm nm} = 5\,{\rm nm}$, we find for TD (including only the outer surface)

$$C_{\rm TD} = \frac{3.14\times 80\times 8.85\times 10^{-12}\times 8\times 10^{-9}}{\ln\left(1+\frac{0.67}{5}\right)}\,{\rm F} = 1.4\times 10^{-16}\,{\rm F}. \tag{3.2}$$

Analogously, we can consider an extended TT as a smaller cylinder with the radius $r_{\rm TT} = 0.5\,{\rm nm}$ and the thickness of its IC equal to $\lambda_{\rm TT} = 1\,{\rm nm}$. Its extended effective length should be $l_{\rm TT}^{\rm eff} = 4.5\,{\rm nm} - 2.5\,{\rm nm} = 2\,{\rm nm}$, meaning that its part close to the tubulin surface is already embedded in the IC accounted for in (3.2). Thus we now estimate the corresponding capacitance as:

$$C_{\rm TT} = \frac{2\times 3.14\times 80\times 8.85\times 10^{-12}\times 2\times 10^{-9}}{\ln\left(1+\frac{0.67}{1.5}\right)}\,{\rm F} = 0.26\times 10^{-16}\,{\rm F}. \tag{3.3}$$

Accounting for the fact that two TTs are present in each tubulin dimer, we finally obtain

$$2\times C_{\rm TT} = 0.52\times 10^{-16}\,{\rm F}. \tag{3.4}$$

The two capacitance values above are considered to correspond to a parallel arrangement with respect to each other, so that the total maximal capacitance of an EUP is readily estimated as

$$C_0 = C_{\rm TD} + 2\times C_{\rm TT} = 1.92\times 10^{-16}\,{\rm F}. \tag{3.5}$$

We have earlier emphasized that TTs capacitance must change with an increasing concentration of condensed

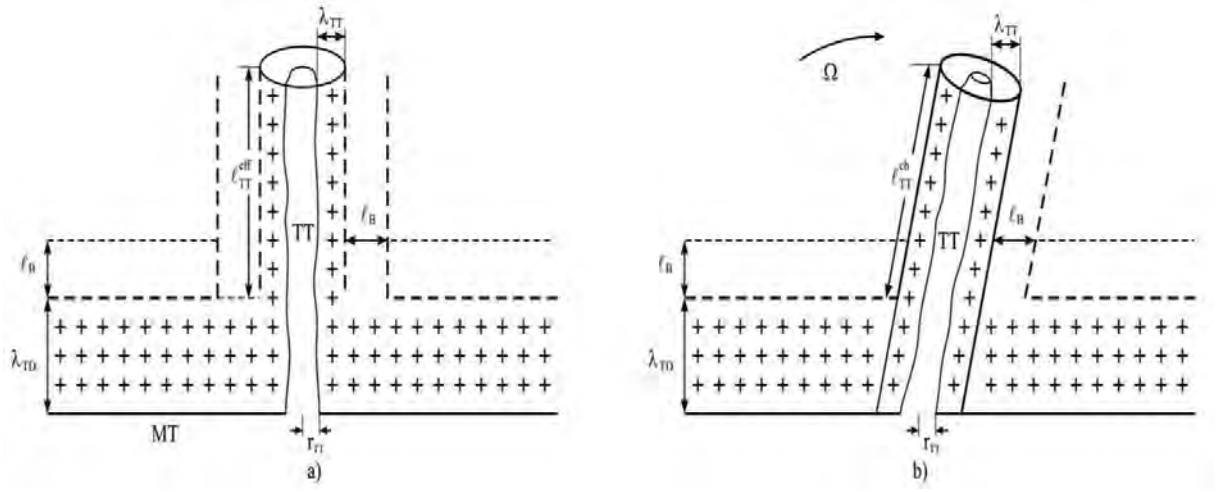

Fig. 7. A comparison between an extended TT (a) and a tilting TT due to oscillations (b).

cations due to the shrinking of flexible TTs. These changes are slightly different due to the different structures of α- and β-type TTs. To include this case we introduce the reduced factor of nonlinearity as follows:

$$b_0 = \frac{b_\alpha b_\beta}{b_\alpha + b_\beta}, \tag{3.6}$$

where b_α and b_β stand for the respective TTs. This implies that the charge of an EUP capacitor diminishes with an increased voltage in a nonlinear way $\Delta C_0 = C_0 b_0 v$, $b_0 v \ll 1$. Additionally, we account for the tilting movements of TTs under the combined action of thermal fluctuations [8] and a changing voltage due to an incoming ionic wave. Thus, the part of EUP capacitance contributed by TTs should also change by TTs tilt as shown in fig. 7. The change of the effective length $l_{\rm TT}^{\rm eff}$ of a TT is an additional factor affecting the capacitance $\Delta C_{\rm TT}$. We assume that this change can be adequately described by the oscillating function

$$\Delta l_{\rm TT}^{\rm eff} = l_{\rm TT}^{\rm eff} \sin[\Omega(t - t_0)] \cong l_{\rm TT}^{\rm eff} \Omega (t - t_0). \tag{3.7}$$

So that the capacitance changes linearly with a change in the effective TTs length $\Delta l_{\rm TT}^{\rm eff}$

$$\Delta C_{\rm TT} = C_0 \Gamma_0 \Omega (t - t_0), \tag{3.8}$$

where the frequency Ω is much lower than the inverse charging time of the EUP capacitor due to the strong viscous damping of the TT tilt, thus justifying the linearization of the above sine function in eq. (3.7). In some sense, this effect is similar in character to the thermal ratchet mechanism combined with an asymmetric ionic potential. Including the two aspects of TTs dynamics described above, the charge of EUP can be expressed as follows

$$Q = C_0[1 - \Gamma_0 \Omega (t - t_0) - b_0 v] v, \tag{3.9}$$

where Γ_0 is a dimensionless parameter.

In the earlier simplified version of the model of ionic currents along MT [10], a proof was given that the order of magnitude of magnetic inductance is so small that its role in these transmission lines can be safely ignored. We accept this statement in the present paper.

3.2 The resistance of an EUP

Regarding the Ohmic resistance, if we ignore ionic current leaks through the depleted layer, the dominant current flows in parallel with the MT axis charging EUP capacitors and partly leaking through NPs. The resistance attributed to this kind of ionic flow can be estimated on the basis of experimental evidence provided by the electro-orientation method performed on MTs *in vitro* [25]. Taking the reported measured value of MT ionic conductivity as

$$\sigma = (0.15 \pm 0.01)\,{\rm S\,m^{-1}}, \tag{3.10}$$

and adopting a simplifying assumption that the resistivity within an IC patch beyond an EUP is homogeneous, the resistance of an EUP with the length $l = 8\,{\rm nm}$ and the cross-sectional area $A = \pi r_{\rm DT} \lambda_{\rm DT} = 3.14 \times 2.5\,{\rm nm} \times 2.5\,{\rm nm} = 19.625\,{\rm nm}^2$, see fig. 6, is estimated as $R_0 = \frac{1}{\sigma}\frac{l}{A} = 2.7 \times 10^9\,\Omega$. This is obviously an extremely high value of resistance which is most likely an over-estimate.

We therefore prefer the computed resistance shown in table 3 of ref. [8], referred to as the outer sheath-outer sheath resistance for complete 13 protofilaments, namely $R_{13} = 4.75 \times 10^6\,\Omega$. The resistance for our EUP will be 13 times greater, *i.e.*

$$R_0 = 6.2 \times 10^7\,\Omega. \tag{3.11}$$

This value appears to be more consistent with the resistance of two NPs which follows from eq. (3.12).

Finally, we could include the conductance of both NPs to account for the leakage of IC cations into the lumen area. Thus we have

$$G_0 = \sigma_1 + \sigma_2 = (2.93 + 7.8)\,{\rm nS} = 10.7\,{\rm nS}; \quad \frac{1}{G_0} = 9.3 \times 10^7. \tag{3.12}$$

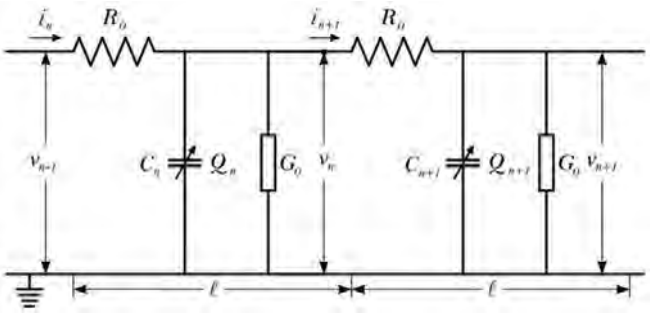

Fig. 8. An effective circuit diagram for the n-th ER with characteristic elements for Kirchhoff's laws.

It is expected that NPs exert greater resistance than the volume of IC around EUP. The above features of EUP electric parameters will lead to biophysical implications of our model. The next section develops the underlying equations governing the ionic flows along MTs.

4 The generalized model of an MT as a nonlinear transmission line

We now construct a simple periodic electric circuit simulating one protofilament of an MT. It consists of a long ladder network composed of a lumped section equal to identical EUPs as represented in fig. 8.

The longitudinal ionic current is represented by the series of resistors with Ohmic resistance R_0 for one EUP, as represented in (3.11). The nonlinear capacity with the charge Q_n for the n-th site of the ladder network is in parallel with the total conductance G_0 of the two TTs expressed by eq. (3.12). This is true if the bulk cytosol and MT lumen are considered to be grounded. This permits the application of Kirchhoff's law as

$$i_n - i_{n+1} = \frac{\partial Q_n}{\partial t} + G_0 v_n, \tag{4.1}$$

$$v_{n-1} - v_n = R_0 i_n. \tag{4.2}$$

Using eq. (3.9) and taking the time derivative results in a nonlinear form of the governing equation since

$$\frac{\partial Q}{\partial t} = C_0 \frac{\partial v_n}{\partial t} - C_0 \Gamma_0 \Omega v_n - C_0 \Gamma_0 \Omega (t - t_0) \frac{\partial v_n}{\partial t} - 2 b_0 C_0 v_n \frac{\partial v_v}{\partial t}. \tag{4.3}$$

Inserting eq. (4.3) into eq. (4.1) we arrive at the explicit system of equations describing the ionic current within IC, and an accompanying voltage

$$i_n - i_{n+1} = C_0 \frac{\partial v_n}{\partial t} - C_0 \Gamma_0 \Omega v_n - C_0 \Gamma_0 \Omega (t - t_0) \frac{\partial v_n}{\partial t} - 2 b_0 C_0 v_n \frac{\partial v_v}{\partial t} + G_0 v_n, \tag{4.4}$$

$$v_{n-1} - v_n = R_0 i_n. \tag{4.5}$$

The next step is to establish the auxiliary function $u(x,t)$ unifying the voltage and its accompanying ionic current as follows:

$$u_n = Z^{1/2} i_n = Z^{-1/2} v_n, \tag{4.6}$$

where the characteristic impedance of EUP is defined in the usual way as

$$Z = \frac{1}{\omega C_0}. \tag{4.7}$$

Since the discrete voltage v_n as well as the associated current i_n change gradually from an EUP to its neighbors, we can safely justify the expansion of u_n in a continuum approximation using a Taylor series with respect to a small spatial parameter l ($l = 8\,\mathrm{nm}$ is the length of an EUP). Then using the travelling-wave form of the function $u(x,t)$ with dimensionless space and time variables (ξ, τ), we eventually get the following inhomogeneous nonlinear partial differential equation (for details see appendix B):

$$\left(\frac{ZC_0 s}{T_0} - 2\right) \frac{\partial u}{\partial \tau} + \frac{1}{3} \frac{\partial^3 u}{\partial \xi^3} + ZC_0 \Gamma_0 \Omega (\xi - \xi_0) \frac{\partial u}{\partial \xi} + 2 \frac{Z^{3/2} b_0 C_0 s}{T_0} u \frac{\partial u}{\partial \xi} + (ZG_0 + Z^{-1} R_0 - ZC_0 \Gamma_0 \Omega) u = 0. \tag{4.8}$$

Here, the characteristic charging (discharging) time of an EUP capacitor C_0 through the resistance R_0, $T_0 = R_0 C_0$, on the basis of eqs. (3.5) and (3.11) yields the value

$$T_0 = 6.2 \times 10^7\,\Omega \times 1.92 \times 10^{-16}\,\mathrm{F} = 1.2 \times 10^{-8}\,\mathrm{s}. \tag{4.9}$$

The characteristic propagation velocity of the ionic wave is defined as follows:

$$v_0 = \frac{8 \times 10^{-9}\,\mathrm{m}}{1.2 \times 10^{-8}\,\mathrm{s}} = 0.67 \frac{\mathrm{m}}{\mathrm{s}}. \tag{4.10}$$

The dimensionless speed, space and time variables are chosen to be, respectively,

$$s = \frac{v}{v_0} \leq 1; \quad \xi = \frac{x}{l} - \tau; \quad \tau = s \frac{t}{T_0}. \tag{4.11}$$

Imposing that the condition

$$\frac{ZC_0 s}{T_0} > 2 \tag{4.12}$$

holds, we then estimate the characteristic impedance of EUP as

$$Z > \frac{2R_0}{s} \quad \text{or} \quad Z > 1.24 \times 10^8\,\Omega \quad \text{for} \quad s = 1. \tag{4.13}$$

For $s = 1$ one obtains the cutoff frequency

$$\omega_{\max} = 4.3 \times 10^7\,\mathrm{s}^{-1} \qquad \text{or} \qquad \nu_{\max} = 6.8 \times 10^6\,\mathrm{Hz}. \tag{4.14}$$

This indicates that the characteristic frequency matches the order of magnitude of frequency Ω which describes

$$W(\xi,\tau)=\frac{u_0}{\cosh^2\left\{\left[\frac{\alpha u_0}{4\beta}\exp(-2\gamma_0\tau)\right]^{1/2}\left[\xi-\xi_0\left(1-\exp(\gamma_0\tau)\right)+\frac{\alpha u_0}{3\beta}\left(1-\exp(3\gamma_0\tau)\right)\exp(-2\gamma_0\tau)\right]\right\}}, \tag{4.28}$$

$$u(\xi,\tau)=\frac{u_0\exp(-2\gamma_0\tau)}{\cosh^2\left\{\left[\frac{\alpha u_0}{4\beta}\exp(-2\gamma_0\tau)\right]^{1/2}\left[\xi-\xi_0\left(1-\exp(\gamma_0\tau)\right)+\frac{\alpha u_0}{3\beta}\left(1-\exp(3\gamma_0\tau)\right)\exp(-2\gamma_0\tau)\right]\right\}}. \tag{4.29}$$

the TTs oscillations. We now establish the compact form of eq. (4.8) as

$$\frac{\partial u}{\partial\tau}+\beta\frac{\partial^3 u}{\partial\xi^3}+\alpha u\frac{\partial u}{\partial\xi}+\gamma(\xi)\frac{\partial u}{\partial\xi}+\delta u=0, \tag{4.15}$$

where the abbreviations were introduced as follows:

$$\left.\begin{aligned}
&\alpha=\frac{2Z^{3/2}b_0C_0s}{T_0\left(\frac{ZC_0s}{T_0}-2\right)};\quad \beta=\frac{1}{3\left(\frac{ZC_0s}{T_0}-2\right)};\\
&\delta=\frac{ZG_0+Z^{-1}R_0-ZC_0\Gamma_0\Omega}{\left(\frac{ZC_0s}{T_0}-2\right)};\\
&\gamma(\xi)=\frac{ZC_0\Gamma_0\Omega(\xi-\xi_0)}{\left(\frac{ZC_0s}{T_0}-2\right)}=\gamma_0(\xi-\xi_0);\\
&\gamma_0=\frac{ZC_0\Gamma_0\Omega}{\left(\frac{ZC_0s}{T_0}-2\right)}.
\end{aligned}\right\} \tag{4.16}$$

We can further perform the following transformation of space-time variables $(\xi,\tau)\to(\rho,\theta)$:

$$\left.\begin{aligned}
&\rho(\xi,\tau)=(\xi-\xi_0)\exp(-\gamma_0\tau),\\
&\theta(\tau)=-\frac{1}{3\gamma_0}\exp(-3\gamma_0\tau),\\
&u(\xi,\tau)=W(\rho,\theta)\exp(-2\gamma_0\tau),
\end{aligned}\right\} \tag{4.17}$$

so that eq. (4.15) takes the simplified form

$$\frac{\partial W}{\partial\theta}+\alpha W\frac{\partial W}{\partial\rho}+\beta\frac{\partial^3 W}{\partial\rho^3}+\frac{\kappa}{\theta}W=0, \tag{4.18}$$

where the new parameter κ reads

$$\kappa=\frac{2}{3}-\frac{\delta}{3\gamma_0}. \tag{4.19}$$

If we assume that the Ohmic losses in this circuit are balanced by the "thermal ratchet" action of TTs, then the last term in eq. (4.15) vanishes so that

$$\frac{2}{3}-\frac{\delta}{3\gamma_0}=0;\quad \delta=2\gamma_0. \tag{4.20}$$

This gives the following condition:

$$ZG_0+Z^{-1}R_0=3ZC_0\Gamma_0\Omega;\quad Z=\frac{1}{\omega C_0}. \tag{4.21}$$

Furthermore, if we impose the simple condition

$$\left(\frac{ZC_0s}{T_0}-2\right)=1,\quad \text{with}\quad s=1,$$

we then obtain the values

$$Z=1.87\times10^8\,\Omega\quad\text{and}\quad\omega=2.7\times10^7\,\mathrm{s}^{-1}. \tag{4.22}$$

Subsequently, equating $\omega=\Omega=2.7\times10^7\,\mathrm{s}^{-1}$ we estimate the parameter Γ_0 directly from eq. (4.21) as

$$\Gamma_0=\frac{G_0}{3C_0\omega}+\frac{C_0R_0\omega}{3}=0.07+0.11=0.18. \tag{4.23}$$

Eventually, the spatial inhomogenity parameter is found to be

$$\Gamma_0\,\Omega=4.8\times10^6\,\mathrm{s}^{-1}, \tag{4.24}$$

which is one order of magnitude smaller than the inverse characteristic time $T_0^{-1}=1.83\times10^7\,\mathrm{s}^{-1}$, thus justifying eq. (3.7). In such a case ($\kappa=0$), eq. (4.18) reduces to the modified nonlinear KdV equation with spatial inhomogeneity which exhibits a single bell-shaped soliton solution subjected to the distortion due to the Ohmic dissipation. In reality, the condition in eq. (4.20) seems to be reasonably met. Otherwise, if $\kappa=1$ or $\kappa=2$, eq. (4.18) reduces to a nonlinear spherical (cylindrical) KdV equation which has already been derived in the context of ionic-acoustic plasma waves [28,29]. In general, by introducing the new transformation [30]

$$F=W\exp\left(\sigma\int\frac{\mathrm{d}\theta}{\theta}\right), \tag{4.25}$$

and substituting to eq. (4.18) we obtain

$$\frac{\partial F}{\partial\theta}=\Lambda(\theta)\cdot F\frac{\partial F}{\partial\xi}+\beta\frac{\partial^3 F}{\partial\xi^3}=0, \tag{4.26}$$

where the new function $\Lambda(\theta)$ reads

$$\Lambda(\theta)=\alpha\exp\left(-\alpha\int\frac{\mathrm{d}\theta}{\theta}\right). \tag{4.27}$$

The solution of (4.18) with $\kappa=0$ is expressed as

see equation (4.28) *above*

so that the function $u(\xi,\tau)$ has the form

see equation (4.29) *above*

If we use the set of estimated and chosen parameters in eqs. (3.5), (3.11), (3.12), (4.21) and (4.24), we readily see that all dimensionless parameters (4.16) lie between zero and one ($\beta = 0.33$, $\gamma_0 = 0.17$, $\delta = 0.34$) staying within the same order of magnitude. This suggests that we should inspect numerically the behavior of the solution of eq. (4.29) when the parameters α, β, γ_0, ξ_0 take slightly different values which is done next.

Analyzing the set of plots in fig. 9 we can see the competition between nonlinearity α and the dispersion β, as well as the role of inhomogenity γ_0. In the case represented in fig. 9b we have balanced all parameters. The soliton solution preserves its width but its amplitude decays rather rapidly so that over the length of about $500l$ it becomes negligible. The above view shows the deceleration of the soliton solution along its path. Figure 9c shows the case with increased nonlinearity ($\alpha = 0.5$). It is remarkable that it exhibits not only a higher localization but also a slower decay of its amplitude. The advantage of this case lies in the fact that the velocity of the soliton solution decreases very slightly. We estimate its average velocity as follows:

$$\Delta x \approx 400l = 400 \times 8\,\mathrm{nm} = 3.2\,\mu\mathrm{m},$$
$$\Delta t = 1000T_0 = 10^3 \times 1.2 \times 10^{-8}\,\mathrm{s} = 1.2 \times 10^{-5}\,\mathrm{s},$$
$$v = \frac{\Delta x}{\Delta t} = 0.26\frac{\mathrm{m}}{\mathrm{s}}\,.$$

The range of this soliton is $3.2\,\mu$m which is of the order of the cell's diameter. Therefore, it appears that the ionic pulse with such parameter values could be efficiently transferred within the cell.

5 Conclusions and discussion

In this paper we have developed a nonlinear model of ionic currents along MTs in the context of the polyelectrolyte character of these cytoskeletal filaments. We have taken into account the role of two aspects of this cylindrical biopolymer, its NPs and very sensitive TTs. Both of them are responsible for the nonlinear character of the overall electrical capacitance of MTs. Segmenting an MT into identical EUPs and estimating the values of corresponding electrical parameters, we were able to establish the difference equations of lumped EUP sections, eq. (4.1) and eq. (4.2). On the basis of a gradual change of voltage along MT protofilaments we imposed a continuum approximation limit leading to the nonlinear KdV type equation in (4.15) with dissipative and inhomogeneity terms, δ and $\gamma(\xi)$, eq. (4.16). This sort of equation was derived earlier within non-uniform plasma applications where ion acoustic solitons were identified, both in the cases of cylindrical and spherical geometry.

Our solution, eq. (4.29), was analysed numerically for the set of parameters in fig. 9. It is apparent that the solitonic wave loses its energy due to Ohmic resistance but it preserves the stable localised form. In the case presented in fig. 9c with an increased nonlinearity parameter, the solitonic pulse exhibits greater robustness and it progresses with an almost constant velocity and only a slight decay of its initial amplitude. This demonstrates the role of flexible TTs which could be of decisive importance for the stable localized character of ionic pulses along MTs. Interestingly, TTs are the structural elements of tubulin with the greatest diversity across cells and biological species which could be of functional significance. Moreover, it was earlier shown that MTs posses ferroelectric properties creating an intrinsic electric field [31]. It is expected that this intrinsic electric field within an MT provides the necessary electrostatic energy which may compensate for the losses due to viscosity and thus enable the near lossles propagation of solitonic pulses over long distances along MTs.

We expect that this type of localized ionic waves could play a fundamental role in many cellular processes. First the process of cell division, in the context described by Hepler [3,4], needs the synchronized depolymerisation of MTs. This can be caused by the localized Ca^{++} waves described by our model which could reach MT plus ends and trigger the onset of massive detachment of TDs from MT tips [32]. If this process were to be based on pure diffusion of Ca^{++} ions through the bulk cytosol, the resulting depolymerisation would be prone to frequent mistakes making this process very unreliable which known not to be the case.

In a very interesting paper Duke [33] explained that in hair bundles (kinocilium) in the inner ear consisting of MT doublets, the myosin motor-driven oscillation are controlled by Ca^{++} ions directed from ion channels along MTs. These ions cause a fraction of myosin motors to detach and thus tune the oscillations of kinocilium as reaction to a corresponding acoustic signal. This mechanism can also be seen in the context of localized Ca^{++} waves described in the present paper.

Finally, the experimental work of Priel *et al.* [23] demonstrated that the electrical signal amplification resulting from the presence of MTs can be directly attributed to nonlinear ionic currents guided by MTs in close similarity to the framework developed by our present model. In fact, these measurements inspired the authors to consider the role MTs can play as bio-transistors taking part in cognitive processes which is another interesting application of nonlinear ionic conductance of MTs.

This research was supported by funds from Serbian Ministry of Science, Grants: III43008 and 171009. Jack A. Tuszynski acknowledges support for his research from NSERC (Canada).

Appendix A. Glossary

ER: endoplasmic reticulum
EUP: elementary unit of protofilament
IC: ionic cloud
KdV: Korteveg de Vries
MT: microtubule
NP: nano-pore
TD: tubulin dimer
TT: tubulin tail

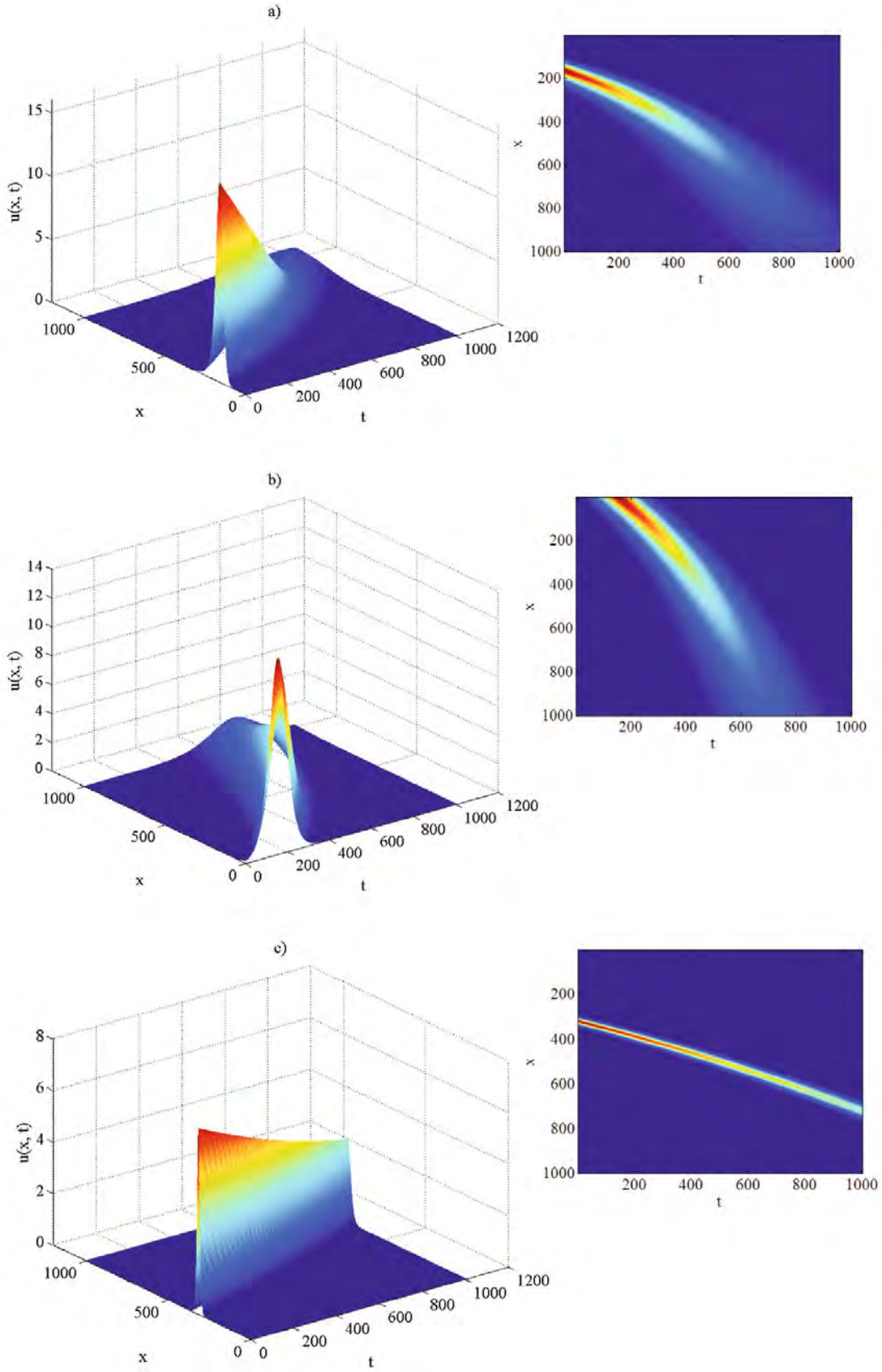

Fig. 9. Numerical solutions of $u(\xi, \tau)$ for: a) $\alpha = 0.2$; $\gamma_0 = 0.17$; $\beta = 0.33$; $\xi_0 = 0.1$. b) $\alpha = 0.1$; $\gamma_0 = 0.1$; $\beta = 0.1$; $\xi_0 = 0.1$. c) $\alpha = 0.5$; $\gamma_0 = 0.1$; $\beta = 0.1$; $\xi_0 = 0.1$.

Appendix B.

Using a Taylor series as follows:

$$u_{n\pm1} = u \pm l\frac{\partial u}{\partial x} + \frac{l^2}{2!}\frac{\partial^2 u}{\partial x^2} \pm \frac{l^3}{3!}\frac{\partial^3 u}{\partial x^3} + \frac{l^4}{4!}\frac{\partial^4 u}{\partial x^4} \pm \frac{l^5}{5!}\frac{\partial^5 u}{\partial x^5} + \ldots, \tag{B.1}$$

and applying on eqs. (4.4) and (4.5) this system now reads

$$-\frac{\partial u}{\partial x} - \frac{l}{2}\frac{\partial^2 u}{\partial x^2} - \frac{l^2}{6}\frac{\partial^3 u}{\partial x^3} - \frac{l^3}{24}\frac{\partial^4 u}{\partial x^4} - \frac{l^4}{120}\frac{\partial^5 u}{\partial x^5} - \frac{ZG_0}{l}u - \frac{ZC_0}{l}\frac{\partial u}{\partial t} + \frac{ZC_0\Gamma_0\Omega}{l}u + \frac{ZC_0\Gamma_0\Omega}{l}(t-t_0)\frac{\partial u}{\partial t} + 2\frac{Z^{3/2}b_0C_0}{l}u\frac{\partial u}{\partial t} = 0, \tag{B.2}$$

$$-\frac{\partial u}{\partial x} + \frac{l}{2}\frac{\partial^2 u}{\partial x^2} - \frac{l^2}{6}\frac{\partial^3 u}{\partial x^3} + \frac{l^3}{24}\frac{\partial^4 u}{\partial x^4} - \frac{l^4}{120}\frac{\partial^5 u}{\partial x^5} - \frac{Z^{-1}R_0}{l}u = 0. \tag{B.3}$$

Adding up the last two equations and retaining the terms up to the order of the third derivative, due to smallness of l^4, we obtain

$$-2\frac{\partial u}{\partial x} - \frac{l^2}{3}\frac{\partial^3 u}{\partial x^3} - \frac{ZC_0}{l}\frac{\partial u}{\partial t} + \frac{ZC_0\Gamma_0\Omega}{l}(t-t_0)\frac{\partial u}{\partial t} + 2\frac{Z^{3/2}b_0C_0}{l}u\frac{\partial u}{\partial t} - \frac{1}{l}(ZG_0 + Z^{-1}R_0 - ZC_0\Gamma_0\Omega)u = 0. \tag{B.4}$$

Then the standard travelling wave with speed v, for the unified function $u(x,t)$, can be employed as follows:

$$\left.\begin{aligned} &u(x,t) = u\left(\frac{x}{l} - v\frac{t}{l}\right) = u\left(\frac{x}{l} - \frac{v}{v_0}v_0\frac{t}{l}\right) = \\ &u\left(\frac{x}{l} - s\frac{t}{T_0}\right) = u(\xi), \\ &\xi = \frac{x}{l} - \tau; \quad \tau = s\frac{t}{T_0}; \quad v_0 = \frac{l}{T_0}; \quad s = \frac{v}{v_0}. \end{aligned}\right\} \tag{B.5}$$

In that respect, the set of the following transformations holds:

$$\frac{\partial u}{\partial x} = \frac{1}{l}\frac{\partial u}{\partial \xi}; \quad \frac{\partial^3 u}{\partial x^3} = \frac{1}{l^3}\frac{\partial^3 u}{\partial \xi^3}; \quad \frac{\partial u}{\partial t} = \frac{s}{T_0}\frac{\partial u}{\partial \tau} = -\frac{s}{T_0}\frac{\partial u}{\partial \xi}. \tag{B.6}$$

Using the transformations given by eqs. (B.5) and (B.6) and retaining the first derivatives of τ and going over to space derivatives of ξ in the inhomogeneous (fourth) term and nonlinear (fifth) term of eq. (B.4), we readily find

$$\left(\frac{ZC_0 s}{T_0} - 2\right)\frac{\partial u}{\partial \tau} + \frac{1}{3}\frac{\partial^3 u}{\partial \xi^3} + ZC_0\Gamma_0\Omega(\xi - \xi_0)\frac{\partial u}{\partial \xi} + 2\frac{Z^{3/2}b_0C_0 s}{T_0}u\frac{\partial u}{\partial \xi} + \left(ZG_0 + Z^{-1}R_0 - ZC_0\Gamma_0\Omega\right)u = 0. \tag{B.7}$$

References

1. L.A. Amos, Trends Cell Biol. **5**, 48 (1995).
2. G. Matsumoto, M. Ishikawa, A. Tasaki, H. Murofushi, H. Sakai, J. Membr. Biol. **77**, 77 (1989).
3. P.K. Hepler, Plant Cell **17**, 2142 (2005).
4. D.H. Chang, P. Wadsworth, P.K. Hepler, J. Cell Sci. **102**, 79 (1992).
5. L. Matsson, J. Biol. Phys. **31**, 303 (2005).
6. L. Matsson, J. Phys.: Condens. Matter **21**, 502101 (2009).
7. E. Nogales, H.W. Wang, Curr. Opin. Cell Biol. **18**, 179 (2006).
8. H. Freedman, V. Rezania, A. Priel, E. Carpenter, S.Y. Noskov, J.A. Tuszynski, Phys. Rev. E **81**, 051912 (2010).
9. J.F. Diaz, I. Barasoain, J.M. Andren, J. Biol. Chem. **278**, 8407 (2003).
10. M.V. Satarić, D.I. Ilić, N. Ralević, J.A. Tuszynski, Eur. Biophys. J. **38**, 637 (2009).
11. M.V. Satarić, D. Sekulić, M. Živanov, J. Comput. Theor. Nanosci. **7**, 2281 (2010).
12. Z.S. Siwy, M.R. Powell, A. Petrov, E. Kalman, C. Trantmann, R.S. Eisenberg., Nano Lett. **6**, 1729 (2006).
13. W. Im, B. Roux, J. Mol. Biol. **322**, 851 (2002).
14. L. Serrano, J. de la Torre, R.B. Maccioni, Y. Avila, Biochemistry **23**, 4675 (1984).
15. M.V. Satarić, J.A. Tuszynski, Phys. Rev. E **67**, 011901 (2003).
16. N.A. Baker, D. Sept, S. Joseph, M.J. Holst, J.A. McCammon, Proc. Natl. Acad. Sci. U.S.A. **98**, 10037 (2001).
17. J.A. Tuszynski, J.A. Brown, E. Crowford, E.J. Carpenter, M.L.A. Nip, J.M. Dixon, M.V. Satarić, Math. Comput. Modell. **41**, 1055 (2005).
18. G.S. Manning, Rev. Biophys. **2**, 179 (1978).
19. J.A. Tuszynski, A. Priel, J.A. Brown, H.F. Cantiello, J.M. Dixon, *Nano and Molecular Electronics Handbook, Electronic and Ionic Conductivities of Microtubules and Actin Filaments: Their Consequences for Cell Signaling and Applications to Bioelectronics* (Taylor and Francis, London, 2007).
20. A. Priel, J.A. Tuszynski, H. Cantielo, *Molecular Biology of the Cell, Ionic Waves Propagation Along the Dendritic Cytoskeleton as a Signaling Mechanism* (Elsevier, 2006).
21. A. Priel, J.A. Tuszynski, EPL **83**, 68004 (2008).
22. J.A. Tuszynski, S. Portet, J.M. Dixon, C. Luxford, H.F. Cantiello, Biophys. J. **86**, 1890 (2004).
23. A. Priel, A.J. Ramos, J.A. Tuszynski, H.F. Contiello, Biophys. J. **90**, 4639 (2006).
24. B. O'Shanghnessy, Q. Yang, Phys. Rev. Lett. **94**, 048302 (2005).
25. I. Minoura, E. Muto, Biophys. J. **90**, 3739 (2006).
26. C. Lin, H.F. Cantiello, Biophys. J. **65**, 1371 (1993).
27. K. Wang, W.J. Rappel, H. Levine, Phys. Biol. **1**, 27 (2004).
28. S. Maxon, J. Viecelli, Phys. Rev. Lett. **32**, 4 (1974).
29. S. Maxon, J. Viecelli, Phys. Fluids **17**, 1614 (1974).
30. T. Yagy, J. Phys. Soc. Jpn. **50**, 2737 (1981).
31. J.A. Tuszynski, S. Hameroff, M.V. Satarić, B. Tripisova, M.L.A. Nip, J. Theor. Biol. **174**, 371 (1995).
32. L.J. Gagliardi, J. Electrostat. **54**, 219 (2002).
33. T. Duke, J. Phys.: Condens. Matter **15**, S1747 (2003).

International Journal of Modern Physics B
Vol. 23, No. 22 (2009) 4697–4711

DOI: 10.1142/S021797920905331X

ACTIN FILAMENTS AS NONLINEAR RLC TRANSMISSION LINES

M. V. SATARIĆ, N. BEDNAR*, B. M. SATARIĆ and G. STOJANOVIĆ

Faculty of Technical Sciences, University of Novi Sad,
Trg D. Obradovića 6, 21000 Novi Sad, Serbia
** bednar.nikola@gmail.com*

Received 12 January 2009

We elucidate the model introduced by Tuszynski *et al.*[1] in order to obtain more biophysically tractable results regarding the role of actin filaments in ionic transport throughout living cells.

Keywords: Cytoskeleton; actin filaments; ionic waves; RLC transmission line; kink; intrinsic electric fields.

PACS numbers: 87.14.Gg, 81.07.Nb

1. Introduction

The cytoskeleton consists of three major types of thin rodlike filaments that span the cytoplasm: actin-based filaments, tubulin-based filaments called microtubules and intermediate filaments.[2] There are at least three well-studied mechanical functions of the cytoskeleton in vivo: providing mechanical strength of the cell, segregating the chromosomes and active participation in the transport of macromolecules via motor proteins, primarily kinesin and dynein. Actin is the most abundant protein in cytoplasm of mammalian cells accounting for 10–20% of the total protein content.

Here we are dealing with actin filament (F-actin) which represents polymerized two-stranded helical chain of actin monomers (Fig. 1). They display a high charge density.[3] This phenomenon is further manifested by the extensive changes in electric dipole moment observed in actin filament oriented by shear flow and a nonlinear electro osmotic response to weak osmotic stress.[4] The ability of F-actin to enable electrical currents in the form of ionic movements is of biological relevance in intracellular signaling mechanisms by being functionally coupled to membrane–embedded ion channels.[5]

As negatively charged polyelectrolytes, F-actins may contain a proportion of their surrounding counterions in the form of a dense or "condensed" cloud about their surface which may be highly insensitive to large changes in the ionic strength conditions of the surrounding saline solution.[6] Lin and Cantiello[7] studied the

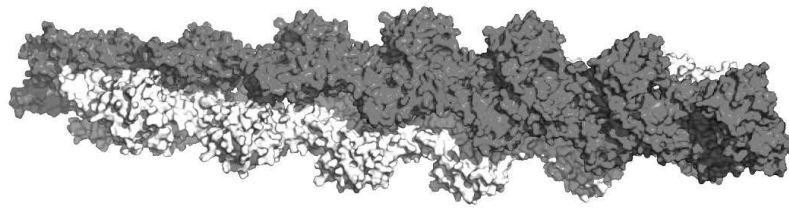

Fig. 1. The sketch of F-actin helicoidally polymerized with discernible monomers.

electrodynamic behavior of electrically stimulated single F-actin using a variation of the "patch-clamp" technique applied to an isolated F-actin in solution.

Electrical currents were observed about the surface of an F-actin under both high and low counter ionic strength conditions. Counter ionic waves were highly nonlinear and remained long after the electrical stimulation of F-actin ceased. This was an argument that F-actins can function as biological "electrical wires" and thus being conceived as inhomogenous transmission lines.

An important point is that because of the helical structure of F-actin, the distribution of counterions will be nonuniform along the polymers length. The local shape of surface landscape of polymer could be the reason for local changes of the density of counterions around it and spatially dependant electric field could be arranged in respective peaks and troughs as was postulated many years ago.[8] In order to use the polyelectric theory for F-actin chain, we start from the so-called Bjerrum length λ_B, the distance where the thermal fluctuations of ions are balanced by Coulomb interactions between their charges. For monovalent ions it yields:

$$\frac{e^2}{4\pi\varepsilon\varepsilon_0\lambda_B} = k_B T \tag{1}$$

Here, e is the charge of an electron, ε_0 the permittivity of vacuum, ε the relative permittivity of cytosol and k_B is Boltzmann's constant. For physiological temperature of 310 K, and taking $\varepsilon = 80$, it is easy to find from Eq. (1) that

$$\lambda_B = 6.7 \cdot 10^{-10}\ \mathrm{m}\,. \tag{2}$$

Counterion condensation occurs when the mean distance between intrinsic polymer charges is such that $\lambda_B/\beta > 1$. Each actin monomer carries an effective excess of 11 negative charges. Assuming an average of 370 monomers per μm, one finds that there is $(-4e/\mu\mathrm{m})$. So linear charge spacing of $\beta = 2.5 \cdot 10^{-10}$ m, giving $\lambda_B/\beta \sim 2.7 > 1$.

Thus the majority of counterion population is predominantely constrained within the layer of thickness λ_B around F-actin filament. The length of an actin monomer is $l = 5.4$ nm and the radius of actin filament is approximately $R = 5.4$ nm.[9] In this paper we further elaborate the model introduced by Tuszynski *et al.*[1] but making more plausible estimations of model parameters.

2. The Model of F-actin as a Nonlinear Transmission Line

Here we will introduce the electrical components which are ingredients of respective nonlinear circuit which simulates the conductive properties of an F-actin in solution. The described cloud of counterions with thickness λ_B is wrapped around F-actin. This cloud provides both resistive and capacitive components for ionic currents confined in this layer resembling the role of coaxial cable in electrical engineering. The inductive component to the electrical properties of ionic waves along F-actin is due to its double-stranded helical structure that induces the ionic flow in a solenoidal manner following the winding throughs of local electric potential.

2.1. *The estimation of elementary capacitance attributed to one F-actin monomer*

In continuum model, F-actin as a polyelectrolyte is represented by a volume which is bounded by a charged cylindrical surface in contact with an electrolyte (cytosol) whose dielectric constant is assumed to be time invariant and uniform. In that case, Poisson's equation has the form:

$$\nabla^2 V = -\frac{\rho}{\varepsilon_0 \varepsilon}\,, \tag{3}$$

where ρ is the volume charge density at any point in the cytosol. The charge density ρ results from the presence of counterions and co-ions. These are assumed to have a distribution obeying Boltzmann's law. This means that in a solution containing n_s dissociated molecules of salt (for example NaCl) the number n_1 of counterions Na^+ with charge $q_1 = e$, at a distance r from F-actin axis, is given by the expression:

$$n_1(r) = n_s \exp\left(\frac{eV}{k_B T}\right), \tag{4a}$$

since q_1 and V have opposite signs. The number of negative Cl^- ions is:

$$n_2(r) = n_s \exp\left(-\frac{eV}{k_B T}\right). \tag{4b}$$

It implies that total charge density reads:

$$\rho(r) = n_s e\left[-\exp\left(\frac{eV}{k_B T}\right) + \exp\left(-\frac{eV}{k_B T}\right)\right] = -2n_s e \sinh\left(\frac{eV}{k_B T}\right). \tag{5}$$

Using this result in Eq. (3) yields the Poisson–Boltzmann equation (PBE):

$$\nabla^2 V = \left(\frac{2n_s e}{\varepsilon_0 \varepsilon}\right) \sinh\left(\frac{eV}{k_B T}\right). \tag{6}$$

This nonlinear differential equation can be brought into more compact form by introducing two dimensionless variables:

$$\Psi = \frac{eV}{k_B T}\,; \quad x = \frac{r}{\Delta}\,, \tag{7a}$$

where the Debye length Δ is defined as:

$$\Delta = \sqrt{\frac{\varepsilon_0 \varepsilon k_B T}{2 n_s e^2}}\,. \tag{7b}$$

It gives:

$$\nabla^2 \Psi(x) = \sinh[\Psi(x)]\,. \tag{8}$$

In the Debye-Hückel approximation, it is assumed that $eV \ll k_B T$ or $\Psi \ll 1$ holds, so that Eq. (8) could be linearized by approximation $\sinh[\psi(x)] \approx \psi(x)$.

Thus PBE in cylindrical coordinates now reads:

$$\frac{1}{x}\frac{d}{dx}\left(x\frac{d\Psi}{dx}\right) = \Psi\,, \quad \text{or} \quad \frac{d^2\Psi}{dx^2} + \frac{1}{x}\frac{d\Psi}{dx} - \Psi = 0\,. \tag{9}$$

On the surface of F-actin cylinder we have $x_0 = R/\Delta$ and $\psi_0 = eV_0/k_B T$, where $R = 2r_{ac} = 5.4$ nm, see (Fig. 2).

The solution of PBE, Eq. (9) is modified Bessel function of zero order denoted by $K_0(x)$, so we have:

$$\Psi(x) = cK_0(x)\,, \tag{10a}$$

where c is the constant of integration. The above Bessel function does not oscillate and behaves like $\exp(-x)$ as $x \to \infty$. From Eq. (10a) one has:

$$\frac{d\Psi}{dx} = -cK_1(x)\,, \tag{10b}$$

where $K_1(x)$ is the modified Bessel function of the first order.

Using relation for electric field:

$$E = \frac{k_B T}{e\Delta}\left(\frac{dV}{dx}\right), \tag{10c}$$

we have

$$-\,x_0\left(\frac{d\Psi}{dx}\right)_{x=x_0} = \frac{e^2}{4\pi\varepsilon_0\varepsilon k_B T b} = \zeta\,; \quad b = \frac{L}{N}\,, \tag{10d}$$

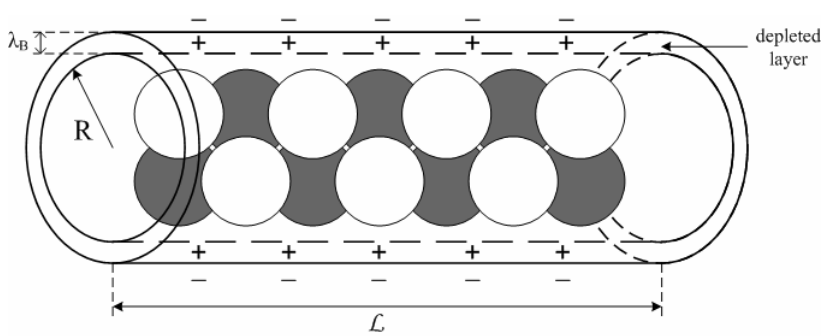

Fig. 2. The rough shape of cylindrical capacitor with characteristic dimensions.

where q represents the density parameter of intrinsic surface charges of F-actin; L is the length of an F-actin, and Ne its total surface charge.

Returning to variable r, the above equations yield:

$$\Psi(r) = \frac{2\zeta\Delta K_0\left(\frac{r}{\Delta}\right)}{RK_1\left(\frac{r}{\Delta}\right)}\,. \tag{11}$$

This equation for the case of low ionic strengths ($r/\Delta \to 0$) behaves like $\ln(r/\Delta)$, and hence we have the solution of our PBE:

$$V(r) = -\frac{eN}{2\pi\varepsilon_0\varepsilon L}(\ln r - \ln\Delta) = -\frac{Q}{2\pi\varepsilon_0\varepsilon L}\ln\left(\frac{r}{\Delta}\right). \tag{12a}$$

The first term corresponds to the potential due to the surface charge of F-actin, and the second term ($\ln\Delta$) to the potential due to the counterions.

The potential difference between the F-actin surface cylinder and outer cylinder of cloud zone at distance λ_B is therefore given by:

$$\Delta V = -\frac{Q}{2\pi\varepsilon_0\varepsilon L}\ln\left(1+\frac{\lambda_B}{R}\right). \tag{12b}$$

If we restrict to one element of F-actin consisting of one monomer of length $l = 5.4$ nm we have:

$$\Delta V_0 = -\frac{Q_0}{2\pi\varepsilon_0\varepsilon l}\ln\left(1+\frac{\lambda_B}{R}\right). \tag{12c}$$

The capacitance of this element is defined by:

$$C_0 = \frac{Q_0}{\Delta V_0} = \frac{2\pi\varepsilon_0\varepsilon l}{\ln\left(1+\frac{\lambda_B}{R}\right)}\,. \tag{13}$$

Taking the introduced values of above parameters $\varepsilon_0 = 8.85\cdot 10^{-12}$ F/m, $\varepsilon = 80$, $l = 5.4$ nm, $\lambda_B = 0.67$ nm, $R = 5.4$ nm, we get:

$$C_0 = 2\cdot 10^{-16}\ \mathrm{F}\,. \tag{14}$$

This result is a pretty rough estimation which ignores the already mentioned local peaks and troughs due to globular shapes of actin monomers. These troughs wind helically along F-actin.

This circumstance will be taken into account by assuming that the capacitance contribution from such unevenness could be conceived as linearly changing with increase of local potential. If we denote one arbitrary monomer along F-actin with index n, the corresponding charge of counterions within λ_B could be expressed as:

$$Q_n = C_0(V_n - bV_n^2)\,, \tag{15}$$

where b is expected to be small ($bV_n \ll 1$). This point has profound consequences regarding considered model.

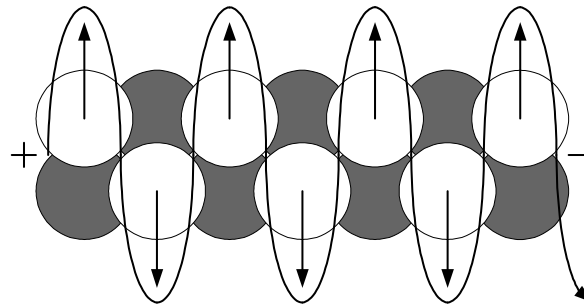

Fig. 3. Schematic shape of F-actin monomers with pertaining dipole moment and winding current.

2.2. *The estimation of the effective inductance*

In F-actin the monomers are arranged in head to head order to form actin dimers resulting in alternating distribution of electric dipole moments along the length of the filament,[3] see (Fig. 3).

This fact, together with explained winding troughs, would be the reason that F-actin may be thought of as a "solenoid". This solenoid flow geometry leads to an equivalent electrical element possessing self inductance.

The well-known formula from basic curses gives an effective inductance of solenoid with N coils of area A and length d:

$$L = \frac{\mu N^2 A}{d}\,. \tag{16a}$$

In Ref. 1 the calculation was deliberately overestimating, taking circular rings of current instead of helical turns. Substituting appropriate parameters in Eq. (16a), they found the value of inductance for the length of one monomer to be:

$$L_0 = 1.7 \cdot 10^{-12} H\,. \tag{16b}$$

This is an overestimated result and later will be clear why we do not need an exact value of this parameter.

2.3. *Modeling the thermal resistance components*

The current trough layer of ionic cloud about F-actin can be divided into two components, longitudinal and transversal. If we suppose that the connectivity of ionic cloud is homogenous then the expression for longitudinal resistivity along one monomer reads:

$$R_1 = \rho\frac{l}{A_1}\,; \quad A_1 = 2\pi R\lambda_B\,, \tag{17a}$$

while the transversal component is:

$$R_2 = \rho\frac{\lambda_B}{A_2}\,; \quad A_2 = 2\pi R l\,. \tag{17b}$$

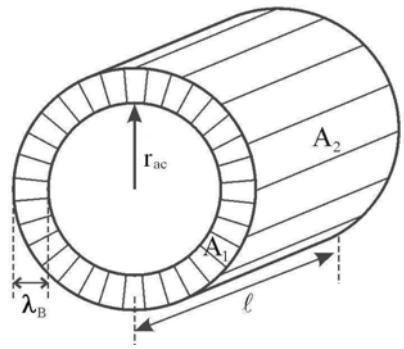

Fig. 4. The representation of two elementary resistors transversal and longitudinal with characteristic dimensions.

These resistors are shown in Fig. 4.

Due to lack of experimental evidencies, Tuszynski *et al.*[1] estimated theoretically the conductivity of solution with counterions in cytosol. They obtained the value of conductivity:

$$\rho^{-1} = \sigma = 1.21(\Omega m)^{-1}\,. \tag{17c}$$

Using the values of parameters as before we get:

$$R_1 = 2 \cdot 10^8 \Omega\,, \tag{18a}$$

$$R_2 = 3 \cdot 10^6 \Omega\,. \tag{18b}$$

It should be emphasized that recent experimental evidencies were made for conductivity of microtubules in cytosol,[10] giving $\sigma = 0.15(\Omega\mathrm{m})^{-1}$, which is one order of magnitude lower than in Eq. (17c). If we use this conductivity, corresponding resistances should be increased for one order of magnitude but retaining the above ratio, which is important for forthcoming evaluations.

3. RLC Transmission Line

On the basis of already estimated components of elementary units (actin monomer), we are now able to establish an electrical model by applying Kirchoff's laws to the series of elementary units as the coupled circuits. We expect a potential difference between the F-actin charged surface with condensed counterions and ions laying along coaxial cylinder at one Bjerrum length away. These "Bjerrum ions" are responsible for time dependant current which makes the inductance L_0, Eq. (16b). In series with L_0 should be inserted resistive component R_1, Eq. (18a), see (Fig. 5).

In parallel to the above components there is a cylindrical capacitance C_0, Eq. (14), in series with transversal resistivity R_2, Eq. (18b), acting between two coaxial cylinders separated by λ_B. We have already noticed that the capacity C_0 should change with increasing concentration of counterions due to uneven landscape of F-actin surface. This was described by Eq. (15). From Kirchoff's laws, on

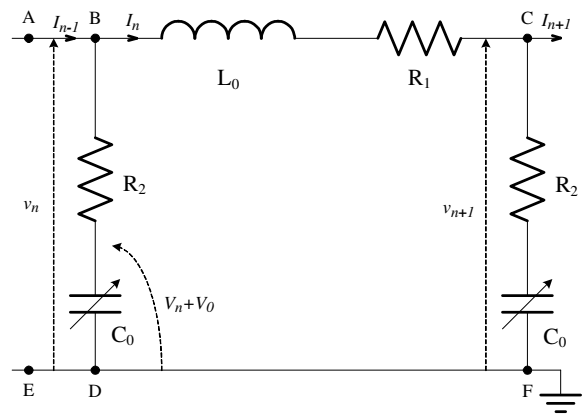

Fig. 5. The scheme of transmission line for ion propagation along F-actin with characteristic resistivities.

the basis of (Fig. 5), if I_n is the current through the inductance L_0 and the resistor R_1, and I_{n-1} is the other current flowing along AB, the current through line DB should be $I_n - I_{n-1}$. Thus for the section BC of the nth actin monomer must hold:

$$v_n - v_{n+1} = L_0 \frac{dI_n}{dt} + I_n R_1 \,, \tag{19a}$$

where v_n and v_{n+1} are the voltage across AE and CF, respectively. Similarly, if the voltage across the variable capacitor C_0 $(V_n - bV_n^2)$ is $V_n + V_0$, where V_0 is the bias voltage of the capacitor, we have:

$$v_n = R_2(I_{n-1} - I_n) + V_0 + V_n \,. \tag{19b}$$

Moreover, the current through the section BD should be the rate of change of Q_n, Eq. (15).

$$I_{n-1} - I_n = \frac{dQ_n}{dt} \tag{19c}$$

From Eq. (19a) we have:

$$L_0 \frac{dI_{n-1}}{dt} = v_{n-1} - v_n - I_{n-1}R_1 \quad \text{and} \quad L_0 \frac{dI_n}{dt} = v_n - v_{n+1} - I_n R_1 \,, \tag{19d}$$

and including these in Eq. (19c), we get:

$$L_0 \frac{d^2 Q_n}{dt^2} = v_{n+1} + v_{n-1} - 2v_n + R_1(I_n - I_{n-1}) \,. \tag{19e}$$

Replacing v_{n+1}, v_n and v_{n-1} from Eq. (19b) to Eq. (19e), it reads:

$$L_0 \frac{d^2}{dt^2}[C_0(V_n - bV_n^2)]$$

$$= V_{n+1} + V_{n-1} - 2V_n - R_1 C_0 \frac{d}{dt}(V_n - bV_n^2)$$

$$- R_2 C_0 \left\{ 2\frac{d}{dt}(V_n - bV_n^2) - \frac{d}{dt}(V_{n+1} - bV_{n+1}^2) - \frac{d}{dt}(V_{n-1} - bV_{n-1}^2) \right\}. \quad (20)$$

Bearing in mind that voltage V_n changes gradually from actin monomer n to its neighbors, we safely could expand $v_{n\pm1}$ in continuum approximation using a Taylor expansion in a small spatial parameter l (diameter of monomer):

$$V_{n\pm1} = V \pm l\frac{\partial V}{\partial x} + \frac{l^2}{2!}\frac{\partial^2 V}{\partial x^2} \pm \frac{l^3}{3!}\frac{\partial^3 V}{\partial x^3} + \frac{l^4}{4!}\frac{\partial^4 V}{\partial x^4} \pm \cdots . \quad (21a)$$

We discarded higher terms starting from l^5 since $l^5 \sim 10^{-42}$ m^5 is a very small value.

The above expansion leads to the following relation:

$$V_{n+1} - 2V_n + V_{n-1} = l^2\frac{\partial^2 V}{\partial x^2} + \frac{l^4}{12}\frac{\partial^4 V}{\partial x^4}. \quad (21b)$$

Replacing Eqs. (15), (21a), (21b) in Eq. (20) yields:

$$\begin{aligned} & L_0 C_0 \frac{\partial^2}{\partial t^2}(V - bV^2) \\ & = l^2\frac{\partial^2 V}{\partial x^2} + \frac{l^4}{12}\frac{\partial^4 V}{\partial x^4} - R_1 C_0 \frac{\partial}{\partial t}(V - bV^2) + R_2 C_0 \frac{\partial}{\partial t}\left(l^2\frac{\partial^2 V}{\partial x^2} + \frac{l^4}{12}\frac{\partial^4 V}{\partial x^4} \right) \\ & \quad - R_2 C_0 b \frac{\partial}{\partial t}\left[2l^2\frac{\partial^2 V}{\partial x^2} + 2l^2\left(\frac{\partial V}{\partial x}\right)^2 + \frac{l^4}{6}V\frac{\partial^4 V}{\partial x^4} + \frac{2l^4}{3}\frac{\partial V}{\partial x}\frac{\partial^3 V}{\partial x^3} + \frac{l^4}{2}\left(\frac{\partial^2 V}{\partial x^2}\right)^2 \right] \end{aligned} \quad (21c)$$

Considering that the time variations of local voltage V are small compared to the constant background voltage V_0, we could safely assume that time derivative is of the order of small parameter ε as well as the nonlinear voltage terms bV^2 are of the order of ε^2. Thus Eq. (21c) could be reduced to the collections of leading terms:

$$L_0 C_0 \frac{\partial^2 V}{\partial t^2} = l^2\frac{\partial^2 V}{\partial x^2} - R_1 C_0 \frac{\partial V}{\partial t} + R_2 C_0 \frac{\partial}{\partial t}\left(l^2\frac{\partial^2 V}{\partial x^2} \right) + R_1 C_0 2bV\frac{\partial V}{\partial t}. \quad (22a)$$

Taking into account values L_0 and C_0, Eqs. (14) and (16b), it is clear that factor $L_0 C_0 \sim 3.4 \cdot 10^{-28}$ s^2 is so small compared with $l^2 \sim 3 \cdot 10^{-17}$ m^2, making the term with second time derivative safely negligible. Since Eq. (16b) gives an overestimated value, the above conclusion holds for real value of L_0.

Moreover Eqs. (18a) and (18b) give $R_1 \gg R_2$, justifying that the term with factor $R_2 C_0$ could also be discarded leading Eq. (22a) to the final form:

$$l^2\frac{\partial^2 V}{\partial x^2} - R_1 C_0 \frac{\partial V}{\partial t} + R_1 C_0 2bV\frac{\partial V}{\partial t} = 0. \quad (22b)$$

In the first step we could linearize this equation taking $b \to 0$, thus getting:

$$\frac{l^2}{R_1 C_0}\frac{\partial^2 V}{\partial x^2} = \frac{\partial V}{\partial t}. \quad (22c)$$

This is nothing but Fick's law of diffusion with coefficient of diffusion:

$$D = \frac{l^2}{R_1 C_0} = 7.2 \cdot 10^{-10} \frac{\mathrm{m}^2}{\mathrm{s}}\,, \tag{22d}$$

a value that is one order of magnitude greater than the value for calcium waves in intracellular calcium dynamics from endoplasmatic reticulum.[11] The voltage accompanying diffusion of ions from Eq. (22c) has the solution in the well-known form of smearing in time Gaussian wave package:

$$V(x,t) = V_0 \left(\frac{R_1 C_0}{\pi l^2 t}\right)^{\frac{1}{2}} \exp\left(-\frac{x^2}{2\left(\frac{l^2 t}{R_1 C_0}\right)^{\frac{1}{2}}}\right). \tag{22e}$$

Let us now analyze Eq. (22b) going over to the set of dimensionless variables as follows:

$$\begin{aligned} &\frac{x}{l} = \eta\,; \quad \frac{t}{R_1 C_0} = \tau\,; \quad \xi = \eta - \nu_0 \tau \\ &\nu_0 = \frac{v}{v_0}\,; \quad v_0 = \frac{l}{R_1 C_0}\,; \quad W = \frac{V}{V_0}\,. \end{aligned} \tag{23a}$$

The characteristic cut off velocity of ionic waves is:

$$v_0 = \frac{5.4 \cdot 10^{-9}}{2 \cdot 10^8 \cdot 2 \cdot 10^{-16}} \frac{\mathrm{m}}{\mathrm{s}} = 0.13 \frac{\mathrm{m}}{\mathrm{s}}\,, \tag{23b}$$

and it is three orders of magnitude greater than the velocity of calcium waves in bulk cytoplasm.[11] But since the actual velocity v obeys inequality $v < v_0 (v_0 < 1)$ it appears to be a pretty good estimation likely to meet the velocity of ionic waves along F-actin *in vivo*.

On the basis of new variables Eq. (23a), nonlinear partial differential equation Eq. (22b) now becomes ordinary differential equation which reads:

$$\frac{d^2 W}{d\zeta^2} + \nu_0 \frac{dW}{d\zeta} - 2\nu_0 V_0 b W \frac{dW}{d\zeta} = 0\,. \tag{24}$$

Integrating once, we easily get:

$$\frac{dW}{d\zeta} + \nu_0 W - \nu_0 V_0 b W^2 = c_1\,; \quad c_1 = \text{const.} \tag{24a}$$

In order to determine c1 in Eq. (24a) we impose the natural initial condition of type:

$$\frac{dW}{d\zeta} = A < 0 \quad \text{for} \quad W = 0\,. \tag{24b}$$

Separating variables in Eq. (24a) and factorizing we have:

$$\int \frac{dW}{W - W_1} - \int \frac{dW}{W - W_2} = \alpha\zeta + \ln c_2\,, \tag{24c}$$

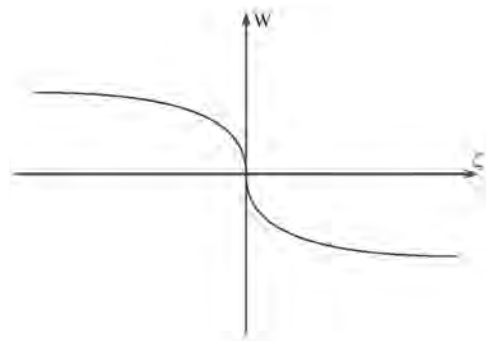

Fig. 6. The shape of antikink front profile of ionic wave.

$$W_{1/2} = \frac{1}{2V_0 b}\left(1 \pm \sqrt{1 + 4\frac{AV_0 b}{\nu_0}}\right); \quad \alpha = (W_1 - W_2)V_0\nu_0 b\,. \tag{24d}$$

The integration of Eq. (24c) with initial conditions ($\zeta = 0, w = 0$) yields:

$$W(\zeta) = W_1\left[\frac{1 - \exp(\alpha\zeta)}{1 - \frac{W_1}{W_2}\exp(\alpha\zeta)}\right]. \tag{25}$$

Let us consider the interesting case of more convenient slow waves with velocities ν_0 obeying the inequality:

$$\frac{4AV_0 b}{\nu_0} \gg 1\,, \tag{25a}$$

which implies that Eq. (25) becomes:

$$W_0(\zeta) = -\left(\frac{A}{bV_0\nu_0}\right)^{\frac{1}{2}}\tanh(\alpha\zeta)\,; \quad \alpha = 2(AbV_0\nu_0)^{\frac{1}{2}}\,. \tag{26}$$

This is symmetric antikink represented in (Fig. 6).

In order to examine Eq. (24) with respect to stability of its solution, Eq. (25), we start from slightly distorted trial solution:

$$W = W_0 + \delta\,; \quad \delta \ll W_0 \tag{26a}$$

Inserting the trial solution, Eq. (26) into Eq. (24) we easily obtain linear equation:

$$\frac{d^2\delta}{d\zeta^2} + \nu_0(1 - \nu_0 b)\frac{d\delta}{d\zeta} - \left[\left(\frac{dW_0}{d\zeta}\right)V_0 b\right]\delta = 0\,. \tag{26b}$$

Since inequalities:

$$V_0 b \ll 1\,; \quad \frac{dW_0}{d\zeta} < 0 \tag{26c}$$

always hold, it firmly indicates that the solution Eq. (25) represents the robust stable front of propagating ionic wave along F-actin.

4. The Impact of Intrinsic Electric Fields on the Motion of Ionic Wave, Eq. (25)

It is well-known that besides Brownian motion, intracellular oscillating electric fields drive the transfer of biological molecules. Fraunfelder *et al.*[11] analyzed the forces in biological systems and claimed clearly that "In biological systems the governing force is known and it is the electromagnetic interaction".

One of us with coworkers,[2] already elaborated the existence of intrinsic electric fields in microtubules which play important biological roles in their dynamics.

We here first start from the experimental evidence that F-actin represents a big dipole with oppositely charged tips as a consequence of the fact that every actin monomer possesses an intrinsic electric dipole. This circumstance implies that every F-actin has intrinsic, almost constant, electric field E, parallel along filament, and with magnitude depending on pH conditions and F-actin length. This field is confined and channeled through the layer of ionic cloud about F-actin, and it gives an additional potential $V_{\rm int}$. In this context the dimensionless Eq. (24) could be considered numerically by taking into account $V_{\rm int}$.

If we choose the set of parameters:

$$\nu_0 = 0.1\,, \quad \nu_0 b V_0 = 0.05\,, \quad \frac{V_{\rm int}}{V_0} = 0.4\,, \tag{27a}$$

we have:

$$\frac{d^2W}{d\zeta^2} + 0.1\frac{dW}{d\zeta} - 0.05W\frac{dW}{d\zeta} + 0.1 = 0\,. \tag{27b}$$

Taking the initial conditions:

$$\left(\frac{dW}{d\zeta}\right)_0 = -0.5\,; \quad W(0) = 0\,, \tag{27c}$$

we get the trajectory of the center of antikink Eq. (26) as a function of dimensionless time represented at (Fig. 7).

It shows that antikink is being initially driven by acceleration and after $\tau = 50$ ($t \sim 0.5$ μs) it attains constant terminal velocity $\nu_0 = 0.1$ ($\nu = 0.1 \cdot \nu_0 = 1.3$ cm/s).

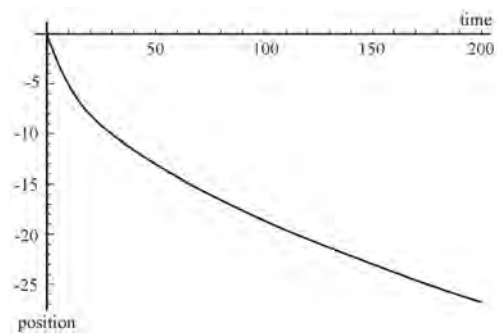

Fig. 7. The trajectory of the center of mass of antikink pertaining to Eq. (27b).

Besides the above mentioned intrinsic electric field, generated by F-actin itself, we further examine the possibility that some compartments of cell could produce oscillating electric fields.

Any molecule with an electric dipole moment can generate an oscillating electromagnetic field with a dominant electrical component. The strong electrically polar character of biological constituents makes the longitudal oscillations of the electric dipolar field (EDF) possible, as was first proposed by Fröhlich.[13] The metabolic supply from metabolic sources can excite these oscillations to be far from thermodynamic equilibrium. The specific excitation depends on the amount of energy supplied to the pertinent compartment of cell.

For example, it is believed that the ordered (vicinal) water molecules could form the EDFs occuring on either side of cell membrane. Within the interior of the cell, the water molecules generate the EDF in the vicinity of the cytoskeleton (actin filaments and microtubules).

Del Guidice *et al.*[14] have proposed that electromagnetic fields arising from EDF coherent oscillations create the electromagnetic signals comparable in size with the dimensions of cell. M. Satarić already widely used this concept in connection with traffic of cellular cargos along microtubules.[15,16]

Here we envisage that the oscillating EDFs could significantly influence the motion of afore elaborated ionic waves along F-actins. Let us now consider the motion of a ionic wave front, functions (25) and (26) described by Eq. (24) subjected to the harmonic electric force generated by EDF.

We assume that such dimensionless driving force has a wavelength that is greater than the cell's size and harmonically depends on dimensionless time τ:

$$f(\tau) = f_0 \cos(\Omega\tau + \varphi_0)\,, \tag{28}$$

where f_0 is the amplitude, Ω the frequency and φ_0 is the initial phase of driving force. By adding Eq. (28) to Eq. (24) we could examine numerically dynamics of ionic wave front in such new forced regime.

Using the same parameters for homogenous part of Eq. (27b) as before and taking $f_0 = 0.5$, $\Omega = 0.5$ and $\varphi_0 = 0$, we have:

$$\frac{d^2W}{d\zeta^2} + 0.1\frac{dW}{d\zeta} - 0.05W\frac{dW}{d\zeta} + 0.1 = 0.5\cos(0.5\tau)\,. \tag{29}$$

Again we have similar characters of unidirectional motion of antikink center with the same average velocity but now superimposed with harmonic oscillations of its center (Fig. 8). It is apparent that intrinsic electric fields could serve as a control mechanism for tuning of ionic wave motion along F-actin.

We believe that some of the cell's compartments use this mechanism to "order" ionic flux to be directed along particular F-actins and microtubules towards specific locations where the need for ions occurs.

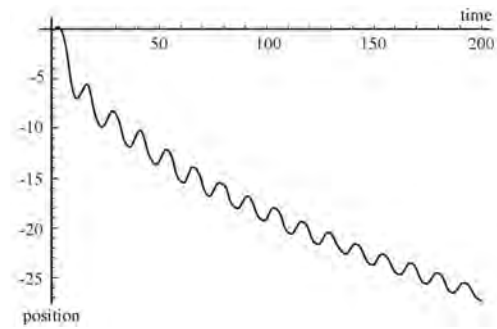

Fig. 8. The trajectory of the center of mass of antikink in the case of EDF with parameters of Eq. (28).

5. Conclusion and Discussion

Strongly reliant on the polyelectrolyte concept, we elaborated a new model for ionic currents along F-actin filaments in cell. The background for the model is the molecular structure and geometry of F-actin and its interaction with solvent ions. In that context, F-actin filament surrounded by ions from cytosol is considered as an electrical transmission line with R, C and L elements estimated on the basis of available experimental data and known geometry. The important feature of nonlinearity of F-actin capacitance was arisen naturally from rough landscape of its surface. As a result the nonlinear second order differential equation for electric potential along F-actin was evaluated. The traveling wave solution of this Eq. (24) is localized frontal profile of antikink type. This front is resembling to "nanotsunami" and propagates with velocity which is estimated to be pretty close to the experimental findings for example for waves of Ca^{++} ions excited by endosome reticulum compartments. These antikinks appear to be stable and robust against perturbations.

The remaining part of paper we dedicated to possible impact of cell's intrinsic electric fields onto the dynamics of the above antikinks. It appears that the velocity of their propagation could be tuned by changing parameters of fields (amplitude, frequency and phase).

Acknowledgment

M. V. Satarić is grateful for grants Nos. 141018A and 23036 by Ministry of Sciences, Government of Serbia.

References

1. J. A. Tuszynski, S. Portet, J. M. Dixon, C. Luxford and H. F. Cantiello, *Biophys. J.* **86**, 1890 (2004).
2. M. V. Satarić, J. A. Tuszynski and R. B. Žakula, *Phys. Rev. E* **48**, 589 (1993).
3. S. Kobayasi, *Biochim. Biophys. Acta* **88**, 541 (1964).
4. H. F. Cantiello, C. R. Patenaude and K. S. Zoner, *Biophys. J.* **59**, 1284 (1991).

5. A. G. Prat, A. M. Bertorello, D. A. Ausiello and H. F. Cantiello, *Am. J. Physiol.* **265**, 224 (1993).
6. G. H. Zimm, in Coulombic Interactions in Macromolecular Systems, ed. J. M. Comstock (Washington, DC, 1980), p. 212.
7. E. C. Lin and H. F. Cantiello, *Biophys. J.* **65**, 1371 (1993).
8. F. Oosawa, *Polyelectrolytes* (Marcel Dekker, New York, 1971).
9. B. F. Chasan, N. Geisse, K. Pedatella, D. Wooster, M. Teintze, M. Carattino, W. Goldmann and H. Cantiello, *E. Biophys. J.* **63**, 794 (2002).
10. I. Minoura and E. Muto, *Biophys. J.* **90**, 3739 (2006).
11. K. Wang, W. J. Rappel and H. Levine, *Phys. Biol.* **1**, 27 (2004).
12. H. Fraunfelder, P. G. Wolynes and R. H. Austin, *Rev. Mod. Phys. Centenary* **71**(2), 419 (1999).
13. H. Fröhlich, *Advances in Electronics and Electron Phys.* **53**, 85 (1980).
14. D. Giudice, G. Preparata and G. Vitiello, *Phys. Rev. Lett.* **61**, 1085 (1988).
15. M. V. Satarić, B. M. Satarić and J. A. Tuszynski, *Electrom. Biol. Medicine* **24**, 255 (2005).
16. M. V. Satarić, Lj. Budinski-Petković and I. Lon?arević, *Int. Journ. Med. Phys. B* **21**(32), 5387 (2007).

Ionic Pulses along Cytoskeletal Protophilaments

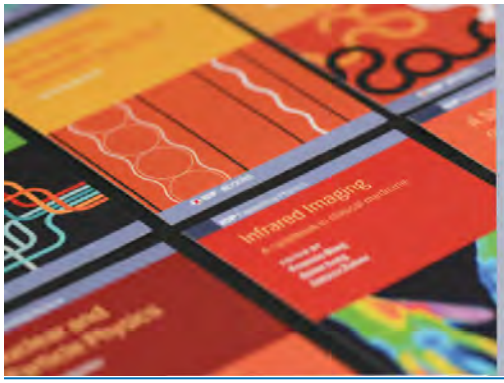

Journal of Physics: Conference Series **329** (2011) 012009 doi:10.1088/1742-6596/329/1/012009

Ionic Pulses along Cytoskeletal Protophilaments

M V Satarić [1] and B M Satarić [1]

[1] Faculty of Technical Sciences, University of Novi Sad, Serbia Trg D. Obradovića 6

E-mail: bomisat@neobee.net

Abstract. The experimental evidences regarding ionic waves generation and propagation along both microtubules (MT_s) and actin filaments (AF_s) motivated us to develop the physical models that provide the framework for the explanation and analysis of these interesting biophysical phenomena.

In pertaining analysis we partly relied on some experimental as well as numerical data, but also on theoretical estimations enabling us to establish the concept of nonlinear transmission lines which could lead to reasonable clearing up of experimental facts.

We are convinced that these ionic currents actually exist and serve to sustain some important biological cellular mechanisms.

1. Introduction

The cytoskeleton is basic ingredient of all living cells. It is composed of three major types of filamental structures, including tubulin-protein based MT_s, actin-protein based AF_s and intermediate filaments. All of them are organized into networks which are interconnected through different auxiliary proteins [1].

There are at least three well-studied mechanical functions of the cytoskeleton in vivo; providing mechanical strength of the cell, segregating the chromosomes in cell division and active participation in the transport of macromolecules via motor proteins, primarily kinesin, dynein and myosin [2,3,4].

Here we pay the particular attention on the roles of MT_s and AF_s in facilitating intra cellular ionic currents which participate in some fundamental biological processes.

First experimental evidences for ionic waves propagating along AF_s are found out by the group led by H Cantiello [5,6]. These assays had clearly shown that the input ionic signals are being localized and propagate along AF_s in the forms resembling solitonic pulses. The theoretical explanations of these features were done by J Tuszynski et al [7] and later by M Satarić et al [8].

On the other hand, the experiment of measurement of ionic current along a single MT was performed within the same group [9]. Theoretical considerations of ionic currents along MT_s were performed by J Tuszynski et al [10] and in many stages by M Satarić et al [11,12,13,14].

In the following we will first present the outlines of polyelectrolitic concept of cytoskeleton and then briefly consider the main results concerning localized ionic pulses along AF_s and MT_s.

2. Manning-Oosava counterion condensation

Manning showed [15] that a highly charged cylinderlike polymers exert strong attraction on their counterions that a certain fraction condenses onto the polymer forming the so called ionic cloud (IC). Typical representative of this class of biopolymers is DNA. This condensation is triggered when the Manning parameter $M = \frac{l_B}{l_0}$ is greater than unity. Here the Bjerrum length is defined as follows

$$l_B = \frac{e^2}{\varepsilon k_B T} \quad , \tag{1}$$

where e is the electron charge, ε is the dielectric constant of cytosol and $k_B T$ is the thermal energy ($k_B = 1,38 \times 10^{-23} J$).

Taking the physiological temperature $T = 310K$ and $\varepsilon = 80 \times 8,85 \times 10^{-12} F/m$, we get

$$l_B = 0,67nm. \tag{2}$$

On the other hand, l_0 follows from cylindrical polymer's linear charge density q_0:

$$q_0 = \frac{e}{l_0} = \frac{q}{L} \quad , \tag{3}$$

where L is the cylinder's total length and q its total surface charge.

This charge causes counterion condensation around polymer in the cases where the concentration of counterions (n) is small enough that the inequality $\xi_D \gg a$ holds (a is the radius of the cylinder).

Here the Debye length ξ_D is defined as follows

$$\xi_D = (8\pi n l_B)^{-1/2}. \tag{4}$$

Relying on the above conditions we found out that both AF_s and MT_s in physiological conditions could be safely considered as polyelectrolites of Manning's class.

We estimated, on the basis of Manning's theory [15], that the thickness of IC in physiological conditions is for AF and MT respectively

$$\lambda_{AF} = 5nm \quad \text{and} \quad \lambda_{TD} = 2,5nm.$$

On the basis of such concept we established the models where these cytoskeletal cylindrical polymers can be viewed as "coaxial cables" having the features of nonlinear transmission lines. These lines in general could be sequenced in ladders of repeated identical electric elementary units (EEU) which posses specific values of capacity, resistivity and conductivity. We estimated that corresponding inductivities of EEU_s are small enough that can be safely ignored [12].

Between IC of condensed counterions around EEU and repelled rest of bulk ions there exists the depleted layer (with no ions present) with the thickness equal to l_B, Fig. 1. Thus we consider the IC around cylinder as one conductive plate and the depleted layer as the dielectric corroborating the validity of analogy with coaxial cable.

The important point of developed models is the presence of nonlinearity in this concept of "transmission lines".

In both cases, for AF_s and MT_s, the nonlinearity is attributed to capacitance of EEU_s. For AF_s this nonlinearity originates from local pockets between actin proteins arranged helically, while in MT_s the main contribution arises from so called tubulin tails (TT_s) which are very flexible. These TT_s can shrink or stretch and oscillate, thus changing capacity of IC around MT.

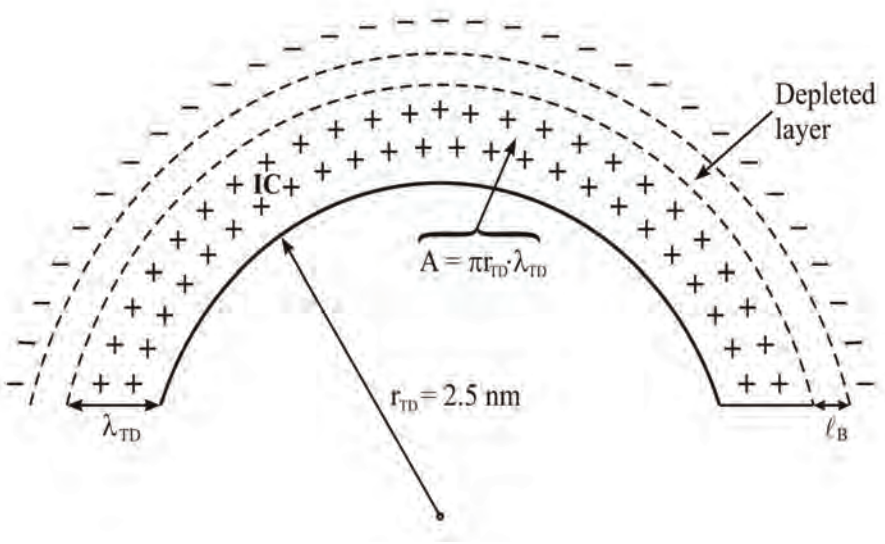

Figure 1. Cytoskeletal cylindrical polymers viewed as "coaxial cables".

3. The case of AF_s

The detailed consideration of AF_s in the context of nonlinear transmission lines is presented in Ref [8].

The equation which describes the time-space voltage of ionic pulse reads (x is the orientation of AF)

$$l^2\frac{\partial^2 V}{\partial x^2} - R_1C_0\frac{\partial V}{\partial t} + 2bR_1C_0V\frac{\partial V}{\partial t} = 0. \tag{5}$$

The length $l = 5,4nm$ is the dimension of an EEU, ie. the diameter of one actin protein molecule; C_0 is the leading constant term of EEU capacitance and R_1 is its longitudinal resistance in direction of x-axis; b stands for the parameter of nonlinear term of $EEU's$ capacitance. The solution of Eq (5) reads [8]:

$$V(x,t) = W_1[1-\exp(\alpha\xi)]\cdot[1-\frac{W_1}{W_2}\exp(\alpha\varsigma)]^{-1} \tag{6}$$

with following abbreviations

$$W_{1/2} = (2bV_0)^{-1}\left[1 \pm \left(1+4\frac{AbV_0}{v_0}\right)^{1/2}\right]$$

$$\alpha = (W_1 - W_2)bV_0v_0; \quad \varsigma = \left(\frac{x}{l} - v_0\frac{t}{R_1C_0}\right). \tag{7}$$

The characteristic wave velocity is

$$v_0 = \frac{l}{R_1C_0} = \frac{5,4\times10^{-9}}{2\times10^8\times2\times10^{-16}}\left(\frac{m}{s}\right) = 13\frac{cm}{s}.$$

V_0 is the voltage amplitude defined by the influx of ions directed along AF; At last,

$$A = \left(\frac{dW}{d\xi}\right)_{W=0} < 0.$$

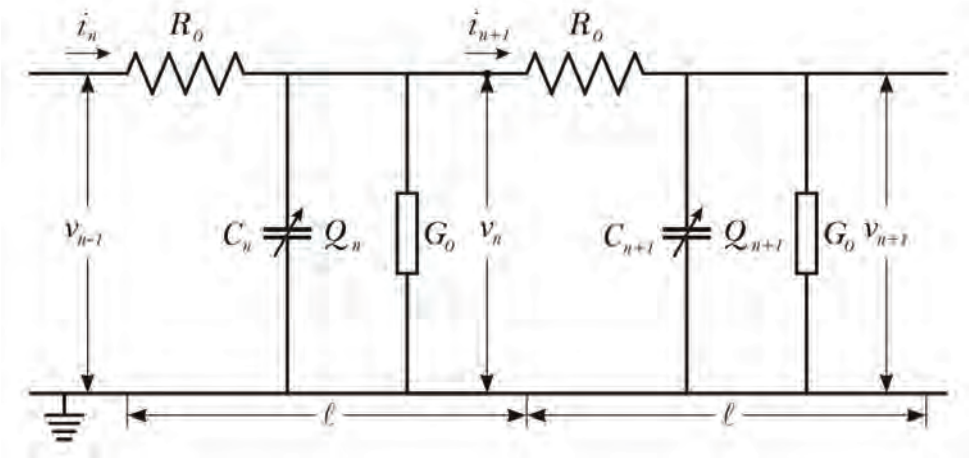

Figure 2. An effective circuit diagram for the n-th EEU with characteristic elements involved in Kirchoff's laws.

The solution Eq (6) is a typical anti-kink wave propagating with the velocity of the order of (cm/s), which has very reasonable order of magnitude.

4. The case of MT_s

Microtubules are hollow cylinders of 13 parallel protofilaments consisting of $\alpha - \beta$ tubulin heterodimers [1].

The experimental evidences regarding ionic currents along MT_s revealed that MT_s exhibit some kind of amplifying roles which resemble the "biotransistors" [9].

Our theoretical modeling of these currents was developed in three stages [11,12,13,14].

The first stage [11,12] is similar to that one applied for AF_s [8] in the way that the roles of nano-pores (NP_s) existing between protofilaments of MT were ignored.

Second version [13] is more complete, where the roles of NP_s are modeled in the context of an approach developed by Siwy et al [16]. This model involves the nonlinear negative incremental resistance of NP_s in parallel with nonlinear capacitance of EEU_s caused by mentioned property of TT_s. The important point of this stage is that the ohmic loss of transmission line should be balanced by the fresh ions injected into IC from NP_s since these act as ionic pumps in suitable voltage regime along MT. As the result, the solution of Kirhoff's equations of nonlinear circuit is the stable bell-shaped soliton voltage pulse which propagates along MT with the velocity of the order of mm/s.

Recently the more advanced version of the same concept was presented [14] in which the NP_s are treated according to within the numerical simulations performed the group led by Tuszynski [17].

We established simple periodic ladder network composed of the lumped sections equal to identical EEU_s (every tubulin dimer of one protofilament is an EEU) as represented in Fig.2

According to Kirchoff's laws from Fig.2 we have

$$\begin{aligned} i_n - i_{n+1} &= \tfrac{\partial Q_n}{\partial t} + G_0 v_n, \\ v_{n-1} - v_n &= R_0 i_n, \end{aligned} \tag{8}$$

where Q_n represents the charge of EEU capacitor as nonlinear function of voltage v;

$$Q_n = C_0[1 - \Gamma_0\Omega(t - t_0) - b_0 v]v \tag{9}$$

which is deeply elaborated in Ref (14).

Introducing the characteristic impedance Z of an EEU corresponding to characteristic frequency ω

$$Z = \frac{1}{\omega C_0}, \tag{10}$$

and the function $u(x,t)$ unifying the voltage and ionic current along a MT

$$u_n = Z^{1/2} i_n = Z^{-1/2} v_n, \tag{11}$$

and going over to the continuum approximation with respect to space variable x, we get from Eqs (8), in terms of Eqs (9,10),

$$\frac{\partial^3 u}{\partial \xi^3} + 3\left(\frac{ZC_0 s}{T_0} - 2\right)\frac{\partial u}{\partial \tau} + 3ZC_0\Gamma_0\Omega(\xi - \xi_0)\frac{\partial u}{\partial \xi} + 6\frac{Z^{3/2} b_0 C_0 s}{T_0}\left(u\frac{\partial u}{\partial \xi}\right)$$

$$+3(ZG_0 + Z^{-1}R - ZC_0\Gamma_0\Omega)u = 0. \tag{12}$$

Here the characteristic charging (discharging) time of an EEU capacitor C_0 through the resistance R_0 is $T_0 = R_0 C_0 = 6,2 \times 10^7 \Omega \times 1,92 \times 10^{-16} F = 1,2 \times 10^{-8} s$.

The dimensionless space and time variables are

$$\xi = \frac{x}{l} - \tau; \quad \tau = s\frac{t}{t_0}; \quad s = \frac{v}{v_0}.$$

The characteristic speed is $v_0 = \frac{l}{T_0} = \frac{8\times 10^{-9} m}{1{,}2\times 10^{-8} s} = 0,67\frac{m}{s}$; $l = 8 \times 10^{-9} m$ is the length of one tubulin dimer (EEU).

G_0 is the conductance of a NP and Ω the frequency of thermal oscillations of a TT; b_0 is the parameter of nonlinear capacity of a TT.

After a tedious procedure the solution of Eq (11) reads

$$u(\xi,\tau) = \frac{u_0 \exp(-2\gamma_0\tau)}{\cos h^2\left\{\left[\frac{\alpha u_0}{4\beta}\exp(-2\gamma_0\tau)\right]^{1/2}\left[\xi - \xi_0(1 - \exp(\gamma_0\tau)) + \frac{\alpha u_0}{3\beta}(1 - \exp(3\gamma_0\tau))\exp(-2\gamma_0\tau)\right]\right\}}, \tag{13}$$

where the abbreviations have the values

$$\begin{aligned} &\alpha = \frac{2Z^{3/2} b_0 C_0 s}{T_0\left(\frac{ZC_0 s}{T_0} - 2\right)}; \quad \beta = \left[3\left(\frac{ZC_0 s}{T_0} - 2\right)\right]^{-1} \\ &\gamma_0 = ZC_0\Gamma_0\Omega\left(\frac{ZC_0 s}{T_0} - 2\right)^{-1}. \end{aligned} \tag{14}$$

u_0 is the amplitude defined by the initial conditions.

We here mention one of possible numerical solutions of Eq (11) for the specific set of parameters, Fig. 3

$$\alpha = 0,5; \quad \beta = 0,1; \quad \gamma_0 = 0,1; \quad \xi_0 = 0,1.$$

It is apparent that localized pulse-like wave propagates with slightly decreasing amplitude along distances of hundreds EEU_s with constant velocity.

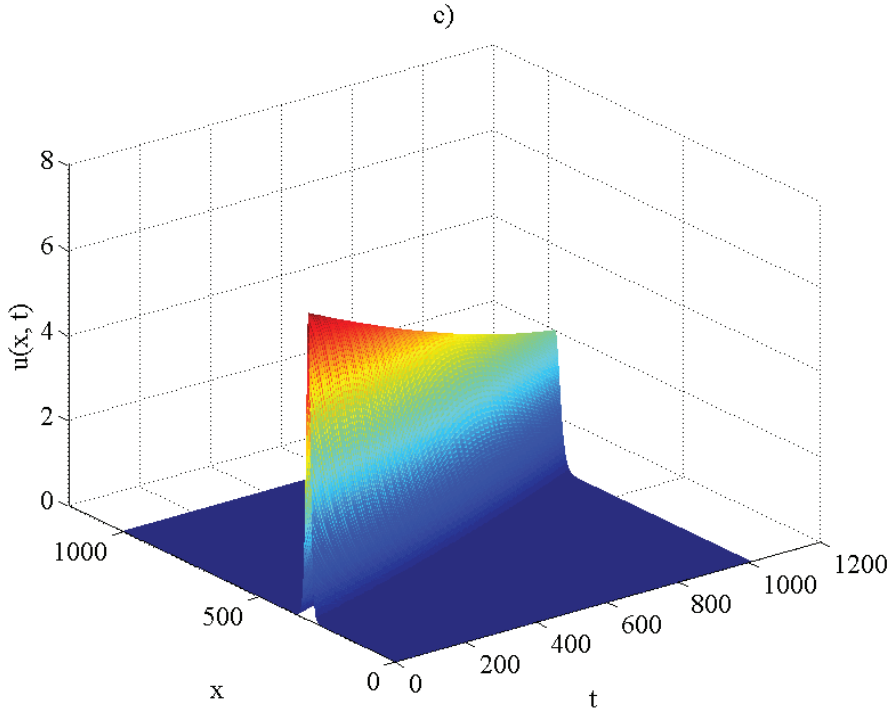

Figure 3. One of possible numerical solutions of Eq (11).

This velocity can be estimated from Fig. 3 as follows:

$$\Delta x = 400l = 400 \times 8nm = 3,2\mu m$$
$$\Delta t = 1000T_0 = 10^3 \times 1,2 \times 10^{-8}s = 1,2 \times 10^{-5}s$$
$$v = \frac{\Delta x}{\Delta t} = 0,26\frac{m}{s}. \tag{15}$$

The range of this soliton is $3,2\mu m$ which is of the order of cell's diameter.

5. Discussion and conclusion

In this paper we briefly reviewed the recent contributions regarding the role of cytoskeletal filaments (AF_s and MT_s) in ionic propagation within the living cells.

The general feature of all mechanisms is the concept of nonlinear transmission lines. The origin of nonlinear effects is mostly attributed to capacitance of these filaments. The coaxial cable-like geometry of transmission lines relies on their polyelectrolite properties in accordance with Manning's theory.

The order of magnitude of soliton like localized pulses arising within the scope of our theory ranges from mm/s to a several cm/s which are very reasonable values.

Acknowledgements

This research was supported by funds from the Serbian Ministry of Education and Sciences, Grant OI 171009.

References

[1] Dustin P, Microtubules (Springer, Berlin 1984).
[2] Gross S P, Vershinin M and Shubeita G T, 2007, Curr. Biol. **17**, R, 478.
[3] Vale R D, 2003, Cell **112**, 467.
[4] Satarić M V, Budinski-Petković Lj and Lončarević I, 2007, IJMPB **21**, No32, 5387.
[5] Contiello H, Patenande C and Zaner K, 1991, Biophys. J. **59**, 1284.
[6] Lin E C, Cantiello H F, 1993, Biophys. J. **65**, 1371.
[7] Tuszynski J A, Portet S, Dixon J M, Luxford C and Cantiello H F, 2004, Biophys. J. **86**, 1890.
[8] Satarić M V, Bednar N, Satarić B M and Stojanović G, 2009, IJMPB **23**, No22, 4697.
[9] Priel A, Ramos A J, Tuszynski J A and Cantiello H F, 2006, Biophys. J. **90**, 4639.
[10] Pril A and Tuszynski J A, 2008, EPL **83**, 68004.
[11] Satarić M V, Ilić D and Ralević N, 2009, Chin. Phys. Lett **26**, No3, 073101.
[12] Satarić M V, Ilić D, Ralević N and Tuszynski J A, 2009, Eur. Biophys. J. **38**, 637.
[13] Satarić M V, Sekulić D and Živanov M, 2010, Journ. of Comp. Theor. Nanosci. **7**, 2281.
[14] Sekulić D L, Satarić B M, Tuszynski J A and Satarić M V, 2011, Eur. Phys. J. **34**, 49.
[15] O'Shaughnessy B and Yang Q, 2005, Phys. Rev. Lett. **94**, 048302.
[16] Siwy Z S, Powell M R, Petrov A, Kalman E, Trantmann C and Eisenberg R S, 2006, Nano. Lett. **6**, No8, 1729.
[17] Freedman H, Rezania N, Priel A, Carprenter E, Noskov S Y and Tuszynski J A, 2010, Phys. Rev. E **81**, 051912.

Nonlinear Dynamics of Microtubules: Biophysical Implications

Article *in* Journal of Biological Physics · December 2005

DOI: 10.1007/s10867-005-7288-1 · Source: PubMed

2 authors, including:

Miljko V Satarić
University of Novi Sad
119 PUBLICATIONS **1,629** CITATIONS

SEE PROFILE

Journal of Biological Physics 31: 487–500, 2005.
DOI: 10.1007/s10867-005-7288-1

Nonlinear Dynamics of Microtubules: Biophysical Implications

M.V. SATARIC[1] and J.A. TUSZYNSKI[2,*]
[1]*Faculty of Technical Sciences, University of Novi Sad, Novi Sad, Serbia 21 000, Serbia and Montenegro;* [2]*Department of Physics, University of Alberta, Edmonton, Alberta, Canada T6G 2J1*
*(*Author for correspondence, e-mail: jtus@phys.ualberta.ca)*

Abstract. A recently developed model of nonlinear dynamics for microtubules is further expanded based on the biophysical arguments involving the secondary structure of the constitutive protein tubulin and on the ferroelectric properties of microtubules. It is demonstrated that kink excitations arise due to GTP hydrolysis that causes a dynamical transition in the structure of tubulin. The presence of an intrinsic electric field associated with the structure of a microtubule leads to unidirectional propagation of the kink excitation along the microtubule axis. This mechanism offers an explanation of the dynamic instability phenomenon in terms of the electric field effects. Moreover, a possible elucidation of the unidirectional transport of cargo *via* motor proteins such as kinesin and dynein is proposed within the model developed in this paper.

Key words: microtubule, tubulin, ferroelectricity, kink propagation, GTP hydrolysis, dynamic instability

1. Introduction

Microtubules (MTs) are major cytoskeletal proteins assembled from the protein called tubulin that plays a crucial role in all eukaryotic cells. The structure of microtubules is cylindrical and it typically involves 13 protofilaments (see Figure 1).

The building block of a microtubule is a tubulin dimer that contains approximately 900 amino acids comprising some 14 000 atoms with a combined mass of 110 kDa. The tubulin dimer is made up of two slightly different monomers, called α and β tubulin, respectively.

Tubulin's secondary structure is of crucial importance to the model proposed in this paper. The α-monomer contains mostly α-helices terminated with loops protruding partially through the globular structure of the protein. These loops are important for the formation of weak bonds between neighbouring proteins, enabling polymerization of tubulin into microtubules. Additionally, they provide a binding site for the energy-giving molecule GTP that is non-exchangeable in the α-monomer while exchangeable in the β-monomer. The flexible loops are ideally suited for adjusting the positions of the many amino acid residues that participate

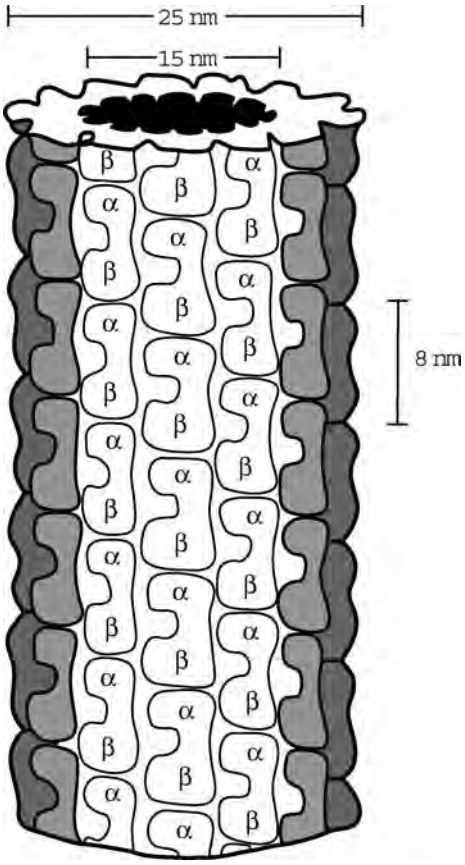

Figure 1. A cartoon showing the construction of a MT from individual tubulin dimers.

in the binding between two neighbouring dimers. The core part of the β-monomer consists of β-sheets of peptide chains surrounded by α-helices that terminate with protruding flexible loops whose properties are similar to those in the α-monomer. Functionally, the β-monomer plays a more important role than the α-monomer owing to its exchangeable GTP binding site as well as many other ligand-binding sites.

Microtubules form an important part of the cellular scaffold providing the required rigidity and plasticity in addition to creating a network of "railroad tracks" for active intracellular transport *via* motor proteins. Active transport is critical for cellular organization and the multitude of functions performed by sub-cellular structures. Impaired transport has been linked to a range of diseases such as neuronal degeneration [1]. Long-distance transport in cells uses opposite-polarity molecular motors of the kinesin and dynein super-families that move cargo along MTs.

MTs are structurally rigid against thermal fluctuations since their persistence length is in the mm-range, far exceeding that of either actin or DNA. On the other

hand, MTs are flexible when subjected to bending and buckling forces. MTs rupture when stretched beyond 50% of their original length [2]. Their flexibility can be attributed to the presence of flexible protruding loops that contribute to the protein polymerization binding forces.

MTs also play a crucial role during cell division forming a dynamic structure that spatially segregates the duplicated chromosomes. *In vitro*, MTs exhibit dynamic instability that was discovered some 20 years ago [3] and so far has been proven unique to MTs only. During this process, MTs switch stochastically between periods of persistent assembly and catastrophic disassembly. This paper develops a physical model that is an attempt to explain the possible trigger mechanism for the seemingly random catastrophe events.

The mechanism of initiating tubulin assembly into MTs depends strongly on the binding of a Mg^{2+} ion to tubulin. It has been recently shown [4] that the six-coordinated Mg^{2+} complex with water, glutamic acid and GTP in singlet and triplet states is formed. In the triplet state, the magnesium complex concentrates its spin density toward one of the coordinated water molecules. Within that molecule, a redox reaction occurs and one of the hydrogen atoms is released from the complex at a speed of 330 m/s. The released hydrogen moves over a distance of 1.5 nm through water molecules surrounding the GTP centre. Eventually, the hydrogen atom collides inelastically with one water molecule, producing H_3O^+ and a free electron. Free electrons have been shown to have a tendency to accumulate in the bound water shell surround the tubulin dimer. This process results in the formation of a local electric field in the form of a Faraday cage for the intrinsic dipole moment of tubulin, protecting it from the ions in solution.

The role of electrons in the bound water shell surrounding tubulin has been confirmed experimentally [4] whereby a buffer solution containing non-polymerized tubulin was irradiated by a beam of electrons and subjected to laser impulses in the femtosecond range. Upon irradiation, tubulin began to assemble in the absence of Mg^{2+} ions.

2. Ferroelectric Properties of Microtubules

Our departure point in this section is the secondary structure of tubulin. Virtually every peptide group in an α-helix possesses a considerable dipole moment, on the order of $p_0 = 1.2 \times 10^{-29}$ Cm $= 3.5$ D. All these dipoles are almost parallel to the helical axis, giving rise to an overall dipole moment of this particular helix. It is generally accepted that this large dipole moment of an α-helix has an important biological role [5]. Since the tubulin dimer contains several α-helices that are not oriented randomly, it is not surprising that each tubulin dimer possesses a large net dipole moment p. On the other hand, closed loops lend themselves to the cancellation of an overall dipole moment.

The idea that MTs are ferroelectric was proposed some 30 years ago [6] on the basis of their piezoelectric properties. It is apparent that due to the strong

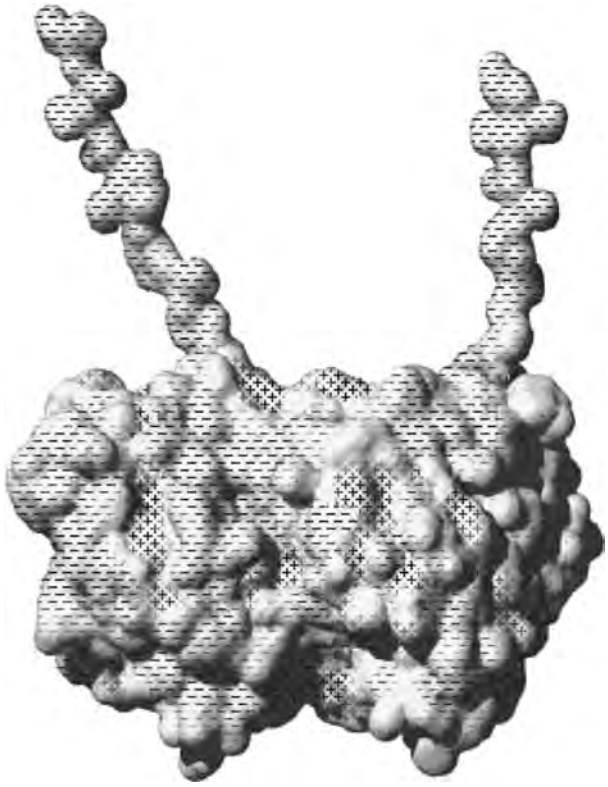

Figure 2. A map of the surface electric potential on a tubulin dimer with an elongated C-terminal conformation. The "+" and "−" symbols indicated the local field strengths. Figure prepared using MolMol.

curvature of an MT cylinder (see Figure 1), the inner parts of the dimer structure are compressed in order to fit into a microtubule while the outer ones are stretched by a substantial amount of tension. This additional redistribution of excess negative charge enhances the transverse component of the net dipole moment of every dimer comprising a MT. This effect is very analogous to that observed for the cylindrical hair cells [7]. This has also been corroborated by a detailed map of the electric charge distribution for the tubulin dimer [8].

As shown in Figure 2, it is clear that the C-termini that extend outwardly from the MT surface carry a significant amount of negative electric charge (as much as 40% of the total monomer charge can be attributed to a C-terminus). These negative charges on each C-terminus are responsible for its extended conformational state since the surface charge is also negative leading to Coulomb repulsion.

Taking into account the bound water layer with electrons released due to the Mg^{2+} complex activity, it is highly plausible to envisage the MT structure as a ferroelectric system with the dipole moments of tubulin oriented as shown in Figure 3.

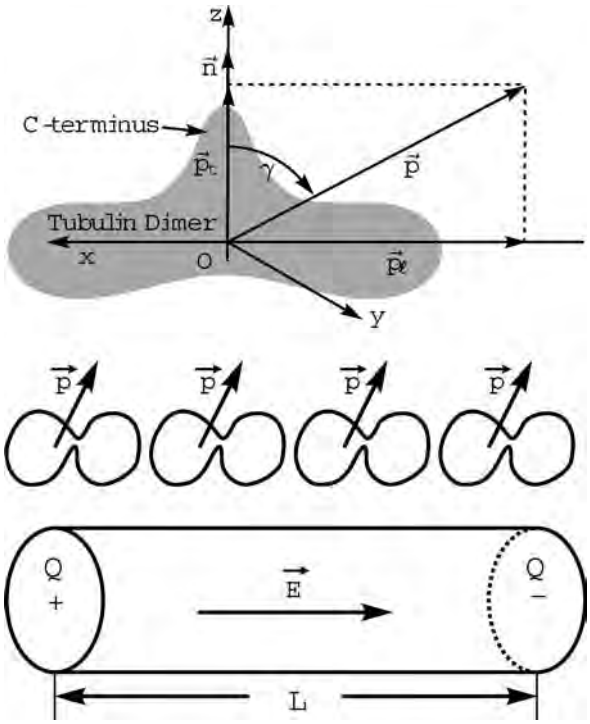

Figure 3. An individual dimer with its dipole decomposed, a protofilament with the dipoles of individual dimers, and a MT with the giant dipole due to these individual contributions.

The ends of a MT therefore possess a different amount of net charge as was recently demonstrated through massive molecular dynamics computations [9]. We therefore conclude that the MT cylinder supports an intrinsic electric field E [10].

3. Role of GTP Hydrolysis in MT Dynamics

Conformational flexibility of proteins refers to molecular motions on a time scale ranging from picoseconds (thermal fluctuations) to large-scale conformational motions important for functional dynamics occurring over microseconds or even milliseconds. Neutron scattering experiments [11] showed that at lower temperatures proteins are biologically inactive since thermal motions are basically harmonic. At higher temperatures, activation energy becomes accessible and thermal motions are predominantly anharmonic since molecules can make transitions between two different equilibrium states. The protein becomes structurally "soft" and biologically active. This phenomenon is called a dynamical transition.

Non-thermal energy sources are important for proteins in terms of facilitating these dynamical transitions. In the present case of tubulin and microtubules, a β-tubulin monomer in the dimeric structure has an exchangeable GTP site that is

an active domain. The chemical potential energy of GTP hydrolysis is converted into mechanical motion when some key chemical bonds are broken. The loss of a phosphate group occurs when the bound GTP molecule is hydrolysed to GDP in a reaction that is catalyzed by tubulin.

The dissociation of the inorganic phosphate group (P_i) in the reaction

$$\mathrm{GTP} \rightarrow \mathrm{GDP} + \mathrm{P_i} \tag{1}$$

causes a shift of a few angstroms in the GTP binding site that contains a polypeptide loop called a sensor loop. This small displacement causes a further conformational change that propagates along an associated α-helix (called a switch helix).

The switch helix serves as a "piston" that transmits a stimulus to adhere to a specific site of the same β-tubulin latching it in a "closed" conformation. This state of the α-helix pertains to a pre-stressed spring to use a mechanical analogy. The next stage of the conformational change triggered by the release of GDP causes the switch helix to unlatch allowing tubulin to tilt, rotating through an angle θ in the (r, x)-plane (in the filament direction as shown in Figure 4). This transformation is consistent with the conformational changes exhibited by motor proteins due to ATP hydrolysis [12]. The main difference between them is that in the case of motor proteins, their conformational changes are much larger due to their overall geometry and the need to overcome the viscosity of the medium while tubulin is incorporated in the cylindrical structure of an MT.

Next, we estimate the magnitude of the force associated with the conformational change due to the effect of GTP hydrolysis in tubulin. We deduce that the switch

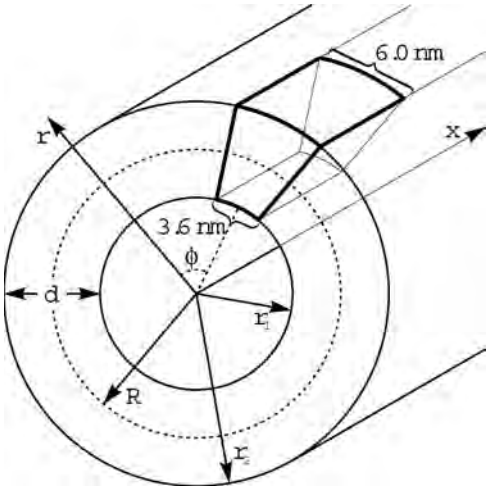

Figure 4. Characteristic dimensions of an MT cylinder with wedge-like dimers as its building blocks. The parameters are $d = 5$ nm, $R = 10$ nm, $r_1 = 7.5$ nm, $r_2 = 12.5$ nm.

helix has the approximate length of $l = 3$ nm. The force exerted by the helix and involving a translation by length Δl is [13]:

$$F = 3EI\, l^{-3} \Delta l = \kappa \Delta l \tag{2}$$

where EI is the flexural rigidity of the helix which is related to the persistence length l_p according to the formula:

$$l_p = EI/(k_B T) \tag{3}$$

where k_B is the Boltzmann constant and T the temperature in degrees Kelvin. The stiffness parameter κ can be estimated as

$$\kappa = 3EI\, l^{-3} = 3k_B T l_p l^{-3}. \tag{4}$$

Taking the persistence length of the switch to be $l_p = 100$ nm and its length as $l = 3$ nm one obtains

$$\kappa = 19\,\text{p N/nm}. \tag{5}$$

If the expected conformational change that occurs during GTP hydrolysis is of the order of $\Delta l = 1$ nm, the force generated by it is $F = 19$ pN. This force results in the tilt of the tubulin dimer by an angle $\theta = (1\text{ nm}/2.5\text{ nm}) = 0.4$ rad where 2.5 nm is the approximate radius of the β-tubulin monomer.

The above discussion provides a strong argument in favour of expanding the elastic potential energy of the dimer-dimer interaction to the fourth order with respect to the tilt angle since it implies a double-well situation with two local minima. Consequently, we calculate the work done by the force in Eq. (2) over the displacement of $\Delta l = 1$ nm to be $W = 1.9 \times 10^{-20}$ J $= 0.12$ eV. Since the energy released in one GTP hydrolysis event is known to be approximately 0.15 eV, it follows that a large part of this energy is utilized in generating the elastic deformation, while the remainder is dissipated into the surroundings. The elastic deformation following GTP hydrolysis will also affect the inter-dimer bonds between neighbouring tubulin units in a microtubule. The resultant displacements may lead to a dynamic collective phenomenon of a traveling wave of conformational changes propagating down the length of an MT. This effect is discussed in the next section.

4. The Nonlinear Model of a Propagating Conformational Tilt

The two main aspects of our theory are the nonlinear character of the inter-dimer potential energy and the ferroelectric behaviour of an MT. In an earlier publication

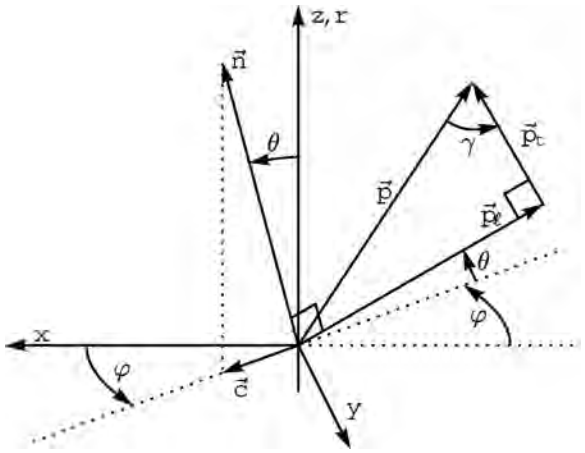

Figure 5. The ferroelectric geometry of a tubulin dimer; x is in the MT direction.

[14] we have provided a detailed justification of the free energy functional for an MT in cylindrical co-ordinates (r, θ, φ) that are schematically illustrated in Figure 5. Since the azimuthal angle φ is largely restricted due to the pronounced curvature of the MT cylinder, here we pay special attention to the tilt angle θ that dominates the overall conformational dynamics.

The free-energy density in the MT model presented here consists of the following four terms.

a) The elastic energy of the dimer-dimer interaction within a protofilament expands in terms of the tilt angle θ up to the fourth order as:

$$W_{\text{el}} = (-A\theta^2 + B\theta^4)/r^2 \tag{6}$$

where A and B are coefficients that are expressed in terms of the cylindrical components of the elasticity tensor [14].

b) The splay energy density has the form:

$$W_{\text{sp}} = k/2(\partial\theta/\partial x)^2 \tag{7}$$

where the coefficient k denotes the smectic splay elastic modulus. The presence of splay deformation has been experimentally demonstrated by bending MT filaments [15].

c) The polarization energy (see Figures 3 and 5 for illustration) takes the form:

$$W_{\text{pol}} = \left(p_t^2/\chi_t + p_\ell^2 2/\chi_\ell\right)/2 - Ep_\ell - \mu_p p_t\theta \tag{8}$$

where the longitudinal and transverse dielectric susceptibilities are denoted by χ_ℓ and χ_t, respectively. The intrinsic electric field E is directed along the long axis of the MT cylinder (x-axis), and μ_p is a phenomenological constant that depends on various model parameters such as the anisotropic polarizability of tubulin and the chirality effect due to C-termini.

d) The rotational kinetic energy of the tilting motion of the tubulin dimers is:

$$W_{\text{kin}} = \frac{1}{2} J(\partial\theta/\partial t)^2 \tag{9}$$

where J stands for tubulin's rotational moment of inertia divided by its volume (specific rotational inertia).

The total free energy functional of the system can be written as

$$F = 2\pi \int_{R-d/2}^{R+d/2} r\,\mathrm{d}r \int_0^L (W_{\text{el}} + W_{\text{sp}} + W_{\text{pol}} + W_{\text{kin}})\,\mathrm{d}x. \tag{10}$$

Before a free-energy minimization procedure is performed, we comment here on the necessity of accounting for the presence of viscosity in the medium surrounding the MT (cytosol). This effect can be modeled by including a friction term in the equation of motion that is subsequently derived using the Euler–Lagrange procedure. Hence a viscous torque is added

$$\tau_{\text{vis}} = -\Gamma\,\partial\theta/\partial t \tag{11}$$

where Γ depends both on the viscosity coefficient and the structural details of the MT through the Stokes–Einstein formula.

Combining the torque in Eq. (11) with the Euler–Lagrange equation stemming from the free-energy functional in Eq. (10) leads to a nonlinear differential equation of motion for the tilt angle θ. Using scaled variables and adopting a traveling wave form one obtains the following ordinary differential equation:

$$\mathrm{d}^2\eta/\mathrm{d}\xi^2 + \beta\,\mathrm{d}\eta/\mathrm{d}\xi + \eta - \eta^3 + \varepsilon = 0 \tag{12}$$

where we have introduced the following notation:

$$\eta = \theta/\theta_0; \qquad \theta_0 = (a/b)^{1/2}; \qquad \xi = \sqrt{a/\left[RdJ\pi\left(v_0^2 - v^2\right)\right]}(x - vt) \tag{13a}$$

$$\beta = \Gamma R v/\sqrt{RdJ\left(v_0^2 - v^2\right)} \tag{13b}$$

$$\varepsilon = a^{-3/2} b^{1/2} c = a^{-3/2} b^{1/2} R q_{\text{eff}} E \tag{13c}$$

$$a = 2\pi\,\ln(5/2) A d R^{-1} - 2\pi R\,\mathrm{d}\psi\,\mu_p^2 \cos^2(\gamma) \tag{13d}$$

$$b = 4\pi\,\ln(5/3) B\,\mathrm{d}R^{-1} \tag{13e}$$

$$c = \pi R d\psi\,\sin(2\gamma)\mu_p E = q_{\text{eff}} R E \tag{13f}$$

and

$$\psi = [\sin^2(\gamma)/\chi_\ell + \cos^2(\gamma)/\chi_t]^{-1} \tag{13g}$$

where v_0 is the sound velocity along the MT filament and v stands for the kink propagation velocity.

The most important result coming from Eq. (12) is the existence of an analytical solution in the form of a kink-type domain wall given by

$$\eta(\xi) = \eta_2 + (\eta_1 - \eta_2)/[1 + \exp \xi(\eta_1 - \eta_2)/\sqrt{2})] \tag{14}$$

with the asymptotic values of η_1 and η_2 depending on E *via* ε as follows:

$$\eta_1 = (2/\sqrt{3}) \cos[\cos^{-1}(3\sqrt{3}\varepsilon/2)] \tag{15}$$

$$\eta_2 = (2/\sqrt{3}) \cos[2\pi/3 + \cos^{-1}(3\sqrt{3}\varepsilon/2)/3]. \tag{16}$$

The maximum value of the field strength has been estimated earlier [16] and is expected to reach $E_{\max} = 2.6$ MV/m. Note that even in this extreme case the condition $\varepsilon < 1$ still holds. It implies a simplified formula for the kink's propagation velocity as

$$v = 3\sqrt{JbdR/2} v_0 q_{\text{eff}} E/(aR\Gamma) = \mu_{\text{kink}} E \tag{17}$$

representing the so-called terminal velocity for the given constant electric field E. It is analogous to the drift velocity of electrons as described by Ohm's law. The kink's mobility μ_{kink} depends on the model parameters including the ferroelectric character of the MT *via* the effective charge q_{eff} that enters into the parameter c and elastic properties of the MT that are reflected in the form of the coefficients a and b. The role of viscosity is reflected in the damping coefficient Γ that reduces the kink's propagation velocity.

The analysis of the kink's stability in the absence of an electric field [14] indicates random motion of the kink under the influence of thermal fluctuations. The mean free path of the kink's translational motion is given by the formula:

$$\lambda = b v_0 a^{-\frac{3}{2}} \sqrt[2]{3/2\pi RdJ}. \tag{18}$$

This demonstrates that the strength of nonlinearity manifested by the parameter b increases the length of translational motion. Figure 6 illustrates the kink's spatial dependence.

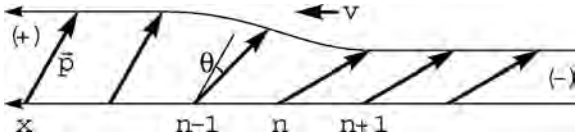

Figure 6. The kink's spatial dependence in terms of the local dipole moment's orientation.

In the following section we will comment on the linear response mechanism for the kink's terminal velocity electric field dependence as a possible control mechanism for a number of intra-cellular processes.

5. Summary and Conclusions

In this paper we argued that GTP hydrolysis, taking place as a result of tubulin assembly into MTs, leads to a combination of mechanical and electrical energy propagating along the MT axis in the form of a kink excitation. The first point made in this connection was that the difference in the electrical properties of the two MT ends leads to the emergence of piezoelectric properties of MTs, creating an intrinsic electric field along the MT axis. The intensity of this field depends on the length of the MT as well as on the physiological conditions of the solution (pH, ion concentration and temperature) due to screening effects by counter-ions. The shorter the MTs, the stronger the field (potential gradient) and the greater the kink's propagation velocity. Faster kinks possess a greater kinetic energy and hence a greater impact is expected on the MT structure that may become destabilized by this energy deposition at the distant end. If the distant tip is already weakened by either mechanical tension or a diminished lateral cap, the effects of kink energy can cause a catastrophic disassembly of the entire MT. Below we list some experimental evidence in support of this hypothesis:

a) If tubulin used in assembly experiments contains a non-hydrolysable analog of GTP, very stable MTs are polymerized. This precludes the formation of kink excitations [17].
b) Conversely, the addition of Ca^{2+} ions to the solution leads to an increased rate of GTP hydrolysis and hence a higher frequency of catastrophes [18] which would indicate a faster production of kink excitations.
c) Adding vinblastine to the solution results in the capping of MT tips and an increased MT stability despite GTP hydrolysis [19]. We postulate that the kinks can still be formed but that their effects are eliminated by the capping process.
d) Similarly, microtubule-associated proteins (MAPs) stabilize MTs, especially in neurons, by interconnecting them and forming a scaffold-like structure. The presence of MAPs reduces dramatically the frequency of catastrophes and we suggest that part of their role is to impede the generation and movement of kinks by forming inhomogeneities and structural obstacles to their propagation. The scattering potentials created in this manner lead to either trapping or reflection of propagating kinks preventing them from reaching the MTs tips [16]. Consequently, increasing the number of MAPs enhances the stability of interconnected MTs.

We now turn our attention to the role played by MTs in motor protein transport involving the kinesin and dynein super-families. Note that the terminal velocity of a propagating kink is an average velocity due to electric field effects (see Eq. 17),

combined with random effects due to thermal fluctuations (see Eq. 18). If a propagating kink encounters a motor protein bound to the filament, it may cause a tug-of-war effect on the motor [1], disrupting the otherwise unidirectional movement of the kink. In this connection, it is instructive to estimate the kink's propagation velocity. For a stable MT with an approximate length of $L = 4\ \mu$m, the intrinsic electric field in the central region can be calculated to be:

$$E = Q/(\pi \varepsilon_0 \varepsilon_r L^2). \tag{19}$$

Taking $Q = 13$ e, i.e. one excess charge per protofilament, and estimating the relative dielectric constant to lie in the range $10 < \varepsilon_r < 80$, we find that the electric field is expected to lie in the range $0.5\ \text{V/m} < E < 5\ \text{V/m}$ resulting in the window of kink propagation velocities being

$$0.2\ \mu\text{m/s} < v_{\text{kink}} < 2\ \mu\text{m/s}. \tag{20}$$

It is interesting to note that, depending on the ATP and salt concentrations, and the load placed on the kinesin molecule, kinks propagate along MTs with velocities ranging between $0\ \mu$ m/s $< v_{\text{kinesin}} < 0.9\ \mu$m/s, i.e. there is a strong overlap in the velocities of the two types of biological motions that may interact with each other. Using an easy-to-grasp analogy, the kinesin motor can be viewed as a surfer and the moving kink as a water wave. Thus, when properly matched, the motor may be able to "catch the wave" and travel on its crest for a while. Conversely, when the two objects travel in opposite directions, the motor protein may experience a "tug-of-war" effect in trying to overcome the disruptive influence of the wave impacting on its motion.

How are proteins, with their very diverse functional roles in the cell, able to produce mesoscopic and even macroscopic movements in a co-ordinated fashion? The answer to this question is still largely unknown. For example, the formation of the mitotic spindle apparatus and the process of chromosome segregation require a concerted effort of force generation by kinetochore microtubules and a simultaneous action of kinesin and dynein motors. In a process as important as cell division, mistakes that would be a frequent occurrence if random thermal fluctuation were to rule, must be necessarily eliminated. Within the framework of our model proposed in this paper, MTs are not only passive tracks for active transport in the cell but also signal relays for electrical, mechanical and chemical stimuli that may be transduced over distances compared to the cell size. Additionally, the cell can control the magnitude of the electric field induced by a MT by changes in the salt and ion concentration as well as pH values. In summary, the present hypothesis and the model developed in this paper offers new insights into intracellular molecular processes related to MT dynamics. Some of the predictions made here can be tested with experimental tools such as Mössbauer spectroscopy [20] or neutron scattering with deuterium labelling that would enable the verification of

the magnitude of tubulin conformational changes and their propagation due to GTP hydrolysis [11].

Acknowledgments

This research was supported by grants from NSERC and MITACS.

References

1. Gross, S.P.: Hither and Yon: A Review of Bi-Directional Microtubule-Based Transport, *Phys. Biol.* **1** (2004), R1–R11.
2. Alberts, B., Bray, A., Lewis, D., J., Ratt, M. Roberts, K. and Watson, J.D.: *Molecular Biology of the Cell*, Garland Press, New York, 2000.
3. Mitchison, T.J. and Kirchner, M.V.: Dynamic Instability of Microtubule Growth, *Nature* **312** (1984), 232–235.
4. Tulub, A.A.: Mg^{2+} Cofactor in a Triplet State Reduces a Proton pf a Coordinated Water Molecule to the Hydrogen Atom and Pushes it out of the Complex at a High Speed, *Biofizika* (Russian) **47** (2002), 20–26.
5. Hol, W.G.: The Role of the α-Helix Dipole in Protein Function and Structure, *Prog. Biophys. Mol. Biol.* **45** (1985), 149–195.
6. H. Athenstaedt, Pyroelectric and piezoelectric properties of vertebrates, *Ann. NY Acad. Sci.* **238** (1974), 68–93.
7. Weitzel, E.K., Tasker, R. and Brownell, W.E.: Outer Hair Cell Piezoelectricity; Frequency Response Enhancement and Resonance Behavior, *J. Acoust. Soc. Am.* **114** (2003), 1462–1466.
8. Tuszynski, J.A., Carpenter, E.J., Crawford, E., Brown, J.A., Malinski, W. and Dixon, J.M.: Molecular dynamics calculations of the electrostatic properties of tubulin and their consequences for microtubules, in W. Badawy and W. Moussa (eds.) *Proceedings of ICMENS 2003, International Conference on MEMS, NANO and Smart Systems, Banff*, IEEE Computer Society, Los Alamitos, CA, 2003, pp. 56–61.
9. Baker, N., Sept, D., Joseph, S., Holst, M.J. and McCammon, J.A.: Electrostatics of Nanosystems: Application to Microtubules the Ribosome, *Proc. Natl. Acad. Sci. U.S.A* **98** (2001), 10037–10041.
10. Sataric, M.V., Tuszynski J.A. and Zakula R.B.: Kinklike Excitations as an Energy-Transfer Mechanism in Microtubules, *Phys. Rev. E* **48** (1993), 589–597.
11. Zaccai, G.: How Soft is a Protein? A Protein Dynamic Force Constant Measured by Neutron Scattering, *Science* **288** (2000), 1604–1607.
12. Vale, R.D. and Milligan, R.A.: The Way Things Move; Looking Under the Hood of Molecular Motor Proteins, *Science* **228** (2000), 88–95.
13. Uyeda, T.Q.P., Abramson, P.D. and Spudich, J.A.: The Neck Region of the Myosin Motor Domain Acts as a Lever Arm to Generate Movement, *Proc. Nat. Acad. Sci. U.S.A* **93** (1996), 4459–4464.
14. Sataric, M.V. and Tuszynski, J.A.: The Relationship Between the Nonlinear Ferroelectric and Liquid Crystal Models for Microtubules, *Phys. Rev. E* **67** (2003), 011901-1–011901-11.
15. Chretien, D., Flyvbjerg, H. and Fuller, S.: Limited Flexibility of the Inter-Protofilament Bonds in Microtubules Assembled from Pure Tubulin, *Eur. Biophys. J.* **27** (1998), 490–500.
16. Trpisova, B. and Tuszynski, J.A.: A Possible Link Between GTP Hydrolysis and Solitary Waves in Microtubules, *Phys. Rev. E* **55** (1997), 3288–3302.
17. Mejillano, M.R., Barton, J.S. and Himes, R.H.: Stabilization of Microtubules by GTP Analogues, *Biochem. Biophys. Res. Commun.* **166** (1990), 653–660.

18. O'Brien, E. T., Salmon, E.D. and Erickson, H.P.: How Calcium Causes Microtubule Depolymerization, *Cell Motil. Cytoskeleton* **36** (1997), 125–135.
19. Dhamodharm, R., Jordan, M.A., Thrower, D., Wilson, L. and Wadsworth, P.: Vinblastine Suppresses Dynamics of Individual Microtubules in Living Interphase Cells, *Mol. Biol. Cell* **6** (1995), 1215–1229.
20. Sataric, M.V., Zekovic, S., Tuszynski, J.A. and Pokorny, J.: The Mössbauer Effect as a Possible Tool in Detecting Nonlinear Excitations in Microtubules, *Phys. Rev. E* **58** (1998), 6333–6339.

Results: 10
(from All Databases)

You searched for: AUTHOR: (satari c b*) ...More

Create an alert

Refine Results

Search within results for...

Filter results by:

Open Access (1)

Refine

Publication Years

2020 (1)
2018 (1)
2016 (2)
2015 (2)
2011 (2)

more options / values...

Refine

Research Domains

SCIENCE TECHNOLOGY (10)
SOCIAL SCIENCES (1)

Refine

Databases

Web of Science Core Collection (10)

Refine

Document Types

Funding Agencies

Authors

Authors - Korean

View all options

For advanced refine options, use
Analyze Results

Select Page Export... Add to Marked List

Analyze Results
Create Citation Report

1. **Calcium ions tune the beats of cilia and flagella**
By: Sataric, Miljko, V; Nemes, Tomas; Sataric, Bogdan; et al.
BIOSYSTEMS Volume: 196 Article Number: 104172 Published: OCT 2020
View Abstract
Times Cited: 0 *(from All Databases)*
Usage Count

2. **Nonlinear calcium ion waves along actin filaments control active hair-bundle motility**
By: Tuszynski, Jack A.; Sataric, Miljko V.; Sekulic, Dalibor L.; et al.
BIOSYSTEMS Volume: 173 Special Issue: SI Pages: 181-190 Published: NOV 2018
Full Text from Publisher View Abstract
Times Cited: 2 *(from All Databases)*
Usage Count

3. **Nonlinear dynamics of C-terminal tails in cellular microtubules**
By: Sekulic, Dalibor L.; Sataric, Bogdan M.; Zdravkovic, Slobodan; et al.
CHAOS Volume: 26 Issue: 7 Article Number: 073119 Published: JUL 2016
Full Text from Publisher View Abstract
Times Cited: 8 *(from All Databases)*
Usage Count

4. **Hybrid OpenMP/MPI programs for solving the time-dependent Gross-Pitaevskii equation in a fully anisotropic trap**
By: Sataric, Bogdan; Slavnic, Vladimir; Belic, Aleksandar; et al.
COMPUTER PHYSICS COMMUNICATIONS Volume: 200 Pages: 411-417 Published: MAR 2016
Full Text from Publisher Free Published Article From Repository
View Abstract
Times Cited: 52 *(from All Databases)*
Usage Count

5. **Role of nonlinear localized Ca2+ pulses along microtubules in tuning the mechano-sensitivity of hair cells**
By: Sataric, Miljko V.; Sekulic, Dalibor L.; Sataric, Bogdan M.; et al.
PROGRESS IN BIOPHYSICS & MOLECULAR BIOLOGY Volume: 119 Issue: 2 Pages: 162-174 Published: NOV 2015
Full Text from Publisher View Abstract
Times Cited: 3 *(from All Databases)*
Usage Count

6. **Actin filaments as the fast pathways for calcium ions involved in auditory processes**
By: Sataric, Miljko V.; Sekulic, Dalibor L.; Sataric, Bogdan M.
JOURNAL OF BIOSCIENCES Volume: 40 Issue: 3 Pages: 549-559 Published: SEP 2015
Full Text from Publisher View Abstract
Times Cited: 4 *(from All Databases)*
Usage Count

7. **Ionic Pulses along Cytoskeletal Protophilaments**
By: Sataric, M. V.; Sataric, B. M.
Conference: 9th International Frohlich's Symposium on Electrodynamic Activity of Living Cells - Including Microtubule Coherent Modes and
Times Cited: 5 *(from All Databases)*
Usage Count

Cancer Cell Physics Location: Prague, CZECH REPUBLIC Date: JUL 01-03, 2011
Sponsor(s): Acad Sci, Inst Photon & Elect; Charles Univ, First Fac Med; IEEE; HEKA Elekt

9TH INTERNATIONAL FROHLICH'S SYMPOSIUM: ELECTRODYNAMIC ACTIVITY OF LIVING CELLS (INCLUDING MICROTUBULE COHERENT MODES AND CANCER CELL PHYSICS) Book Series: Journal of Physics Conference Series Volume: 329 Article Number: 012009 Published: 2011

View Abstract

8. **Nonlinear ionic pulses along microtubules**

By: Sekulic, D. L.; Sataric, B. M.; Tuszynski, J. A.; et al.

EUROPEAN PHYSICAL JOURNAL E Volume: 34 Issue: 5 Article Number: 49 Published: MAY 2011

Full Text from Publisher View Abstract

Times Cited: 43
(from All Databases)
Usage Count

9. **ACTIN FILAMENTS AS NONLINEAR RLC TRANSMISSION LINES**

By: Sataric, M. V.; Bednar, N.; Sataric, B. M.; et al.

INTERNATIONAL JOURNAL OF MODERN PHYSICS B Volume: 23 Issue: 22 Pages: 4697-4711 Published: SEP 10 2009

Full Text from Publisher View Abstract

Times Cited: 9
(from All Databases)
Usage Count

10. **Nonlinear model of microtubule dynamics**

By: Sataric, MV; Sataric, BM; Tuszynski, JA

Conference: International Symposium on Coherence and Electromagnetic Fields in Biological Systems Location: Prague, CZECH REPUBLIC Date: JUL 01-04, 2005
Sponsor(s): Acad Sci Czech Republ; Charles Univ, Med Fac; Minist Hlth Care Czech Republ; IEEE; Int Union Radio Sci

ELECTROMAGNETIC BIOLOGY AND MEDICINE Volume: 24 Issue: 3 Pages: 255-264 Published: 2005

Full Text from Publisher View Abstract

Times Cited: 6
(from All Databases)
Usage Count

Select Page Export... Add to Marked List

Sort by: Date Times Cited Usage Count Recently Added More

1 of 1

Show: 10 per page

10 records matched your query of the 51,527,230 in the data limits you selected.

Citation report for 10 results from All Databases between 1980 and 2021 Go

You searched for: **AUTHOR:** (sataric b*) ...More

This report reflects citations to source items indexed within All Databases.

Export Data: Save to Excel File

Total Publications	*h*-index	Sum of Times Cited	Citing articles
10 Analyze	5	132	110 Analyze
2001 2020	Average citations per item: 13.2	Without self citations: 119	Without self citations: 103 Analyze

Sum of Times Cited per Year

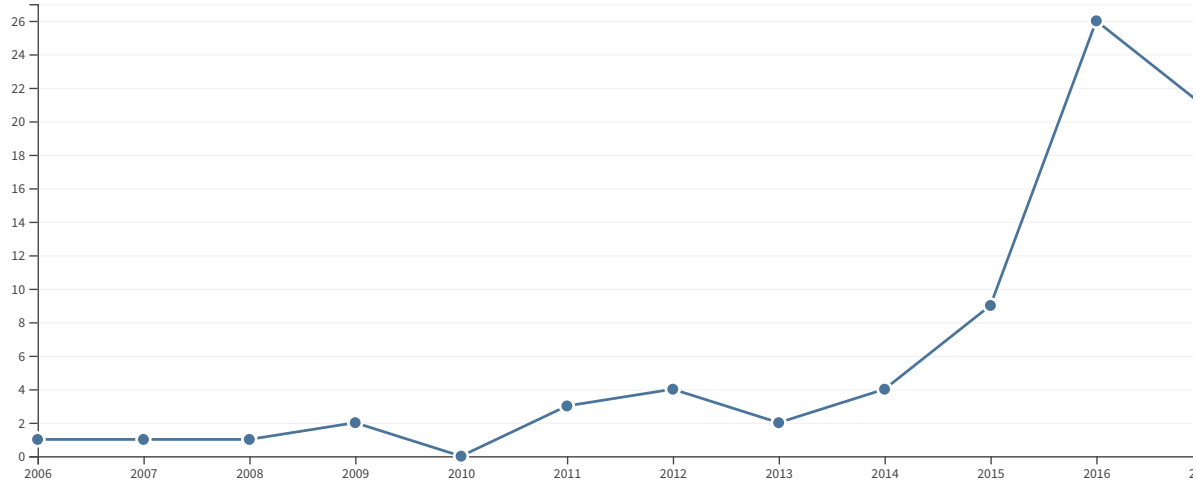

Sort by: Times Cited Recently Added More 1 of 1

How are these totals calculated?

2017	2018	2019	2020	2021	Total	Average Citations per Year
21	20	25	13	0	132	8.80

Use the checkboxes to remove individual items from this Citation Report

or restrict to items published between 1980 and 2021 Go

1.	**Hybrid OpenMP/MPI programs for solving the time-dependent Gross-Pitaevskii equation in a fully anisotropic trap** By: Sataric, Bogdan; Slavnic, Vladimir; Belic, Aleksandar; et al. **COMPUTER PHYSICS COMMUNICATIONS** Volume: 200 Pages: 411-417 Published: MAR 2016	14	7	12	4	0	52	10.40
2.	**Nonlinear ionic pulses along microtubules** By: Sekulic, D. L.; Sataric, B. M.; Tuszynski, J. A.; et al. **EUROPEAN PHYSICAL JOURNAL E** Volume: 34 Issue: 5 Article Number: 49 Published: MAY 2011	3	7	7	4	0	43	4.30
3.	**ACTIN FILAMENTS AS NONLINEAR RLC TRANSMISSION LINES** By: Sataric, M. V.; Bednar, N.; Sataric, B. M.; et al. **INTERNATIONAL JOURNAL OF MODERN PHYSICS B** Volume: 23 Issue: 22 Pages: 4697-4711 Published: SEP 10 2009	2	1	0	0	0	9	0.75
4.	**Nonlinear dynamics of C-terminal tails in cellular microtubules** By: Sekulic, Dalibor L.; Sataric, Bogdan M.; Zdravkovic, Slobodan; et al. **CHAOS** Volume: 26 Issue: 7 Article Number: 073119 Published: JUL 2016	0	3	2	3	0	8	1.60
5.	**Nonlinear model of microtubule dynamics** By: Sataric, MV; Sataric, BM; Tuszynski, JA Conference: International Symposium on Coherence and Electromagnetic Fields in Biological Systems Location: Prague, CZECH REPUBLIC Date: JUL 01-04, 2005 Sponsor(s): Acad Sci Czech Republ; Charles Univ, Med Fac; Minist Hlth Care Czech Republ; IEEE; Int Union Radio Sci **ELECTROMAGNETIC BIOLOGY AND MEDICINE** Volume: 24 Issue: 3 Pages: 255-264 Published: 2005	0	0	0	0	0	6	0.38
6.	**Ionic Pulses along Cytoskeletal Protophilaments** By: Sataric, M. V.; Sataric, B. M. Conference: 9th International Frohlich's Symposium on Electrodynamic Activity of Living Cells - Including Microtubule Coherent Modes and Cancer Cell Physics Location: Prague, CZECH REPUBLIC Date: JUL 01-03, 2011 Sponsor(s): Acad Sci, Inst Photon & Elect; Charles Univ, First Fac Med; IEEE; HEKA Elekt **9TH INTERNATIONAL FROHLICH'S SYMPOSIUM: ELECTRODYNAMIC ACTIVITY OF LIVING CELLS (INCLUDING MICROTUBULE COHERENT MODES AND CANCER CELL PHYSICS)** Book Series: Journal of Physics Conference Series Volume: 329 Article Number: 012009 Published: 2011	0	1	3	1	0	5	0.50
7.	**Actin filaments as the fast pathways for calcium ions involved in auditory processes** By: Sataric, Miljko V.; Sekulic, Dalibor L.; Sataric, Bogdan M. **JOURNAL OF BIOSCIENCES** Volume: 40 Issue: 3 Pages: 549-559 Published: SEP 2015	2	1	0	0	0	4	0.67
8.	**Role of nonlinear localized Ca2+ pulses along microtubules in tuning the mechano-sensitivity of hair cells** By: Sataric, Miljko V.; Sekulic, Dalibor L.; Sataric, Bogdan M.; et al. **PROGRESS IN BIOPHYSICS & MOLECULAR BIOLOGY** Volume: 119 Issue: 2 Pages: 162-174 Published: NOV 2015	0	0	0	0	0	3	0.50
9.	**Nonlinear calcium ion waves along actin filaments control active hair-bundle motility** By: Tuszynski, Jack A.; Sataric, Miljko V.; Sekulic, Dalibor L.; et al. **BIOSYSTEMS** Volume: 173 Special Issue: SI Pages: 181-190 Published: NOV 2018	0	0	1	1	0	2	0.67
10.	**Calcium ions tune the beats of cilia and flagella** By: Sataric, Miljko, V; Nemes, Tomas; Sataric, Bogdan; et al. **BIOSYSTEMS** Volume: 196 Article Number: 104172 Published: OCT 2020	0	0	0	0	0	0	0.00

Select Page Save to Excel File

УНИВЕРЗИТЕТ
У НОВОМ САДУ

ФАКУЛТЕТ
ТЕХНИЧКИХ НАУКА

Трг Доситеја Обрадовића 6, 21000 Нови Сад, Република Србија
Деканат: 021 6350-413; 021 450-810; Централа: 021 485 2000
Рачуноводство: 021 458-220; Студентска служба: 021 6350-763
Телефакс: 021 458-133; e-mail: ftndean@uns.ac.rs

ИНТЕГРИСАНИ СИСТЕМ МЕНАЏМЕНТА СЕРТИФИКОВАН ОД:

Број уверења: ФТН-012-12006
Број досијеа: ДР 348/2009
Нови Сад, 26. 06. 2017.

На основу члана 161. Закона о општем управном поступку („Сл. лист СРЈ“ бр. 33/97 и 31/2001) и („Сл. гласник РС“ бр. 30/2010), у складу са чланом 99. Закона о високом образовању („Сл. гласник РС“ бр. 76/05, 100/07 - аутентично тумачење, 97/08, 44/2010, 93/2012, 89/2013, 99/2014, 45/2015 - аутентично тумачење, 68/2015 и 87/2016) и члана 145. Статута Факултета техничких наука, издаје се:

У В Е Р Е Њ Е
О СТЕЧЕНОМ ВИСОКОМ ОБРАЗОВАЊУ НА ДОКТОРСКИМ АКАДЕМСКИМ СТУДИЈАМА
САТАРИЋ (МИЉКО) БОГДАН

Рођен 12. 12. 1983. године у Београду, општина Звездара, Република Србија, уписан школске 2009/2010. године, а дана 26. 06. 2017. године завршио је докторске академске студије трећег степена на студијском програму: Рачунарство и аутоматика.

Кандидат је завршио студије у трајању од три године, обима 180 (сто осамдесет) бодова ЕСПБ са просечном оценом 10,00 (десет и 00/100).

Наслов докторске дисертације је: ПАРАЛЕЛНО ТРАНСПОНОВАЊЕ ПОДАТАКА У ОКВИРУ НУМЕРИЧКОГ АЛГОРИТМА ЗА РЕШАВАЊЕ ГРОС-ПИТАЕВСКИ ЈЕДНАЧИНЕ.

На основу тога издаје се ово уверење о стеченом високом образовању и научном називу ДОКТОР НАУКА - ЕЛЕКТРОТЕХНИКА И РАЧУНАРСТВО.

Уверење се издаје на лични захтев и може се употребити до издавања дипломе под бројем: 012-ДС-30/Е2, серијски број: UNS06PD15165.

Декан

Проф. др Раде Дорословачки